Highly-resolved numerical simulation of turbulent premixed and stratified combustion under adiabatic and non-adiabatic conditions with tabulated chemistry

Von der Fakultät für Ingenieurwissenschaften, Abteilung Maschinenbau und Verfahrenstechnik

der

Universität Duisburg-Essen

zur Erlangung des akademischen Grades

eines

Doktors der Ingenieurwissenschaften

Dr.-Ing.

genehmigte Dissertation

von

Fabian Proch
aus
Leverkusen

Gutachter: Univ.-Prof. Dr.-Ing. Andreas M. Kempf
Prof. Dr. Luc Vervisch

Tag der mündlichen Prüfung: 17.11.2016

Preface

This thesis was developed during my time as a doctoral candidate at the Chair of Fluid Dynamics at the University of Duisburg-Essen. I am very grateful to the head of the chair, Prof. Dr.-Ing. Andreas Kempf, for giving me the opportunity of a PhD under his supervision, for the support and inspiration he gave me during my PhD time and for the opportunity to present my work at the leading international conferences in the field of turbulent combustion which led to many helpful contacts with other researches.

I would like to thank Prof. Luc Vervisch and Dr. Pascale Domingo from the CORIA laboratories at the University of Rouen for the time I spent working in their group and for fruitful discussions and collaborations. I further want to thank Prof. Luc Vervisch for his willingness to report on my work.

I am grateful to my colleagues at the Chair of Fluid Dynamics for the great working atmosphere, helpful discussions and for the good time we had together. Specials thanks to Andreas Rittler and Martin Rieth for proof-reading this work and furthermore for many nice hours at conferences and after work. I also would like to thank Dr.-Ing. Irenäus Wlokas for helpful discussions and furthermore the colleagues at the CORIA laboratories and at the Imperial College London for being so nice and helpful during my stays there.

Finally, I want to thank my parents Ute and Peat and my siblings Rabea, Simon and Severin for who I am and for always believing in me. I am deeply grateful to Tanja for her love and support and for making life so wonderful.

Everything should be made as simple as possible, but no simpler.

attributed to Albert Einstein

Contents

List of Figures

List of Tables

Nomenclature

Latin symbols

a	Model parameter in dynamic power law sub-filter wrinkling factor model
a_{jk}	Number of j-atoms in a molecule of the species k
A_l	Surface area of the control volume surface l [m^2]
a_l	Runge-Kutta coefficient for the sub-step l
a_n	Strain rate component in flame normal direction [1/s]
a_t	Strain rate component tangential to the flame front [1/s]
b_l	Runge-Kutta coefficient for the sub-step l
b_m	Filter coefficients
C	Normalized reaction progress variable
c	Speed of sound [m/s]
c_p	Specific heat capacity at constant pressure of the mixture [J/(kg K)]
$c_{p,k}$	Specific heat capacity at constant pressure of the species k [J/(kg K)]
C_m	Modeling constant for turbulent viscosity model
C_S	Modeling constant for turbulent viscosity model by Smagorinsky
D	Fractal dimension
d	Dimensionality of the problem
d	Nozzle diameter [m]
D_k	Mixture-averaged diffusion coefficient for the species k [m/s^2]
D_{kj}	Binary diffusion coefficient between the species k and j [m/s^2]
D_m	Differential operator depending on the filtered velocity field
E	Efficiency function
F	Thickening factor ATF model
f_i	Components of an arbitrary vectorial quantity
f_L	Heat loss factor
σ	Characteristic domain size
h	Sum of chemical and sensible enthalpy of the mixture [J/kg]
h_k	Sum of chemical and sensible enthalpy of the species k [J/kg]
h_N	Normalized sum of chemical and sensible enthalpy of the mixture
$j_{i,C}$	Correction velocity in i-direction to ensure mass continuity for the Hirschfelder and Curtiss approximation [kg/(m$^2 s$)]
$j_{i,k}$	Diffusive mass flux of the species k in i-direction [kg/(m$^2 s$)]
K	Filter Kernel
K	Number of chemical species
$k_{i,k}$	Volume force acting on the species k in i-direction, e.g. gravity or electromagnetic forces [m/s^2]
L	Characteristic length for the turbulence of the flow [m]
L	Turbulent integral lengthscale [m]

l	Index for Runge-Kutta sub-step
L_i	Amplitude variation of the ith characteristic wave
L_{ij}	Leonard stresses [Pa]
$\dot{m}$	Mass flow rate [kg/s]
N	Number of filter points
n	Number of grid point on which the flame is resolved in the ATF approach
n_i	Components of face normal vector
n_t	Number of time steps
P	Filtered density function
p	Pressure [Pa]
q_i	Rate of progress of the i^{th} reaction [kg/(m^3 s)]
R	Gas constant, $R = 8.3144621$ [J/(K mol)]
r	Ratio of successive gradients along the mesh
$\mathrm{r_{xy}}$	Pearson correlation coefficient
S	Fitting constant for Sutherland law [K]
S_c	Consumption speed of the flame [m/s]
S_d	Displacement speed of the flame [m/s]
s_l^0	Laminar flame speed [m/s]
T	Temperature [K]
T_0	Reference temperature [K]
U	Characteristic velocity for the turbulence of the flow [m/s]
u_i	Components of the velocity vector [m/s]
u_b	Bulk velocity [m/s]
$\hat{u}_l$	Inlet fluctuations for velocity component l [m/s]
u'	Turbulent velocity fluctuations [m/s]
V	Volume of a control volume [m^3]
W	Molecular weight of the mixture [kg/mol]
W_k	Molecular weight of the species k [kg/mol]
w_l	Runge-Kutta coefficient for the sub-step l
$[X_k]$	Molar concentration of the species k [mol/m^3]
$\mathcal{X}_k$	Chemical symbol for the species k
X_k	Molar fraction of the species k
Y_k	Mass fraction of the species k
Y_C	Reaction progress variable
Z	Mixture fraction as described by Bilger
Z_{fl}	Lean flammability limit
Z_{fr}	Rich flammability limit
Z_j	Element mass fraction of the species k

Greek symbols

β	Modeling parameter in Charlette sub-filter wrinkling model
γ	Effective filter width ratio
γ	Ratio of specific heats
Δ	Filter width [m]
Δ	Grid resolution [m]

δ_{ij}	Components of the Kronecker delta, one for i equal j and zero otherwise
$\Delta h^0_{f,k}$	Enthalpy of formation of the species k at the reference temperature T_0 [J/kg]
δ^0_l	Laminar flame thickness [m]
Δ_m	Grid resolution [m]
Δt	Time step width [s]
ϵ	Rate at which energy is transferred within the inertial subrange [m^2/s^3]
η_K	Kolmogorov length scale [m]
Θ_i	Alignment angle between the principal strain rate i and the flame normal vector [rad]
κ_m	Mean principal curvature of the progress variable field [1/m]
λ	Thermal conductivity of the mixture [W/(m K)]
λ_k	Thermal conductivity of the species k [W/(m K)]
μ	Dynamic viscosity of the mixture [Pa s]
μ_0	Viscosity at the reference temperature T_0 for Sutherland law [Pa s]
μ_k	Dynamic viscosity of the species k [Pa s]
μ_t	Turbulent dynamic viscosity [Pa s]
ν	Kinematic viscosity [m^2/s]
ν'_{ki}	Stoichiometric coefficient of the species k in the forward reaction i
ν''_{ki}	Stoichiometric coefficient of species k in the backward reaction i
Ξ	Wrinkling factor
ρ	Fluid density [kg/m^3]
σ	Standard deviation
σ	Under-relaxation factor for the non-reflecting outlet boundary condition
Σ_{gen}	Generalized flame surface density [m^2/m^3]
σ_i	Singular values
τ	Tortuosity of flamelet
τ_{ij}	Components of the stress tensor [Pa]
τ_{ij}^{sgs}	Unresolved fluxes for the LES filter width [Pa]
τ_{ij}^{test}	Unresolved fluxes for the test filter width of the dynamic Germano procedure [Pa]
ϕ	Arbitrary quantity
ϕ_{vc}	Value of the quantity ϕ at the centroid of the control volume surface
ϕ_{vc}	Value of the quantity ϕ at the centroid of the control volume
Ψ	Limiter function for the TVD schemes
ψ	Arbitrary independent variable
Ω	Flame sensor
$\dot{\omega}_k$	Chemical reaction rate of the species k [$kg/(m^3 s)$]

Superscripts

b	State in the burnt gas
N	Normalized quantity
n	Time step
$''$	Temporal fluctuations
s	Computed from the chemical model
$*$	Predicted value
u	State in the unburnt gas

Subscripts

B, b	Bottom cell center, bottom surface
E, e	Eastern cell center, eastern surface
f	Flamelet related quantity
i	Coordinate direction
i	Index of chemical reaction
∞	Undisturbed ambient conditions
k	Species index
l	Index of control volume surface, for cubic control volumes: eastern (e), western (w), southern (s), northern (n), bottom (b) and top (t)
l	Laminar
N, n	Northern cell center, northern surface
r	Resolved
S, s	Southern cell center, southern surface
t	Turbulent
T, t	Top cell center, top surface
W, w	Western cell center, western surface

Mathematical symbols and operators

$\langle\phi\rangle$	Spatial averaging
$\bar{\phi}$	Filtering operation (LES context)
$\widetilde{\phi}$	Mass weighted Favre-filtering operation (LES context)
$\widetilde{\phi}$	Mass weighted Favre temporal averaging operation (RANS context)
$\bar{\phi}$	Temporal averaging operation (RANS context)
$\widehat{\phi}$	Test-filtering operation for dynamic models

Dimensionless numbers

CFL	Courant, Friedrichs, Lewy stability condition number
Da	Damköhler number
Le	Lewis number
Ma	Mach number
Re	Reynolds number
Re_t	Turbulent Reynolds number
Sc	Schmidt number
Sc_t	Turbulent Schmidt number

Abbreviations

ATF	Artificial thickened flame
CCSS	Center for Computational Sciences and Simulation, University of Duisburg-Essen
CDS	Central differencing scheme
CFD	Computational fluid dynamic
DFG	Deutsche Forschungsgemeinschaft (German Research Foundation)
DLR	Deutsches Zentrum für Luft- und Raumfahrt (German aerospace center)
DNS	Direct numerical simulation
FDF	Filtered density function
FGM	Flamelet generated manifolds

FVM	Finite-volume method
GCC	GNU Compiler Collection
HPC	High performance computing
IEA	International Energy Agency
JSC	Jülich Supercomputing Centre
LDA	Laser Doppler anemometry
LES	Large eddy simulation
LHS	Left-hand side of an equation
MPI	Message passing interface
NIC	John von Neumann Institute for Computing
JDF	Joint probability density function
PDF	Probability density function
PFGM	Premixed flamelet generated manifolds
PIV	Particle image velocimetry
RANS	Reynolds-averaged Navier-Stokes simulation
RHS	Right-hand side of an equation
rms	Root mean square
SGS	Sub-grid scale
SOR	Gauss-Seidel method with successive overrelaxation
TNF	Workshop on measurement and computation of turbulent non-premixed flames
TVD	Total variation diminishing
UDS	Upwind differencing scheme
URANS	Unsteady Reynolds-averaged Navier-Stokes simulation

1. Introduction

1.1. Motivation for this work

Combustion is one of the oldest technologies used by mankind, it has always been of vital importance for the development of the human society and technology. For hundreds of thousands of years, combustion of wood was used as a source of heat and light. Attempts to use combustion for the generation of mechanical power reach back to the 1st century AD, where Hero of Alexandria described a simple steam engine. The first relevant implementation of this principal was the atmospheric steam engine presented by Thomas Newcomen in 1712 and improved by James Watt later. This technology initiated the industrial revolution, during which the use of combustion processes for the production of mechanical and electrical power was developed further, resulting in the Otto- and Diesel-engine and the stationary gas turbine at the end of the 19^{th} century.

Today, combustion is still the most important source for the world's energy supply. According to the International Energy Agency (IEA), 91.6% of the world's primary energy supply were generated by combustion in 2013 [78]. This primary energy was delivered to 31.5%, 34.0%, 23.4% and 11.1% from the combustion of coal, oil, natural gas and biofuels including waste, respectively [78]. The energy demand is expected to grow by one-third until 2040, where the share of fossil fuels will decline by approximately 6.0% which will mainly be due to a reduced share of oil and coal [77]. This means that combustion will continue to play a key role in the future energy supply of the world, for certain industrial areas, as the transport of people or goods over long distances by ship or plane, it will stay the dominating power supply technology.

Compared to other available energy sources as nuclear, hydro, wind, solar and geothermal power, the use of combustion is attractive as it allows to build relatively cheap and technically well-understood devices with a high power density that are safe, reliable and easy to maintain and can be operated continuously in all kind of environments. The main disadvantages of combustion are the consumption of fossil fuels and the release of greenhouse gases and pollutants. A solution for the first problem is an enhanced use of biomass and hydrogen obtained from electrolysis as fuels, which is partially done already today. This will also reduce the release of greenhouse gases by a significant amount, which is of crucial importance to limit the global warming [178]. However, the supplementation of fossil fuels will not avoid the emission of pollutants by the combustion process, which is harmful for living beings and the environment. A detailed understanding of the underlying physical and chemical phenomena is required in

order to reduce the pollutant emissions and increase the efficiency of the combustion process. This understanding can be gained from experiments and from numerical simulations, where the simulations have the potential to deliver more detailed insights into the combustion process at lower costs in comparison to the experiments. To keep the computational time required for the numerical simulations in a feasible range, simplified models are required. The subject of this work is to contribute to the validation and further development of models for the numerical simulation of the combustion process.

1.2. Structure of this work

In the subsequent Chapter 2, the physical fundamentals for the description of turbulent reacting flows are presented. The numerical methods that are used to solve the systems of governing equations on modern parallel computer architectures are described in Chapter 3.

Afterwards, the performed model validations and developments are presented in the four Chapters 4-7. These chapters have previously been published in leading international journals in the field of combustion research and are reprinted with the permission of the respective journal.

Chapter 4 presents a large eddy simulation (LES) study of a stratified bluff-body burner with tabulated chemistry, different models for the inclusion of heat losses in tabulated chemistry are compared with LES of a confined gas-turbine model combustor in Chapter 5. To enable a further model development, a direct numerical simulation (DNS) without a sub-filter closure for the combustion model of the same bluff-body burner as investigated in Chapter 4 has been performed, a detailed analysis of the results is presented in Chapter 6. In Chapter 7, the results of the DNS in Chapter 6 have been used to validate models for the sub-filter closure and develop them further in the first step. In the second step, these models were compared in LES with the same setup as the DNS.

The final conclusions and an outlook how the obtained results and models can be used in future work are given in Chapter 8. In addition, the Appendix A gives an overview over the co-author publications of the author of this thesis, and the Appendix B shows the parallel scaling behavior of the developed CFD solver.

2. Physical fundamentals of reacting turbulent flows

The mathematical and physical fundamentals for the description of reacting turbulent flows are presented in this chapter.

2.1. Governing equations

For most engineering applications, the gas phase can be considered as a continuum, as the mean free path length of the gas molecules is sufficiently small compared to the size of the characteristic flow scales. A single-phase flow at constant temperature is then fully described by the temporal and spatial distributions of the values of the three velocity vector components u_i and the pressure p. If chemical reactions are involved, the distributions of the temperature T and of the species mass fractions Y_k need to be known in addition. To obtain the distributions of all these quantities, a coupled system of partial differential equations has to be solved that is described next.

2.1.1. Continuity equation

For a single-phase flow in the absence of nuclear reactions, the mass in a given control volume can only change over time due to convective transport, which is expressed by the continuity equation, where ρ denotes the density of the fluid:

$$\frac{\partial \rho}{\partial t} + \frac{\partial \rho u_i}{\partial x_i} = 0 \tag{2.1}$$

For flows with constant density, Eq. 2.1 reduces to a divergence-free condition for the velocity field.

2.1.2. Momentum equations

The components of the momentum vector inside a given control volume can not only change due to convection but also due to friction and due to the effect of volume forces, this is described

by the Navier-Stokes equations:

$$\frac{\partial \rho u_i}{\partial t} + \frac{\partial \rho u_i u_j}{\partial x_j} = \frac{\partial \tau_{ij}}{\partial x_j} - \frac{\partial p}{\partial x_i} + \rho \sum_{k=1}^{K} Y_k k_{i,k} \tag{2.2}$$

Here, $k_{i,k}$ denotes volume forces as gravity or electromagnetic forces acting on species k in the direction i, the components of the stress tensor τ_{ij} read for a Newtonian fluid:

$$\tau_{ij} = -\frac{2}{3}\mu \frac{\partial u_k}{\partial x_k}\delta_{ij} + \mu \left(\frac{\partial u_i}{\partial x_j} + \frac{\partial u_j}{\partial x_i} \right) \tag{2.3}$$

Here, the dynamic viscosity and the Kronecker delta are denoted by μ and δ_{ij}, respectively.

2.1.2.1. Viscosity

The viscosity of a gas mixture can be computed by the averaging formula given by Wilke [214] and modified by Bird et al. [12]:

$$\begin{aligned} \mu &= \sum_{k=1}^{K} \frac{X_k \mu_k}{\sum_{j=1}^{K} X_j \Phi_{kj}} \\ \Phi_{kj} &= \frac{1}{\sqrt{8}} + \left(1 + \frac{W_k}{W_j}\right)^{-\frac{1}{2}} \left(1 + \left(\frac{\mu_k}{\mu_j}\right)^{\frac{1}{2}} \left(\frac{W_j}{W_k}\right)^{\frac{1}{4}}\right)^2 \end{aligned} \tag{2.4}$$

Here, W_k and μ_k denote the molecular weight and the viscosity of the species k, where the latter are determined from the standard kinetic gas theory expression [74, 83]. The molar fraction of the species k is denoted by X_k, it is computed from:

$$X_k = Y_k \frac{W}{W_k} \tag{2.5}$$

Alternatively, a polynomial fit as given by Sutherland [83, 192] might be used in the CFD-computation to avoid the numerically expensive evaluation of Eq.2.4:

$$\mu = \mu_0 \frac{T_0 + S}{T + S} \left(\frac{T}{T_0}\right)^{\frac{3}{2}} \tag{2.6}$$

Here, μ_0 is the viscosity at the reference temperature T_0, and S represents a fitting constant.

2.1.2.2. Pressure gradient

When inspecting Eqs. 2.1 - 2.3, it can be seen that there exists no transport equation for the pressure p. However, the gradient components of the pressure are needed in the momentum equations 2.2. For gases, the pressure can be computed from an equation of state, which can be

approximated by the ideal gas law for moderate pressures and not too low temperatures:

$$p = \frac{\rho T R}{W} \tag{2.7}$$

Here, R represents the gas constant and W the mean molecular weight of the gas mixture that is computed from:

$$W = \frac{1}{\sum_{k=1}^{K} Y_k / W_k} \tag{2.8}$$

The density ρ is obtained from the continuity equation (2.1), the temperature is either prescribed or computed from the energy equation (2.25) and the mixture composition as described below. The way information is propagated inside the solution domain is determined by the Mach number:

$$\mathrm{Ma} = \frac{u}{c} \tag{2.9}$$

Here, c denotes the speed of sound which can be computed for an ideal gas from:

$$c = \sqrt{\gamma R T / W} \tag{2.10}$$

The ratio of specific heats is denoted by γ. If the Mach number becomes small, as it is the case for the flows investigated in this work, the resulting density change for a given pressure change becomes very small. This results in an ill-conditioned system of equations, which causes problems in the numerical solution. To avoid these problems, a pressure correction method is used that is described in Chapter 3.3.

2.1.3. Species transport equation

For every species k involved, an additional transport equation is formulated for the respective mass fraction Y_k:

$$\frac{\partial \rho Y_k}{\partial t} + \frac{\partial \rho u_i Y_k}{\partial x_i} = -\frac{\partial j_{i,k}}{\partial x_i} + \dot{\omega}_k \tag{2.11}$$

Here, $j_{i,k}$ denotes the diffusive mass flux of the species k in i-direction. The chemical reaction rate of the species k is denoted by $\dot{\omega}_k$.

2.1.3.1. Diffusive mass fluxes

The exact evaluation of the diffusive mass fluxes $j_{i,k}$ requires the solution of a linear equation system of size $K \times K$ at every computational point, with K being the total number of species [152]. A commonly used simplification is the Hirschfelder-Curtiss approximation [74], which can be recast to [83]:

$$j_{i,k} = j^*_{i,k} - Y_k \, j_{i,C} \quad \text{with} \quad j^*_{i,k} = -\rho D_k \frac{\partial Y_k}{\partial x_i} \quad \text{and} \quad j_{i,C} = \sum_{k=1}^{K} j^*_{i,k} \tag{2.12}$$

As the Hirschfelder-Curtiss approximation is not exact, a correction velocity with the components $j_{i,C}$ is needed to ensure continuity (diffusive flux components must sum up to zero). An alternative approach to the correction velocity is to transport only $K-1$ species and then compute the mass fraction of the K^{th} species from:

$$Y_K = 1 - \sum_{k=1}^{K-1} Y_k \tag{2.13}$$

To minimize the error resulting from the use of Eq. 2.13, the K^{th} species mass fraction should be as large as possible, for combustion processes involving air usually nitrogen is chosen. The mixture-averaged species diffusion coefficient D_k is determined for the species k from [83]:

$$D_k = \left(\sum_{j \neq k}^{K} \frac{X_j}{D_{kj}} + \frac{X_k}{1 - Y_k} \sum_{j \neq k}^{K} \frac{Y_j}{D_{kj}} \right)^{-1} \tag{2.14}$$

Here, D_{kj} are the binary diffusion coefficients between the species k and j that are determined from the standard kinetic gas theory expression [74, 83].

A further simplification is the assumption of a constant Lewis number Le (often with a value of unity) for all species:

$$\mathrm{Le} = \frac{\lambda}{\rho D c_p} \tag{2.15}$$

Then, the diffusive mass fluxes $j_{i,k}$ can simply be determined from Fick's law, no correction velocity is needed in this case:

$$j_{i,k} = -\frac{\lambda}{\mathrm{Le}\, c_p} \frac{\partial Y_k}{\partial x_i} \tag{2.16}$$

Here, λ is the thermal conductivity and c_p the mean specific heat capacity at constant pressure of the mixture:

$$c_p = \sum_{k=1}^{K} c_{p,k} Y_k \tag{2.17}$$

$$\lambda = \frac{1}{2} \left(\sum_{k=1}^{K} X_k \lambda_k + \frac{1}{\sum_{k=1}^{K} X_k / \lambda_k} \right) \tag{2.18}$$

Here, the pure species thermal conductivities λ_k are computed based on the viscosities from the standard gas kinetic theory expression as described by Warnatz [83, 140] and others. The pure species heat capacities at constant pressure $c_{p,k}$ are determined from the NASA polynomials as described by McBride et al. [116] or Kee et al. [83].

2.1.3.2. Chemical reaction rates

The conversion from educt to product species does actually not occur in the form of simple global reactions, but rather via a system of I (intermediate) reactions which can be expressed in the general form:

$$\sum_{k=1}^{K} \nu'_{ki} \mathcal{X}_k \Leftrightarrow \sum_{k=1}^{K} \nu''_{ki} \mathcal{X}_k \tag{2.19}$$

Here, i, $\mathcal{X}_k$, ν'_{ki} and ν''_{ki} denote the number of the reaction, the chemical symbol for the species k, the stoichiometric coefficient of the forward reaction and the stoichiometric coefficient of the reverse reaction, respectively. The rate of progress of the i^{th} reaction is computed from:

$$q_i = k_{f,i} \prod_{k=1}^{K} [X_k]^{\nu'_{ki}} - k_{r,i} \prod_{k=1}^{K} [X_k]^{\nu''_{ki}} \tag{2.20}$$

Here, $[X_k]$ represents the molar concentration of the species k, which is calculated from:

$$[X_k] = Y_k \frac{\rho}{W_k} \tag{2.21}$$

The forward and reverse rate constant of the i^{th} reaction are denoted by $k_{f,i}$ and $k_{r,i}$, respectively. The forward rates are computed from Arrhenius expressions, more complex expression become necessary for three-body reactions, pressure dependent reactions and fall-off reactions. The reverse rates are determined based on the forward rate constant and the equilibrium constant from the law of mass action. The detailed formulation for the computation of the forward and reverse rate constants can be found for example in the book of Kee et al. [83]. The reaction rate for a species k is then determined by summing up the rates of progress from all reactions that the species is involved in:

$$\dot{\omega}_k = \sum_{i=1}^{I} \left(\nu''_{ki} - \nu'_{ki}\right) q_i \tag{2.22}$$

2.1.4. Energy equation

Various possibilities exist for the choice of the energy equation, an overview is given in the book of Poinsot & Veynante [152]. In the present work, the sum of sensible and chemical enthalpy is chosen as the transported quantity:

$$h_k = \int_{T_0}^{T} c_{p,k} \mathrm{d}T + \Delta h^0_{f,k} \tag{2.23}$$

Here, $\Delta h^0_{f,k}$ denotes the enthalpy of formation at the reference temperature T_0. Transported is the mean enthalpy of the mixture computed from:

$$h = \sum_{k=1}^{n_k} h_k Y_k \tag{2.24}$$

Here, the pure species enthalpy h_k is determined from the NASA polynomials as described in [83, 116]. The transport equation for the mean enthalpy then reads:

$$\frac{\partial \rho h}{\partial t} + \frac{\partial \rho u_i h}{\partial x_i} = \frac{\partial}{\partial x_i}\left(\frac{\lambda}{c_p}\frac{\partial h}{\partial x_i} - \sum_{k=1}^{K} h_k\, j_{i,k}\right) + \tau_{ij}\frac{\partial u_i}{\partial x_j} + \frac{\mathrm{D}p}{\mathrm{D}t} + \left(\sum_{k=1}^{K} k_{i,k}\, j_{i,k}\right) + \dot{Q} \tag{2.25}$$

The first term on the RHS gives the heat flux due to heat conductivity, the second term the enthalpy flux caused by the species diffusive fluxes. The remaining RHS terms are due to viscous heating, temporal and spatial pressure variation, the effect of volume forces and enthalpy changes due to radiation or other sources of energy, respectively. All of these remaining RHS terms are approximately zero in the computations considered in this work and therefore are neglected. It will be shown in Chapter 5 that neglecting the radiation is a valid assumption for the investigated cases, although radiation can play a very important role in other combustion processes. For higher Mach-numbers, the effect of the pressure variation term also becomes important.

2.2. Modeling of combustion

The process that is investigated in this work is the combustion process, during which fuel and oxidizer react to exhaust gas and release heat. The combustion process consists of a large number of elementary reactions and intermediate species, for example the combustion of a simple hydrocarbon fuel as methane already results in a chemical mechanism of several dozen species and several hundred reactions. For simple one and two dimensional cases the full system of equations can be solved, but for three dimensional turbulent flames as investigated in this work this is mostly prohibitive due to the excessive computational costs. Therefore, reduction techniques have been developed to reduce the size of the chemical system under certain simplifying assumptions.

2.2.1. Reduced chemical mechanisms

The most general approach to model the combustion process is based on the observation that chemical mechanisms often can be reduced drastically in size if only a certain range of initial composition, temperature and pressure needs to be covered. Furthermore, often one is only interested in accurate prediction of a limited number of species, which enables a further reduction

of the chemical mechanism size. Different methods exist to perform the reduction either based on detailed knowledge of the chemical processes or on optimization techniques as generic algorithms [185, 186] or brute-force methods [217]. A comprehensive overview on the topic was given by Tomlin et al. [198]. Although the resulting mechanisms are strongly reduced in size, they are most of the time still too large to be applied within CFD simulations of realistic geometries. Therefore, specially designed chemical mechanisms consisting of just a few reactions are usually used in CFD simulations, which are basically multi-dimensional fits that preserve certain global flame properties as flame propagation speed, flame thickness or ignition delay time but do not necessarily give a realistic distribution of all involved species.

2.2.2. Premixed flames

Often, further assumptions can be made on the flame structure, which enables one to develop models that require less numerical effort and have higher accuracy than strongly reduced mechanisms. In premixed flames, fuel and oxidizer are mixed before the combustion occurs, which usually results in a thin flame front that propagates at a certain displacement speed towards the unburnt gas.

One possible modeling strategy is to consider the flame front as a thin interface between fresh and burnt gas which propagates in normal direction with the speed of a laminar one-dimensional flame S_L. The laminar one-dimensional flame can often be solved using the full chemical mechanism in a few minutes with specialized reaction kinetic libraries as 'Cantera' [64]. If available, experimental measured values for S_L can also be used.

The flame front can either be tracked by a level-set method referred to as the G-equation [47, 123, 139, 147], or by solving a transport equation for the normalized reaction progress variable C [13]:

$$\frac{\partial \rho C}{\partial t} + \frac{\partial \rho u_i C}{\partial x_i} = \rho_u S_L |\nabla C| \quad \text{with} \quad C = \frac{Y - Y_u}{Y_b - Y_u} \tag{2.26}$$

Here, the subscripts u and b denote the state in the unburnt and burnt gas, respectively. The normalized progress variable C can be based on any species Y that evolves monotonically throughout the laminar flame.

A less restrictive technique than tracking the flame front is the flamelet approach, where it is assumed that the (turbulent) three-dimensional flame structure consists of an ensemble of one-dimensional laminar model flames. These one-dimensional laminar model flames are computed prior to the CFD simulation with a reaction kinetic library, quantities needed for the CFD simulation such as transport coefficients and sources terms are stored in a lookup-table as a function of one or more representative species mass fractions. Mostly, either freely-propagating flames or premixed counter-flow flames are used as laminar one-dimensional model flames. This technique has been introduced for premixed flames as FPI (flame prolongation of intrinsic low-dimensional manifolds (ILDM) [113]) [54, 63], in this work the similar PFGM (premixed flamelet generated manifolds) approach by van Oijen et al. [202, 204] is used. During the CFD

simulation, transport equations are solved for the controlling species mass fractions, the source terms and transport coefficients are then obtained from the lookup-table as a function of the local values of the controlling species mass fractions.

2.2.3. Non-premixed flames

In non-premixed flames, fuel and oxidizer enter the reaction zone separately, the combustion is hence mixing-controlled and occurs in a thicker layer than in a premixed flame. As in the premixed case, the flamelet approach is widely used also for non-premixed flames. The flamelets are generated based on laminar one-dimensional non-premixed counter-flow flames. As the combustion is diffusion controlled, it can be described by one or more element mass fractions:

$$Z_j = \sum_{k=1}^{K} a_{jk} \frac{W_j}{W_k} Y_k \tag{2.27}$$

Here, a_{jk} denotes the number of j-atoms in a molecule of the species k, W_j and W_k denote the atomic weight of the j-atom and the k-molecule, respectively. Often, the mixture fraction Z is used which is the normalized element mass fraction as described by Bilger [11]. As the element mass fractions are preserved during a reaction, the transport equations that need to be solved in the CFD-simulation have a chemical reaction rate of zero and thus describe a passive scalar transport, for example the transport equation for the mixture fraction Z reads [139]:

$$\frac{\partial \rho Z}{\partial t} + \frac{\partial \rho u_i Z}{\partial x_i} = \frac{\partial}{\partial x_i} \left(\frac{\lambda}{\mathrm{Le}\, c_p} \frac{\partial Z}{\partial x_i} \right) \tag{2.28}$$

Here, a Lewis number of unity has been assumed for all species as described in Section 2.1.3.1.

2.2.4. Partially premixed flames

In many practical cases, the combustion process occurs neither completely under premixed nor completely under non-premixed conditions. This is either because partial mixing occurs before the combustion process starts in a non-premixed burner or because the mixture is not perfectly homogeneous (unwanted or on purpose to enable a globally leaner combustion process) in a premixed burner. For such cases, either a premixed or a non-premixed approach can be extended. The flame tracking methods can be extended by computing the local flame speed as a function of the mixture fraction, which is transported as an additional quantity in the CFD-simulation as done e.g. by Cavallo Marincola et al. [21]. The flamelet approach can also be modified by using the mixture fraction as an additional control variable and computing multiple model flames for varying initial compositions, this has been used e.g. by Kuenne et al. [102] and is also applied in the Chapters 4, 6 and 7. The non-premixed flamelet model can also be extended by a progress variable to work also for partially premixed conditions [181], in this

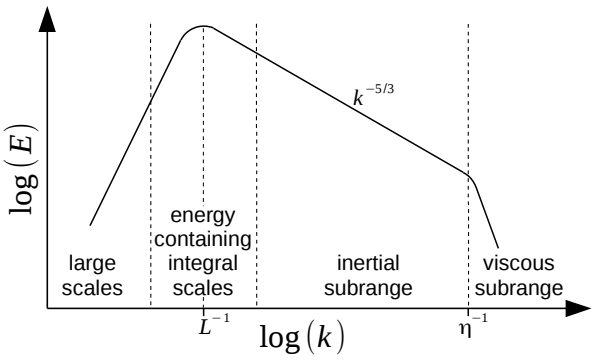

Figure 2.1.: Schematic representation of the spectrum of the turbulent kinetic energy E as a function of the wavenumber k.

case unsteady non-premixed laminar counter-flow flames can be used to generate the flamelet table.

2.3. Modeling of turbulence

Most of the relevant flows in engineering and nature are turbulent, which means that the resulting temporal and spatial profiles of the flow quantities are not smooth and regular as in a laminar flow but fluctuate in a random and chaotic manner. The amount of turbulence in a flow depends on the value of the Reynolds number, which describes the ratio of inertial to viscous forces:

$$\mathrm{Re} = \frac{\rho U L}{\mu} \tag{2.29}$$

Here, U and L denote a characteristic velocity and geometrical length of the flow, respectively. The flow behaves laminar as long as the Reynold number stays below a problem specific critical value and starts to become turbulent if the Reynolds number increases above this value. For example, the flow in a pipe and over a flat plate has a critical Reynolds number based on the pipe diameter and the plate length of around 2,300 and 10^5, respectively.

According to Richardson [169], a turbulent velocity field can be considered as an ensemble of eddies, where the size of the individual eddies varies over a wide range. The largest eddy size is directly proportional to the geometrical dimensions of the flow problem, these largest eddies break up into a number of smaller eddies which they transfer their kinetic energy to. This process is referred to as 'energy cascade', it continues down to a certain smallest eddy size where the kinetic energy of the eddies is dissipated to heat by molecular friction. The smaller the eddies become, the more universal and homogeneous they get and the lower becomes the kinetic energy carried by an individual eddy.

This concept was subsequently developed further by Kolmogorov [100], who described the detailed shape of the resulting energy spectrum as shown in Fig. 2.1. In the range of the large scale eddies, the turbulent kinetic energy increases approximately following a power law with powers between two and four [139]. The maximum turbulent kinetic energy is reached when

the wavenumber corresponds approximately to the inverse integral length scale L as defined in Chapter 6.5. For larger wave numbers than the inverse integral length scale, the turbulent kinetic energy decreases following a power law with a power of approximately $-5/3$, this region is called the 'inertial subrange' and ends when the inverse Kolmogorov scale is reached:

$$\eta_K = \left(\frac{\nu^3}{\epsilon}\right)^{1/4} \tag{2.30}$$

Here, ν denotes the kinematic viscosity and ϵ describes the rate at which the energy is transfered within the inertial subrange, it is related to the integral lengthscale and the related turbulent kinetic energy by:

$$\epsilon \sim \frac{u'^3}{L} \tag{2.31}$$

The definition of the velocity fluctuations u' is also given in Chapter 6.5. For wave numbers higher than the inverse Kolmogorov scale, the remaining eddies are dissipated by molecular friction leading to an exponential decrease of the turbulent kinetic energy.

For turbulent scalar fields, the smallest length scale is the Batchelor scale [8]:

$$\lambda_B = \left(\frac{\nu D^2}{\epsilon}\right)^{1/4} = \frac{\eta_K}{\sqrt{\mathrm{Sc}}} \tag{2.32}$$

Here, Sc denotes the Schmidt number:

$$\mathrm{Sc} = \frac{\nu}{D} \tag{2.33}$$

2.3.1. Direct numerical simulation (DNS)

If the temporal and spatial resolution is high enough to resolve all relevant length scales, the system of the governing equations 2.1, 2.2, 2.11 and 2.25 can be solved without any further modeling. In most of the cases the smallest scale in the flow will be the Kolmogorov scale, the required grid resolution Δ_m is thus:

$$\Delta_m \sim \eta_K \tag{2.34}$$

Substituting Eq. 2.31 in Eq. 2.30 yields the approximate number of grid points to resolve the integral length scale, which depends on the turbulent Reynolds number:

$$\frac{L}{\eta_K} \sim \left(\frac{L\,u'}{\nu}\right)^{3/4} = \mathrm{Re}_t^{3/4} \tag{2.35}$$

As turbulence is three-dimensional and time-dependent, the total required computational effort is proportional to:

$$\left(\mathrm{Re}_t^{3/4}\right)^4 = \mathrm{Re}_t^3 \tag{2.36}$$

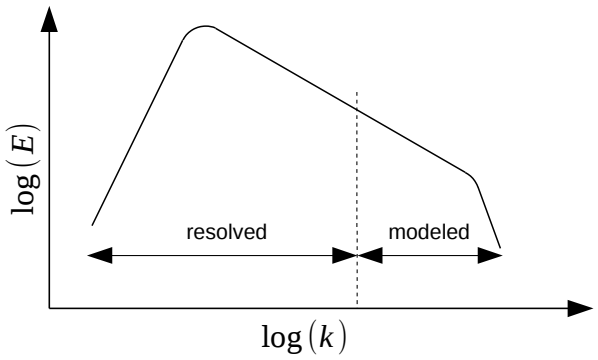

Figure 2.2.: Schematic representation of the resolved and modeled part of the kinetic energy spectrum in a LES.

Due to this cubic dependency on the Reynolds number, DNS is limited to basic research today and will not be possible for most technical relevant flow configurations in the foreseeable future.

However, for the investigation of combustion sub-filter models it is often sufficient to only resolve the major species profiles and the flow scales in the reaction zone. This reduces the numerical cost, as the kinematic viscosity entering Eq. 2.30 is temperature dependent and thus increases inside the flame by one to two orders of magnitude, which results in an increase of the Kolmogorov scale by around one order of magnitude. Such computations might be termed as 'quasi-DNS' and have become computationally affordable at least for realistic lab-scale experiments in the last years. Such a quasi-DNS of a bluff-body burner experiment forms the basis of the analysis presented in the Chapters 6 and 7.

2.3.2. Large eddy simulation (LES)

The idea behind the large eddy simulation approach is to only compute the larger flow scales from the governing equations and to describe the smaller scales by simpler models, as shown in Fig. 2.2. This way the excessive computational costs of a DNS can be avoided and thus more realistic flow problems can be simulated. As the smaller scales are more homogeneous and universal than the larger scales, they can be described by relatively simple models. The removal of the small scales from the solution in a LES is achieved by filtering of the governing equations.

2.3.2.1. Filtering of the governing equations

The filtering operation required by the LES can be generally expressed for an arbitrary quantity ϕ by the following convolution operator [122, 152, 157]:

$$\bar{\phi}\left(\vec{x}\right) = \int \phi\left(\vec{x}'\right) K\left(\vec{x} - \vec{x}'\right) \mathrm{d}\vec{x}' \tag{2.37}$$

For quantities that are multiplied by density, the mass-weighted Favre-filtering is used instead:

$$\widetilde{\phi} = \frac{\overline{\rho\,\phi}}{\bar{\rho}} \tag{2.38}$$

Several possibilities exist for the formulation of the filter Kernel K, comprehensive overviews can be found in the literature [152, 157]. However, in the vast majority of the LES the filtering operation is not actually performed, but the sub-filter scales are suppressed by the dissipative numerical error of the discretization schemes as described in Chapter 3 and an additional increase of the viscous and diffusive fluxes. These technique is referred to as 'implicitly filtered' LES, the shape of the filter can then no longer be expressed precisely but depends on the dissipative numerical error.

The Favre-filtered transport equations for mass, momentum, species transport and enthalpy read [122, 152] (terms that are neglected in this work are omitted for clarity):

$$\frac{\partial\bar{\rho}}{\partial t} + \frac{\partial\bar{\rho}\,\widetilde{u}_i}{\partial x_i} = 0 \tag{2.39}$$

$$\frac{\partial\bar{\rho}\,\widetilde{u}_i}{\partial t} + \frac{\partial\bar{\rho}\,\widetilde{u}_i\widetilde{u}_j}{\partial x_j} = \frac{\partial\bar{\tau}_{ij}}{\partial x_j} - \frac{\partial\bar{p}}{\partial x_i} - \frac{\partial\bar{\rho}\left(\widetilde{u_i u_j} - \widetilde{u}_i\widetilde{u}_j\right)}{\partial x_j} \tag{2.40}$$

$$\frac{\partial\bar{\rho}\,\widetilde{Y}_k}{\partial t} + \frac{\partial\bar{\rho}\,\widetilde{u}_i\widetilde{Y}_k}{\partial x_i} = -\frac{\partial\bar{j}_{i,k}}{\partial x_i} + \bar{\dot{\omega}}_k - \frac{\partial\bar{\rho}\left(\widetilde{u_i Y_k} - \widetilde{u}_i\widetilde{Y}_k\right)}{\partial x_i} \tag{2.41}$$

$$\frac{\partial\bar{\rho}\,\widetilde{h}}{\partial t} + \frac{\partial\bar{\rho}\,\widetilde{u}_i\widetilde{h}}{\partial x_i} = \frac{\partial}{\partial x_i}\left(\overline{\frac{\lambda}{c_p}\frac{\partial h}{\partial x_i}}\right) - \frac{\partial\bar{\rho}\left(\widetilde{u_i h} - \widetilde{u}_i\widetilde{h}\right)}{\partial x_i} \tag{2.42}$$

Compared to the respective unfiltered transport equations 2.1, 2.2, 2.11 and 2.25, all quantities occur now in the filtered form. The filtered viscous, diffusive and heat fluxes are approximated as [152]:

$$\bar{\tau}_{ij} = -\frac{2}{3}\bar{\mu}\frac{\partial\widetilde{u}_k}{\partial x_k}\delta_{ij} + \bar{\mu}\left(\frac{\partial\widetilde{u}_i}{\partial x_j} + \frac{\partial\widetilde{u}_j}{\partial x_i}\right) \tag{2.43}$$

$$\bar{j}_{i,k} = -\bar{\rho}\bar{D}_k\frac{\partial\widetilde{Y}_k}{\partial x_i} \tag{2.44}$$

$$\overline{\frac{\lambda}{c_p}\frac{\partial h}{\partial x_i}} = \frac{\bar{\lambda}}{\bar{c}_p}\frac{\partial\widetilde{h}}{\partial x_i} \tag{2.45}$$

The last terms on the RHS of the momentum, species mass fractions and energy equations occur additionally compared to the unfiltered equations. These terms describe the unresolved fluxes on the sub-filter scales and need to be modeled.

2.3.2.2. Modeling of the sub-filter fluxes

Commonly the unresolved fluxes occurring in the filtered governing equations are modeled by increasing the transport coefficients with a turbulent contribution following the Boussinesq eddy-viscosity and the eddy-diffusivity approaches [122, 152]:

$$\bar{\rho}\left(\widetilde{u_i u_j} - \widetilde{u}_i \widetilde{u}_j\right) = \overline{\rho u_i u_j} - \frac{\overline{\rho\, u_i}\;\overline{\rho\, u_j}}{\bar{\rho}} \approx \frac{2}{3}\mu_t \frac{\partial \widetilde{u}_k}{\partial x_k}\delta_{ij} - \mu_t\left(\frac{\partial \widetilde{u}_i}{\partial x_j} + \frac{\partial \widetilde{u}_j}{\partial x_i}\right) \tag{2.46}$$

$$\bar{\rho}\left(\widetilde{u_i Y_k} - \widetilde{u}_i \widetilde{Y}_k\right) = \overline{\rho u_i Y_k} - \frac{\overline{\rho\, u_i}\;\overline{\rho\, Y_k}}{\bar{\rho}} \approx -\frac{\mu_t}{\mathrm{Sc}_t}\bar{\rho}\bar{D}_k \frac{\partial \widetilde{Y}_k}{\partial x_i} \tag{2.47}$$

$$\bar{\rho}\left(\widetilde{h u_i} - \widetilde{h}\widetilde{u}_i\right) = \overline{\rho h u_i} - \frac{\overline{\rho\, h}\;\overline{\rho\, u_i}}{\bar{\rho}} \approx -\frac{\mu_t}{\mathrm{Sc}_t}\frac{\bar{\lambda}}{\bar{c}_p}\frac{\partial \widetilde{h}}{\partial x_i} \tag{2.48}$$

Equation 2.46 only models the traceless part of the sub-filter momentum flux, the isotropic part is mostly not modeled but assumed to implicitly add up to the filtered pressure field, although a separate modeling of this part is also possible [122]. The turbulent Schmidt number Sc_t is usually set to values around 0.7. The turbulent viscosity is usually either modeled from a transport equation for the turbulent kinetic energy [118] or from an algebraic model, in this work the latter approach is chosen which reads:

$$\mu_t = \bar{\rho}\left(C_m \Delta\right)^2 D_m\left(\widetilde{u}_i\right) \tag{2.49}$$

Here, Δ, D_m and C_m denote the filter width (equal to the grid resolution in implicitly filtered LES), a differential operator depending on the filtered velocity field and a modeling constant, respectively.

The classical model for the turbulent viscosity μ_t that is still used frequently today is the one by Smagorinsky [187], in which the magnitude of the filtered strain rate is used for the differential operator D_m:

$$D_m = \sqrt{2\widetilde{S}_{ij}\widetilde{S}_{ij}} \quad \text{where} \quad \widetilde{S}_{ij} = \frac{1}{2}\left(\frac{\partial \tilde{u}_i}{\partial x_j} + \frac{\partial \tilde{u}_j}{\partial x_i}\right) \tag{2.50}$$

The modeling constant $C_m = C_S$ is usually set to values between 0.05 and 0.2. The Smagorinsky model tends to overpredict the turbulent fluxes in near wall regions and in shear layers, which leads to an artificial damping of the turbulence in these regions. More recent models that improve this weaknesses are for example the model by Vreman [207], or the WALE [130] and the σ [131] models by Nicoud et al. The σ model is used in this work, it computes the differential operator based on the singular values of the velocity gradient:

$$D_m = \frac{\sigma_3\left(\sigma_1 - \sigma_2\right)\left(\sigma_2 - \sigma_3\right)}{\sigma_1^2} \quad \text{with} \quad \sigma_1 \geq \sigma_2 \geq \sigma_3 \geq 0 \tag{2.51}$$

The singular values σ_i are the square roots of the eigenvalues of the tensor:

$$G_{ij} = \frac{\partial \tilde{u}_k}{\partial x_i} \frac{\partial \tilde{u}_k}{\partial x_j} \tag{2.52}$$

Nicoud et al. [131] found that a value of 1.5 for the modeling constant C_m works well for different test cases.

As an alternative to the use of a constant value for the C_m, it might also been evaluated dynamically as introduced by Germano et al. [61]. The underlying assumption of the respective dynamic procedure is that the modeling constant varies only weakly with the wavenumber and thus the information of the smallest resolved scales can be used to determine a suitable modeling constant for the whole sub-filter range. For that purpose, an additional test-filtering operation denoted by '$\widehat{\ }$' is introduced, where the test-filter width $\widehat{\Delta}$ is usually chosen to be twice the LES filter width and grid size Δ. The unresolved fluxes for the LES filter width τ_{ij}^{sgs} and the test filter width τ_{ij}^{test} read:

$$\tau_{ij}^{sgs} = \overline{\rho u_i u_j} - \frac{\overline{\rho\, u_i}\;\overline{\rho\, u_j}}{\bar{\rho}} \tag{2.53}$$

$$\tau_{ij}^{test} = \widehat{\overline{\rho u_i u_j}} - \frac{\widehat{\overline{\rho\, u_i}}\;\widehat{\overline{\rho\, u_j}}}{\widehat{\bar{\rho}}} \tag{2.54}$$

Following the Germano identity [61] in the variable density formulation given by Moin et al. [122], the Leonard stresses L_{ij} are linked to the sub-filter fluxes for the LES filter width τ_{ij}^{sgs} and the test filter width $\widehat{\tau_{ij}^{sgs}}$ by:

$$L_{ij} = \tau_{ij}^{test} - \widehat{\tau_{ij}^{sgs}} = \widehat{\bar{\rho}\,\widetilde{u}_i\widetilde{u}_j} - \frac{\widehat{\bar{\rho}\,\widetilde{u}_i}\;\widehat{\bar{\rho}\,\widetilde{u}_j}}{\widehat{\bar{\rho}}} \tag{2.55}$$

The model for the traceless part of the unresolved fluxes reads for the test-filter width and the LES filter width:

$$\tau_{ij}^{test} - \frac{\delta_{ij}}{3}\tau_{kk}^{test} = \alpha_{ij} \,/\, C_m^2 = \widehat{\bar{\rho}}\,\widehat{\Delta}^2\, D_m\left(\widehat{\widetilde{u}}_i\right)\left[\frac{2}{3}\frac{\partial \widehat{\widetilde{u}}_k}{\partial x_k}\delta_{ij} - \left(\frac{\partial \widehat{\widetilde{u}}_i}{\partial x_j} + \frac{\partial \widehat{\widetilde{u}}_j}{\partial x_i}\right)\right] \tag{2.56}$$

$$\tau_{ij}^{sgs} - \frac{\delta_{ij}}{3}\tau_{kk}^{sgs} = \beta_{ij} \,/\, C_m^2 = \bar{\rho}\,\Delta^2\, D_m\left(\widetilde{u}_i\right)\left[\frac{2}{3}\frac{\partial \widetilde{u}_k}{\partial x_k}\delta_{ij} - \left(\frac{\partial \widetilde{u}_i}{\partial x_j} + \frac{\partial \widetilde{u}_j}{\partial x_i}\right)\right] \tag{2.57}$$

Substituting Eqs. 2.56 and 2.57 in the traceless part of Eq. 2.55 yields an overdetermined system of six independent equations (five in the case of constant density) for the determination of C_m:

$$L_{ij} - \frac{\delta_{ij}}{3}L_{kk} = \widehat{C_m^2\,\beta}_{ij} - C_m^2\,\alpha_{ij} = M_{ij} \tag{2.58}$$

One possible solution method given by Lilly [108] is to assume that C_m is independent of the filter operation and to contract with the RHS of the equations, this minimizes the error in a least

square sense and leads to:

$$C_m^2 = \frac{M_{ij}\left(L_{ij} - \frac{\delta_{ij}}{3}L_{kk}\right)}{M_{kl}\,M_{kl}} \tag{2.59}$$

To avoid numerical instabilities when the denominator of the Eq. 2.59 becomes small, both numerator and denominator are usually averaged in two or three spatial directions, assuming that C_m is homogeneous along these directions. An alternative solution method was given by Piomelli and Liu [146], where the value of C_m is computed based on the value of the modeling constant at the last time or iteration step C_m^{*2}:

$$C_m^2 = \frac{-\alpha_{ij}\left(L_{ij} - \frac{\delta_{ij}}{3}L_{kk} - \widehat{C_m^{*2}\beta}_{ij}\right)}{\alpha_{kl}\,\alpha_{kl}} \tag{2.60}$$

This procedure is claimed to be more robust than the Lilly one due to the fact that the modeling constant is left inside the filtering operation, this allows to avoid the assumption of (partially) spatial homogeneous C_m fields. For both solution methods, negative values of the squared modeling constant may occur, which sometimes is partially attributed to energy transfer from small up to large scales (the so-called 'backscatter'). This can lead to numerical instabilities due to the resulting negative turbulent viscosity, therefore C_m^2 is usually clipped to zero in numerical implementations.

2.3.2.3. Modeling of the filtered reaction source term

The last term that needs closure is the filtered reaction rate $\bar{\dot{\omega}}_k$ in the species transport equation. One obvious solution would be to compute the source term based on the filtered quantities:

$$\bar{\dot{\omega}}_k = f\left(\vec{\widetilde{Y}}, \widetilde{h}, \bar{p}\right) \tag{2.61}$$

Due to the non-linear dependency f of the source term on the species mass fractions, the enthalpy and the pressure (usually exponentially), this approach can only be applied for very fine grid resolutions as otherwise the numerical error gets too large. A method to extend the validity of the approach to coarser grid resolutions is to artificially thicken the reaction zone to make it resolvable on coarser grid resolutions. This can be achieved by a reduction of the reaction source term and an increase of the diffusion coefficient in the species transport equations by a thickening factor F:

$$\frac{\partial \bar{\rho}\,\widetilde{Y}_k}{\partial t} + \frac{\partial \bar{\rho}\,\widetilde{u}_i\widetilde{Y}_k}{\partial x_i} = \Xi\left(-\frac{\partial F\,\bar{j}_{i,k}}{\partial x_i} + \frac{\bar{\dot{\omega}}_k}{F}\right) - \frac{\partial \bar{\rho}\left(\widetilde{u_i Y_k} - \widetilde{u}_i\widetilde{Y}_k\right)}{\partial x_i} \tag{2.62}$$

In the classical formulation of the artificially thickened flame model (ATF), the factor F is set to a constant value [20, 37]. To avoid unnecessary thickening in regions which are already resolved on the LES grid, the ATF model is often used with a variable factor F depending on

the progress of the reaction [46, 101, 107, 158]. Besides the ATF approach, further models exist that obtain the variable factor F from filtered laminar flamelets [48, 55].

The sub-filter flame wrinkling in Eq. 2.62 is considered with the wrinkling factor Ξ:

$$\Xi = \frac{\overline{|\nabla C|}}{\left|\nabla \overline{C}\right|} \tag{2.63}$$

Here, C denotes the dimensionless progress variable. Similar to the turbulent viscosity, the wrinkling factor Ξ can either be obtained from algebraic models derived from filtered DNS data [2, 59, 111, 125], a dynamic procedure [32, 205] or a transport equation [167, 213], respectively. The details of the ATF model and the wrinkling factor models are discussed in Chapters 4-7.

Instead of modeling the diffusive flux and the source term separately, it might also be directly modeled from:

$$\Xi \left(-\frac{\partial F \, \bar{j}_{i,k}}{\partial x_i} + \frac{\bar{\dot{\omega}}_k}{F} \right) = \Xi \left| \nabla \overline{C} \right| = \Sigma_{gen} \tag{2.64}$$

This approach is referred to as the generalized flame surface density Σ_{gen} approach [13], often the factor F is set to unity which leaves the thickening of the flame front to the interaction of numerical dissipation and dilatation.

A further possibility when the grid size is larger than the flame thickness is to consider the flame front as an infinitely thin interface between unburnt and burnt state. The flame front can then be tracked by a level-set method referred to as the G-equation [47, 123, 139, 147].

In all the presented approaches, additional considerations for the sub-filter distribution of the independent variables might be necessary if the functional dependency is non-linear on the computational grid. The cell value of a dependent variable ϕ is then computed by integrating over the joint sub-filter probability distribution P of the N independent variables ψ:

$$\bar{\Phi} = \int\limits_{\psi_1 \ldots \psi_N} \Phi(\psi_1, \ldots, \psi_N) P(\psi_1, \ldots, \psi_N) \, \mathrm{d}\psi_1 \ldots \mathrm{d}\psi_N \tag{2.65}$$

The sub-filter distribution P is usually referred to as the filtered density function (FDF). Assuming statistical independence of the independent variables allows to rewrite the joint FDF as the product of the marginal FDFs:

$$P(\psi_1, \ldots, \psi_N) = \prod_{n=1}^{N} P(\psi_n) \tag{2.66}$$

The FDF can either be of assumed shape, where the β and the top-hat shape [57, 135] are mostly used, or be determined from Eulerian or Lagrangian transport equations which then again require additional closure models [157]. The transported FDF approach can also be used stand-alone without any further combustion models (i.e. solving the chemistry directly for many

homogeneous reactors on the subgrid).

2.3.3. Reynolds-averaged Navier-Stokes simulation (RANS)

In a Reynolds-averaged Navier-Stokes simulation the solution is not filtered in space as in the LES before but instead averaged over a given time interval at every point in space:

$$\bar{\phi}\left(\vec{x}, t_1\right) = \frac{1}{t_1 - t_0} \int_{t=t_0}^{t=t_1} \phi\left(\vec{x}, t\right) \mathrm{d}t \tag{2.67}$$

The time interval can either be chosen infinitely large for a steady-state simulation (RANS) or large enough to capture a number of integral time scales for an unsteady problem (URANS). For quantities that are multiplied by density, again a Favre-averaging is applied:

$$\widetilde{\phi} = \frac{\overline{\rho\,\phi}}{\bar{\rho}} \tag{2.68}$$

Formally, the resulting averaged governing equations for the URANS differ from the filtered LES equations 2.39-2.42 only in the formulation of the additional terms on the RHS of the momentum, mass fraction and enthalpy transport equation:

$$\frac{\partial \bar{\rho}}{\partial t} + \frac{\partial \bar{\rho}\,\widetilde{u}_i}{\partial x_i} = 0 \tag{2.69}$$

$$\frac{\partial \bar{\rho}\,\widetilde{u}_i}{\partial t} + \frac{\partial \bar{\rho}\,\widetilde{u}_i\widetilde{u}_j}{\partial x_j} = \frac{\partial \bar{\tau}_{ij}}{\partial x_j} - \frac{\partial \bar{p}}{\partial x_i} - \frac{\partial \bar{\rho}\widetilde{u_i'' u_j''}}{\partial x_j} \tag{2.70}$$

$$\frac{\partial \bar{\rho}\,\widetilde{Y}_k}{\partial t} + \frac{\partial \bar{\rho}\,\widetilde{u}_i\widetilde{Y}_k}{\partial x_i} = -\frac{\partial \bar{j}_{i,k}}{\partial x_i} + \bar{\dot{\omega}}_k - \frac{\partial \bar{\rho}\widetilde{u_i'' Y_k''}}{\partial x_i} \tag{2.71}$$

$$\frac{\partial \bar{\rho}\,\widetilde{h}}{\partial t} + \frac{\partial \bar{\rho}\,\widetilde{u}_i\widetilde{h}}{\partial x_i} = \frac{\partial}{\partial x_i}\left(\overline{\frac{\lambda}{c_p}\frac{\partial h}{\partial x_i}}\right) - \frac{\partial \bar{\rho}\widetilde{u_i'' h''}}{\partial x_i} \tag{2.72}$$

The superscript $''$ denotes the temporal fluctuations of the respective quantity. The unclosed momentum flux is usually referred to as 'Reynolds stress tensor', as it acts like an additional viscous stress. As a consequence of the temporal averaging, the whole turbulent spectrum as given in Fig. 2.1 needs to be modeled. This means that the scales that need to be modeled are much less universal than in the LES, thus the RANS models are usually more complex and computationally expensive than the LES ones. As the focus of this work is on LES and DNS, the exact formulation of the RANS models is omitted, comprehensive overviews can be found in the literature [152, 157]. In general, the LES mostly yields more accurate results than the RANS or URANS due to the smaller impact of the (unavoidable) modeling error and does not require the scale separation in time that the URANS would require, this especially holds for the turbulent mixing and reaction processes investigated in this work. Nevertheless, RANS is still predominantly used in industrial application because either the RANS accuracy is sufficient or

the costs of a LES are prohibitive, the latter applies mainly for large and complex geometries and for high Reynolds number flows.

3. Numerical solution methods

The system of governing equations for a reactive fluid flow as described in the last chapter needs to be solved numerically, as analytical solutions only exist for strongly simplified problems. In order do so, the solution domain needs to be decomposed in a number of small elements. In each of these elements the solution is assumed to follow simple algebraic functions, which allows to transform the governing partial differential equations into a set of simpler algebraic equations which can be solved on a computer.

3.1. Finite-volume discretization

Different methods exist for the discretization of the governing equations, in this work the finite-volume method (FVM) is used as in the vast majority of CFD solvers. The starting point for the FVM discretization is the integral form of the governing equations, all the descriptions in this chapter are given for the generic transport equation of a quantity ϕ [52]:

$$\int_V \frac{\partial \rho\phi}{\partial t}\,\mathrm{d}V + \int_V \frac{\partial \rho u_i \phi}{\partial x_i}\,\mathrm{d}V = \int_V -\frac{\partial j_{i,\phi}}{\partial x_i}\,\mathrm{d}V + \int_V \dot{\omega}_\phi\,\mathrm{d}V \tag{3.1}$$

The volume integral of a vector divergence, which occurs in the convective and the diffusive terms of Eq. 3.1, can be replaced by the integral of the surface normal fluxes by applying Gauss's theorem [19]:

$$\int_V \frac{\partial f_i}{\partial x_i}\,\mathrm{d}V = \int_A f_i\, n_i\,\mathrm{d}A \tag{3.2}$$

Here, n_i denotes the components of the face normal vector, and f_i the components of the vectorial quantity. Additional swapping of the temporal differentiation and the volume integral finally yields [52]:

$$\frac{\partial}{\partial t}\int_V \rho\phi\,\mathrm{d}V = -\int_A \rho\, u_i\, \phi\, n_i\,\mathrm{d}A + \int_A -j_{i,\phi}\, n_i\,\mathrm{d}A + \int_V \dot{\omega}_\phi\,\mathrm{d}V \tag{3.3}$$

The computational domain is decomposed into a number of small non-overlapping control volumes with simple geometric shapes. Commonly used control volume shapes are triangles or quadrangles in two dimensions and tetrahedrons or hexahedrons in three dimensions. In the present work, control volumes of cubic shape are applied as sketched in Fig. 3.1. The volume

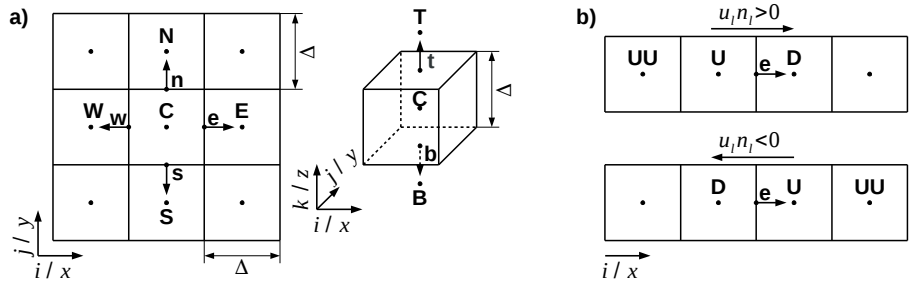

Figure 3.1.: a) Sketch of the FV discretization with cubic control volumes. The face normal vectors are denoted by small arrows. The neighbors of the cell (C) are denoted as west (W), east (E), south (S), north (N), bottom (B) and top (T), depending on the normal vector alignment with the coordinate axis. The faces adjacent to the neighboring cells are denoted by the respective small letters.
b) Determination of the downwind (D) and upwind (U) neighboring cell centers and the upwind neighboring cell center of the latter (UU), depending on the sign of the velocity component in the direction of the face normal vector for the eastern face (e).

and surface integrals in Eq. 3.3 can be approximated by the mid-point rule [52]:

$$\int_V \phi \, \mathrm{d}V \approx \phi_{vc} \, V \quad \wedge \quad \int_A \phi \, \mathrm{d}A \approx \phi_{ac} \, A \tag{3.4}$$

Here, ϕ represents an arbitrary quantity, where ϕ_{vc} and ϕ_{ac} are the values of the quantity at the centroid of the volume and the surface, respectively. (The volume and the surface areas of the control volume are denoted by V and A_l, respectively.) For the applied cubic control volumes, these quantities are simply computed as $V = \Delta^3$ and $A_l = \Delta^2$, with Δ denoting the edge length of the control volume as sketched in Fig. 3.1. The mid-point rule has an accuracy of second order and is used in most CFD solvers, for special cases also higher order methods exist [52]. The final discretized form of Eq. 3.3 reads:

$$\underbrace{\frac{\partial}{\partial t} \rho \phi \, V}_{\text{temporal change}} \approx \underbrace{-\sum_{l=1}^{N} \left(\rho \, u_i \, \phi \, n_i \, A\right)_l}_{\text{convective flux}} + \underbrace{\sum_{l=1}^{N} \left(-j_{i,\phi} \, n_i \, A\right)_l}_{\text{diffusive flux}} + \underbrace{\dot{\omega}_\phi \, V}_{\text{source term}} = \text{RHS} \tag{3.5}$$

The index l runs over all faces of the control volume, i.e. the eastern (e), western (w), southern (s), northern (n), bottom (b) and top (t) faces for the cubic control volume in Fig. 3.1.

3.1.1. Convective flux

The computation of the convective flux in Eq. 3.5 requires the interpolation of the values of a quantity ϕ from the centers of the control volumes to the center of the control volume surfaces as sketched in Fig. 3.1. In most of the CFD solvers, this interpolation is achieved by methods which have an accuracy between first and second order, existing higher order methods are mainly used in specialized codes for DNS purposes. The upwind differencing scheme (UDS) sets the ϕ value

Table 3.1.: Selection of flux limiter functions.

Name	$\Psi(r)$	$\lim_{r\to\infty} \Psi(r)$
UDS	0	0
MINMOD [172]	$\max\left[\min\left(r,1\right),0\right]$	1
VANLEER [201]	$\left(r+\lvert r\rvert\right)/\left(1+\lvert r\rvert\right)$	2
EXP	$2\left\{1-\exp\left[\ln\left(0.5\right)\max\left(r,0\right)\right]\right\}$	2
CHARM [219]	$\max\left(r,0\right)\left(3\max\left(r,0\right)+1\right)/\left(\max\left(r,0\right)+1\right)^2$	3
SUPERBEE [172]	$\max\left[\min\left(r,2\right),\min\left(2r,1\right),0\right]$	2
CDS	r	∞

at the face center to the value at the upstream cell center [52, 150] as shown in Fig. 3.1:

$$\phi_e = \phi_U \tag{3.6}$$

The UDS is the most stable interpolation scheme, but has only an accuracy of first order. The central differencing scheme (CDS) computes the ϕ value at the face center from linear interpolation between the two adjacent cell centers [52, 150]:

$$\phi_e = 0.5\left(\phi_C + \phi_E\right) \tag{3.7}$$

The CDS is of second order accuracy but also prone to numerical instabilities.

Different schemes have been developed that aim to combine the favorable accuracy of the CDS with the stability of the UDS, many of them are based on the total variation diminishing (TVD) approach. The idea behind the TVD approach is to use CDS in regions where the solution is smooth and to blend over towards UDS in regions with high local gradients to avoid numerical instabilities, the flux at the face is computed as:

$$\phi_e = \phi_U + 0.5\ \Psi(r)\left(\phi_U - \phi_{UU}\right) \tag{3.8}$$

Here, $\Psi(r)$ is the flux limiter function which depends on the ratio of successive gradients along the mesh:

$$r = \frac{\phi_D - \phi_U}{\phi_U - \phi_{UU}} \tag{3.9}$$

A large number of different formulations has been proposed for the limiter function $\Psi(r)$ in the past [212], a selection is given in Table 3.1. To facilitate the discussion of the limiter properties, also the limiter formulations that lead to UDS and CDS are included in Table 3.1.

A comparison of the different limiter functions $\Psi(r)$ from Table 3.1 is given in Fig. 3.2. It has been shown by Sweby [193] that a limiter function must lie entirely within the grayly shaded region in Fig. 3.2 to yield a second order scheme with TVD properties. To study the effect of the different limiter functions on the scalar transport, Fig. 3.3 present results for the transport

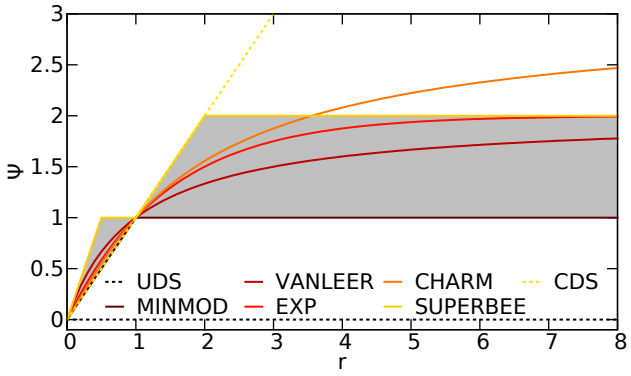

Figure 3.2.: Comparison of the different flux limiters given in Table 3.1 as a function of the ratio of successive gradients r as introduced by Sweby [193]. The second-order TVD region is shaded in gray.

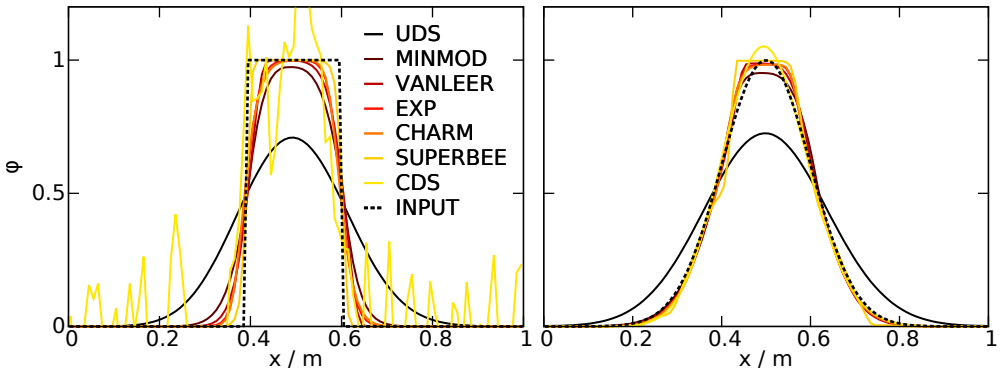

Figure 3.3.: Comparison of the flux limiters in Table 3.1 for the convective transport of a step profile (left) and a Gaussian profile (right). The cell size was 0.01 m, the (uniform) velocity 1 m/s and the profiles were transported through the whole domain once using periodic boundary conditions. The time integration was performed with the explicit Euler scheme, the time step width was 0.0001 s and 0.001 s for the step and the Gaussian profile, respectively.

of a step function and a Gaussian function through a one-dimensional periodic domain. The UDS scheme comes along with large numerical dissipation, which results in strong smoothing of the original profiles in Fig. 3.3. The CDS, in contrast, leads to numerical oscillations when the steep step profile is transported, but is able to transport the smooth Gaussian profile with the smallest deviation from the original shape compared to the other schemes. The MINMOD and the SUPERBEE limiter are located entirely at the lower and upper limit of the second order TVD region in Fig. 3.2, respectively. This makes the MINMOD limiter the most dissipative possible TVD limiter, which results in a clearly visible smoothing of especially the step function in Fig. 3.3. On the other hand, the SUPERBEE limiter is the least dissipative possible TVD limiter, which enables to transport steep profiles as the step profile in Fig. 3.3 with the smallest deviation from the original shape compared to the other schemes. The SUPERBEE limiter is, however, not suited for the transport of smooth fields as it tends to steepen the local gradients which becomes obvious for the Gaussian profile in Fig. 3.3. The VANLEER flux limiter is a classical example for a continuous limiter function that runs smoothly through the second order TVD region in Fig 3.2 and approaches the limiting value of two for large values of r. The

VANLEER limiter is able to transport both the step and the Gaussian profile in Fig. 3.3 with moderate deviations from the original shape. The limiter that was used for the computations in this work is the CHARM limiter, which has as similar shape as the VANLEER limiter but lies closer to the CDS for r values lower unity and approaches the upper limit of the second order TVD region faster for larger r values, as it can be seen in Fig. 3.2. This results in a slightly better agreement of the transported functions with the original shapes in Fig. 3.3 compared to the VANLEER limiter. A disadvantage is that the CHARM limiter slightly leaves the second order TVD region in Fig. 3.2 and approaches a limiting value of three, which might cause stability problems for very steep local gradients. One possibility to avoid this problem is to clip the values larger than two [143]. An alternative is to use a different limiter formulation that gives a similar shape as the CHARM limiter but has the correct limiting value of two. For this purpose, the present work introduces a limiter that uses a simple exponential function, the formulation is given as EXP in Table 3.1. It can be seen in Fig. 3.2 that the EXP limiter has a comparable shape to the CHARM limiter for small r values, but converges smoothly towards the correct value of two for large values of r. The resulting transported profiles in Fig. 3.3 with the EXP limiter are comparable to the ones obtained with the CHARM limiter. More detailed comparisons revealed that the symmetry of the original step and Gaussian functions in Fig. 3.3 is preserved more during the transport by the EXP limiter than by all other investigated TVD limiters.

3.1.2. Diffusive flux

For the computation of the diffusive flux in Eq. 3.5, the scalar gradient of the quantity ϕ needs to be evaluated at the face centers. Using the second-order mid-point rule results in the following discretization of the gradient at the face center [52, 150]:

$$\left(\frac{\partial \phi}{\partial x}\right)_e \approx \frac{\phi_E - \phi_C}{\Delta} \tag{3.10}$$

If the face normal vectors are not perfectly aligned with the coordinate directions, an additional correction procedure is required. These procedure and further higher-order schemes for the face normal gradient can be found in the literature [52, 150].

3.2. Time integration

To solve the discretized form of the generic transport equation 3.5, the solution needs to be advanced in time starting from a given initialization. The most simple temporal discretization is the Euler scheme:

$$\frac{\partial}{\partial t} \rho \phi \, V \approx \frac{\left[(\rho\phi)^{n+1} - (\rho\phi)^n\right] V}{\Delta t} = \text{RHS} \tag{3.11}$$

The Euler scheme is of first order accuracy, the stability properties depend on the time level at which the RHS is evaluated. If the RHS is evaluated based on the (known) values at the time level n, the resulting schemes is denoted as explicit Euler scheme. The explicit Euler scheme only yields stable solutions as long as the CFL number [38] does not exceed unity:

$$\text{CFL} = \frac{|u|\Delta t}{\Delta} \leq 1 \tag{3.12}$$

If the solution is not dominated by convective transport but by diffusive transport, the following conditions must be fulfilled for stability [52, 150]:

$$\frac{D\Delta t}{\Delta^2} \leq \frac{1}{2d} \Leftrightarrow 2d\,\frac{D\Delta t}{\Delta^2} \leq 1 \tag{3.13}$$

Here, d denotes the dimensionality of the problem, thus for the three-dimensional problems investigated in this work ($d = 3$) the criterion must be less than 1/6.

The implicit Euler scheme is obtained if the RHS is evaluated based on the values at the time level $n + 1$. As these values are unknown, the implicit Euler scheme requires the solution of a system of equations at every time step. This makes the implicit Euler scheme computationally more expensive than the explicit Euler scheme, but therefore the implicit Euler scheme is unconditionally stable and allows arbitrarily large time steps, which can be beneficial for computations with stationary solutions.

As the first order Euler scheme is neither stable nor precise enough for LES or DNS of reactive flows, in this work a third order low-storage Runge-Kutta scheme proposed by Williamson [215] is applied:

$$\begin{aligned} l =& \{1, 2, 3\} \\ & a_l = (0, -5/9, -153/128) \\ & b_l = (1/3, 15/16, 8/15) \\ & w_l = (1/3, 5/12, 1/4) \\ & q_l = a_l\, q_{l-1} + \Delta t\, \text{RHS}(\phi_{l-1}) \\ & \phi_l = \phi_{l-1} + b_l q_l \\ & t_l = t_{l-1} + w_l \Delta_t \end{aligned} \tag{3.14}$$

The solution at the new time step is computed via three successive sub-steps, where the index l denotes the count of the sub-steps. The coefficients a_l, b_l and w_l can be chosen in many different ways, Williamson [215] found that the used set of coefficients yields a very good compromise between numerical precision and stability, comprehensive discussions on further low-storage Runge-Kutta schemes can be found in the literature [89, 90]. Higher order implicit schemes are also used frequently in CFD solvers [150], the most common one is probably the

one by Crank and Nicolson [39]. However, higher order implicit schemes are not so attractive for LES and DNS due to the need for time-accurate solutions, which can only be achieved with a CFL number smaller than unity - which also allows the use of computationally cheaper explicit schemes.

3.3. Pressure correction

As already mentioned in Section 2.1.2.2, the pressure gradient entering the momentum equations needs to be determined, here by a projection method as introduced by Chorin [35] for low Mach number or incompressible flows.

3.3.1. Isothermal flows

For an incompressible flow at constant temperature without influence of gravity or other external forces the continuity Equation 3.15 and the momentum Equations 3.16 read:

$$\frac{\partial \rho u_i}{\partial x_i} = 0 \tag{3.15}$$

$$\frac{\partial \rho u_i}{\partial t} + \frac{\partial \rho u_i u_j}{\partial x_j} = \frac{\partial \tau_{ij}}{\partial x_j} - \frac{\partial p}{\partial x_i} \tag{3.16}$$

The construction of the solution algorithm starts with the discretization of the momentum Equations 3.16 in time:

$$(\rho u_i)^{n+1} = (\rho u_i)^n + \frac{\Delta t}{V}\left(-\frac{\partial \rho u_i u_j}{\partial x_j} + \frac{\partial \tau_{ij}}{\partial x_j} - \frac{\partial p}{\partial x_i} V\right) \tag{3.17}$$

For clarity, the derivation is based on the simple Euler time discretization scheme, with an implicit discretization for pressure and an explicit discretization for all other quantities. Rearranging the momentum equations yields:

$$\underbrace{(\rho u_i)^{n+1}}_{divergence-free} + \underbrace{\left(\Delta t \frac{\partial p}{\partial x_i}\right)^{n+1}}_{irrotational} = (\rho u_i)^n + \frac{\Delta t}{V}\left(-\frac{\partial \rho u_i u_j}{\partial x_j} + \frac{\partial \tau_{ij}}{\partial x_j}\right)^n \tag{3.18}$$

The LHS of Eq. 3.18 can be interpreted as the Helmholtz-Hodge decomposition of the solution at the new time step $n+1$ into a divergence-free and an irrotational part. In the first step of the solution algorithm, a momentum prediction for the new time step $n+1$ is computed based on the old time step n from the RHS of Eq. 3.18:

$$(\rho u_i)^* = (\rho u_i)^{n+1} + \left(\Delta t \frac{\partial p}{\partial x_i}\right)^{n+1} = (\rho u_i)^n + \frac{\Delta t}{V}\left(-\frac{\partial \rho u_i u_j}{\partial x_j} + \frac{\partial \tau_{ij}}{\partial x_j}\right)^n \tag{3.19}$$

The resulting momentum prediction $(\rho u_i)^*$ does normally not fulfill the continuity equation for the new time step $n+1$, which reads:

$$\left(\frac{\partial \rho u_i}{\partial x_i}\right)^{n+1} = 0 \tag{3.20}$$

By combining Eq. 3.19 and Eq. 3.20, the pressure equation is obtained:

$$\left(\frac{\partial \rho u_i}{\partial x_i}\right)^{n+1} = \frac{\partial}{\partial x_i}\left[(\rho u_i)^* - \left(\Delta t \frac{\partial p}{\partial x_i}\right)^{n+1}\right] = 0 \tag{3.21}$$

$$\Longleftrightarrow \frac{\partial}{\partial x_i}\left(\frac{\partial p}{\partial x_i}\right)^{n+1} = \frac{1}{\Delta t}\left(\frac{\partial \rho u_i}{\partial x_i}\right)^* \tag{3.22}$$

Equation 3.22 is of the Poisson type and can be solved for the unknown pressure distribution at the new time step. The solution is usually obtained by an iterative technique, e.g. by the Gauss-Seidel method with successive overrelaxation (SOR). It must be stressed that the resulting pressure is the dynamic pressure due to the fluid motion, and not the thermodynamic pressure that enters the equation of state. The final momentum field for the new time step is then obtained by correcting the predicted momentum field according to Eq. 3.19:

$$(\rho u_i)^{n+1} = (\rho u_i)^* - \Delta t \left(\frac{\partial p}{\partial x_i}\right)^{n+1} \tag{3.23}$$

The complete solution algorithm can be summarized as [92, 165]:

1. Compute the momentum prediction $(\rho u_i)^*$ based on the old time step n using Eq. 3.19. Apply the momentum boundary conditions as described in Section 3.4 to $(\rho u_i)^*$.

2. Compute the pressure resulting from the fulfillment of the continuity equation by solving Eq. 3.22, apply the pressure boundary conditions as described in Section 3.4.

3. Correct the momentum prediction based on the pressure gradient to obtain the final momentum $(\rho u_i)^{n+1}$ from Eq. 3.23. Apply the momentum boundary conditions as described in Section 3.4 to $(\rho u_i)^{n+1}$.

3.3.2. Reactive flows

For reactive flows, the density is a function of one or more variables ϕ varying in time and space. Depending on the chemical model, these variables are a certain subset of the species mass fractions Y_k, the element mass fractions Z_j and the temperature T, as described in Chapter 2:

$$\rho = f(\phi_1, \ldots, \phi_N) \tag{3.24}$$

Due to the varying density, the continuity equation at the new time step $n+1$ reads:

$$\frac{\partial \rho}{\partial t} + \left(\frac{\partial \rho u_i}{\partial x_i} \right)^{n+1} = 0 \tag{3.25}$$

Again, the combination of Eq. 3.19 and Eq. 3.25 yields the modified pressure equation:

$$\frac{\partial \rho}{\partial t} + \left(\frac{\partial \rho u_i}{\partial x_i} \right)^{n+1} = \frac{\partial \rho}{\partial t} + \frac{\partial}{\partial x_i} \left[(\rho u_i)^* - \left(\Delta t \frac{\partial p}{\partial x_i} \right)^{n+1} \right] = 0 \tag{3.26}$$

$$\iff \frac{\partial}{\partial x_i} \left(\frac{\partial p}{\partial x_i} \right)^{n+1} = \frac{1}{\Delta t} \left[\frac{\partial \rho}{\partial t} + \left(\frac{\partial \rho u_i}{\partial x_i} \right)^* \right] \tag{3.27}$$

When comparing the pressure Eq. 3.27 for the reactive case to the pressure Eq. 3.22 for the isothermal case, it can be seen that the reactive case requires the additional evaluation of the time derivative of the density. In the present work, this time derivative is computed via the solution of an additional continuity equation as described by Kempf [84, 190], related methods can be found in the literature [144, 145, 216]. The complete solution algorithm for the reactive case can be summarized as:

1. Compute the momentum prediction $(\rho u_i)^*$ based on the old time step n using Eq. 3.19. Apply the momentum boundary conditions as described in Section 3.4 to $(\rho u_i)^*$.

2. Solve transport equations with the velocity field of the old time step n to obtain the conserved variables $(\rho\,\phi_1)^{n+1}, \ldots, (\rho\,\phi_N)^{n+1}$ at the next time step. As the density from the chemical model usually depends on the primitive variables $\phi_1, \ldots, \phi_N$, an additional continuity equation is solved to obtain a prediction for the density at the next time step ρ^{n+1} that is used to compute $\phi_1^{n+1}, \ldots, \phi_N^{n+1}$. Use these values to compute the density $\rho^s = f(\phi_1^{n+1}, \ldots, \phi_N^{n+1})$ from the chemical model. Apply boundary conditions to all conserved variables, as described in Section 3.4.

3. Compute the pressure resulting from the fulfillment of the continuity equation by solving Eq. 3.27, apply the pressure boundary conditions as described in Section 3.4. The required time derivative of the density is computed as:

$$\left(\rho^s - \rho^{n+1}\right) / \Delta t \tag{3.28}$$

   The divergence of the momentum prediction is computed with the same convection scheme as used for the continuity equation (TVD scheme with CHARM limiter in this work), where the velocity at the cell faces u^* is computed from Eq. 3.29 and the transported quantity is the density prediction ρ^{n+1}.

4. Correct the momentum prediction based on the pressure gradient to obtain the final momentum $(\rho u_i)^{n+1}$ from Eq. 3.23. Apply the momentum boundary conditions as described

in Section 3.4 to $(\rho u_i)^{n+1}$. The density prediction ρ^{n+1} is used as starting point for the next time step.

If the Runge-Kutta method as described in the last section is used for the time integration instead of the Euler method, the solution algorithm is applied for every Runge-Kutta sub-step. The only necessary modification is the replacement of Δt with $b_l \Delta t$ (see Section 3.2) in all equations except for Eq. 3.28, where still Δt must be used.

3.3.3. Staggering

If both the momentum equations and the pressure correction equation as described in the last section are computed at the cell centers and are discretized with CDS, a decoupling of pressure and momentum fields can occur that leads to checker-board patterns in the resulting pressure field [52, 136]. The classical solution for this problem is the use of staggered grids as introduced by Harlow and Welch [70], where the momentum equations are computed for control volumes which are centered at the face centers of the control volumes used for pressure and the other transported quantities. As the use of staggered grids comes along with additional computational overhead and is very difficult to formulate for unstructured grids, in the present work the transport equations for all quantities including momentum are solved for the same control volumes. To avoid the pressure and momentum decoupling, the method of Rhie and Chow [166] is used. This method avoids the decoupling of the pressure and momentum fields by correcting the intermediate velocity at the face centers as (see Fig. 3.1):

$$u_e^* = 0.5 \left[\frac{(\rho u)_C^*}{\rho_C^{n+1}} + \frac{(\rho u)_E^*}{\rho_E^{n+1}} \right] \tag{3.29}$$

$$u_e^{n+1} = u_e^* - \Delta t \, \frac{\left(p_E^{n+1} - p_C^{n+1}\right)/\Delta}{0.5 \left(\rho_C^{n+1} + \rho_E^{n+1}\right)} \tag{3.30}$$

That way, the transport velocity on the faces that is entering the convective fluxes is corrected as if the grid would be staggered. This ensures that checker-board patterns in the pressure modify the velocity at the faces and thereby affect the mass transport, which results in a removal of the checker-board patterns.

3.4. Boundary conditions

At the boundaries of the computational domain, special treatments are necessary to impose the correct flow behavior. Nearly all possible boundary conditions can be expressed as a combination of two basic type. The first type is the Dirichlet boundary condition, where a fixed value of the quantity ϕ is imposed at the boundary. The second type is the Neumann boundary condition, where the face normal gradient $n_i \, \partial\phi/\partial x_i$ is prescribed. Most of the time, a face normal gradient of zero is prescribed, this simply corresponds to a face normal flux of zero and is often

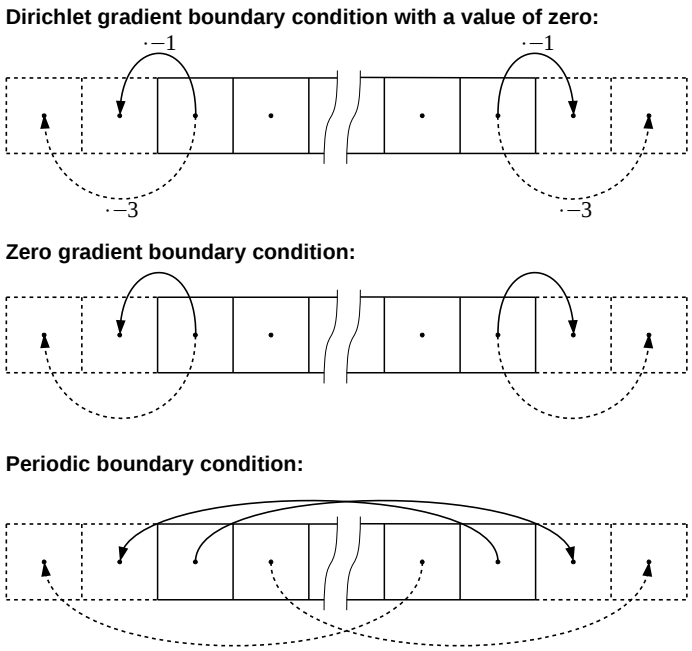

Figure 3.4.: Illustration of the ghost cell implementation of the basic boundary conditions as used in the present work.

referred to as zero gradient boundary condition. Furthermore, a weighted combination of the flux resulting from the Dirichlet and the Neumann boundary condition might be imposed at the boundary face, this is referred to as Robin boundary condition. Another type is the periodic boundary condition, where the adjacent cells at one boundary are used to determine the fluxes at another boundary and vice versa. A common way to implement this boundary condition is the use of so-called 'ghost cells', as illustrated in Fig. 3.4. The values in the ghost cells are determined based on the results from the interior points of the last time step as shown in Fig. 3.4. In the present work, all kinds of boundary conditions are implemented using the ghost cell method, the respective implementations for the Dirichlet boundary condition with a face value of zero and the zero gradient boundary condition are also shown in Fig. 3.4. With the ghost cell method, all computational cells including the ones adjacent to the boundaries can be computed with the same numerical scheme, as all faces have the required number of neighboring cells.

3.4.1. Parallel boundary conditions

Typical CFD computations for industrial and scientific purposes do usually require an amount of computational effort that can only be delivered in a reasonable amount of time by the use of multiple processor cores in parallel. The computations that were performed for the present work have been even more computationally expensive, especially the quasi DNS that forms the basis of the Chapters 6 and 7 that required approximately one week runtime on 64,000 processor cores. The parallelization in the present work is achieved by a distributed memory approach, where the cuboid computational domain is divided into a number of smaller parallel subdomains. The number of subdomains is equal to the number of processor cores used for the

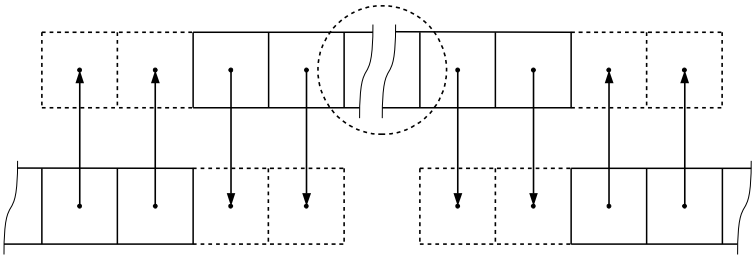

Figure 3.5.: Illustration of the exchange of information between the ghost cells of adjacent parallel domains. The interior cells that can be computed independent of the exchanged values are marked by a dashed circle.

simulation, so that every processor core computes one of the subdomains. This procedure requires the exchange of information at the boundaries of the subdomains between the individual processor cores, which is performed with the Message Passing Interface (MPI). The boundaries between the subdomains are also realized with the ghost cell method as described in the last section. This time the ghost cells of a subdomain are filled with the values of the respective quantity in the computational cells adjacent to the boundary on the neighboring subdomain, as illustrated in Fig. 3.5 for a one-dimensional domain decomposition. In the simulations performed for this work a three-dimensional domain decomposition was applied, which requires communication operations with up to six neighboring subdomains. This data exchange is repeated after every time and iteration step, depending on the number of processor cores and the speed of the communication operations this can require a notable amount of the run time of the CFD solver.

To reduce the computational costs of the communication, the MPI standard provides non blocking communication operations where the execution of the program can be continued while the data is communicated between the processors. In the present work, two different methods were used to exploit this feature in order to speed up the run time of the solver. The first method is used to speed up the Poisson solver required for the projection method, it is based on the observation that for the computation of the interior cells of the subdomains, as shown in Fig. 3.5, the communicated ghost cell values are not needed. Therefore, these interior cells can already be computed while the values in the ghost cells are communicated. Only the cells adjacent to the subdomain boundaries must wait for the finishing of the communication operation before they can be computed. The second method is used to hide the communication of the transported quantities behind computational work. As the numerical solution algorithms described in this work require the computation of multiple transported quantities in a sequential order, the communication of the already transported quantities can be performed while the following quantities are computed.

3.4.2. Turbulent inlet

The LES and DNS simulations performed in this work require the specification of a temporally and spatially varying turbulent velocity field at the inlet of the computational domain. The most

realistic solution would be to extend the inlet part of the domain far enough upstream, so that an initially laminar inlet velocity profile can evolve to a fully turbulent profile before entering the actual region of interest. However, this would lead to prohibitively large computational domains, the only exception are simple geometries as channel- or pipe flows where the spatial extension can be approximated by periodic boundary conditions as described in the last section. Therefore, in the vast majority of LES and DNS of non-periodic setups artificially generated turbulence is imposed at the inflow. In the present work, the digital filtering method introduced by Klein et al. [94] is used. The starting point for this method are fields filled with random numbers for all three velocity components. Using these random velocity fluctuations directly is not sufficient, as they would be dissipated away very quickly [86, 94]. Therefore, the random fields are filtered to obtain artificial homogeneous turbulent structures with a prescribed length scale L [88, 94]:

$$\hat{u_l}(i,j,k) = \sum_{k'=-N}^{N} b_{k'} \sum_{j'=-N}^{N} b_{j'} \sum_{i'=-N}^{N} b_{i'}\, u_l(i+i', j+j', k+k') \tag{3.31}$$

$$b_m = \frac{\tilde{b}_m}{\sqrt{\sum_{n=-N}^{N} \tilde{b}_n^2}} \quad \text{with} \quad \tilde{b}_m = \exp\left(-\frac{\pi\,(m\Delta)^2}{2L^2}\right) \tag{3.32}$$

Here, the separability of the Gaussian filter is exploited as suggested by Kempf et al. [88], which allows to perform the three-dimensional filtering operation as three consecutively performed one-dimensional filtering operations. This reduces the computational effort from the order of $(2N+1)^3$ to the order of $3\,(2N+1)$. Following the suggestion by Klein et al. [94], the number of filter points is chosen as $N \geq 2L/\Delta$. The obtained fluctuations fields are then normalized and shifted to obtain a mean value of zero and a standard deviation of unity:

$$\hat{u_l}^N = \frac{\hat{u_l} - \overline{\hat{u_l}}}{\sigma\,(\hat{u_l})} \tag{3.33}$$

Here, the mean value and the standard deviation of the filtered fluctuation field are denoted by $\overline{\hat{u_l}}$ and $\sigma\,(\hat{u_l})$, respectively. The resulting fluctuation fields might be further modified to fulfill an arbitrary stress tensor following the procedure given by Lund et al. [110]. Finally, the fluctuation fields are multiplied with the desired standard deviations of the velocity components and added to the mean velocity component fields prescribed at the inlet.

To avoid the necessity to communicate the larger number of ghost cells that is required by larger filter stencils in parallel computations, the present work uses a random number generator with a deterministic random seed depending on the spatial coordinate as suggested by Kempf et al. [88]:

$$\text{seed[m]} = (m + i^2 + j^2 + k^2)/l \tag{3.34}$$

Here, m denotes the respective entry of the seed vector and l the direction of the velocity

component. We found that this kind of seeding produces suitable random number fields when used with the random number generator by Marsaglia [115], which is part of the GNU Compiler Collection (GCC). If different random numbers are desired for every run of the program, the value of the Unix system clock, which counts the number of seconds past since the beginning of the year 1970, can be added to the random seed. The coordinate i can be transformed to the number of time steps n_t at the inflow plane using Taylor's hypothesis [88, 94]:

$$n_t = \frac{i\Delta}{u_b \, \Delta t} \tag{3.35}$$

Here, u_b denotes a bulk velocity that is representative for the investigated configuration.

3.4.3. Combination of boundary conditions for reactive flows

The system of equations describing the (reactive) fluid flow needs a certain combination of boundary conditions for the individual quantities in order to produce physically meaningful and numerically stable results. The exact choice of the boundary conditions depends on whether the pressure is computed from the projection method (see Section 3.3, sometimes also denoted as pressure-based or incompressible solver) or from the transported density (see Section 2.1.2.2, sometimes also denoted as density-based solver). A pressure-based solver can usually be applied up to Mach numbers of 0.2 - 0.3, for larger Mach numbers a density based solver should be used. It must however be stressed that the described boundary conditions are only valid for Mach numbers below unity, for larger Mach numbers all quantities must be prescribed at the inlet.

3.4.3.1. Incompressible solver

For incompressible flows at low Mach numbers, usually the mass flow at the inlet is prescribed by setting Dirichlet boundary conditions for the momentum equations, where turbulent fluctuations are superimposed as described in the previous section. The values of the density and other transported quantities are also fixed by Dirichlet boundary conditions at the inlet.

At walls, zero slip is adjusted by setting the momentum to zero with Dirichlet boundary conditions. For impermeable walls, zero gradient boundary conditions are applied for the transported species. Adiabatic and isothermal walls are described by zero gradient and Dirichlet boundary conditions for the temperature, respectively. When the transport equation for enthalpy is solved instead of the one for temperature as in this work, the enthalpy value at an isothermal wall depends on the chemical composition at this wall and thus must be updated if the composition changes due to the zero gradient conditions applied for species.

At the outlet, zero gradient conditions are usually prescribed for momentum, density and other transported quantities, where backflow is avoided by clipping negative values of the face normal momentum component. For problems dominated by convection, as the ones investigated

in the present work, the physical influence of these boundary conditions is rather small due to the predominantly downstream propagation of information. However, setting suitable boundary conditions at the outlet is very important to ensure a stable numerical solution.

The boundary conditions for the pressure equation must be set depending on the ones used for momentum. Where the momentum is fixed by Dirichlet conditions, i.e. at the inflow and at walls, a zero gradient condition must be used for pressure, as a pressure gradient would require a modification of the (prescribed) momentum (see Eqs. 3.23 and 3.30). The pressure is prescribed at the outlet by a Dirichlet condition, where the absolute value of the pressure is not important as only the gradient and the curvature of the pressure field are needed during the computation. Therefore, the pressure is usually set to zero to minimize the effect of round-off errors.

3.4.3.2. Density based solver

For the density based solver, principally the same boundary conditions are applied as for the pressure based solver. However, special care must be devoted to the computation of the pressure and density boundary conditions. Although the transported quantity is the density, the actual boundary conditions are usually prescribed for the pressure. To achieve this, the pressure at all computational points is computed from the density, the composition and the temperature first. Afterwards, the pressure boundary conditions are applied to the resulting pressure field. As for the pressure based solver, a zero gradient condition is applied at the inflow and at walls and a Dirichlet condition at the outlet. Afterwards, Dirichlet boundary conditions are set for the density at all boundaries for the next time step, where the face value is computed from the resulting pressure value, the composition and the temperature at the face. This update of the density boundary condition does not affect the momentum boundary conditions, but might require an update of the inlet boundary condition for other transported quantities if the non-conservative value of the respective quantity is prescribed at the boundary.

The pressure value at the outlet might simply be set to the value of the ambient pressure p_∞, in this case potentially occurring pressure waves are fully reflected at the outlet. In truncated geometries, as frequently used in CFD simulation, this behavior is often undesired and can cause numerical instabilities. A solution is the use of a non reflecting or partially reflecting boundary condition for the pressure [151, 152] at the outlet. For such a non- or partially reflecting boundary condition, the pressure at the outlet faces varies in time following [151, 152]:

$$\frac{\partial p}{\partial t} = 0.5\,(L_5 + L_1) \quad \text{with} \quad L_5 = (u_1 + c)\left(\frac{\partial p}{\partial x_1} + \rho c \frac{\partial u_1}{\partial x_1}\right) \tag{3.36}$$

Equation 3.36 assumes that the normal vector of the outlet faces is parallel to the x-axis, if this is not the case the face normal component of the velocity vector and the gradients must be used. The gradients of pressure and velocity at the outlet faces are computed from a one-sided

difference based on the adjacent interior grid points, e.g. for the face e in Fig. 3.1:

$$\left.\frac{\partial p}{\partial x_1}\right|_e \approx \frac{p_C - p_W}{\Delta} \quad \text{and} \quad \left.\frac{\partial u_1}{\partial x_1}\right|_e \approx \frac{u_{1C} - u_{1W}}{\Delta} \tag{3.37}$$

The reflection behavior of the boundary condition is determined by the choice of L_1. For $L_1 = -L_5$ the pressure at the boundary is unchanged, which would correspond to the fully reflecting boundary condition. A perfectly non reflection boundary condition corresponds to $L_1 = 0$. For a partially reflecting boundary condition, Rudy and Strikwerda [173] suggested to use:

$$L_1 = K\left(p - p_\infty\right) \quad \text{with} \quad K = \sigma\left(1 - \mathrm{Ma}_{\text{max}}^2\right) c/H \tag{3.38}$$

Here, Ma_{max} and H denote the maximum Mach number of the flow and a characteristic domain size, respectively. It was recommended by Selle et al. [183] and Poinsot and Veynante [152] to choose the factor σ in between 0.1 and π. For consistency, the time integration of Eq. 3.36 at the outlet boundary faces should ideally be carried out with the same method as used for the governing equations. Instead of using zero-gradient boundary conditions to determine the values of all other quantities except the pressure at the outlet, these values might also be determined based on the characteristic method as suggested by Poinsot and Lelef [151].

3.4.4. Geometry description

In most CFD-codes, the used meshes are adapted to the geometrical shape and only consist of cells inside the fluid region. This requires a so called unstructured storage format of the mesh, where not only the information about the geometrical shape and the position of every cell, but also the topology of the mesh needs to be stored. An alternative approach, which is applied in the present work, is to use a completely regular cuboid mesh structure, which has a trivial topology but also leads to computational cells inside the walls. These wall cells need a special numerical treatment and are usually denoted as immersed boundaries. In the first step of the solution, the discretized governing equations are solved for all cells including the immersed boundary cells, which results in a good computational efficiency due to the sequential memory access. Afterwards, the values in the immersed boundary cells are reset to values that imitate a wall. The velocities and thus the convective fluxes at all faces adjacent to an immersed boundary cell are set to zero for all quantities. The diffusive fluxes are also set to zero for zero gradient boundary faces, Dirichlet boundary conditions at the wall are achieved by setting the adjacent immersed boundary cell to the desired value. Zero gradient conditions for the Poisson solver are achieved by setting the pressure value in all immersed boundary cells to the average value of all surrounding fluid cells in every iteration step. The immersed boundary technique is also well suited for handling of moving or deforming geometries, more details can be found in the work of Nguyen et al. [129].

4. Numerical analysis of the Cambridge stratified flame series using artificial thickened flame LES with tabulated premixed flame chemistry [158]

Authors: F. Proch, A.M. Kempf

This chapter including all figures and tables was previously published in 'Combustion and Flame, 161(10), F. Proch and A. M. Kempf, Numerical analysis of the Cambridge stratified flame series using artificial thickened flame LES with tabulated premixed flame chemistry, 2627 – 2646, Copyright © Elsevier (2014)' and is reprinted with permission from Elsevier. The author F. Proch developed the code and the combustion model, ran all the simulations, wrote the paper and generated all figures and tables. The author A.M. Kempf contributed corrections, discussions and proof-reading.

4.1. Abstract

Detailed comparisons of LES results against measurement data are presented for the turbulent lean and rich stratified Cambridge flame series. The co-annular methane/air burner with a central bluff body for flame stabilization has been investigated experimentally by Sweeney et al. [194, 195]. Three cases with varying levels of stratification in the lean and rich combustion regime are taken into account. Turbulent combustion is modeled by using the artificial thickened flame (ATF) approach in combination with flamelet generated manifolds (FGM) lookup tables. The model is adapted for stratified combustion and an alternative formulation for the flame sensor is presented. Three different grids are used to investigate the influence of the filter width and the sub-filter modeling on the overall results. Velocities, temperatures, equivalence ratios, and major species mass fractions predictions are compared with measurements for three different stratification rates and an overall good overall agreement was found between simulation and experiment. Some deviations occur near the bluff body, which are analyzed further by evaluation of atomic and species mass fractions. The stratified combustion process was further

investigated and characterized by probability density functions extracted from the simulation results.

4.2. Introduction

Premixed combustion plays an important role in modern concepts for gas-turbines and IC-engines because of the reduced pollutant formation. However, to make these systems operable under the lean conditions desired, stratification of the mixture is often required. To predict and optimize the complex interaction between mixing and combustion occuring within these systems, large eddy simulation (LES) has proven to be a suitable and convenient approach.

In contrast to non-premixed combustion, the flame thickness in premixed and stratified combustion processes is normally too small to resolve it properly on a typically LES grid. Different approaches have been developed to overcome this difficulty. One possibility is tracking of the flame front by means of a level-set method. This approach was originally introduced as the G-equation model for Reynolds-averaged Navier-Stokes (RANS) simulations by Peters [139], and later has been adapted to extend its validity to the LES context [47, 123, 147].

A second group of models is based on computing the flame structure on the LES grid. In order to properly perform this computation on the too coarse grid, the flame needs to be spatially thickened in the flame normal direction. This can be achieved by reducing the source term and increasing the diffusion term in the transport equations for the chemical species. This technique is referred to as the artificially thickened flame (ATF) [20] approach, which has been successfully applied first in the RANS and later in the LES context [31, 37]. Another possibility is to solve a transport equation for the progress variable and filter it with a filter size larger than the computational mesh, as introduced by Boger et al. [13]. The sum of molecular diffusion and chemical source term for the progress variable is evaluated as a function of the laminar flame speed, similar to the Bray-Moss-Libby model in the RANS context [18]. This method, usually referred to as the flame surface density (FSD) approach, needs modeling of the additional flame surface caused by flame wrinkling on the sub-filter scale level. A wide range of algebraic [2, 59, 125] as well as dynamic models have been developed for that purpose, Ma et al. recently presented a detailed study on the subject [111, 112].

A further approach for modeling premixed flames is based on the tabulation of precomputed detailed-chemistry flames. There are two simultaneously developed flamelet-type tabulation strategies for premixed flames, these are the FPI (flame prolongation of ILDM) [54, 63, 113] and the PFGM (premixed flamelet generated manifolds) [202, 204]. Vreman et al. [208] and later Kuenne et al. [101] combined ATF with PFGM, whereas Galpin et al. [60] extended the filtered progress variable approach into FPI-PCM (presumed conditional moment), which was further modified by Fiorina et al. [55] resulting in the F-TACLES model.

Recently, these models have been further extended to account for stratified conditions. Different groups have adapted their combustion models for varying mixture fractions inside the

This chapter was previously published [158] and is reprinted with permission of the journal.

lean combustion regime [21, 102, 199] to simulate the Darmstadt stratified flame series [182]. Auzillon et al. [5] modified the F-TACLES model for lean stratified combustion and investigated the Darmstadt MOLECULES combustion chamber [79]. Nambully et al. [126, 127] performed LES computations of the Cambridge stratified flame series with the filtered laminar flame (FLF) - PDF model.

The present work aims to continue the investigations on the LES of turbulent stratified flames in the lean and rich combustion regime. The investigated turbulent methane/air burner has recently been developed and investigated at the University of Cambridge and the Sandia National Laboratories by Sweeney, Hochgreb, Dunn and Barlow [194]. Our modeling of turbulent combustion is done by the ATF approach, which is combined with a PFGM tabulation of precomputed premixed flames. Three cases with different levels of stratification are taken into account within this work.

In the first part of the paper, the combustion and sub-filter model and the LES-solver are described, pointing at the necessary adaptions to make the approach suitable for stratified combustion over the whole flammability range. A brief description of the experimental setup is also included here. The presentation and discussion of the results starts with a description of the global flame behavior for the different cases investigated. Subsequently, results on different grids are compared to measurements by analyzing radial profiles of mean and rms at different heights above the burner for velocities, equivalence ratio, temperature and species mass fractions. The behavior in the weakly turbulent zone near the bluff body is discussed. After the validity of the approach has been demonstrated, the simulation data is analyzed further to gain a clearer understanding of the influence of different levels of stratification on the flame behavior. For that purpose, probability distributions of relevant quantities are analyzed.

4.3. Modeling approach

4.3.1. Generation and accessing of the FGM

In the flamelet generated manifolds (FGM) approach, the chemical state and reaction progress space is tabulated over just a small subset of control variables. This is described only briefly here, the detailed derivation was presented by van Oijen et al. [202, 204]. The basis for the FGM is a set of one-dimensional freely propagating premixed flames, which are computed using a detailed chemical mechanism.

In the present work, these computations are performed using the reaction kinetics library Cantera [64] with the GRI-3.0 [188] mechanism for methane-air flames. The resulting chemical state is tabulated over a progress variable, which is chosen as the sum $Y_C = Y_{\mathrm{CO_2}} + Y_{\mathrm{CO}} + Y_{\mathrm{H_2O}}$ of the major product species mass fractions. We found that this progress variable definition works well for the cases investigated, although more complete formulations surely exist [76, 134].

This chapter was previously published [158] and is reprinted with permission of the journal.

To make the tabulation suitable for stratified combustion, multiple flames with varying initial gas composition are computed. This assumes that stratified combustion can be described by an ensemble of perfectly premixed flames with different initial compositions. Unity Lewis number assumption for all species is used which results in constant atomic mass fractions over the flame. As the Cantera library normally does not support such unity Lewis number computations, it was modified to compute the transport coefficients for that purpose. It is known that this assumption has a notable influence on the laminar flame speed of methane/air flames for equivalence ratios bigger than approximately 0.8 [152]. Nevertheless, this assumption has turned out to work well in the context of turbulent combustion, and therefore has been and is used by numerous groups in different combustion models with good success [5, 13, 55, 91, 101, 102, 104, 149]. The advantage of this assumption is that it is consistent with the applied model for the sub-filter treatment as introduced below, which has been derived based on single-step chemistry with constant Lewis number [31]. Furthermore, the mixture fraction remains constant along the flame, which simplifies the tabulation and avoids an additional source term in the respective transport equation. In the present work, the mixture fraction formulation by Bilger [11] has been used, which is related to the fresh gas equivalence ratio in the following manner:

$$\phi = \frac{Z}{1-Z}\frac{1-Z_s}{Z_s} \tag{4.1}$$

The stoichometric mixture fraction takes a value of $Z_s = 0.054$. The flammability limits of methane are set to $Z_{fl} = 0.026$ or $\phi_{fl} = 0.45$ and ($Z_{fr} = 0.093$ or $\phi_{fr} = 1.8$) on the lean (rich) side [106, 184]. Outside the flammability limits, a linear interpolation of the species mass fractions and the enthalpy is applied, assuming ideal mixing towards the state of pure air ($Y_{\mathrm{O_2}} = 0.23$, $Y_{\mathrm{N_2}} = 0.77$) and pure fuel ($Y_{\mathrm{CH_4}} = 1$) at ambient conditions. The remaining quantities like temperature, density and transport coefficients can be determined consistently with the thermophysical models used within the flammability limits.

The resulting manifold is stored in a two-dimensional equidistant lookup-table with the mixture fraction Z and the dimensionless progress variable

$$C = \frac{Y_C - Y_C^{min}(Z)}{Y_C^{max}(Z) - Y_C^{min}(Z)} \tag{4.2}$$

as independent variables, permitting fast non-searching access within the CFD-solver. The FGM includes quantities required by the CFD-solver such as laminar viscosity, density or progress variable reaction rate, but also post processing quantities like temperature and species mass fractions. Figure 4.1 shows the corresponding entries of the table for progress variable reaction rate and temperature. The table is based on 68 premixed one-dimensional flame computations to cover the whole range of flammable mixture fractions, and it has 201 entries in progress variable and 1001 entries in mixture fraction direction.

This chapter was previously published [158] and is reprinted with permission of the journal.

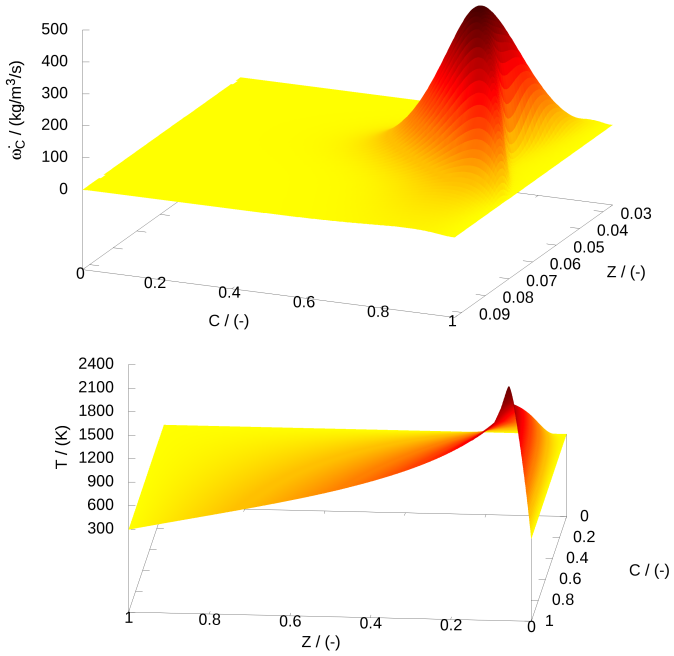

Figure 4.1.: Progress variable reaction rate $\dot{\omega}_C$ and temperature T as function of mixture fraction Z and dimensionless progress variable C. The temperature plot shows the entire mixture fraction range, whereas the illustration of the source term only shows the flammability range, as it vanishes outside [158].

4.3.2. ATF approach

In the ATF approach, the flame (typical thickness of $0.1 - 0.5$ mm) is artificial thickened with the goal of resolving it on a practically affordable LES grid with typical cell sizes bigger than 0.5 mm. This is achieved by introducing a thickening factor F into the Favre-filtered transport equation of the progress variable mass fraction:

$$\begin{aligned} \frac{\partial \bar{\rho}\tilde{Y}_C}{\partial t} + \frac{\partial}{\partial x_i}\left(\bar{\rho}\tilde{u}_i\tilde{Y}_C\right) = \\ \frac{\partial}{\partial x_i}\left(\left[FE\bar{\rho}D_C + (1-\Omega)\frac{\mu_t}{Sc_t}\right]\frac{\partial \tilde{Y}_C}{\partial x_i}\right) + \frac{E}{F}\dot{\omega}_C \end{aligned} \tag{4.3}$$

In Eq. 4.3, ρ, u_i, μ_t and Sc_t denote the fluid density, flow velocity, turbulent viscosity and turbulent Schmidt number respectively. The progress variable diffusion coefficient D_C and reaction rate $\dot{\omega}_C$ are obtained from the FGM table. The flame sensor Ω and the efficiency function E are discussed below. The choice of an un-normalized progress variable, also applied in other works (e.g. [5, 102]), avoids cross terms which would occur for a normalized progress variable, e.g. the cross-scalar dissipation rate term.

In contrast to the classical formulation of the ATF model [31], the thickening factor F is only applied inside the flame region, which is characterized by a high gradient of the progress variable, as suggested by Legier et al. [107]. The thickening factor is reduced smoothly to unity outside the flame region to avoid unphysical behavior in regions of pure mixing as well as

excessive and unnecessary thickening of the pre-heat and burnout zones. The detection of the flame region is performed by the flame sensor Ω, which takes a value of zero in fully burnt or unburnt regions and increases up to unity inside the flame. It should be mentioned that the ATF method without a flame sensor is also able to recover the correct flame propagation. However, the flame sensor improves the method by ensuring that the (unphysical) thickening of the flame is limited to the regions where it is numerically necessary. This especially avoids an unphysical spatial extension of the burnout zones, which is of particular importance near the bluff body of the investigated burner. Our investigations have shown that with the use of a constant thickening factor, the burnout zones interfere in this region on the coarse grid, causing an extinction of the flame (which does not represent the physical behavior). With the flame sensor, simulations on the coarse grid were possible without problems. A study of the impact of the flame sensor on the medium grid can be found in 4.8. A common choice for the flame sensor Ω is based on the progress variable, as suggested by Durand and Polifke [46]:

$$\Omega(C) = 16\left[C\left(1-C\right)\right]^2 \tag{4.4}$$

In this work, the normalized gradient of the progress variable from the one-dimensional Cantera flame computations is used instead. It is mapped over progress variable and mixture fraction and stored as an additional quantity inside the FGM table.

$$\Omega(C,Z) = \left[\frac{\frac{dY_C(x)}{dx}}{\max\left(\frac{dY_C(x)}{dx}\right)}\right]_{1-D} \tag{4.5}$$

The advantage of this choice is that the thickening behavior becomes independent of the local mixture fraction, as illustrated in Fig. 4.2. Shown are the profiles of dimensionless progress variable C and the two flame sensors computed with equations 4.4 and 4.5 as a function of the flame coordinate normalized by the laminar flame thickness δ_l^0. The laminar flame thickness is based on the temperature profile

$$\delta_l^0 = \frac{T_b - T_u}{\max\left(\frac{dT}{dx}\right)}\,, \tag{4.6}$$

where the subscripts b and u denote the burnt and unburnt state, respectively. To compare the flame sensors for the whole mixture fraction range, plots are shown for the stoichometric condition, the lean and the rich flammability limit. The gradient based sensor covers the entire C-profile, independent of the mixture fraction value. The C based sensor also works sufficiently well for stoichometric conditions, but rarely covers the high-temperature part of the flame at both flammability limits. This leads to an inconsistent thickening procedure inside regions of stratified combustion, which involves the danger of altering the results in an unphysical way.

The final formulation of the thickening factor is:

$$F = 1 + \Omega\left(F_{max} - 1\right) \tag{4.7}$$

This chapter was previously published [158] and is reprinted with permission of the journal.

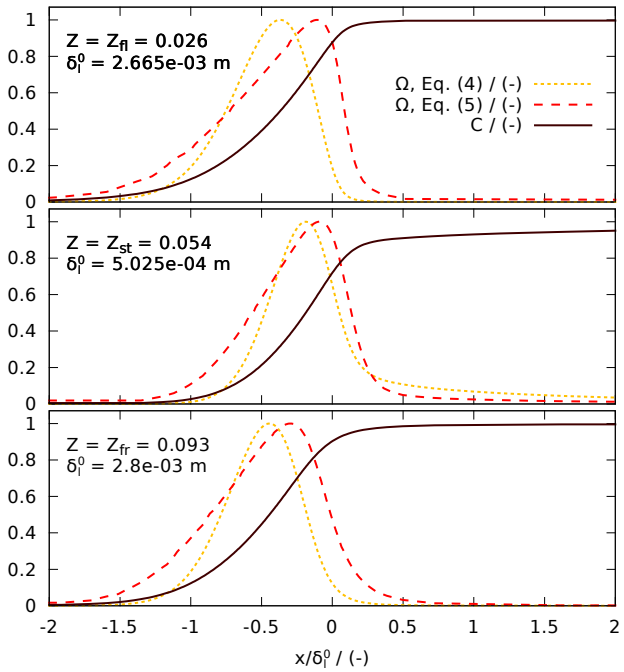

Figure 4.2.: Comparison of profiles of the progress variable C and two different flame sensors Ω over the normalized flame coordinate. Compared are plots for stoichometric (Z_{st}) conditions and the lean (rich) flammability limit Z_{fl} (Z_{fr}) [158].

with

$$F_{max} = \max\left(\frac{n\Delta_{mesh}}{\delta_l^0}, 1\right) \tag{4.8}$$

Here, Δ_{mesh} denotes the cell size of the computational grid and n represents the number of grid-points to resolve the flame thickness, which was set to 5 as suggested by Charlette et al. [31]. The limitation of F_{max} to unity ensures that the flame is not 'thinned' when the grid is sufficiently fine. As the thermal flame thickness δ_l^0 depends on the mixture fraction, it also needs to be tabulated to ensure a consistent thickening procedure in stratified flames.

The modeling of the effect of turbulent velocity fluctuations at the sub-filter level on the progress variable transport also depends on the flame sensor. Inside the flame, the efficiency function E, which corrects for the loss of flame wrinkling by the ATF-approach is evaluated from the commonly used analytical model of Charlette et al. [31]. This model has been chosen as it improves the original formulation by Colin et al. [37] and avoids unphysical stretching of the flame in regions of low turbulence, as found next to the bluff body. The model is used in the modified version by Wang et al. [211]:

$$E = \left(1 + \min\left[F_{max} - 1, \Gamma_\Delta\left(F_{max}, \frac{u'_\Delta}{s_l^0}, Re_\Delta\right)\frac{u'_\Delta}{s_l^0}\right]\right)^\beta \tag{4.9}$$

This formulation makes the model suitable for finer grid resolutions, as the original model implicitly assumed that $F_{max} \gg 1$ (F_{max} takes values between 2.5 and 10 within this work). In Eq. 4.9, s_l^0 denotes the laminar flame speed, which is obtained from a table lookup depending on

the mixture fraction, F_{max} is determined with Eq. 4.8. The model constant is set to the common value of $\beta = 0.5$, which was proposed by Charlette et al. [31] and is also used by other groups [5, 102]. The complete formulation of the remaining terms in Eq. 4.9 can be found in 4.9. Outside the flame region the sub-filter fluxes are modeled by the eddy diffusivity approach, it is smoothly blended over by use of the flame sensor as shown in the first term on the RHS of Eq. 4.3.

4.3.3. Sub-filter closure

As described above, in the FGM approach for stratified combustion the computational quantities are determined from a table lookup depending on mixture fraction and progress variable. However, inside the LES simulation only the filtered values of the independent variables are available. To account for the unknow sub-filter distribution, a common approach is to assume an analytic shape for it and determine the filtered FGM quantities from:

$$\tilde{\Phi} = \int_C \int_Z \Phi(C, Z) P(C, Z)\, dZ dC \tag{4.10}$$

The joint sub-filter distribution of progress variable and mixture fraction is represented by the filtered density function (FDF), $P(C, Z)$. A common simplification in modeling of stratified combustion is the assumption of statistical independence of C and Z, which is motivated by the observation that C usually varies on significantly smaller length scales than Z. The consequence is that the local flame front is only exposed at most to a small variation of mixture fraction, in contrast to the high variation of progress variable. It is then possible to rewrite Eq. 4.10 to:

$$\tilde{\Phi} = \int_C \int_Z \Phi(C, Z) P(C) P(Z)\, dZ dC \tag{4.11}$$

$$= \int_C P(C) \left(\int_Z \Phi(C, Z) P(Z)\, dZ \right) dC \tag{4.12}$$

$$= \int_Z P(Z) \left(\int_C \Phi(C, Z) P(C)\, dC \right) dZ \tag{4.13}$$

The FDF of the respective quantity in the outer integration is approximated by a Dirac delta function (the validity of this assumption is discussed below):

$$\tilde{\Phi} \approx \int_Z \Phi(C, Z) P(Z)\, dZ \tag{4.14}$$

$$\approx \int_C \Phi(C, Z) P(C)\, dC \tag{4.15}$$

In this work, the mixture fraction and progress variable FDF shape is assumed to follow a top-hat distribution as suggested by Floyd et al. [57] and applied with good success to the simulation of a gas turbine model combustor by Olbricht et al. [135]. Vreman et al. [209]

This chapter was previously published [158] and is reprinted with permission of the journal.

carried out a comparison of LES results with different FDFs against DNS data, and found a comparable performance of a top-hat function applied in space to the standard β FDF. The top-hat FDF then avoids the necessity for adding an additional dimension to the FGM table [57, 135], thus reducing the memory requirement and improving the performance of the table lookup. Furthermore, the top-hat FDF is able to represent three-stream mixing in the LES-context, which occurs in the investigated burner between the coflow air and the inner/outer stream, an extensive discussion on the subject and on the comparison of top-hat FDF and β FDF can be found in [57].

To determine the upper (lower) limit of the top-hat FDF for mixture fraction and (if required) progress variable, previous studies [57, 135] computed the value at the cell center plus (minus) the scaled square root of sub-filter variance evaluated from a gradient model like the one by Branley and Jones [15]. Besides introducing the necessity to determine an additional modeling constant, this also causes the problem of handling situations in wich the computed limit falls outside of the valid mixture fraction and normalized progress variable range between zero and unity.

To avoid this problem, within this work the value of the filtered quantities is determined from the average of two top-hat distributions, one ranging from the minimum value on the cell faces to the value at the cell center and the second between the cell center value and the maximum value on the cell faces. The face values are determined by linear interpolation between the neighboring cell centers. It is shown in 4.10 that this converges to the gradient formulation for the case of a linear one-dimensional mixture fraction profile over the cell, the same holds for the normalized progress variable. For cases with curved mixture fraction (normalized progress variable) profiles the order of the approximation is improved in comparison to the gradient formulation.

To investigate the influence of sub-filter modeling, the following coarse grid simulations have been carried out for all three cases: a simulation with a Dirac delta function in C and a top-hat FDF in Z (LES-C-SZ), a simulation with a Dirac delta function in Z and a top-hat FDF in C (LES-C-SC), and finally a simulation with Dirac delta functions in both Z and C (LES-C). As shown in the discussion of the results below, it turned out that the sub-filter modeling has only a small influence on the results for the investigated configurations. Therefore, the medium and fine grid computations have been performed with the assumption of a Dirac distributions for both progress variable and mixture fraction, as the sub-filter contribution can be expected to be smaller on the finer grids.

This chapter was previously published [158] and is reprinted with permission of the journal.

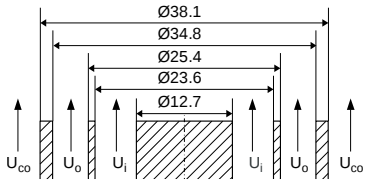

Figure 4.3.: Sketch of the burner setup, all dimensions in mm [158].

Table 4.1.: Operating conditions of the burner for the different cases. Shown are mean axial velocities, ambient temperature and equivalence ratios [158].

Case	U_i	U_o	U_{co}	T	ϕ_i	ϕ_o	ϕ_{co}
	m/s	m/s	m/s	K	-	-	-
SwB1	8.31	18.7	0.4	295	0.75	0.75	0
SwB5	8.31	18.7	0.4	295	1.0	0.5	0
SwB9	8.31	18.7	0.4	295	1.125	0.375	0

4.4. Experimental and numerical setup

4.4.1. Experiment

The Cambridge stratified burner [194] consists of two annular slots surrounding a central bluff body. Each slot supplies a perfectly premixed methane/air mixture with varying composition allowing to investigate different levels of stratification. The burner is embedded in a coflow of air. A sketch of the setup is shown in Fig. 4.3. Three different stratified cases are investigated here. Table 4.1 summarizes the corresponding operating conditions. The resulting Reynolds numbers are $5{,}960$ in the inner and $11{,}500$ in the outer stream. Based on measured values [194] of $u' = 4.37$ m/s and $L_{turb} = 1.72$ mm for the intensity and length scale of the turbulent fluctuations 45 mm downstream of the burner exit, the combustion process falls into the thin reaction zone regime of the modified Borghi diagram for the whole range of equivalence ratios. Velocity data is available from PIV- and LDA-measurements by Zhou et al. [220], the latter ones used as reference in this work. This choice is based on the availability of LDA data at all scalar measurement locations, whereas the PIV data is only available up to 60 mm. Radial profiles for temperature and mass fractions of major species are available from Rayleigh respectively Raman scattering measurements by Sweeney et al. [194].

4.4.2. CFD-solver and numerical setup

The numerical simulations have been performed with the in-house LES-code 'PsiPhi' [21, 87, 142]. The program solves the low-Mach number Favre-filtered governing equations for mass, momentum, progress species and mixture fraction. Continuity is ensured by a projection method, the resulting Poisson equation for pressure is solved iteratively by the Gauss-Seidel method with successive over-relaxation (SOR). The equations are discretized with the finite-

This chapter was previously published [158] and is reprinted with permission of the journal.

volume method (FVM) on an equidistant and orthogonal Cartesian grid. Interpolation of the convective fluxes on the cells faces is performed by a second order central-difference scheme for momentum and a total variation diminishing (TVD) scheme with non-linear CHARM limiter [219] for density and other scalars. The solution is advanced in time with a low-storage third order Runge-Kutta scheme. The code is parallelized with a distributed memory domain decomposition concept using the message passing interface (MPI). The method of immersed boundaries is applied for a computationally efficient treatment of the geometric shape.

The effect of the velocity fluctuations at the sub-filter level is modeled with the eddy-viscosity approach for momentum and the eddy-diffusivity approach for mixture fraction and progress variable, with the turbulent Schmidt number set to 0.7. The turbulent viscosity is evaluated with the σ-model suggested by Nicoud et al. [131]:

$$\mu_t = \rho \left(C_m \Delta\right)^2 D_m \left(\tilde{u}\right) \tag{4.16}$$

In this model, the differential operator D_m is a function of the singular values of the velocity gradient:

$$D_m = \frac{\sigma_3 \left(\sigma_1 - \sigma_2\right) \left(\sigma_2 - \sigma_3\right)}{\sigma_1^2} \tag{4.17}$$

with

$$\sigma_1 \geq \sigma_2 \geq \sigma_3 \geq 0 \tag{4.18}$$

The singular values σ_i are identically equal to the square root of the eigenvalues of the tensor:

$$G_{ij} = \frac{\partial \tilde{u}_k}{\partial x_i} \frac{\partial \tilde{u}_k}{\partial x_j} \tag{4.19}$$

The corresponding modeling constant is set to a value of $C_m = C_\sigma = 1.5$. The σ model has been chosen as it avoids the over-prediction of the turbulent viscosity near walls and in shear layers typical of the classical Smagorinsky model without using a computational expensive dynamic procedure.

The computational domain extends 112 mm in the axial z-direction, and 110 mm in the x- and y-directions. The last 12 mm of the burner have been included in the simulation to obtain realistic flow conditions at the burner exit. To study the influence of filter width on the results, computations have been carried out for three different grid resolutions, which are summarized with the respective computational costs in Table 4.2. The sampling for statistical means and variances was started after 7 and carried out for at least 8 flow-through times based on the inner stream velocity, leading to a simulated time of approximately 0.2 seconds.

Parabolic velocity profiles with mean values corresponding to Table 4.1 and superimposed pseudo-turbulent fluctuations were set at the inflow of the computational domain. The fluctuations were generated with the filtering method of Klein et al. [94] in an efficient numerical implementation proposed by Kempf et al. [88]. The turbulent length scale was set to 1 mm and

This chapter was previously published [158] and is reprinted with permission of the journal.

Table 4.2.: Details of the simulations on three different grids. The computations were run for 15 flow through times at the inner stream velocity $U_i = 8.31$ m/s [158].

Grid	Δ_{mesh} mm	n_{Cells} million	t_{CPU} h	t_{Wall} h	n_{Procs} -
Coarse (C)	1.0	1.6	91	2.5	36
Medium (M)	0.5	13.4	3,533	10.3	343
Fine (F)	0.25	103.2	49,152	96.0	512

the rms of the fluctuations to 2.5 m/s. A zero gradient condition was imposed at the outflow for all quantities.

4.5. Results and discussion

4.5.1. General flame behavior

Figure 4.4 shows instantaneous and mean simulated contour plots of equivalence ratio in a burner cross section, giving a first impression of the flow. Downstream of the burner exit, mixing occurs between the coflow and the outer stream in all three cases and in addition between the inner and outer stream in the SwB5 and SwB9 cases. The mixing rate is increased by additional turbulent motion developing in the shear layers between the coflow and the inner and outer stream. The lean flammability limit is denoted by a black isoline, which starts between the outer stream and the coflow at the burner exit and slowly widens up further downstream for SwB1 and SwB5. For SwB9 the mixture of the outer stream is leaner than the flammability limit, therefore the isoline starts between the inner and outer stream and widens up to a smaller radius than in the other cases. The isolines of the flame sensor (Eq. 4.5), which border the region where combustion takes place, are shown in white.

One can distinguish three characteristic flame regions. The first region is perfectly premixed and characterized by a constant mean flame angle and only moderate broadening of the mean flame brush.

The second region starts where the (instantaneous) flame enters into the region of equivalence ratio gradients, and is exposed to stratification. The curvature decreases (increase) for the isolines of the mean flame sensor at the unburnt (burnt) side of the flame, resulting in a broadening of the mean flame brush. This location is found at approximately 40 mm (SwB1), and 30 mm (SwB5, SwB9). In addition, from about 40 mm onwards the whole flame is exposed to an equivalence ratio gradient in the two latter cases. The equivalence ratio at the burnt side of the flame converges then towards a value of 0.6, which is the mean of the value at the flammability limit and the average value at the inlet, which is 0.75 for all cases.

The transition point to the third region is located where the instantaneous flame touches the flammability limit line. Here, the motion of the unburnt side of the flame is determined by the

This chapter was previously published [158] and is reprinted with permission of the journal.

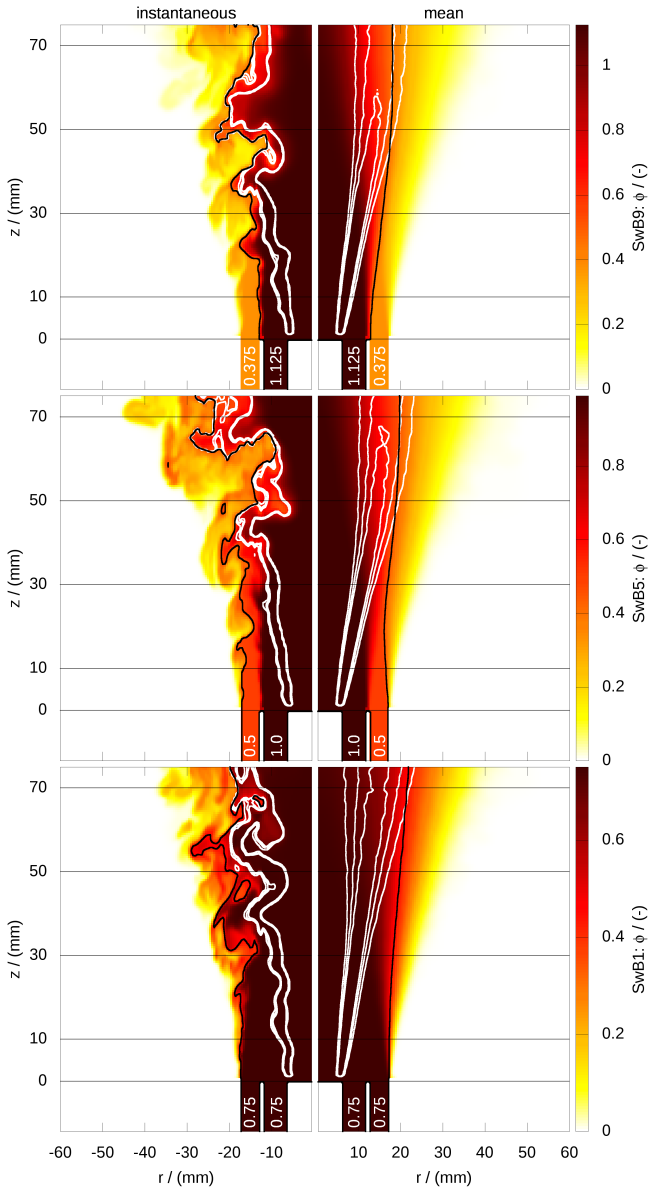

Figure 4.4.: Instantaneous and mean contour plots of equivalence ratio in a burner cross section for the three investigated cases on the medium grid, the lean flammability limit is marked by a black isoline, the flame sensor which marks the combustion region is denoted by white isolines. The values in the nozzle give the respective equivalence ratio [158].

This chapter was previously published [158] and is reprinted with permission of the journal.

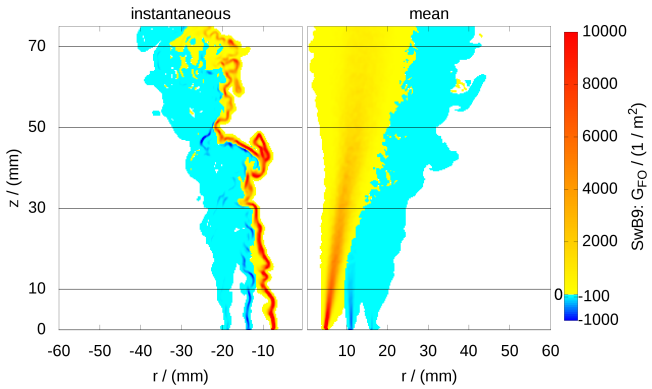

Figure 4.5.: Instantaneous and mean contour plots of the flame index in a burner cross section for SwB9. Values between -0.1 and +0.1 are colored in white [158].

mixing behavior and the outer isoline of the flame sensor coincides with the flammability limit. In contrast to before, the curvature of the isolines of the mean flame sensor increases at the unburnt side of the flame and decreases at the burnt side of the flame resulting in a decrease of the flame angle and a stabilization of the flame brush thickness. This region starts at around 60 mm (SwB1), and 50 mm (SwB5, SwB9).

To demonstrate that the premixed mode is dominant, Fig. 4.5 shows instantaneous and mean contour plots of the flame index evaluated from [54, 218]:

$$G_{FO} = \nabla Y_{CH4} \cdot \nabla Y_{O_2} \tag{4.20}$$

Only the results for the mostly stratified case SwB9 are displayed as the results are comparable for the other cases. The flame index takes positive (negative) values in premixed (non-premixed) regions and becomes zero outside of the reaction zone. Overall the combustion process takes places in a premixed environment. Only in very small regions at the unburnt side of the instantaneous reaction zone the flame index becomes slightly negative locally.

4.5.2. Velocities

Comparisons of mean and rms radial profiles of axial and radial velocity components from simulations and experiments for all three cases are shown in Figures 4.6-4.9. The LDA measurements from Zhou et al. [220] are denoted by black dots. For the coarse grid two additional data sets are shown (LES-C-SZ and LES-C-SC), which were obtained with sub-filter modeling using the top-hat FDF, as explained in section 4.3.3. For all cases the impact of the bluff body and the different velocity magnitudes on the flow field are clearly visible. In the region behind the bluff body a recirculation zone is formed, which disappears further downstream due to momentum exchange with the faster inner flow and thermal expansion. The latter phenomenon is more dominant for SwB5 and SwB9, as the zone of the flame with strong reaction is shorter in these cases, as can be seen from the isolines of the flame sensor in Fig. 4.4. In the shear layers

This chapter was previously published [158] and is reprinted with permission of the journal.

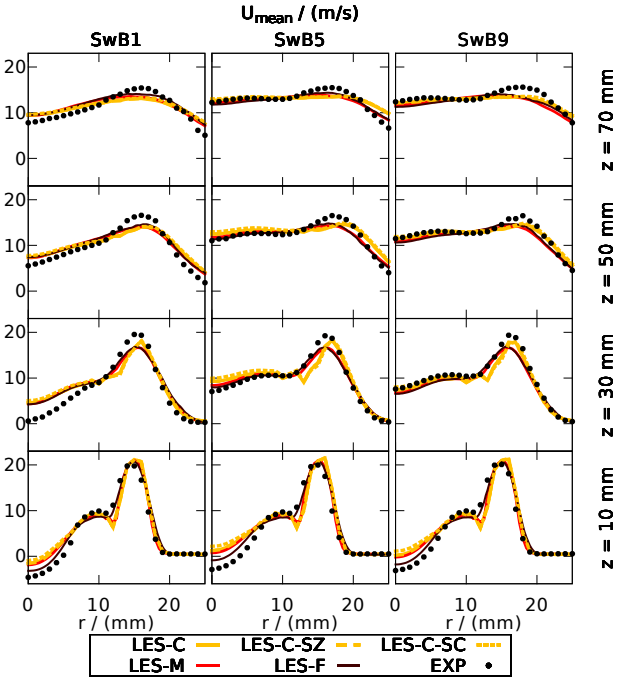

Figure 4.6.: Radial profiles of the mean axial velocity at different downstream locations, showing a comparison for three different grids with the experiments. LES-C-SZ and LES-C-SC refer to a coarse grid simulation with additional sub-filter modeling using a top-hat FDF in mixture fraction and progress variable, respectively [158].

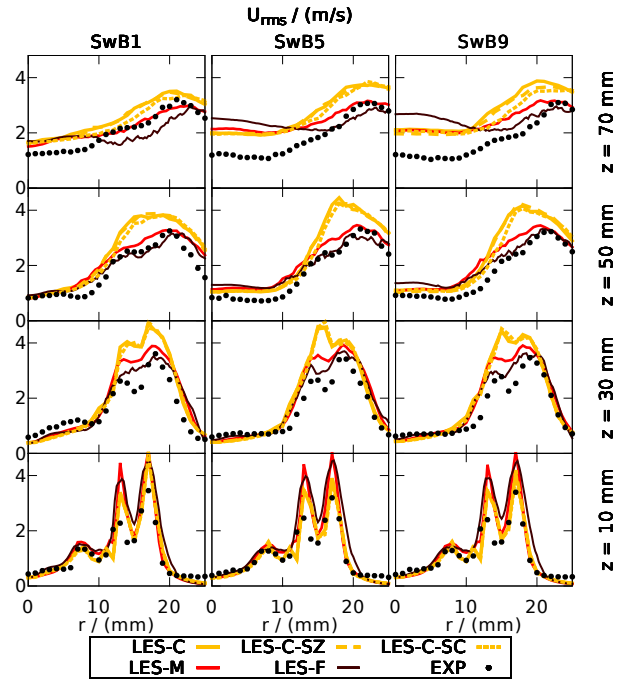

Figure 4.7.: Radial profiles of the axial velocity fluctuations at different downstream locations, showing a comparison for three different grids with the experiments. LES-C-SZ and LES-C-SC refer to a coarse grid simulation with additional sub-filter modeling using a top-hat FDF in mixture fraction and progress variable, respectively [158].

This chapter was previously published [158] and is reprinted with permission of the journal.

between the streams and the coflow the turbulent fluctuations are amplified.

The simulation results are in good agreement with the experiments, the basic trends are matched for all cases and grid resolutions. The quality of the predictions improves with grid refinement, here the differences between the coarse and medium grid are bigger than between the medium and fine grid, implying good convergence. The agreement of the fluctuations with the measurements benefits substantially from the refinement of the grid. The influence of the top-hat sub-filter model on the coarse grid velocity results is generally small. Slight deviations occur for the fluctuations of axial velocity at the last two measurement positions, where also the agreement with the experimental results declines for all cases and grids. This can be attributed to the size of the computational domain, which was chosen to be compact so that fine grid simulations are computationally affordable. (To investigate the influence of the domain size, additional simulations on the coarse grid with doubled domain size in all directions have been performed for all three cases. It was found that the influence of the domain size is negligible for the means of all investigated quantities and the fluctuations of all quantities except for axial velocity at the last two measurement positions. The respective comparisons can be found in 4.11.)

The strength of the recirculation zone is under predicted by the simulation, most visible for SwB1. This is in agreement with simulation results by Nambully et al. [126], and might be an indicator that the flame is slightly lifted at the bluff body, which can not be reproduced with the applied adiabatic combustion model. However, this affects only a limited area of the flow field and has no significant influence on the regions of interest, which are the regions where (stratified) combustion occurs.

The radial velocity component shows a considerable deviation towards the center line where the measurements show a negative velocity, whereas the simulations predict zero velocity. This suggests that the experimental data is slightly asymmetric, which on the one hand could be due to measurement uncertainties caused by the small magnitude of the quantity. On the other hand, such burner configurations are known to be highly sensitive to small deviations in the geometrical shape, so that the measured asymmetry may represent the real flow field. This (unwanted) asymmetry is very hard to take into account within a numerical simulation, and again the effect on the rest of the flow field is small. Overall the flow field is well captured by the simulation, which is a prerequisite for the correct prediction of scalar quantities.

4.5.3. Equivalence ratio, temperature and progress variable

The comparisons of mean and rms profiles of equivalence ratio and temperature against the measurements by Sweeney et al. [194] are shown in Figures 4.10-4.13. The profiles of the equivalence ratio mirror the observations made for the flow field. The steep gradients between the inner and outer streams and the coflow are dissipated downstream, and fluctuations are produced within the shear layers in between. The behavior of the temperature profiles correlates

This chapter was previously published [158] and is reprinted with permission of the journal.

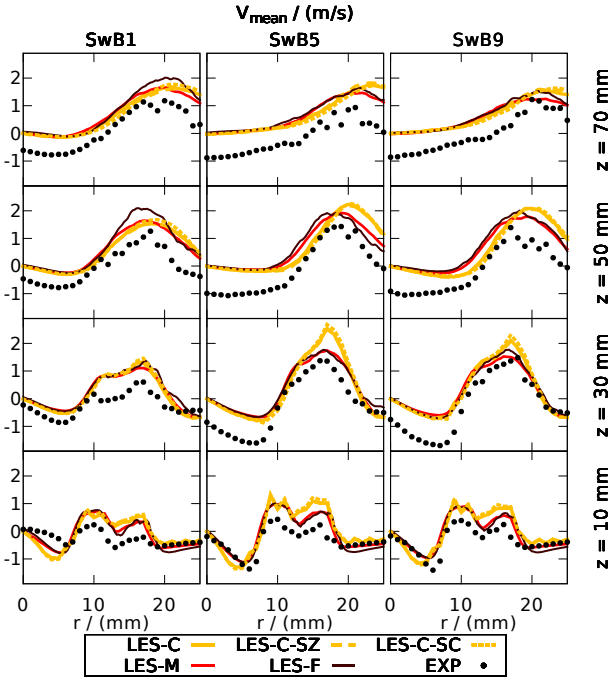

Figure 4.8.: Radial profiles of the mean radial velocity at different downstream locations, showing a comparison for three different grids with the experiments. LES-C-SZ and LES-C-SC refer to a coarse grid simulation with additional sub-filter modeling using a top-hat FDF in mixture fraction and progress variable, respectively [158].

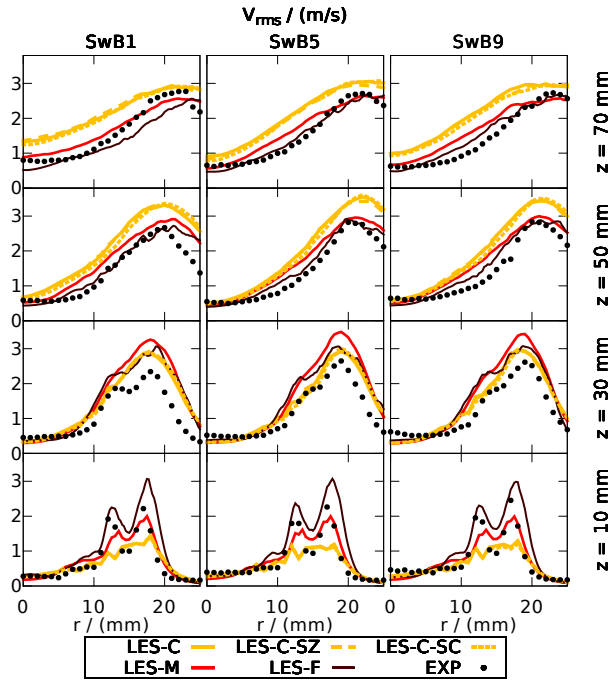

Figure 4.9.: Radial profiles of the radial velocity fluctuations at different downstream locations, showing a comparison for three different grids with the experiments. LES-C-SZ and LES-C-SC refer to a coarse grid simulation with additional sub-filter modeling using a top-hat FDF in mixture fraction and progress variable, respectively [158].

This chapter was previously published [158] and is reprinted with permission of the journal.

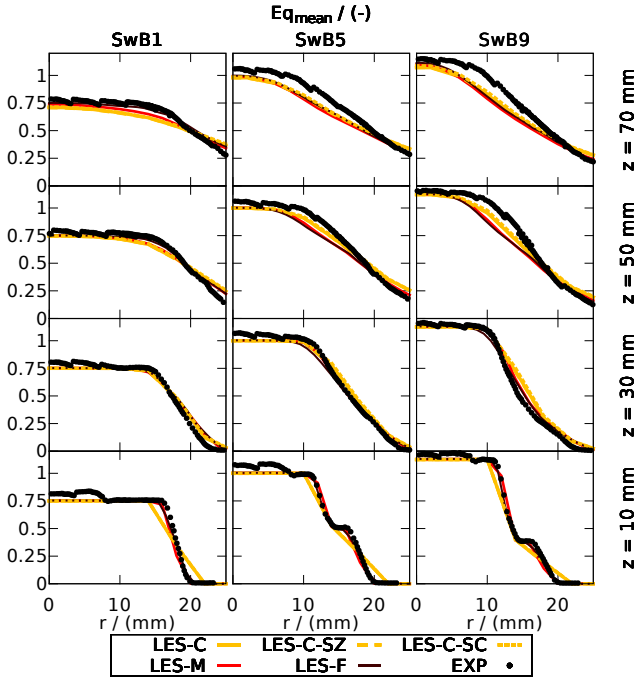

Figure 4.10.: Radial profiles of the mean equivalence ratio at different downstream locations, showing a comparison for three different grids with the experiments. LES-C-SZ and LES-C-SC refer to a coarse grid simulation with additional sub-filter modeling using a top-hat FDF in mixture fraction and progress variable, respectively [158].

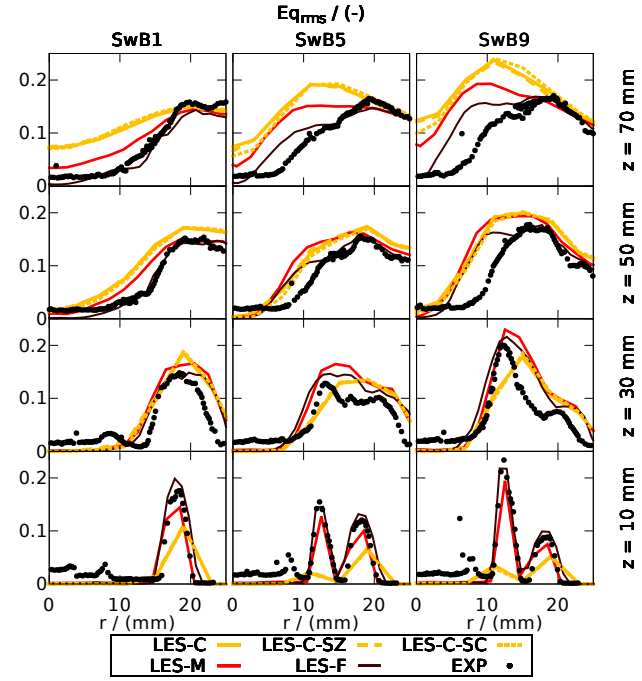

Figure 4.11.: Radial profiles of the equivalence ratio fluctuations at different downstream locations, showing a comparison for three different grids with the experiments. LES-C-SZ and LES-C-SC refer to a coarse grid simulation with additional sub-filter modeling using a top-hat FDF in mixture fraction and progress variable, respectively [158].

This chapter was previously published [158] and is reprinted with permission of the journal.

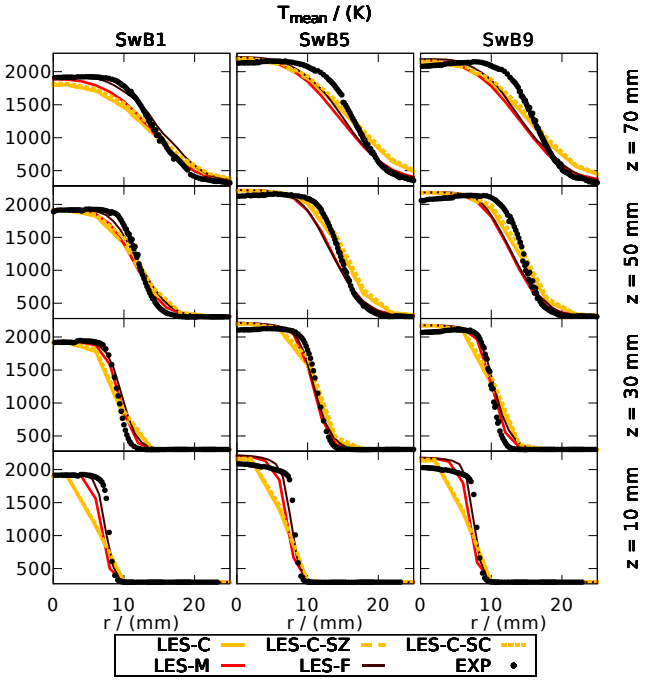

Figure 4.12.: Radial profiles of the mean temperature at different downstream locations, showing a comparison for three different grids with the experiments. LES-C-SZ and LES-C-SC refer to a coarse grid simulation with additional sub-filter modeling using a top-hat FDF in mixture fraction and progress variable, respectively [158].

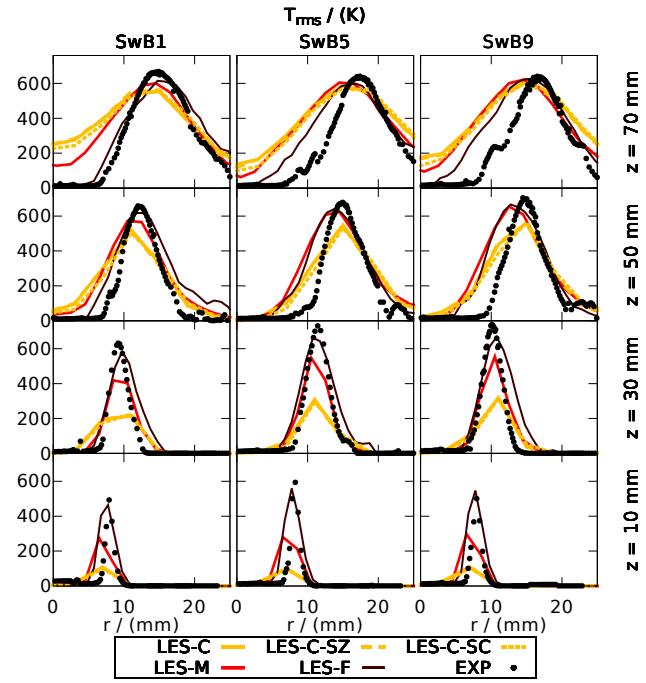

Figure 4.13.: Radial profiles of the temperature fluctuations at different downstream locations, showing a comparison for three different grids with the experiments. LES-C-SZ and LES-C-SC refer to a coarse grid simulation with additional sub-filter modeling using a top-hat FDF in mixture fraction and progress variable, respectively [158].

This chapter was previously published [158] and is reprinted with permission of the journal.

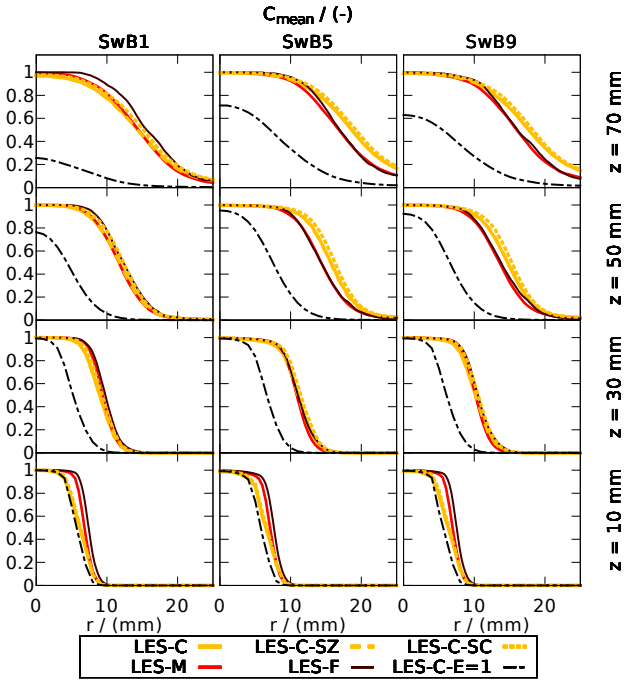

Figure 4.14.: Radial profiles of the mean Favre-filtered progress variable at different downstream locations. LES-C-SZ and LES-C-SC refer to a coarse grid simulation with additional sub-filter modeling using a top-hat FDF in mixture fraction and progress variable, respectively. LES-C-E=1 shows the results of a computation without efficiency function, i.e. setting $E = 1$ in Eq. 4.3 [158].

strongly with the observations made for the mean flame brush in Fig.4.4, as expected for a unity Lewis number assumption. The basic trends from the measurements are matched by the simulations, and the effect of grid refinement and sub-filter model is comparable to the observations made for velocities.

The mean Favre-filtered normalized progress variable is also shown for completeness in Fig. 4.14. The progress variable profiles are comparable to the temperature profiles, which was to expected for a unity Lewis number assumption. The strong effect of the efficiency function is shown in Fig. 4.14, which also includes profiles that were obtained from additional simulations with the efficiency function set to unity inside the whole domain. It becomes obvious that, although the Reynolds numbers are small in the investigated burner, taking into account the loss of flame wrinkling by the thickening procedure is crucial for the correct flame propagation. This is also reflected by the magnitude of the efficiency function observed in the simulations, which lies around three for the coarse grid.

To get a better understanding of the reason why the effect of the mixture fraction sub-filter model is negligible, Fig. 4.15 shows the instantaneous maximum and minimum mean Favre-filtered mixture fraction values at the faces for one time step. In the vast majority of cells, the mixture fraction varies by less than 10% of the stoichometric value between the cell center and the faces, the corresponding range is marked by thin dark-red lines in Fig. 4.15. To check the possible influence of this range on the flame propagation, Fig. 4.16 shows the laminar flame speed over the mixture fraction as used in the simulation. The spacing of the mixture fraction

This chapter was previously published [158] and is reprinted with permission of the journal.

grid lines corresponds also to 10% of the stoichometric value. Assuming an adequately resolved (thickened) progress variable field, it is notable that a piecewise-linear approximation with this mixture fraction sub-filter variance, which corresponds to a computation with the top-hat sub-filter model, is able to reproduce the flame speed correlation with a small error, even around the stoichometric region with high curvature values. At the same time, an approximation by the value at the center of each interval, which would correspond to the assumption of a Dirac peak for the sub-filter distribution, would lead to an almost identical result. In other words, the impact of the sub-filter model is very small. This is in agreement with the findings of Cavallo Marincola et al. [21].

However, Fig. 4.15 shows some distinct features which could become important for other cases with higher sub-filter variance. First, the plot is not perfectly symmetric, as would be implicitly assumed by a gradient model for the sub-filter variance. There even exist some points where the mixture fraction has a local maximum or minimum at the cell center, which is denoted by minimum (maximum) values of $\tilde{Z}$ at the cell faces above (below) the diagonal (in Fig. 4.15, this is shown by red squares below and yellow triangles above the diagonal line). A second notable feature is the presence of a gap between the diagonal and the mixture fraction points towards higher values of the mixture fraction. This gap is shifted towards the minimum mixture fraction values. This implies that the corresponding cell is located in a region where the mixture fraction profile changes mainly towards leaner mixture fractions. Such condition occur at the point where the mixture fraction profiles starts declining from the broad peak at the stoichometric value towards higher radii. In the Fig. 4.10 this would correspond to a radial position of approximately 12 mm. High mixture fraction variances mainly occur around the burner exit conditions, which correspond to mixture fraction values of 0 for the coflow and 0.0277 (0.054) for the outer (inner) stream. Although the magnitude of the mixture fraction variances at these three locations is comparable, the distribution among minimum and maximum values varies. At $\tilde{Z} = 0$ ($\tilde{Z} = 0.054$) high variances mainly occur for Z_{max} (Z_{min}). A similar behavior is observed for $\tilde{Z} = 0.0277$, where large Z_{max} occur for large $\tilde{Z}$, and small Z_{min} for small $\tilde{Z}$. The reason for that can again be found in the shape of the equivalence ratio profiles: As shown in Fig. 4.10, at $\tilde{Z} = 0$ ($\tilde{Z} = 0.054$) a steep gradient exists only towards richer (leaner) conditions. In contrast, the value $\tilde{Z} = 0.0277$ marks an inflection point of the equivalence ratio profile and therefore has considerably gradients towards leaner as well as richer conditions.

The mean temperature profile deviates notably near the bluff body for the coarse grid, which can be explained by the ATF-modeling: The real flame is very thin at the edge of the bluff body due to wall effects, but the ATF approach thickens the flame also at this position to the adjusted 5 grid points according to Eq. 4.8. To enforce the thin flame here, the thickening would have to be blocked in the cells near the wall, causing an insufficient resolution of the flame leading to poor numerical accuracy. The origin of this problem is that modeling approaches based on broadening of the flame, by thickening or filtering, mean a certain loss in spatial accuracy, which can cause deviations in the flame position in such situations. However, the fact that the flame

This chapter was previously published [158] and is reprinted with permission of the journal.

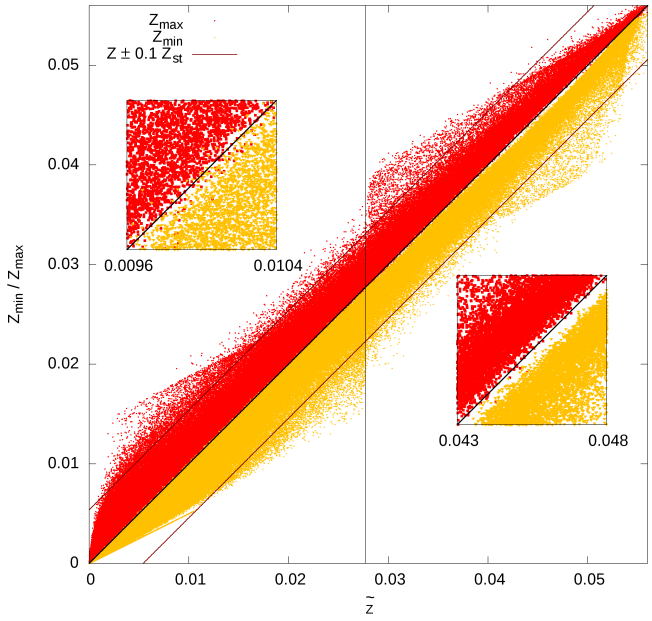

Figure 4.15.: Maximum and minimum mean Favre-filtered mixture fractions at the cell faces as a function of the respective value $\tilde{Z}$ at the cell center for the case SwB5 on the coarse grid with top-hat sub-filter model in Z (LES-C-SZ). The diagonal line corresponds to the values at the cell centers. Enlarged plots are included for regions with distinct features. The range of 10% mixture fraction deviation based on the stoichometric value is bordered by thin lines, the inner stream mixture fraction of 0.277 is marked by a vertical line [158].

position is predicted well further downstream also for the coarse mesh may be seen as evidence that the modeling of the overall flame behavior is not deteriorated significantly by this effect. The rms fluctuations of the temperature are under predicted on the coarse and medium grid up to the middle of the computational domain, which is in agreement with the observations made by Kuenne et al. [102], and is likely to be caused by the effect of the thickening procedure on the flame dynamics.

The equivalence ratio (experimental data) plots show a distinct peak in the bluff body region at a radius lower than 10 mm. This has been investigated closer experimentally by Barlow and coworkers [7, 44] and numerically by Katta and Roquemore [82] and Nambully et al. [127]. The effect is explained by preferential diffusion of H_2O and H_2, which can not be captured with the Lewis number unity assumption applied within this work, but will be analyzed further in the next section. Overall, the simulation results are in good agreement with the measurements for equivalence ratio and temperature.

4.5.4. Major species

To further access the modeling approach and get deeper insights into the chemical structure of the flame, mean and rms radial profiles of major species obtained from the simulation are compared to measurements [194]. The trend and observations made for temperature and mix-

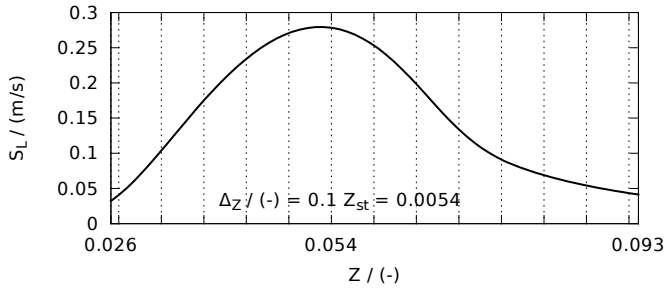

Figure 4.16.: Laminar flame speed vs. mixture fraction for methane/air computed with the GRI-3.0 mechanism and unity Lewis number assumption for all species. The spacing of the mixture fraction grid lines is 10% of the stoichometric value, corresponding to the range indicated in Fig. 4.15 [158].

ture fraction in the last section hold for the species, the respective Figures 4.29-4.38 have been moved to 4.13 for brevity.

Figure 4.17 shows a comparison of mean mass fraction profiles of major species 10 mm above the burner with measurements for the fine grid simulation. The related atomic mass fractions for carbon, hydrogen, oxygen and nitrogen are displayed in Fig. 4.18. Noticeable differences between simulation and experiment can be observed for radii smaller than 10 mm, which will be addressed next.

For SwB1, the element mass fraction is under predicted for carbon and over predicted for oxygen relative to the experiments. Looking at the species profiles, it can be seen that this corresponds to a lack of CO_2 and a surplus of O_2. The under predicition of carbon also occurs for SwB5 and SwB9, this corresponds to a lack of CO here. For the latter case, an additional over prediction of hydrogen and oxygen can be observed, which can be assigned to a surplus of H_2O.

The under prediction of H_2 mass fraction occurring for all three cases does only have a negligible influence on the atomic mass fraction of hydrogen, as this is dominated by the contributions of H_2O and CH_4. It should be considered that the experimental profiles are somewhat discontinuous for oxygen and nitrogen, where nitrogen shows the inverse behavior of oxygen. In accordance with the observations by Sweeney et al. [194], it is also mentioned here that the agreement of CO_2 measurements with predictions based on one-dimensional flame computations (which are the basis for FGM) is worse than for the other educt and product species (CH_4, H_2O, O_2).

The enrichment of CO_2 in the recirculation zone for SwB1 can be explained with the effect of preferential diffusion suggested by Barlow et al. [7], although the depletion of O_2 is unexpected in that context. In contrast, the enrichment of CO for SwB5 as well as SwB9 and the additional depletion of H_2O for the latter case may be rather due to heat transfer than due to preferential diffusion. One indicator for an heat loss effect is that the measured mean temperature profiles have a remaining slope at the centerline and a lower peak value in comparison to the adiabatic simulation results. Another indicator is that the CO and H_2O mass fractions in the FGM-table for the experimental temperatures at the centerline were found to be in good agreement with the

This chapter was previously published [158] and is reprinted with permission of the journal.

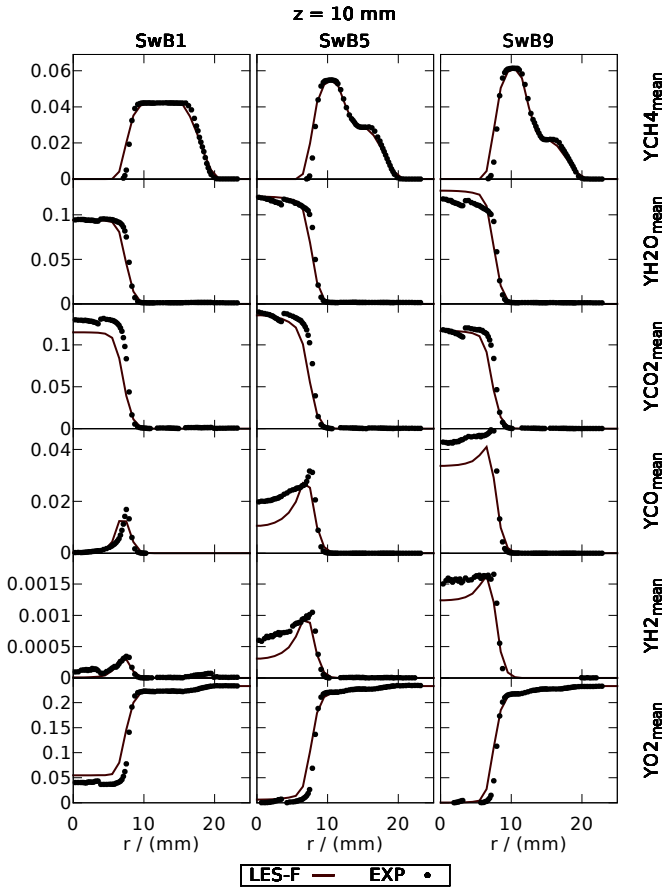

Figure 4.17.: Radial profiles of the mean major species mass fractions 10 mm downstream of the burner exit [158].

measured concentrations of these species. A non-adiabatic extension of the ATF/FGM model has been presented and applied by Ketelheun et al. [91] with good success, assuming a Dirac peak for the sub-filter distributions.

4.5.5. Influence of stratification

The effects of stratification on the flame behavior are investigated further. As this is rather thought as a deeper analysis of the combustion process using the capabilities of the numerical simulation than as an additional validation, only the fine grid results are taken into account.

To classify the dependency of the combustion process on the equivalence ratio globally, the normalized PDF of Favre-filtered reaction source term conditional on Favre-filtered equivalence ratio over the entire domain is shown in Fig. 4.19. To take into account the effects of turbulence and thickening, the last term on the RHS of Eq. 4.3 was used as the source term. This gives a good representation of the influence that reaction at the given equivalence ratio has on the global combustion process and heat release. The sampling was carried out for at least 8 flow-through times in accordance with the other flow statistics.

For all cases, combustion occurs in the whole range of equivalence ratio between the lean flammability limit and the respective equivalence ratio in the inner stream. Towards the lean

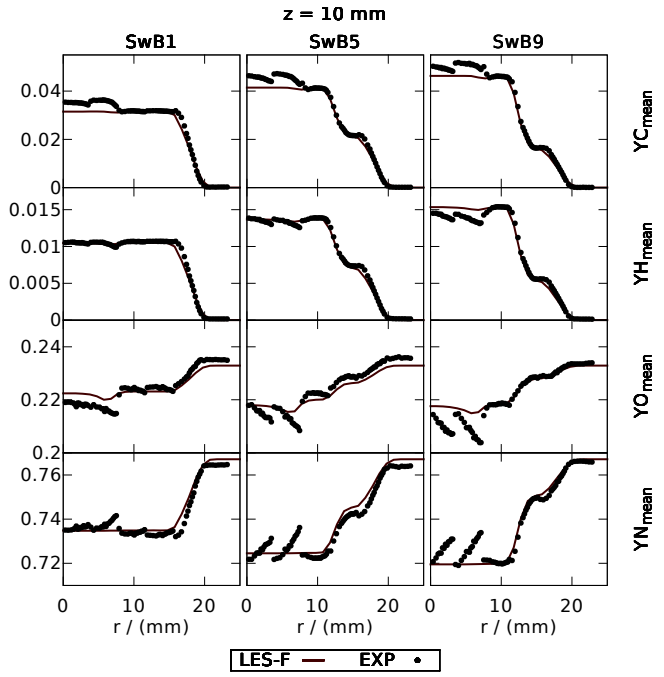

Figure 4.18.: Radial profiles of the mean atomic mass fractions 10 mm downstream of the burner exit [158]

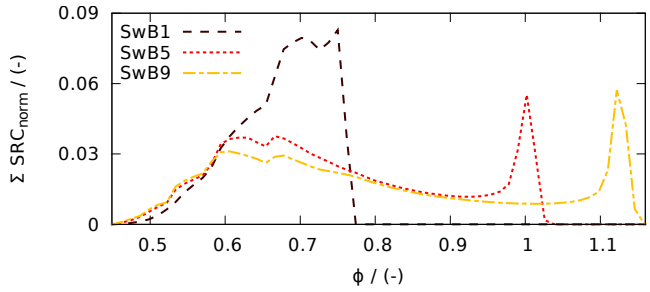

Figure 4.19.: Normalized PDFs of Favre-filtered reaction source term conditional on Favre-filtered equivalence ratio over the entire domain [158].

flammability limit the reaction probability declines to zero at a comparable rate for all cases.

For SwB1, the PDF is continuously rising until reaching an equivalence ratio of 0.7, followed by a broad peak towards the inner (and outer) stream value of 0.75. This shows that already the presence of an air coflow is sufficient to trigger combustion over the whole equivalence ratio range down to the flammability limit.

For SwB5 and SwB9 the PDF increases steadily from the flammability limit until a value of around 0.6, which corresponds to the burnt side of the flame when it is located completely in a stratified enviroment, as already adressed in section 4.5.1. From 0.6 onwards, the PDF decreases constantly until it reaches the respective equivalence ratio in the inner stream, here it develops a sharp second peak. The reason why the first peak is much broader than the second one is that the respective samples are found further downstream, where the flame front has been widened by turbulent effects. It is noticeable that the shape of the PDF is very similar for SwB5 and SwB9. The fact that the latter one is partly located within the rich equivalence ratio regime

This chapter was previously published [158] and is reprinted with permission of the journal.

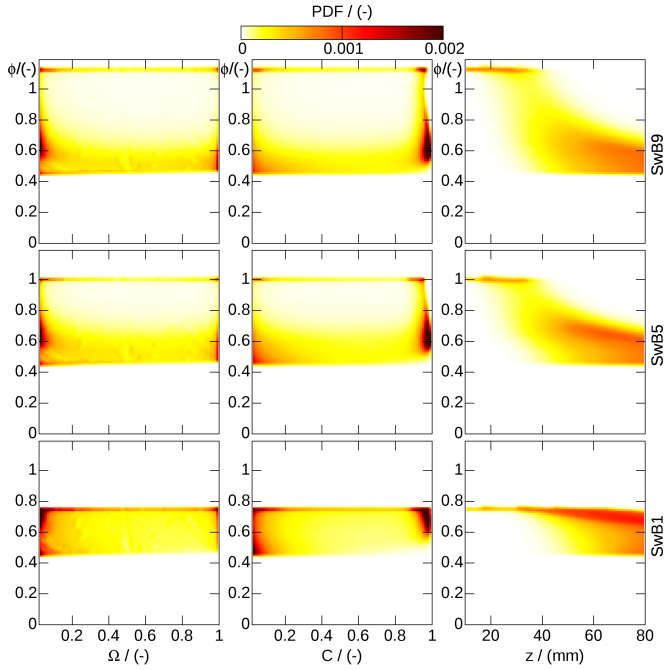

Figure 4.20.: Joint PDFs of Favre-filtered equivalence ratio vs. Favre-filtered flame sensor (left), Favre-filtered normalized progress variable (middle) and distance from the burner exit (right) [158].

does not seem to have a considerably influence on the stratified combustion process.

Figure 4.20 shows the normalized joint PDFs of Favre-filtered equivalence ratio against the Favre-filtered flame sensor, the Favre-filtered normalized progress variable and the axial distance from the burner exit. This characterizes the stratified combustion process further taking into account the interaction between the value of equivalence ratio and the intensity of reaction, the reaction progress and the axial position, respectively. Only the points inside the flame region have been considered, the limit has been set at a flame sensor value of 0.01. Therefore the outer stream equivalence ratio does not occur in the axial position plots for small distances, as the flame burns only at the inner stream equivalence ratio in this regions.

The shape of the already discussed reaction source term PDFs is basically mirrored in the joint PDFs of the flame sensor for values near zero, which are found in regions with low reaction rates at the unburnt or burnt side of the flame. For SwB1 the joint PDF shifts towards the inner (and outer) stream equivalence ratio of 0.75 when proceeding to higher flame sensor values. Within the flame zone with the highest reaction rate corresponding to a flame sensor value of unity, most of the combustion is occurring in a broad peak towards the inner (and outer) stream equivalence ratio of 0.75. Nevertheless, contributions of the whole equivalence ratio range are found for all flame sensor values. For SwB1 and SwB5 the bimodal shape with peaks at the respective inner stream equivalence ratio of 1.0/1.125 and the already discussed value of 0.6 gets more and more distinct when proceeding to higher flame sensor values. At a flame sensor value of unity, there is only a negligible amount of samples found in the equivalence ratio range between approximately 0.8 and the inner stream equivalence ratio of 1.0/1.125, which means that for the high reactive part of the flame it can be distinguished between two types of flames

This chapter was previously published [158] and is reprinted with permission of the journal.

which differ about 0.2 respectively 0.3 in equivalence ratio.

Within the progress variable joint PDFs, it can be observed that for SwB1 most of the combustion at equivalence ratios near to the lean flammability limit occurs at low progress variable values near the unburnt side of the flame. At the burnt side of the flame, which is characterized by progress variable values near unity, the combustion process is only exposed to a narrow range of equivalence ratios between approximately 0.6 and 0.75. In contrast to that, combustion towards the lean flammability limit is found within the whole range of progress variable values for SwB5 and SwB9. Progress variable values close to unity are not found for equivalence ratio values larger than approximately 0.75 for the two latter cases. This implies that the respective flames are located further downstream than 40 mm above the burner, as this is the position from where the whole flame is located in a stratified environment, as discussed in section 4.5.1.

Within the axial position PDFs it can be determined that these two types of flames for SwB5 and SwB9 are also separated spatially, combustion at the inner stream equivalence ratio can be found up to approximately 40 mm. Above this height the flame is burning between the flammability limit and an equivalence ratio of 0.8. The transition between these two regimes takes place relatively rapidly in the region between 25 and 40 mm. This basically correspond to the findings from the analysis of Fig. 4.4, where three different combustion regimes where found. However, the closer analysis with the joint PDFs has shown that the overall flame behavior is dominated by the contribution of the perfectly premixed combustion (inner stream) and the combustion towards the lean flammability limit (mixing layer between air and outer stream). The contribution of the stratified regime away from the flammability limit between 30 mm and 50 mm is small. For SwB1 the combustion towards the flammability limit starts from around 40 mm onwards, in contrast to the two other cases flames with the inner stream equivalence ratio are dominating throughout the whole domain.

The equivalence ratio value at a point alone is not sufficient to fully characterize the stratified combustion process, as it yields no information on the interaction of the local equivalence ratio gradient with the flame structure. A suitable quantity to investigate this interaction is the alignment angle between the gradients of equivalence ratio and progress variable [21, 40, 102]. It is evaluated for every point in the computational domain according to:

$$\alpha = \arccos\left(\frac{\nabla C \cdot \nabla \phi}{|\nabla C||\nabla \phi|}\right)\frac{180^\circ}{\pi}\,. \tag{4.21}$$

The resulting joint PDFs of α versus flame sensor, progress variable and axial position are displayed in Fig. 4.21. For $\alpha < 90^\circ$, the flame propagates towards lower values of equivalence ratio, this is denoted as back-supported stratification for lean conditions and yields a higher flame propagation speed [40]. Front-supported stratification, on the other hand, occurs for lean conditions when $\alpha > 90^\circ$, in this case the propagation of the flame is directed towards higher values of equivalence ratio and the flame propagation speed is thought to be lower [40]. Again, only points with a flame sensor value greater 0.01 have been taken into account, which means

This chapter was previously published [158] and is reprinted with permission of the journal.

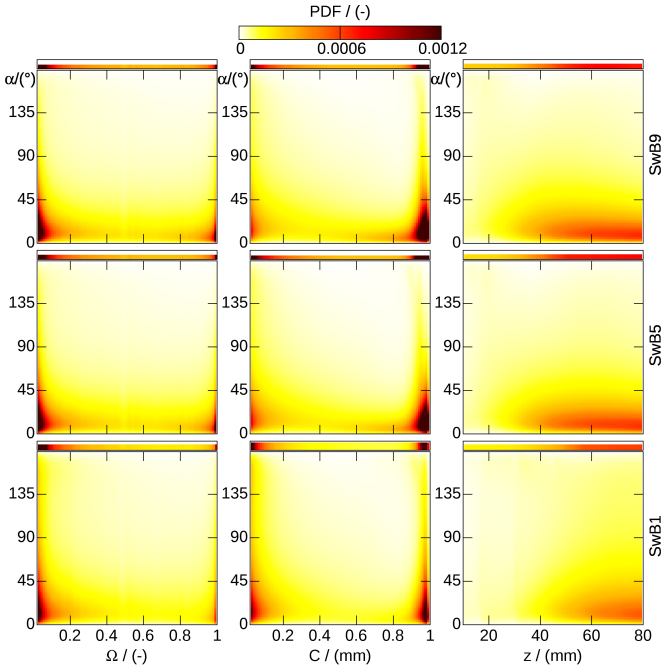

Figure 4.21.: Joint PDFs of alignment angle between progress variable and equivalence ratio vs. Favre-filtered flame sensor (left), Favre-filtered normalized progress variable (middle) and distance from the burner exit (right) [158].

that a certain progress variable gradient is always ensured. However, the denominator in Eq. 4.21 can still become singular in regions with vanishing equivalence ratio gradients, which corresponds to perfectly premixed combustion at this point. To consider this consistently, all points with $|\nabla\phi| < 0.1$ have been collected in a separate bin. This bin is plotted above the actual plots in Fig. 4.21, its width is scaled to obtain a PDF peak value corresponding to the rest of the plot so that the area below the PDFs can be compared.

For all cases, most of the combustion occurs in the perfectly premixed regime. Even further downstream, where the whole flame region is exposed to equivalence ratio gradients as discussed before, a significant amount of perfectly premixed combustion can be observed. This can be explained by the different magnitude of the length scales on which the combustion and the mixing process take place, so that even in a stratified region the equivalence ratio gradient inside the flame is still small in comparison to the progress variable gradient.

For SwB1, back-supported stratification can be found in the region downstream of 40 mm, mainly for low values of the flame sensor and progress variable values of either near unity or near zero. A minimal amount of front-supported stratification can also be observed, this can be explained by turbulent wrinkling, causing the flame to propagate with the equivalence ratio gradient locally.

For SwB5 and SwB9 the basic observations are comparable. The region where back-supported and small amounts of front-supported flames are found starts earlier at approximately 30 mm, as it could be expected. The amount of stratified combustion is bigger than for SwB1, especially for flame sensor values near unity. Most of the stratified combustion is found near progress

This chapter was previously published [158] and is reprinted with permission of the journal.

variable values of unity at the burnt side of the flame for these cases.

4.6. Conclusions

LES computations for three different grid resolutions and stratification levels have been presented for the Cambridge stratified flame series. The ATF approach was used in combination with the FGM technique in a formulation for stratified combustion. The necessary adaptions to make the model suitable for varying mixture fractions were investigated carefully. The commonly used flame sensor formulation was replaced by a version that makes the thickening behavior independent of the mixture fraction.

Radial profiles from the simulation have been compared to measurements for mean value and fluctuations of axial and radial velocity, equivalence ratio, temperature and major species concentrations. An overall good agreement was found with some deviations occurring within the bluff body region. By analyzing atomic mass fractions and species profiles, these deviations could be assigned most likely to effects of preferential diffusion for the case SwB1 and heat transfer in the cases SwB5 and SwB9. To test the influence of the assumed sub-filter FDF, the coarse grid simulations have been carried out with and without using a top-hat distribution for the FDF in mixture fraction and progress variable, respectively. It was found that influence on the results was only small, therefore the simulations on the medium and fine grid have been performed assuming a Dirac-distribution for both mixture fraction and progress variable. Good convergence of the results with grid refinement was observed.

The overall combustion process was analyzed using contour plots, conditional PDFs and joint PDFs. It was found that combustion occurs over the whole range of equivalence ratios from the value in the respective inner stream down to the lean flammability limit. The combustion probability shows a peak at the inner stream equivalence ratio for all cases. Three different flame regions could be distinguished, first a perfectly premixed region, followed by a region in which the flame starts to burn in a stratified regime and finally a region where the unburnt side of the flames touches the lean flammability limit. The overall combustion process was found to be dominated by the contributions of the first and last region. Also in the stratified regions a large amount of the combustion takes place under quasi-premixed conditions due to a negligible equivalence ratio gradient. A significant amount of back-supported and some front-supported stratification was also found for all three cases, most dominant for SwB5 and SwB9.

4.7. Acknowledgements

The authors gratefully acknowledge funding from the state of Nordrhein-Westfalen, Germany. Computations have been carried out using the DFG supported HPC resources of the Center for Computational Sciences and Simulation (CCSS) of the University of Duisburg-Essen, Germany.

This chapter was previously published [158] and is reprinted with permission of the journal.

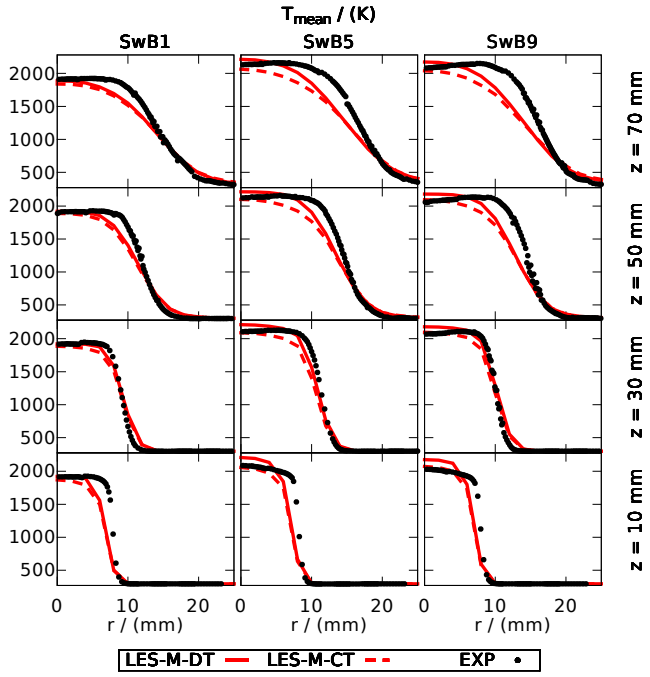

Figure 4.22.: Comparison of the radial mean profiles of temperature obtained with the classical ATF model with constant thickening factor F (LES-M-CT) and the applied version of the model with F determined from Eq. 4.7 (LES-M-DT) on the medium grid [158].

We also would like to thank Robert S. Barlow, Saravanan Balusamy, Matthew J. Dunn, Simone Hochgreb, Mark S. Sweeney and Ruigang Zhou for providing the experimental data and the TNF-community for many helpful discussions.

4.8. Effect of the flame sensor

Figures 4.22 and 4.23 show comparisons of the mean and rms temperature profiles obtained on the medium grid for a simulation with a constant thickening factor (LES-M-CT) and one with the thickening factor determined with the use the flame sensor from Eq. 4.7 (LES-M-DT). The overall position of the flame is not influenced by the type of thickening procedures applied. However, the structure of the burnout zone is affected. The shape of the temperature profiles in the burnout zone is in notable better agreement with the measurements for LES-M-DT. For the constant thickening factor simulation LES-M-CT, the effect of the excessive thickening of the burnout zone becomes visible, most obviously for the stratified cases SwB5 and SwB9. The excessive thickening also causes a certain under-prediction of the fluctuation level for LES-M-CT. Figure 4.24 compares instantaneous snapshots of the resulting temperature field for both methods. The method with the flame sensor (LES-M-DT) reduces the flame thickness and thereby avoids excessive damping of smaller flame structures in comparison to the classical ATF model (LES-M-CT).

This chapter was previously published [158] and is reprinted with permission of the journal.

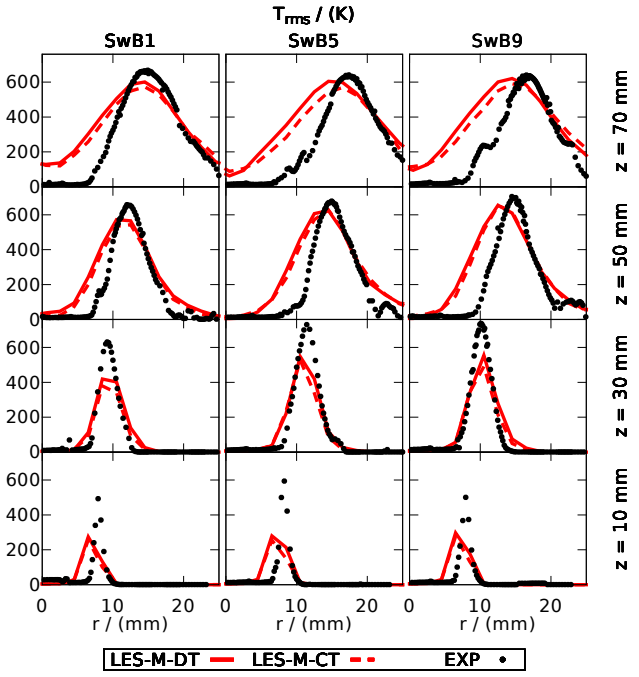

Figure 4.23.: Comparison of the radial fluctuation profiles of temperature obtained with the classical ATF model with constant thickening factor F (LES-M-CT) and the applied version of the model with F determined from Eq. 4.7 (LES-M-DT) on the medium grid [158].

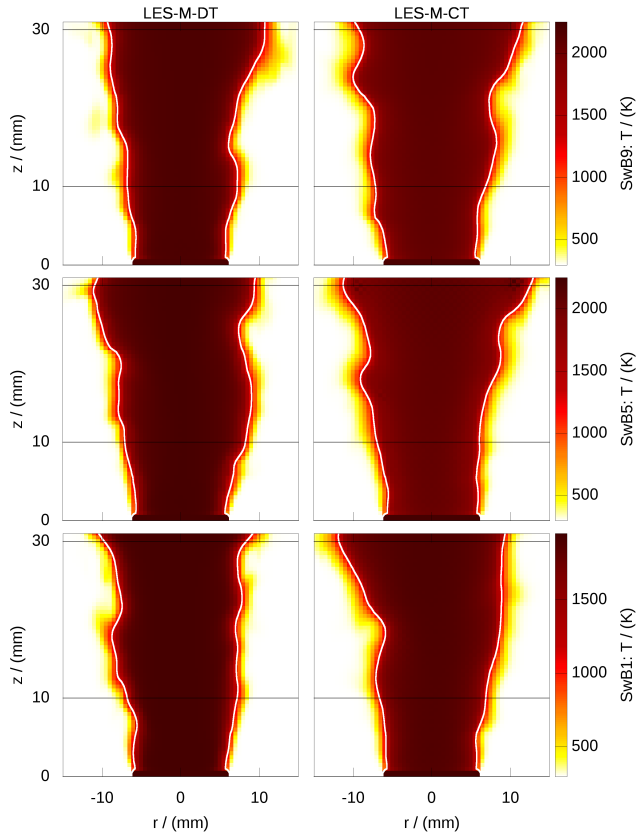

Figure 4.24.: Comparison of instantaneous contour plots of temperature obtained with the classical ATF model with constant thickening factor F (LES-M-CT) and the applied version of the model with F determined from Eq. 4.7 (LES-M-DT) on the medium grid. The white isolines mark a progress variable value of $C = 0.5$ [158].

This chapter was previously published [158] and is reprinted with permission of the journal.

4.9. Velocity fluctuations and fitted efficiency function

The velocity fluctuations in Eq. 4.9 are evaluated from the correlation given by Colin et al. [37] and modified by Wang et al. [211] to work for other values than 10 for the numbers of grid points n to resolve the flame thickness:

$$\begin{aligned} u_{\Delta}^{'} &= 2\Delta_{mesh}^{3} \left| \nabla^2 \left(\nabla \times \vec{\tilde{u}} \right) \right| \left(\frac{n}{10} \right)^{\frac{1}{3}} \\ &= 2\Delta_{mesh}^{3} \left| \nabla \times \left(\nabla^2 \vec{\tilde{u}} \right) \right| \left(\frac{n}{10} \right)^{\frac{1}{3}} \end{aligned} \tag{4.22}$$

The Laplace operator is evaluated on a $(4\Delta_{mesh})$ stencil, to not consider the highest frequencies (noise) [37]. The turbulent Reynolds number on the sub-filter scale is evaluated from [31]:

$$Re_{\Delta} = 4F_{max} \frac{u_{\Delta}^{'}}{s_l^0} \tag{4.23}$$

and the fitted efficiency function from [31]:

$$\Gamma_{\Delta} \left(F_{max}, \frac{u_{\Delta}^{'}}{s_l^0}, Re_{\Delta} \right) = \left[\left\{ \left(f_u^{-a} + f_{\Delta}^{-a} \right)^{-\frac{1}{a}} \right\}^{-b} + f_{Re}^{-b} \right]^{-\frac{1}{b}} \tag{4.24}$$

with

$$f_u = 4 \left(\frac{27 C_k}{110} \right)^{\frac{1}{2}} \left(\frac{18 C_k}{55} \right) \left(\frac{u_{\Delta}^{'}}{s_l^0} \right)^2 \tag{4.25}$$

$$f_{\Delta} = \left[\frac{27 C_k \pi^{\frac{4}{3}}}{110} \left\{ \left(F_{max} \right)^{\frac{4}{3}} - 1 \right\} \right]^{\frac{1}{2}} \tag{4.26}$$

$$f_{Re} = \left[\frac{9}{55} \exp \left(-\frac{3}{2} C_k \pi^{\frac{4}{3}} Re_{\Delta}^{-1} \right) \right]^{\frac{1}{2}} Re_{\Delta}^{\frac{1}{2}} \tag{4.27}$$

$$a = 0.6 + 0.2 \exp \left(-0.1 \frac{u_{\Delta}^{'}}{s_l^0} \right) - 0.2 \exp \left(-0.01 \, F_{max} \right) \tag{4.28}$$

$$b = 1.4 \tag{4.29}$$

where $C_k = 1.5$ is the Kolmogorov constant. It was found that the evaluation of this efficiency function became computationally expensive in comparison to the rest of the CFD solver, consuming up to 25% of the runtime. A significant speedup was achieved by tabulating Eq. 4.9 at the beginning of the computation, and then obtaining the value of E from an additional table lookup depending on the local value of the maximum thickening factor and the velocity ratio.

This chapter was previously published [158] and is reprinted with permission of the journal.

4.10. Variance modeling

For a one-dimensional case, the gradient model for the mixture fraction by Branley and Jones [15] reads:

$$\widetilde{Z''^2} = C_2 \Delta^2 \left(\frac{Z_N - Z_S}{2\Delta} \right)^2 , \tag{4.30}$$

where Z_N and Z_S represent the values at the neighboring cell centers. Floyd et al. [57] have shown that in cases of a linear mixture fraction profile, the resulting value of the modeling constant is:

$$C_2 = \frac{1}{12} , \tag{4.31}$$

which results in in a upper and lower limit of:

$$\tilde{Z}_{u/l} = \tilde{Z} \pm 0.5 \sqrt{12 \widetilde{Z''^2}} = \tilde{Z} \pm 0.25 (Z_N - Z_S) \tag{4.32}$$

For the approach used within this work, the values at the cell faces are obtained from the mean value of the neighboring cells

$$Z_s = 0.5 (Z_S + Z_C) \text{ and } Z_n = 0.5 (Z_N + Z_C) \tag{4.33}$$

where Z_c denotes the value at the cell center. The gradient over the cell is then obtained from

$$\frac{dZ}{dx} = \frac{Z_n - Z_s}{\Delta} = \frac{Z_N - Z_S}{2\Delta} \tag{4.34}$$

This results in an upper and lower limit of :

$$\tilde{Z}_{u/l} = \tilde{Z} \pm 0.5 \Delta \frac{dZ}{dx} = \tilde{Z} \pm 0.25 (Z_N - Z_S) \tag{4.35}$$

which is in agreement with the result for the gradient assumption in Eq. 4.32.

4.11. Influence of domain size

To study the influence of the domain size, additional computations were carried out for the coarse grid on a domain that had doubled size in all directions. The influence on the mean values of all quantities was found to be negligible, Fig. 4.25 shows the respective comparison for axial velocity as an example. Some deviations occurred for the fluctuations of axial velocity further downstream, as displayed in Fig. 4.26. For all other quantities the deviations in the fluctuations were negligible, some example profiles 70 mm above the burner are shown in Fig. 4.27. Therefore, it was decided to choose the smaller domain, as the simulation results benefit significantly from the finer resolution that is computational affordable on the smaller domain.

This chapter was previously published [158] and is reprinted with permission of the journal.

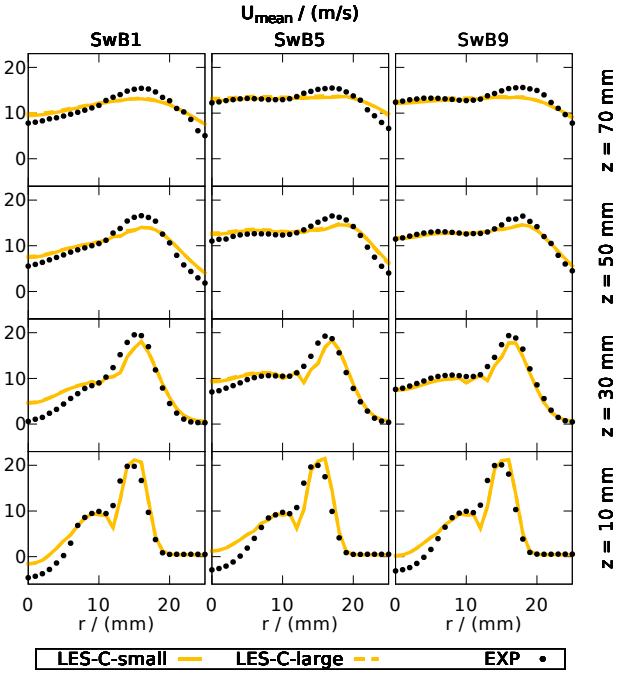

Figure 4.25.: Investigation of the influence of the domain size on the radial mean profiles of axial velocity [158].

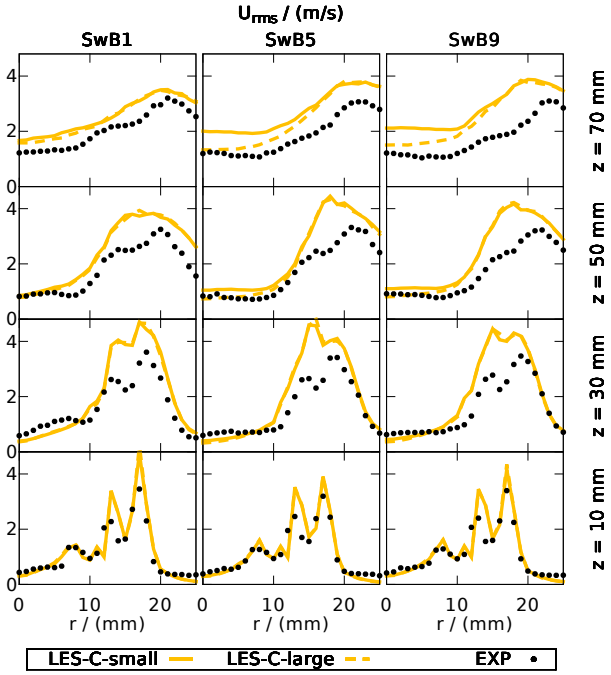

Figure 4.26.: Investigation of the influence of the domain size on the radial fluctuation profiles of axial velocity [158].

This chapter was previously published [158] and is reprinted with permission of the journal.

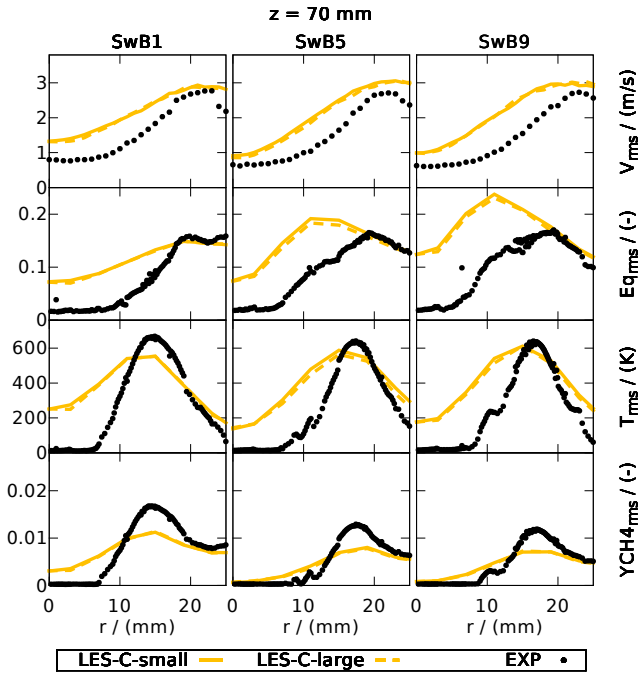

Figure 4.27.: Investigation of the influence of the domain size on the radial fluctuation profiles of selected quantities 70 mm above the burner [158].

4.12. Comparison of thickening and filtering

The ATF model with flame sensor used in this work is compared to the filtering procedure that forms the basis of approaches like the F-TACLES [5] or the (FLF) - PDF model [126] in this section. For that purpose, a one-dimensional flame computation for stoichiometric conditions has been carried out with Cantera. The resulting profiles for the mass fractions of progress variable (product species), methane (educt species) and carbon monoxide (intermediate species) as well as for the temperature have been stored over the flame normal coordinate (Original). Afterwards, these profiles have been filtered with a top-hat filter (FilteredTH, $\Delta = 2.2$ mm) and a Gaussian filter (FilteredGaussian, $\Delta = 6.0$ mm), respectively. Afterwards 'PsiPhi' was used to simulated a laminar one-dimensional flame on a 0.5 mm grid with the classical ATF-model (ATF, constant thickening factor of 5), the ATF-model with flame sensor (ATFomega) and the ATF-model with flame sensor and top-hat FDF in C (ATFomegaTH). The respective comparison is shown in Fig. 4.28, except for the intermediate species similar results are achieved for the different approaches. The influence of the thickening procedure on the pre-heat and burnout zone for the ATF-model without flame sensor becomes obvious. It is notable that the top-hat FDF improves the agreement with the filtered results significantly in the burnout zone, and has negligible influence at the unburnt side of the flame. For the intermediate species carbon monoxide, the filtering procedure preserves the area below the profile and under-predicts its peak value, whereas the thickening procedure preserves the peak value and over-predicts the area below the profile.

This chapter was previously published [158] and is reprinted with permission of the journal.

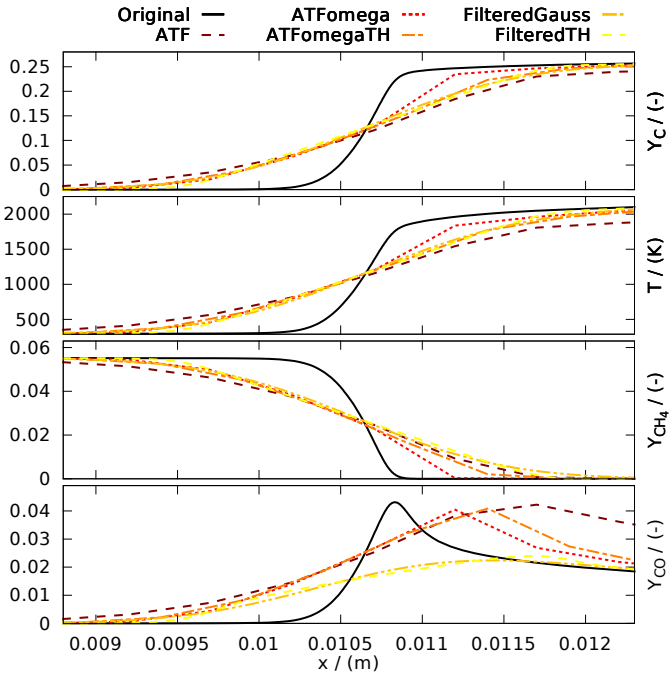

Figure 4.28.: Comparison of the influence of thickening and filtering on the structure of a one-dimensional flame [158].

4.13. Mean and rms profiles of major species mass fractions

The radial profiles of mass fraction means and fluctuations for major species are shown in Figures 4.29-4.38.

This chapter was previously published [158] and is reprinted with permission of the journal.

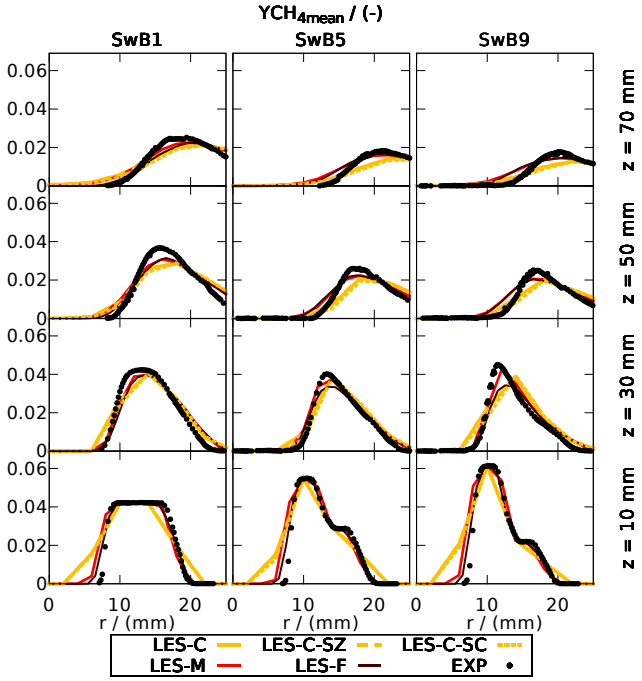

Figure 4.29.: Radial profiles of the mean methane mass fraction at different downstream locations, showing a comparison for three different grids with the experiments. LES-C-SZ and LES-C-SC refer to a coarse grid simulation with additional sub-filter modeling using a top-hat FDF in mixture fraction and progress variable, respectively [158].

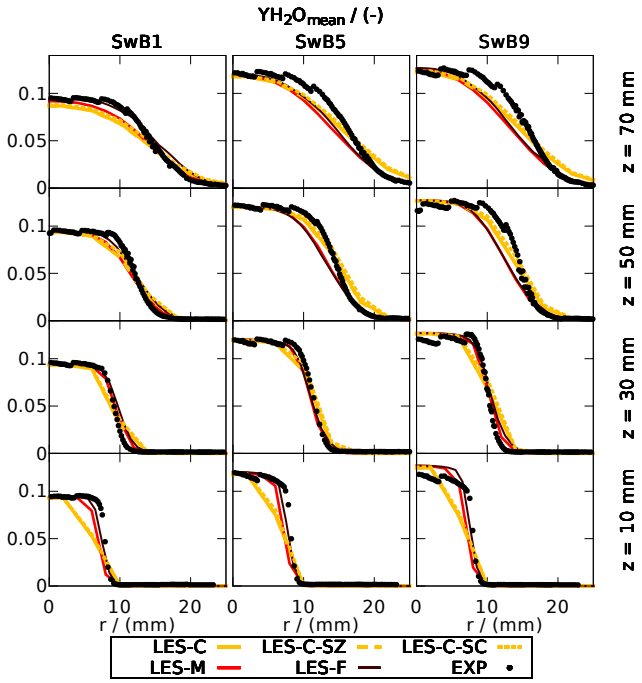

Figure 4.30.: Radial profiles of the mean water mass fraction at different downstream locations, showing a comparison for three different grids with the experiments. LES-C-SZ and LES-C-SC refer to a coarse grid simulation with additional sub-filter modeling using a top-hat FDF in mixture fraction and progress variable, respectively [158].

This chapter was previously published [158] and is reprinted with permission of the journal.

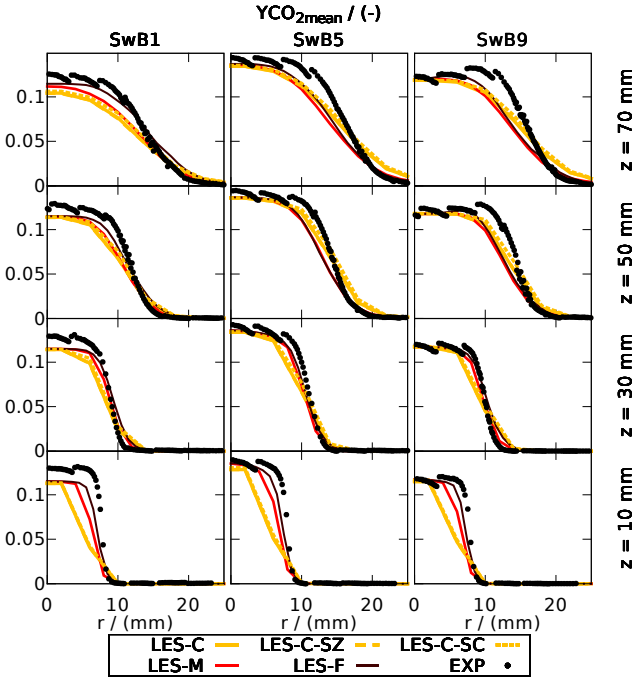

Figure 4.31.: Radial profiles of the mean carbon dioxide mass fraction at different downstream locations, showing a comparison for three different grids with the experiments. LES-C-SZ and LES-C-SC refer to a coarse grid simulation with additional sub-filter modeling using a top-hat FDF in mixture fraction and progress variable, respectively [158].

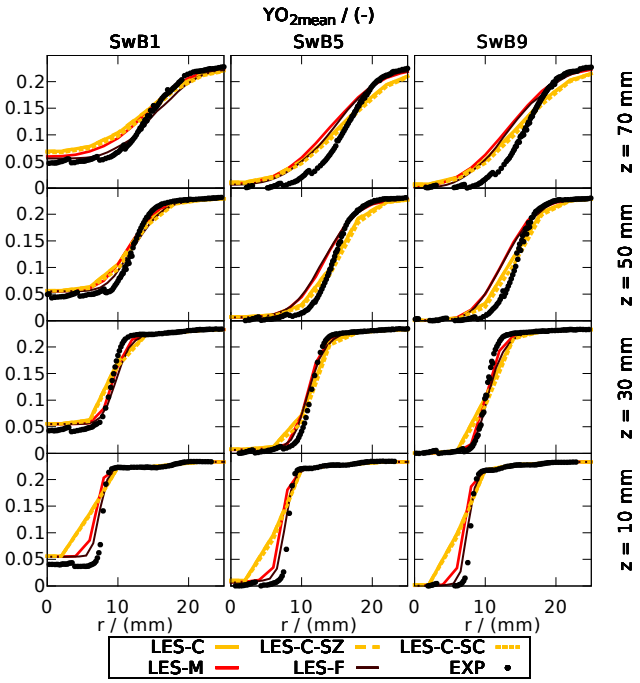

Figure 4.32.: Radial profiles of the mean oxygen mass fraction at different downstream locations, showing a comparison for three different grids with the experiments. LES-C-SZ and LES-C-SC refer to a coarse grid simulation with additional sub-filter modeling using a top-hat FDF in mixture fraction and progress variable, respectively [158].

This chapter was previously published [158] and is reprinted with permission of the journal.

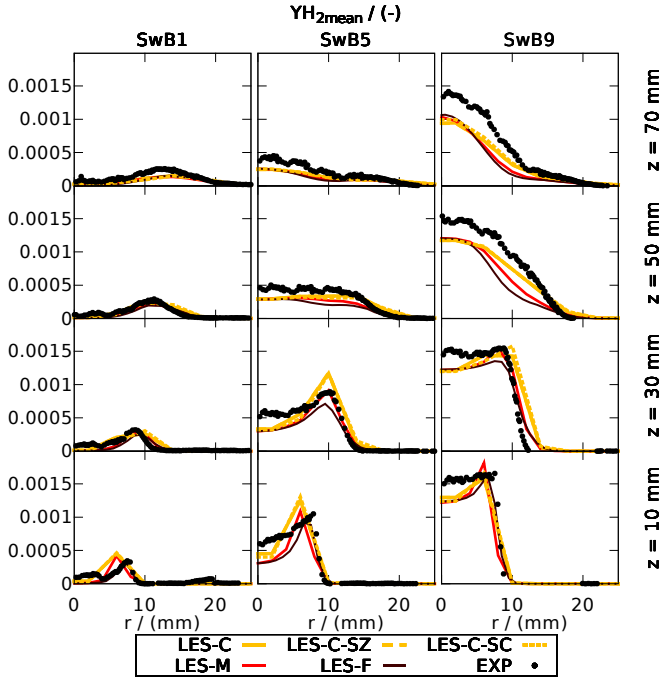

Figure 4.33.: Radial profiles of the mean hydrogen mass fraction at different downstream locations, showing a comparison for three different grids with the experiments. LES-C-SZ and LES-C-SC refer to a coarse grid simulation with additional sub-filter modeling using a top-hat FDF in mixture fraction and progress variable, respectively [158].

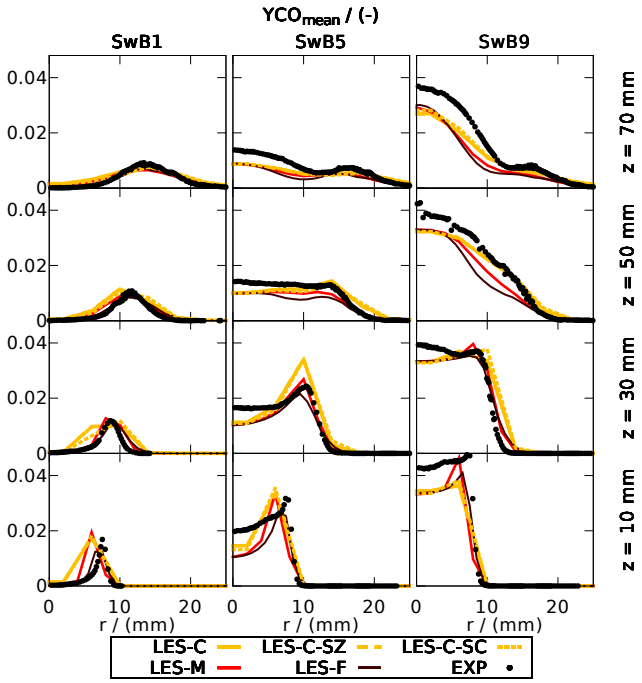

Figure 4.34.: Radial profiles of the mean carbon monoxide mass fraction at different downstream locations, showing a comparison for three different grids with the experiments. LES-C-SZ and LES-C-SC refer to a coarse grid simulation with additional sub-filter modeling using a top-hat FDF in mixture fraction and progress variable, respectively [158].

This chapter was previously published [158] and is reprinted with permission of the journal.

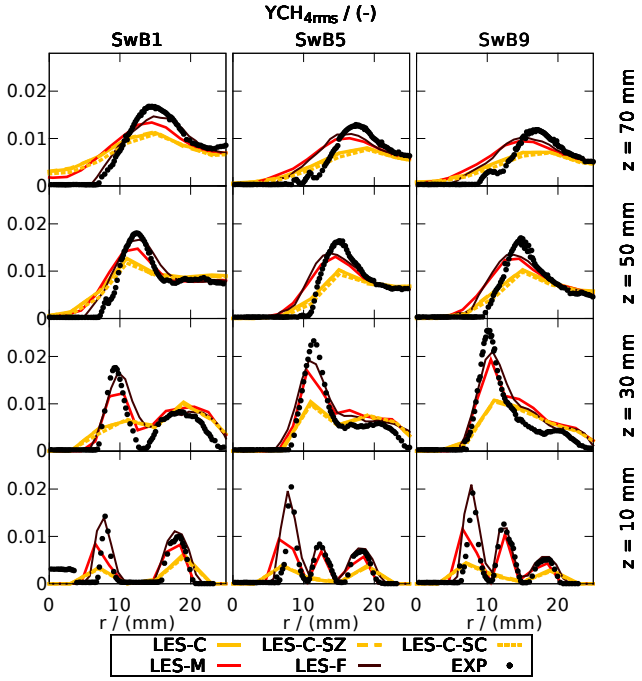

Figure 4.35.: Radial profiles of the methane mass fraction fluctuations at different downstream locations, showing a comparison for three different grids with the experiments. LES-C-SZ and LES-C-SC refer to a coarse grid simulation with additional sub-filter modeling using a top-hat FDF in mixture fraction and progress variable, respectively [158].

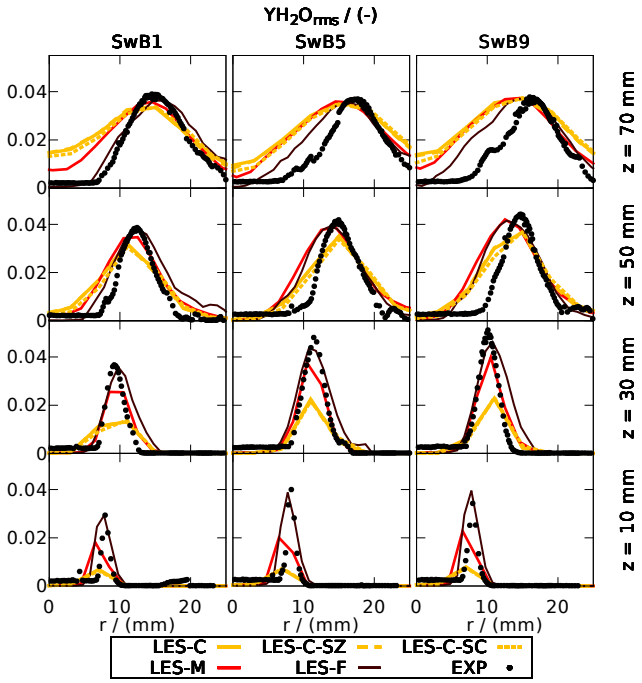

Figure 4.36.: Radial profiles of the water mass fraction fluctuations at different downstream locations, showing a comparison for three different grids with the experiments. LES-C-SZ and LES-C-SC refer to a coarse grid simulation with additional sub-filter modeling using a top-hat FDF in mixture fraction and progress variable, respectively [158].

This chapter was previously published [158] and is reprinted with permission of the journal.

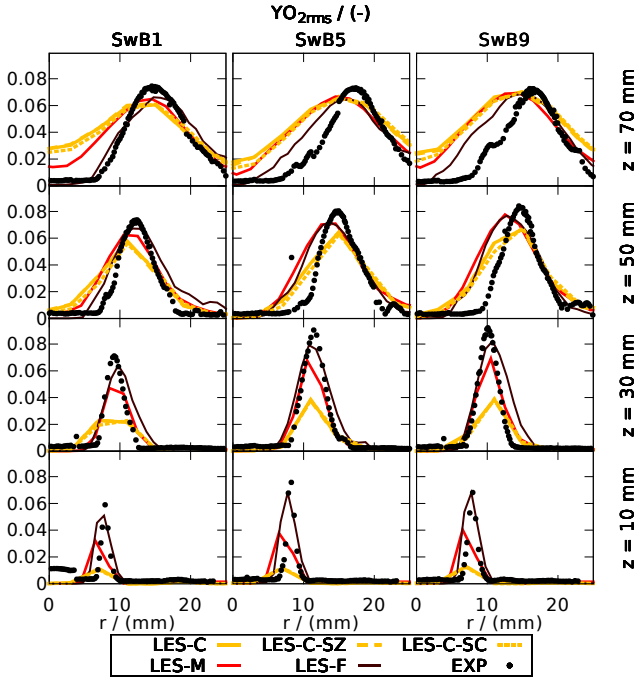

Figure 4.37.: Radial profiles of the oxygen mass fraction fluctuations at different downstream locations, showing a comparison for three different grids with the experiments. LES-C-SZ and LES-C-SC refer to a coarse grid simulation with additional sub-filter modeling using a top-hat FDF in mixture fraction and progress variable, respectively [158].

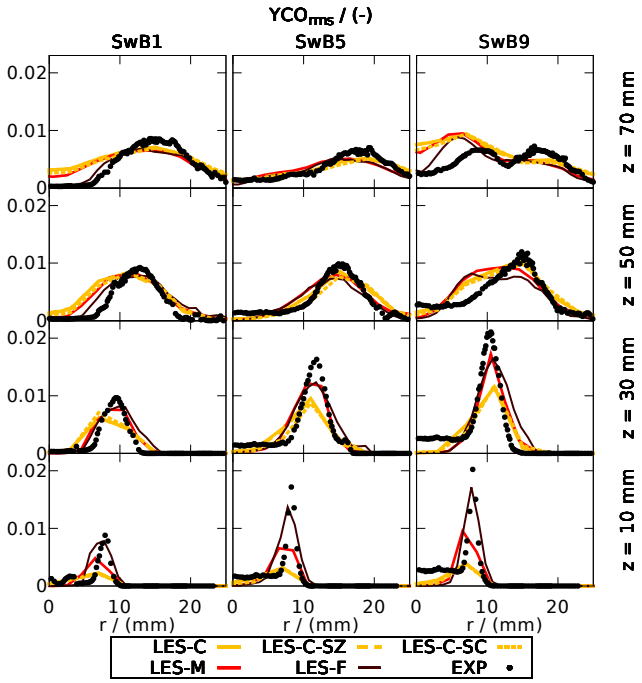

Figure 4.38.: Radial profiles of the carbon monoxide mass fraction fluctuations at different downstream locations, showing a comparison for three different grids with the experiments. LES-C-SZ and LES-C-SC refer to a coarse grid simulation with additional sub-filter modeling using a top-hat FDF in mixture fraction and progress variable, respectively [158].

This chapter was previously published [158] and is reprinted with permission of the journal.

5. Modeling heat loss effects in the large eddy simulation of a model gas turbine combustor with premixed flamelet generated manifolds [159]

Authors: F. Proch, A.M. Kempf

This chapter including all figures and tables was previously published in 'Proceedings of the Combustion Institute, 35(3), F. Proch and A. M. Kempf, Modeling heat loss effects in the large eddy simulation of a model gas turbine combustor with premixed flamelet generated manifolds, 3337 – 3345, Copyright © Elsevier (2015)' and is reprinted with permission from Elsevier. The author F. Proch developed the code and the combustion model, ran all the simulations, wrote the paper and generated all figures and tables. The author A.M. Kempf contributed corrections, discussions and proof-reading.

5.1. Abstract

Large eddy simulation results are presented for a model gas turbine combustion chamber, which is operated with a premixed and preheated methane / air mixture. The off-center position of the high axial momentum confined jet burner causes a strong outer recirculation, which stabilizes the flame. Turbulent combustion is modeled by the flamelet generated manifolds (FGM) technique, which is combined with the artificial thickened flame (ATF) approach. The influence of different heat loss modeling strategies on flame propagation and structure is investigated. Besides the established method of using burner-stabilized flames as basis for the non-adiabatic tabulation, an alternative approach based on freely propagating flames with heat loss inclusion by scaling of the energy equation source term is presented. Different grid resolutions are applied to study the impact of cell size and filter width on the results, the effect of subfilter modeling is also examined. The simulation setup and the modeling approach are validated by comparison of computed statistics against measurements. A good overall agreement between simulation and experiment is observed. However, the length of the flame was slightly under-predicted;

it is shown that a simple method for consideration of strain effects on the flame has the potential to improve the predictions here. The effect of heat loss on the combustion process is then characterized further based on probability density functions obtained from the simulation results.

5.2. Introduction

Concepts for modern gas turbine combustors often feature regions with (partially) premixed combustion, which are exposed to significant heat loss. Large eddy simulation (LES) has proven in the past to be a very capable approach for the numerical simulation of such devices.

Different methods have been established for the modeling of premixed combustion within LES, for example based on tracking of the flame front by the G-equation model [47, 139, 147] or modeling of the flame surface density (FSD) [2, 111]. Another group of models is based on widening of the flame in normal direction by means of either filtering [13, 55, 60] or artificial thickening (ATF) [31, 37]; the latter approach is applied here. The combustion progress and flame propagation are described through the premixed flamelet generated manifolds (PFGM) technique [101, 202, 204]. These approaches are all derived for adiabatic conditions in their basic formulation, and need to be extended by heat loss effects for the proper computation of confined geometries. Heat loss due to radiation has been considered for example by Marracino and Lentini [114], by Ihme and Pitsch [75], by Franchetti et al. [58] and by Schmitt et al. [179]. Fiorina et al. [53] suggested the computation of burner stabilized one-dimensional flames and to use the tabulated results for correcting the source term and the flame speed. This approach has been applied within the RANS [43] and the LES [22, 91] context.

The present work aims to model and investigate the influence of the heat loss on the LES results in the lean premixed combustion regime. Three different models are compared to the adiabatic reference solution: First a very simple model where the heat loss only affects the temperature and the transport coefficients, secondly the model by Fiorina et al. [53], and thirdly an approach with non-constant heat loss inside the flame.

To properly judge the model behavior, a test case with a significant amount of heat loss was required, which was found in a confined laboratory scale burner investigated at DLR Stuttgart by Lammel and coworkers [103]. Its jet-nozzle exit is arranged in an off-center position, resulting in a strong recirculation of the hot combustion products, which stabilizes the flame and causes strong heat loss to the burner walls. We consider a configuration with values of 90 m/s, 0.71 and 573 K for the bulk inflow velocity, the equivalence ratio of the premixed methane /air mixture and the temperature at the inlet, respectively. This burner has also been investigated with RANS by Donini et al. [43], and with hybrid RANS/LES by Di Domenico et al. [41].

This chapter was previously published [159] and is reprinted with permission of the journal.

5.3. Modeling approach

With the PFGM approach [202, 204], one dimensional freely propagating flames are computed with a detailed chemical mechanism. The results are mapped over a small subset of control variables and subsequently stored in a low dimensional lookup-table, which is accessed by the CFD solver. In the present work, the one dimensional flame computations are carried out with the software library Cantera [64] for the GRI-3.0 [188] mechanism. A unity Lewis number assumption for all species is used, which required the implementation of an additional transport model into Cantera. The reaction progress is described by the species mass fraction sum $Y_C = Y_{\mathrm{CO_2}} + Y_{\mathrm{CO}} + Y_{\mathrm{H_2O}} + Y_{\mathrm{H_2}}$. We found that this progress variable definition works well for methane/air over the whole flammability range, although both simpler and more complex formulations exist.

5.3.1. Inclusion of heat loss in FGM

To include the heat loss into the PFGM, the sum of sensible and chemical enthalpy $h = h_s + \sum_{k=1}^{N} \Delta h_{f,k}^0 Y_k$ is used as second progress variable. As mentioned above, different methods are used to generate the non-adiabatic PFGM table:

For the first method (**M1**) only the adiabatic free flame without heat loss is computed. Afterwards the gas temperature is successively reduced from the adiabatic to the ambient temperature. The gas composition, the laminar flame speed, the laminar flame thickness and the reaction rate are kept constant. The heat loss influences the solution by reducing the temperature which alters the density and the transport coefficients.

The second method (**M2**) relies on the computation of burner stabilized flames [53]. At the inlet of the domain, constant values are prescribed for the mass flow and the temperature. By setting a lower mass flow a, higher level of heat loss over the entire flame is induced. Although the underlying assumption of temperature independence of the heat loss is unlikely to hold entirely in a real flame, this approach has been used with good success for the prediction of the flame behavior as well as the inner flame structure by Fiorina et al. [53], Cecere et al. [22], Ketelheun et al. [91] and Donini et al. [43]. Outside the flammability region, the temperature is reduced corresponding to M1, this time not starting from the adiabatic flame but from the burner-stabilized flamelet with the maximum heat loss. As it was found that the results of the CFD simulations performed within this work were insensitive to the exact value of the flammability limit, it was assumed that it is reached when the flame speed falls below 0.05 m/s.

The third method (**M3**) is based on introducing heat loss into a freely propagating flame. This is achieved by scaling the source term due to chemical reaction by a constant factor $(1 - f_L)$

This chapter was previously published [159] and is reprinted with permission of the journal.

over the whole flame. The modified energy equation that was implemented in Cantera reads:

$$\begin{aligned} \dot{m}\, c_p \frac{\partial T}{\partial z} = \frac{\partial}{\partial z}\left(\lambda \frac{\partial T}{\partial z}\right) - \sum_{k_1}^{K} c_{pk} j_{k,z} \frac{\partial T}{\partial z} \\ - \boxed{(1 - f_L)} \sum_{k_1}^{K} h_k \dot{\omega}_k W_k \end{aligned} \tag{5.1}$$

In Eq. (5.1), $\dot{m}$, c_p, λ, $\dot{\omega}_k$, W_k and $j_{k,z}$ denote the mass flow, heat capacity, thermal conductivity, reaction rate, molecular weight and the diffusive mass flux of species k in z-direction, respectively. The second term on the RHS of equation 5.1 represents the energy changes due to differential diffusion, thus it cancels out for the applied unity Lewis number approach. Starting with the adiabatic flame ($f_L = 0$), different flames with successively raised values of f_L are computed to cover the whole range of enthalpy defects until the flame speed value of 0.05 m/s used as the flammability limit is reached at a value of $f_L = 0.5$. For higher enthalpy defects, the temperature is reduced as for the first two methods, starting from the flamelet at the flammability limit ($f_L = 0.5$). This model results in a nearly linear relationship between the heat loss and the temperature over the flame. This promises to be a more suitable approximation of the real physical behavior, since the strength of sources of heat loss as conduction along the flame front and radiation is depending on the temperature. Furthermore, the assumption of a heat sink at the unburned side of the flame is avoided, which is somewhat questionable in an aerodynamically stabilized flame. Consequently, the flame trajectories no longer describe vertical lines in the h-Y_C diagram, which results in a modified modeling strategy than for M1 and M2. The term $f_L \sum_{k_1}^{K} h_k \dot{\omega}_k W_k$ needs to be included as sink term in the energy equation, it is stored as an additional quantity inside the PFGM table. To improve the resolution and simplify the lookup within the CFD code, the two control variables h and Y_C are normalized:

$$h_N = \frac{h - h^{min}(Y_C)}{h^{max}(Y_C) - h^{min}(Y_C)} \tag{5.2}$$

$$C = \frac{Y_C - Y_C^{min}(h)}{Y_C^{max}(h) - Y_C^{min}(h)} \tag{5.3}$$

The resulting manifold is then mapped onto an equidistant h_N-C grid by bilinear interpolation, the minimum and maximum values of $h(Y_C)$ and $Y_C(h_N)$ are also mapped in the same way and stored for usage inside the CFD simulation.

A comparison of the laminar flame speed and flame thickness as a function of the heat loss for M2 and M3 is shown in Fig. 5.1, the adiabatic solution (**AD**) is shown as reference. Also included is a comparison of the resulting flame structure for the respective flame with maximum heat loss. The laminar flame speed s_l^0 is reduced more by the heat loss for M2 than for M3, therefore the necessary heat loss to reach the minimum flame speed is about 10% larger for M3. The laminar flame thickness δ_l^0 is growing stronger with heat loss for M3 than for M2, most

This chapter was previously published [159] and is reprinted with permission of the journal.

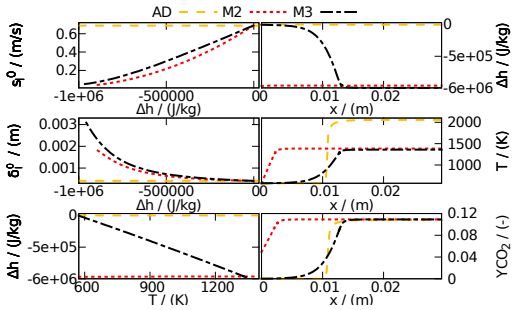

Figure 5.1.: Comparison of global flame properties and resulting flame structure for M2 and M3, the adiabatic solution AD is shown as reference [159].

obvious towards the extinction limit. As already mentioned, the heat loss is increasing almost linearly with the temperature for M3, whereas it stays constant for M2.

The flame structure of the respective flame with maximum heat loss for M2 and M3 is compared to the adiabatic case AD in the plots on the right side of Fig. 5.1. The temperature dependent heat loss for M3 results in a smooth reduction of the enthalpy over the flame. The temperature profile for M3 has longer preheating and oxidation zones and a significantly lower peak temperature compared to AD, nevertheless the general flame position marked by the point of inflection is maintained. For M2, the flame structure differs significantly from AD and M3, the temperature increases to its final value that is comparable to M3 rapidly at the beginning of the domain and stays constant afterwards. The behavior in temperature is basically also mirrored by the mass fraction of CO_2, with the exception that the final value is not affected by the heat loss is and identical for all three cases. On the unburned side of the flame, at ambient temperature, M2 predicts a significant mass fraction of CO_2 in contrast to M3 and AD.

5.3.2. ATF model

The typical thickness of a premixed flame (0.1 - 0.5 mm) is not properly resolved on practically affordable LES grids with cell sizes bigger than 0.5 mm. To tackle this problem, the ATF approach artificially thickens the flame by introducing a thickening factor F into the transport equations for enthalpy and progress variable:

$$\begin{aligned} &\frac{\partial \bar{\rho}\tilde{h}}{\partial t} + \frac{\partial}{\partial x_i}\left(\bar{\rho}\tilde{u}_i\tilde{h}\right) = \\ &\frac{\partial}{\partial x_i}\left(\left[FE\frac{\lambda}{c_p} + (1-\Omega)\frac{\mu_t}{\mathrm{Sc}_t}\right]\frac{\partial \tilde{h}}{\partial x_i}\right) + \frac{E}{F}\dot{\omega}_h \end{aligned} \tag{5.4}$$

$$\begin{aligned} &\frac{\partial \bar{\rho}\tilde{Y}_C}{\partial t} + \frac{\partial}{\partial x_i}\left(\bar{\rho}\tilde{u}_i\tilde{Y}_C\right) = \\ &\frac{\partial}{\partial x_i}\left(\left[FE\bar{\rho}D_C + (1-\Omega)\frac{\mu_t}{\mathrm{Sc}_t}\right]\frac{\partial \tilde{Y}_C}{\partial x_i}\right) + \frac{E}{F}\dot{\omega}_C \end{aligned} \tag{5.5}$$

This chapter was previously published [159] and is reprinted with permission of the journal.

In Eqs. (5.4) and (5.5), ρ, u_i, λ, c_p, D_c, $\dot{\omega}_C$, μ_t and Sc_t represent the fluid density, flow velocity, thermal conductivity, heat capacity, progress variable diffusion coefficient, progress variable reaction rate, turbulent viscosity and turbulent Schmidt number, respectively. The source term for the enthalpy $\dot{\omega}_h$ represents the heat loss for M3 as described above, and becomes zero for M1 respectively M2. To avoid unphysical effects of the thickening procedure in regions without combustion, F is only applied inside the flame region characterized by high gradients of the progress variable [107]. The flame region is detected with the flame sensor Ω, which is computed from the dimensionless progress variable gradient of the one-dimensional Cantera flame computations [158]:

$$\Omega(C,h) = \left[\frac{\frac{dY_C(x)}{dx}}{\max\left(\frac{dY_C(x)}{dx}\right)} \right]_{1-D} \tag{5.6}$$

The actual value of the thickening factor is then computed from:

$$F = 1 + \Omega\,(F_{max} - 1) \tag{5.7}$$

with

$$F_{max} = \max\left(\frac{n\Delta_{mesh}}{\delta_l^0}, 1\right) \tag{5.8}$$

In Eq. (5.8), Δ_{mesh} represents the mesh cell size and n the number of grid points on which the flame thickness is resolved, it is set to a value of 5 following a suggestion by Charlette et al. [31]. The flame thickness is computed based on the maximum gradient of the temperature profile from the one-dimensional computations, T_b and T_u denote the temperature on the burned and unburned side, respectively:

$$\delta_l^0 = \frac{T_b - T_u}{\max\left(\frac{dT}{dx}\right)} \tag{5.9}$$

The effect of the velocity fluctuations on the subfilter level is modeled with the efficiency function E, which is evaluated from the analytical formulation of Charlette et al. [31], which is used with the corrections suggested by Wang et al. [211]. The respective modeling constant was set to the commonly used value of $\beta = 0.5$ [31]. The detailed formulation of the model has been omitted for brevity, it can be found in the available literature [31], [158], [211].

The influence of radiation was neglected, as simulations with a simple radiation model showed that the related effects are one order of magnitude smaller than those of the convective heat transfer.

This chapter was previously published [159] and is reprinted with permission of the journal.

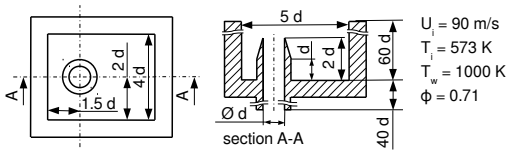

Figure 5.2.: Geometrical burner setup and boundary conditions, the computational domain is shown in Fig. 5.3 [159].

5.4. Experimental and numerical configuration

5.4.1. Experiment

The high-velocity preheated and premixed combustor has a rectangular cross section with a width of 5 and a depth of 4 nozzle diameters, the jet nozzle is mounted in an off-center position. The walls are made from Quartz to provide optical access. The geometrical setup and the boundary conditions are shown in Fig. 5.2. Velocity fields have been obtained from PIV measurements; profiles of species mole fractions and temperature were determined from Raman scattering measurements by Lammel et al. [103].

The wall temperatures have not been measured during the experiment. However, according to O. Lammel the quartz glass surface would melt at approximately $1000\,^{\circ}\mathrm{C}$, crystallization of the glass starts at around $650\,^{\circ}\mathrm{C}$. Based on the aging behavior of the glass, the wall temperature was estimated in-between $650\,^{\circ}\mathrm{C}$ and $800\,^{\circ}\mathrm{C}$ (O. Lammel, personal communication, November 2013), so we have rounded the temperature to 1000 K.

5.4.2. Numerical setup and CFD-solver

Computations are carried out with the in-house LES-solver 'PsiPhi' [21, 58, 142, 158]. Solved are the Favre-filtered governing equations for mass, momentum, progress variable and enthalpy in low-Mach number formulation. Time integration is performed with a low-storage third order Runge-Kutta scheme, the parallelization is carried out using a distributed-memory message passing interface (MPI) domain decomposition. The finite volume method (FVM) is used to discretize the equations on an equidistant Cartesian grid. Convective fluxes are interpolated with a central difference scheme for momentum, for scalar quantities and density a total variation diminishing (TVD) scheme with the non-linear CHARM limiter [219] is applied. The geometry is described by immersed boundaries.

The effect of subfilter transport on momentum and scalar fields is considered with the eddy-viscosity and eddy-diffusivity approach, respectively. The turbulent Schmidt number is adjusted to 0.7, the turbulent viscosity is computed with the σ-model by Nicoud et al. [131], the respective modeling constant is set to $C_m = C_\sigma = 1.5$. This model gives the correct decrease of the turbulent viscosity within the near wall region, avoiding the need for a special wall treatment as required with the classical Smagorinsky model. A turbulent velocity profile with a mean value according to Fig. 5.2 is set at the inflow. Pseudo-turbulent fluctuations with a length scale

This chapter was previously published [159] and is reprinted with permission of the journal.

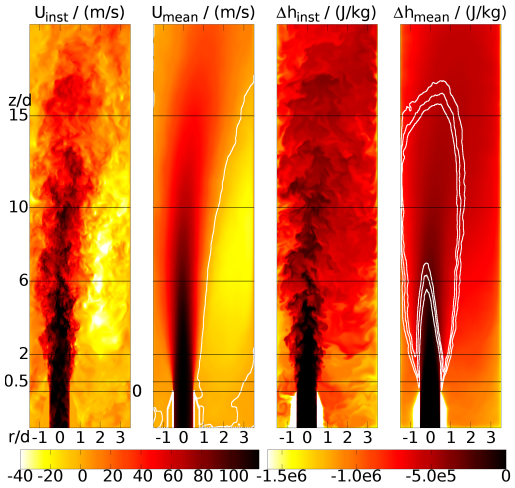

Figure 5.3.: Instantaneous and mean contour plots of axial velocity (left) and enthalpy loss (right) in a burner cross section obtained on the fine grid (M3F). In the mean plots, white isolines denote zero velocity (left) respectively the flame sensor which marks the combustion region (right) [159].

of $0.1d$ and an intensity of 9 m/s are superimposed, they are generated using a version of the filtering method of Klein et al. [88, 94]. The influence of the magnitude and the length scale of the fluctuations on the results was studied and found to be very small. Zero gradient boundary conditions are adjusted at the outlet for all quantities, where clipping avoids entrainment during start-up. The temperatures of the walls are fixed at 1000 K. The sensitivity of the results against a variation of this temperature was found to be negligible; flame position and length were not affected. Based on the conditions at the inlet, the combustion process falls into the thin reaction zones regime of the modified Borghi diagram.

The computational domain has a length of $24d$, the cell size is $0.1d$ (nozzle diameter resolved by 10 cells) on the coarse and $0.025d$ (nozzle diameter resolved by 40 cells) on the fine grid. This results in a total domain size of 38 (0.6) million cells and a computational time of 95000 (280) CPU hours on the fine (coarse) grid. The sampling for the flow statistics was started after 10 flow-through times based on the bulk velocity and performed for another 20 flow-through times to consider the slow but important recirculating zone on the ”right” side of the jet. Tests on the coarse grid have shown that this amount of sampling time is required and sufficient for accurate statistics.

5.5. Results and discussion

A first impression of the resulting flow and heat loss fields is given by Fig. 5.3, which shows instantaneous and mean contour plots of the axial velocity and the enthalpy loss for M3 on the fine grid (M3F). The structure of the axial velocity field is dominated by a large recirculation zone developing on the ”right” side of the domain. Smaller recirculation zones develop at the ”lower left” part of the domain and ”in front of” as well as ”behind” the jet. The main jet starts breaking up after half a nozzle diameter, which induces turbulent fluctuations that are dissipated

This chapter was previously published [159] and is reprinted with permission of the journal.

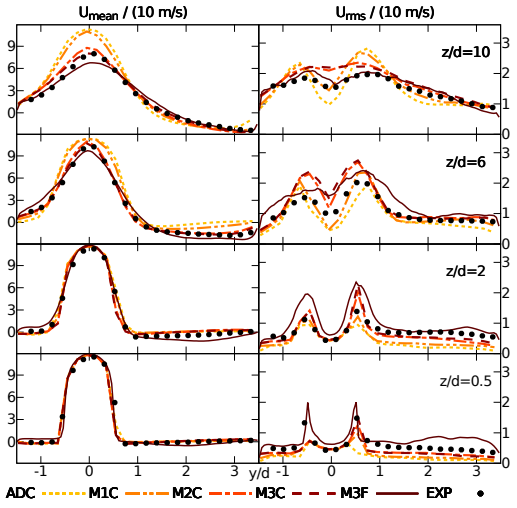

Figure 5.4.: Radial profiles of the mean and rms of axial velocity at different downstream locations [159].

further downstream. The mean jet is bend to the ”right” near the end of the domain and feeds the recirculation zone.

The enthalpy defect is strongest in the lower part of the domain, where recirculated burned gases have been cooled down by around 700 K in comparison to the adiabatic solution MA due to heat exchange with the chamber walls. The reduction of the flame speed by the effect of heat loss results in local extinction near the burner exit.

Radial profiles of velocity and temperature [103] are presented in Figs. 5.4 and 5.5, comparing the results for the adiabatic reference solution and the models described above on the coarse (C) and fine (F) grid.

The axial velocity statistics in Fig. 5.4 are in good agreement with the measurements for M2 and M3, whereas AD and M1 struggle to predict the velocity and the correct position of the recirculation zone. This trend is mirrored in the fluctuation profiles, which are initially under-predicted by AD and M1 and then dissipate too late. Near the nozzle exit, no significant differences between the velocity predictions of the individual models can be observed. The velocity predictions do not improve significantly with grid refinement, implying sufficient grid resolution.

As a result of the significant amount of heat loss visible in Fig. 5.3, the peak temperatures for the adiabatic simulation AD in Fig. 5.5 exceed the measured ones by several hundred Kelvin. In contrast to that, M1 matches the peak temperatures of the experiment, but under-predicts the thickness of the flame. M2 and M3 basically match the mean temperature measurements, some deviations occur towards the ”left” burner wall. The predictions here improve with M3 compared to M2 and with grid refinement. The latter can be explained by the fact that the higher temperature gradients in this region can be resolved more adequately on the fine grid. Except for AD, all other methods are able to reproduce the temperature fluctuations within the burned gas qualitatively. However, the strength of the fluctuations is under-predicted near the burner exit. Physically it seems unlikely that the temperature fluctuations within the recirculation zone,

This chapter was previously published [159] and is reprinted with permission of the journal.

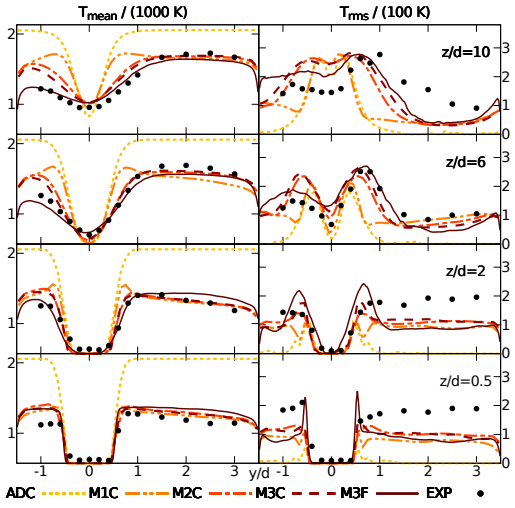

Figure 5.5.: Radial profiles of the mean and rms of temperature at different downstream locations [159].

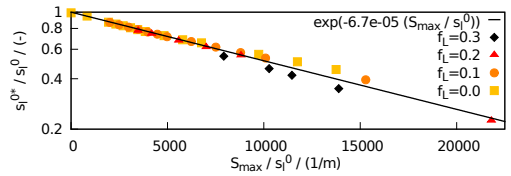

Figure 5.6.: Strain correction factor for different amounts of heat loss from Cantera premixed counterflow flames (symbols) and the respective exponential fit (line) [159].

which mainly consists of burned products, should be as high as in the flame region.

5.5.1. Strain correction

Although the measured temperature field is captured well by the simulation, it turned out that all methods under-predicted the length of the flame to a certain degree. To evaluate if this is related to the relatively high axial velocity magnitude, the tabulation method M3 is extended by a simple strain correction (**M3S**) based on Cantera premixed counterflow flames [197]. One stream represents the hot exhaust gas and the other one the cold unburned mixture from the respective free flame computations. These computations have been carried out for different amounts of heat loss and varying compressive strain rates, where the energy equation was computed according to Eq. (5.1) and the flame speed was evaluated from:

$$s_L^0 = \frac{1}{\rho_u Y_{\mathrm{CO_2},b}} \int_{-\infty}^{\infty} \dot{\omega}_{\mathrm{CO_2}} dx \tag{5.10}$$

In Eq. (5.10), ρ_u, $Y_{\mathrm{CO_2},b}$ and $\dot{\omega}_{\mathrm{CO_2}}$ denote the density of the unburned mixture, mass fraction of $\mathrm{CO_2}$ in the exhaust gas and reaction rate of $\mathrm{CO_2}$, respectively. Figure 5.6 shows the resulting flame speed as a function of the maximum strain rate, the plot has been normalized by the flame speed of the respective free flame. The Favre-filtered strain in the CFD computation is

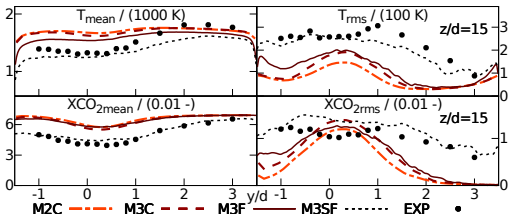

Figure 5.7.: Radial profiles of the mean and rms of temperature and carbon dioxide molar fraction at the last measurement position [159].

computed according to [139], with the flame normal vector $\tilde{n}_i$ pointing into the fresh mixture:

$$S = -\tilde{n}_i \frac{\partial \tilde{u}_i}{\partial x_j} \tilde{n}_j \quad \text{with} \quad \tilde{n}_i = -\frac{\frac{\partial \tilde{Y}_C}{\partial x_i}}{\left| \frac{\partial \tilde{Y}_C}{\partial x_i} \right|} \tag{5.11}$$

The obtained strain value is then normalized by the flame speed of the respective free flame, subsequently the correction factor is evaluated from the exponential fit given in Fig. 5.6 and applied to the progress variable reaction ratio, the flame speed and the flame sensor. As the basis of the fit are the maximum strain rates from the counterflow computations and only the resolved strain rate is taken into account, the described procedure represents a lower limit of the influence of the strain on the flame propagation.

Figure 5.7 shows the comparison of mean value and fluctuations of temperature and carbon dioxide at the most downstream measurement location. The strain correction improves the predictions notably, most visible towards the ”left” side of the domain, the resulting flame length is in agreement with the measurements. However, the impact on the temperature profile seems to be a little bit too high towards the wall, which likely indicates that the correction should not be applied near the wall inside the boundary layer, where high strain rates may occur even in the absence of burned (and cooled down) products. Although the use of the correction improved the results significantly, it must be stressed that the development of this method should not be seen as finalized, and that further investigation on the effects of strain in such flames is required - ideally by DNS. It also remains to be investigated if the strain itself is the main physical reason for the reduction of the flame speed, or rather some closely related phenomenon like internal exhaust gas recirculation, as suggested by Di Domenico et al. [41]. Di Domenico et al. [41] also found no evidence for a relevant contribution of auto ignition on the flame stabilization - even for a faster jet (bulk velocity of 150 m/s).

5.5.2. Analysis of the heat loss

Figure 5.8 compares the normalized PDF of the reaction source term conditional Favre-filtered enthalpy defect for the different models and grid resolutions, AD and M1C are skipped for brevity. In all cases combustion is found over a wide enthalpy range which starts at an enthalpy defect of approximately -0.2 MJ/kg on the fine and -0.4 MJ/kg on the coarse grids, respectively.

This chapter was previously published [159] and is reprinted with permission of the journal.

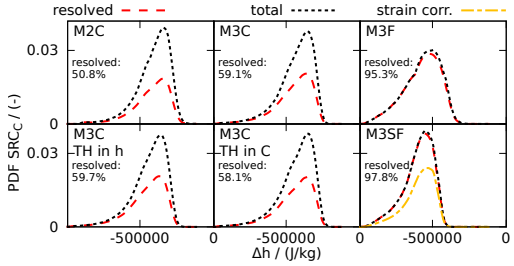

Figure 5.8.: Normalized PDF of the Favre-filtered reaction source term conditional on Favre-filtered enthalpy defect over the entire domain for the presented models. Results are also shown for M3C with an additional top-hat (TH) subfilter model in enthalpy and progress variable, respectively. Shown are the total and the resolved reaction source term, the latter is obtained with an efficiency function of unity ($E = 1$ in Eq. (5.5)). The ratio of the integrated resolved source term and the integrated total source term is also given. For M3SF the total source term after the strain correction is also included [159].

The distributions show a negative skewness with a long tail towards low enthalpies. This can be attributed to the fact that the flame gets more sensitive to small disturbances when approaching the extinction limit, resulting in a stronger influence of the turbulent velocity fluctuations on the flame behavior. To study the influence of the subfilter contribution, two additional simulations have been carried out for M3C with an additional top-hat FDF closure in enthalpy respectively progress variable [57, 135, 158]. The resulting impact on the source term PDFs (and also on the flow statistics) is very small, the amount of resolved source term is approximately identical. M2C predicts a smaller amount of heat release at the decreasing side of the distribution compared to M3C, which results in a lower amount of resolved source term. In the fine grid simulation M3F around 95% of the flame is resolved, the peak value of heat release is shifted towards lower enthalpies compared to the coarse grid simulations. The fine grid predicts a larger amount of combustion towards the extinction limit than the coarse one. An explanation for this behavior is that most of the flames near the extinction limit are found in the near-wall region at the ”left” side of the burner, which is resolved better on the fine grid. The efficiency function E reduces to unity at low enthalpy values due to the increase of flame thickness shown in Fig. 5.1, indicated by matching of the resolved and total source term. The strain correction (M3SF) reduces the skewness and width of the distribution noticeably, which can be explained by flame blow off near the flammability limit by the effect of mean flow strain rate. Thus the probability for re-ignition of these flames is reduced drastically, causing a shift of the combustion process to more stable regions with higher enthalpy values.

5.6. Conclusions

A high velocity confined jet burner has been investigated with different methods for the inclusion of heat loss in FGM. Considering the heat loss was necessary as the adiabatic reference simulation (AD) over-predicted the temperature by several hundred Kelvin and failed to predict the flow field correctly. The combination of an adiabatic combustion model with the solution

This chapter was previously published [159] and is reprinted with permission of the journal.

of the energy equation (M1) was able to predict the correct peak values of the temperature, but neither the correct flame shape and length nor the correct velocity field.

To capture the shape of the flame and the correct velocity field, it was necessary to consider the effect of the heat loss on the flame structure and propagation velocity. Two methods based on Cantera computations with detailed chemistry have been compared, an established one based on burner stabilized flames (M2) and one on scaling the energy equation source term (M3). Both methods performed well and lead to very comparable results. The new method yielded slight improvements in the predictions of temperature towards the ”left” burner wall and of velocity further downstream. Only a small improvement of the results with grid refinement was found (M3F), mostly visible for the temperature due to better resolution of the wall boundary layer. The predictions on the coarse grid showed a very satisfactory agreement with the measurements for M2 and M3.

Even though the last two models were able to predict the flame structure and the flow field, they still under-predicted the flame length by some degree. It was shown that inclusion of a simple strain correction method (M3SF) improves the prediction of the flame length. However, the exact formulation of this model and the details of the underlying physical mechanism require further investigation.

By analyzing and comparing the PDF of the source term conditional on the heat loss for the different models, it was shown that the combustion process takes place over a wide range of enthalpy defect. The probability of combustion towards the extinction limit is increased on the fine grid, implying that the respective parts of the flame are mainly located near to the ”left” wall of the burner, where the effect of the grid refinement is strongest.

5.7. Acknowledgements

The authors gratefully acknowledge funding from the state of Nordrhein-Westfalen, Germany. Computations have been carried out using the DFG supported HPC resources of the Center for Computational Sciences and Simulation (CCSS) of the University of Duisburg-Essen, Germany. We would like to thank DLR Stuttgart and Siemens Energy for providing the experimental data. We further thank Dr. Wolfgang Meier, Dr. Oliver Lammel and Stefan Dederichs for many helpful discussions.

This chapter was previously published [159] and is reprinted with permission of the journal.

6. Flame resolved simulation of a turbulent premixed bluff-body burner experiment. Part I: Analysis of the reaction zone dynamics with tabulated chemistry [161]

Authors: F. Proch, P. Domingo, L. Vervisch, A.M. Kempf
This chapter including all figures and tables was previously published in 'Combustion and Flame, F. Proch, P. Domingo, L. Vervisch and A. M. Kempf, Flame resolved simulation of a turbulent premixed bluff-body burner experiment. Part I: Analysis of the reaction zone dynamics with tabulated chemistry, http://dx.doi.org/10.1016/j.combustflame.2017.02.011, Copyright © Elsevier (2017)' and is reprinted with permission from Elsevier. The author F. Proch developed the codes for the CFD simulations and the post-processing as well as the combustion model, ran all the simulations, wrote the paper and generated all figures and tables. The authors P. Domingo, L. Vervisch and A.M. Kempf contributed corrections, discussions and proofreading.

6.1. Abstract

Results from a highly resolved simulation are presented for a turbulent lean premixed methane-air bluff-body burner investigated experimentally at Cambridge University and Sandia National Laboratories. The Cartesian computational grid consists of 1.6 billion cells with a resolution of $100\ \mu\mathrm{m}$, which is sufficient to capture the laminar (thermal) flame thickness of $500\ \mu\mathrm{m}$. The combustion process is modeled with premixed flamelet generated manifolds (PFGM). The quality of the simulation is assessed by investigating the resolution of the flame- and velocity scales, it is demonstrated that the relevant scales are resolved in a direct numerical simulation (DNS) sense in the flame. The simulation is validated by comparing temporal statistics of velocity, temperature and major species mass fractions against experimental results. It is shown that the combustion regime varies with the distance from the burner and the progress of the reaction. Ensemble-averaged statistics, conditional means and averages along turbulent flamelets

are compared against reference data from unstrained premixed one-dimensional flames. The analysis is carried out with respect to previous findings from DNS of much simpler flame configurations featuring synthetic turbulence. It is concluded that the major physical properties are comparable. In other words, most of the findings from previous DNS studies for canonical cases are relevant, at least for the lab-scale jet-flame examined here. The flame normal strain is found to be aligned with the most compressive strain rate. The mean principal curvature of the progress variable isosurfaces is predominantly zero and skewed towards positive values, the turbulent flame structure is mainly slightly thinned compared to the laminar one. The displacement speed of the flame is found to take partially negative values. The lack of correlation between the displacement speed and the consumption speed is also reported, the correlation being achieved considering the normal component of the diffusive flux only.

6.2. Introduction

Direct numerical simulations (DNS) have been used over the last decades to gain a deeper understanding of the governing physical mechanisms of turbulent combustion. DNS provides three-dimensional velocity and scalar fields, which are resolved in space and time. These results are useful to complement experimental observations and are also the key element in the development of combustion models for Reynolds-averaged Navier-Stokes simulations (RANS) and large eddy simulations (LES) – which will both be the only viable tools for the computation of technically relevant combustors in the foreseeable future. Recent overviews on the topic of combustion DNS are given by Chen [34] and by Poinsot and Veynante [152].

When focusing on premixed turbulent combustion, DNS simulations can be categorized in groups based on the complexity of the chemical mechanism, the type and strength of turbulence occurring, and the complexity of the geometry. A large amount of early and recent work was performed for planar or spherical flames interacting with canonical flow configurations, mostly either homogeneous turbulence or larger single vortices, with reduced chemical mechanisms or tabulated chemistry [27, 30, 42, 133, 153, 174, 200, 203], more detailed chemical mechanisms [68, 72, 132] or detailed chemical mechanisms [4].

Another group of direct numerical simulations deals with more complex slot- or Bunsen-flames, applying more detailed chemical mechanisms [10, 168, 176, 177, 210]. Although these configurations are more realistic than the canonical cases, they are still compact enough to resolve all flame- and velocity scales properly in a DNS sense.

Classically, combustion models can be developed based on DNS results of the aforementioned simplified flame configurations. Nevertheless, the turbulent flow structures in technically relevant burners are usually more complex than in these simplified configurations. It is therefore mandatory to validate the obtained models also in more realistic flame configurations, as occurring in lab-scale experiments. A classical DNS of these experiments would be computationally too expensive, therefore LES or RANS simulations are performed with the developed

This chapter was previously published [161] and is reprinted with permission of the journal.

combustion models instead. The performance of the models is then judged by comparing (time-averaged) simulation results against experimental measurements. One serious issue with this approach is that, due to the complex interaction of sub-filter closures for the unresolved velocity scales and the sub-filter flame wrinkling, errors might compensate or amplify. Therefore, a clear and definitive judgment of the combustion model performance is hardly possible, which makes a further development of these models based on such comparisons questionable.

However, if the focus is on the development of sub-filter closures for models based on strongly reduced or tabulated chemistry, as they are applied in the vast majority of LES or RANS computations, flame resolved simulations are possible with the computational power available today. The saving of computational time with respect to a classical DNS has two major reasons. First, the chemical species that need to be transported for the strongly reduced or tabulated chemistry can be resolved on a significantly coarser grid than it is required for a more detailed chemical mechanism. Second, the Kolmogorov length scale increases significantly from the unburned to the burned side of the flame, due to the increase in viscosity. As the main focus in the development of models for premixed combustion is on the influence of a given level of velocity fluctuations on the flame propagation, a slight under-resolution of the Kolmogorov scales in the fresh gases can be tolerated when full resolution of the signals is secured in the reaction zone. This kind of simulation has the potential to fill the gap in-between highly resolved 'classical DNS' for simpler configurations on the one hand, and LES (for real technical configurations) on the other hand, and may be termed as 'quasi DNS' or 'flame resolved simulation', where the latter term is chosen for the remainder of the paper. This new paradigm in turbulent flame simulation allows for comparing flame resolved simulation data against experiments and to carefully validate the simulated flow physics, as it has been done for 'classical DNS' of non-reactive flows for quite some years [93, 121]. The main advantage is that the lab-scale configurations considered enable a further validation of the simulations and the applied combustion models under much more realistic flow conditions, in which the unsteady motion develops according to real turbulent flow properties. Compare to 'classical DNS', an additional and essential validation step may thus be performed, in which it is verified that the statistical flow properties of the DNS fields agree well with experimental measurements.

The first flame resolved simulation for a lab-scale experiment was presented by Moureau et al. [124], it was performed with a finest grid resolution of $100\ \mu\mathrm{m}$ and tabulated chemistry for a lean premixed methane-air swirl burner, which has been previously investigated experimentally by Meier et al. [117]. The applied grid resolution was sufficient to resolve the progress variable field as well as the velocity field inside the relevant flame region. (A small amount of unresolved velocity scales were still present in the unburned gas close to the walls of the swirler, which were dissipated by the numerical scheme.) A good agreement between simulation and measurement data was demonstrated, the results were then used for developing the filtered laminar flame probability density function (FLF-PDF) modeling approach, in which the unresolved fluctuations of the progress variable are related to an explicit filtering operation applied to one-

This chapter was previously published [161] and is reprinted with permission of the journal.

dimensional flamelets.

In the present paper, a flame resolved simulation of a lab-scale flame is presented for a lean premixed methane-air bluff-body burner investigated experimentally at the University of Cambridge and the Sandia National Laboratories by Hochgreb and co-workers and Barlow and co-workers [51, 80, 81, 194, 195, 220], and also numerically with LES by various groups [16, 120, 126, 127, 158]. In contrast to the work of Moureau et al. [124], the focus of the present paper lies on the analysis of the reaction zone dynamics and the turbulence-flame interaction based on the un-filtered progress variable and velocity fields, rather than on a-priori model development, a topic which is considered in a subsequent paper [162]. The goal is to analyze the flame resolved simulation results for a lab-scale burner with respect to the findings from previous DNS performed in much simpler configurations.

The details of the modeling and the experimental and numerical setup are described in the first section of the paper. Afterwards, a careful analysis of the resolution of flame- and velocity scales is presented and the statistically converged mean and rms profiles obtained from the simulation are compared against the available experimental data. Ensemble-averaged conditioned probability density functions (PDFs) and conditioned joint probability density functions (JPDFs) are then evaluated based on all available data points from the last time step of the simulation. It is shown that a conditioning on the height above the burner and the progress of reaction is necessary to obtain a maximum of information from the data. In the near burner region, the flame is only weakly affected by turbulence. This changes further downstream, due to the interaction of the reaction zone with the turbulence originating from the outer stream and the shear layer between the two streams. The correlations between the strain rate components and the progress variable field are investigated, where the focus is on the comparison with the reference laminar flame structure, used in topology-based subgrid-scale models. The progress variable field is characterized by its gradient, curvature and the local displacement speed of its iso-surfaces. Furthermore, various properties related to the reaction zones are extracted and examined for further analysis.

6.3. Premixed flame modeling

The goal of this work is to provide and investigate a database of a flame resolved simulation of a lab-scale burner experiment, which can be used for future validation and development of sub-filter closures for LES or RANS combustion models. Such LES or RANS computations are very often performed with tabulated chemistry, most of the reported LES studies for the investigated burner have been carried out with this approach [120, 126, 127, 158]. Therefore, tabulated chemistry was also used for the quasi DNS, in order to enhance the comparability.

There are several strategies available for tabulating chemistry [54, 63, 113, 128], in this work the premixed flamelet generated manifolds (PFGM) method was applied, which is described in detail by van Oijen and de Goey [202] and by van Oijen et al. [204] and was already used for

This chapter was previously published [161] and is reprinted with permission of the journal.

the LES of the same burner [158]. The basis for the PFGM table are one-dimensional freely propagating laminar methane-air flames, which are computed with the Cantera library developed by Goodwin [64], using the GRI-3.0 mechanism by Smith et al. [188]. As the premixed methane-air streams mix with the air of the co-flow further downstream, flamelets have to be tabulated for the whole flammability range, in-between equivalence ratio values of 0.45 and 1.8. Outside the flammability limit, ideal mixing towards pure air or fuel at the lean or rich side was assumed, respectively. The resulting manifold was mapped onto a two-dimensional equidistant lookup table discretized in 201 entries in normalized progress variable direction and 1001 entries in mixture fraction direction.

A non-normalized progress variable was constructed from the sum of species mass fractions $Y_\mathrm{C} = Y_{\mathrm{CO_2}} + Y_\mathrm{CO} + Y_{\mathrm{H_2O}}$, which was applied with good success before in the LES of the same burner [158]. More complex fuels and rich mixture fraction conditions can require a more extensive progress variable definition, as presented by Ihme et al. [76], Niu et al. [134], Prüfert et al. [163] and others. The normalized progress variable value for the table-lookup is computed from:

$$C = \frac{Y_\mathrm{C} - Y_\mathrm{C}^\mathrm{min}(Z)}{Y_\mathrm{C}^\mathrm{max}(Z) - Y_\mathrm{C}^\mathrm{min}(Z)} \tag{6.1}$$

The mixture fraction Z is introduced following the definition by Bilger et al. [11]. In the fresh gas, it is linked to the equivalence ratio via:

$$\phi = \frac{Z}{1-Z}\frac{1-Z_s}{Z_s} \tag{6.2}$$

Here $Z_s = 0.054$ denotes the stoichiometric mixture fraction for methane-air. Overall, this tabulated chemistry behaves like a (hypothetical) single-step chemistry, which would be perfectly tuned to capture the flame speed, major species profiles and temperature.

The transport equations for progress variable and the mixture fraction solved during the quasi DNS-computation read:

$$\frac{\partial \rho Y_\mathrm{C}}{\partial t} + \frac{\partial}{\partial x_i}\left(\rho u_i Y_\mathrm{C}\right) = \frac{\partial}{\partial x_i}\left(\left[\rho D + \frac{\mu_t}{\mathrm{Sc}_t}\right]\frac{\partial Y_\mathrm{C}}{\partial x_i}\right) + \dot{\omega}_\mathrm{C} \tag{6.3}$$

$$\frac{\partial \rho Z}{\partial t} + \frac{\partial}{\partial x_i}\left(\rho u_i Z\right) = \frac{\partial}{\partial x_i}\left(\left[\rho D + \frac{\mu_t}{\mathrm{Sc}_t}\right]\frac{\partial Z}{\partial x_i}\right) \tag{6.4}$$

The turbulent viscosity is kept in the formulas with a turbulent Schmidt-number of $\mathrm{Sc}_t = 0.7$. It will be demonstrated in Section 6.5 that the sub-filter contribution is necessary in terms of numerics in the shear layers far upstream of the flame, whereas its overall contribution stays negligible in the vicinity and inside the flame zone, and therefore cannot alter the physics of the quantities examined in this work. The turbulent viscosity is computed based on the σ-model by Nicoud et al. [131], which was chosen as it predicts a viscosity of zero near walls and in expanding flows.

This chapter was previously published [161] and is reprinted with permission of the journal.

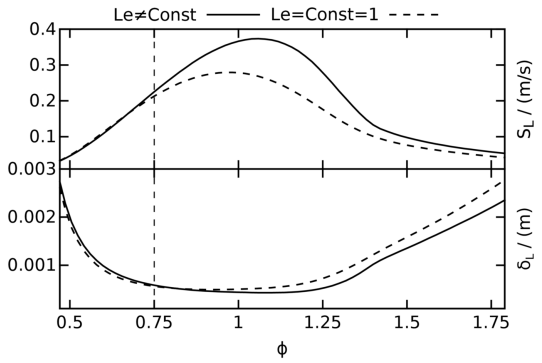

Figure 6.1.: Laminar flame speed (top) and thickness (bottom) as a function of the equivalence ratio ϕ obtained from Cantera [64] freely propagating flame computations with the GRI-3.0 mechanism [188]. Compared are computations with individual Lewis numbers for all species ($\mathrm{Le} \neq \mathrm{Const}$) and with a fixed Lewis number of unity for all species ($\mathrm{Le} = \mathrm{Const} = 1$). The present paper considers a ϕ range from 0 to 0.75. [161]

The diffusion coefficient was set to $D = \lambda/(\rho c_p)$ in Eqs. 6.3 and 6.4, as a Lewis number of unity was assumed for all species during the flamelet computations, which is a common practice in many turbulent flow simulations [e.g 13, 55, 102, 149]. It is demonstrated in Fig. 6.1 that this assumption of a unity Lewis number has only a small influence on the propagation speed and thickness of a laminar methane-air flame for equivalence ratios smaller than ϕ = 0.75, the maximum deviation is around 5% (a larger deviation is observed for richer mixtures that are not considered here). The heat conductivity and the heat capacity are denoted by λ and c_p, respectively. The resulting diffusion coefficient was stored together with the gas density ρ (which is needed for the applied incompressible or low-Mach number solution algorithm), the laminar viscosity μ and the progress variable source term $\dot{\omega}_\mathrm{C}$ in the PFGM lookup table.

6.4. Experimental and numerical setup

The experimental setup of the investigated burner is presented in Fig. 6.2. The measurements have been carried out by Hochgreb and co-workers at the University of Cambridge and Barlow and co-workers at the Sandia National Laboratories [51, 80, 81, 194, 195, 220]. The central bluff-body is surrounded by two co-annular premixed methane-air streams at ambient conditions, which are embedded in a co-flow of air with a velocity of 0.4 m/s. For further details please refer to Table 6.1.

Pseudo-turbulent fluctuations were imposed at the inlet, which were generated with the filtering method by Klein et al. [94] in an efficient numerical implementation [88]. A sensitivity study was performed on a reduced domain to find the parameters for the inflow-generator which result in the best agreement with the measured fluctuations at the first measurement position. It was found that an integral lengthscale of $L = 0.5$ mm and a fluctuation level of 10% of the mean velocity, as given in Table 6.1, led to the best results. This integral lengthscale deviates from the ones measured by Zhou et al. [220], which were in between 2.4 mm and 3.9 mm. One

This chapter was previously published [161] and is reprinted with permission of the journal.

possible explanation is that the imposed pseudo-turbulent fluctuations have only one integral lengthscale, whereas in reality there exists a broader and complex spectrum of flow scales at the inflow, spreading the kinetic energy over a wider variety of scales. We do, however, note that the lengthscales given by the experimentalists are very high in relation to the annular gaps (around 5 mm width, see Fig. 6.2). This may imply that the measured lengthscales rather represent some shedding at low frequencies induced by the geometry.

The laminar flame speed $S_L = 0.212$ m/s and flame thickness $\delta_L = 0.565$ mm were determined from the laminar flame computation for the equivalence ratio of ϕ = 0.75. The flame thickness is based on the maximum temperature gradient and the temperatures in the unburned T_u and burned T_b gas:

$$\delta_L = \frac{T_b - T_u}{\max\left(\frac{dT}{dx}\right)} \tag{6.5}$$

The turbulent Reynolds number Re_T, Damköhler number Da and Kolmogorov lengthscale η_K were computed as follows, with the kinematic viscosity ν set to $1.6\,\mathrm{x}10^{-5}\,\mathrm{m}^2/\mathrm{s}^2$ and all other values taken from Table 6.1:

$$\mathrm{Re}_T = \frac{u'L}{\nu} \tag{6.6}$$

$$\mathrm{Da} = \frac{S_L L}{u'\delta_L} \tag{6.7}$$

$$\eta_K = L\,\mathrm{Re}_T^{-\frac{3}{4}} \tag{6.8}$$

The simulation was performed with the in-house code 'PsiPhi' that solves the governing equations in a low-Mach number finite-volume formulation, details can be found in previous publications by Kempf and co-workers [87, 158, 159, 164, 170, 171]. The spatial discretization relies on a central-differencing scheme for momentum and a total variation diminishing (TVD) scheme for the scalars, where the non-linear CHARM limiter [219] was applied. The solution is advanced in time with an explicit low-storage third order Runge-Kutta scheme using a CFL number of 0.5. The geometry was described by an immersed boundary technique, continuity is ensured by a pressure correction method embedded in a predictor-corrector scheme. A successive over-relaxated Gauss-Seidel solver was applied for the solution of the Poisson-equation for the pressure. Around 80 iteration steps were necessary per Runge-Kutta sub-step to solve the Poisson equation with a maximum residual of 0.1 Pa, this consumed 35% of the total run time.

The code is parallelized using the distributed memory message passing interface (MPI), where non-blocking communication was used to overlay the communication with computation. The computational domain consisted of 1120x1200x1200 equidistant cells with an edge-length of $100\ \mu\mathrm{m}$. The last 12 mm of the burner geometry were included into the computational domain as immersed boundaries. This led to a total amount of 1.6 billion control volumes. The computations were carried out on the Blue Gene/Q machine JUQUEEN at the Jülich Supercomputing Centre on 64,000 processor cores. The simulated physical time was 0.34 seconds corresponding to 195,000 time steps, which required a total amount of 10 million core hours.

This chapter was previously published [161] and is reprinted with permission of the journal.

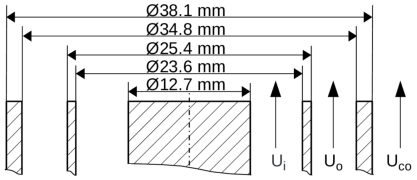

Figure 6.2.: Sketch of the investigated burner setup. [161]

Table 6.1.: Boundary conditions and resulting turbulence-flame interaction parameters for the inner and outer stream. [161]

Stream	u	u'	L	T	ϕ	Re	S_L	δ_L	Re_T	Da	η_K
	m/s	m/s	mm	K	-	-	m/s	mm	-	-	µm
Inner	8.31	0.9	0.5	295	0.75	5960	0.212	0.565	28.1	0.2	40.9
Outer	18.7	1.8	0.5	295	0.75	11,500	0.212	0.565	56.3	0.1	24.3

6.5. Resolution of flame- and velocity scales

The sufficient resolution of the velocity scales on the computational grid is checked by two different measures, on the one one hand based on the estimated Kolmogorov length scales, and on the other hand based on the remaining turbulent viscosity as predicted from the σ-model. The level of resolution of the progress variable source term on the computational grid is addressed also, to conclude on the quality of the reaction zone description.

6.5.1. Kolmogorov length scales

The Kolmogrov length scale is computed as [139, 157]:

$$\eta_K = \left(\frac{\nu^3}{\epsilon}\right)^{1/4} \tag{6.9}$$

Here, ν denotes the kinematic viscosity and ϵ describes the rate at which the energy is transfered within the inertial subrange, it is approximated based on the integral lengthscale and the turbulent kinetic energy [139, 157]:

$$\epsilon \approx \frac{\overline{u'}^3}{L} \tag{6.10}$$

To compute the integral lengthscales and the velocity fluctuations, the data for all transported quantities in the burner mid-section, as shown in Fig. 6.12, has been collected for the last 240 statistical sample steps during the simulation. The turbulent velocity fluctuations have been evaluated by subtracting the time-averaged mean velocity fields (denoted by a bar operator)

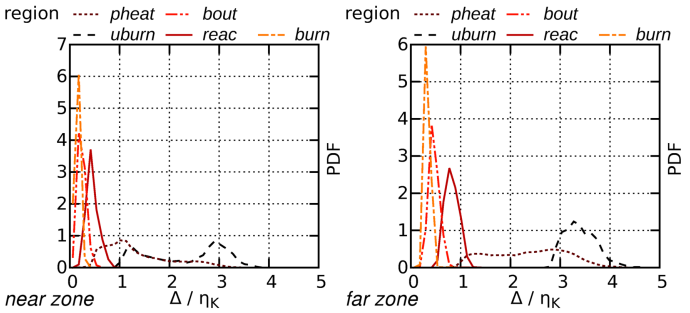

Figure 6.3.: Ratio of the grid resolution to the Kolmogorov length scales. *The different plots show the conditioning on the height above the burner, whereas the different lines represent the conditioning on the progress of the reaction (see Section 6.5).* [161]

from the instantaneous velocity fields:

$$u_i'(t) = u_i(t) - \overline{u}_i \quad \text{with} \quad \overline{u}_i = \frac{1}{T}\int_{t=0}^{t=T} u_i(t)\mathrm{d}t \tag{6.11}$$

The averaged rms of all three velocity components was used for the computation of the turbulent kinetic energy:

$$\overline{u'} = \sqrt{\frac{1}{3}\overline{u_i' u_i'}} \tag{6.12}$$

The integral lengthscales were obtained from integration of the normalized time-averaged spatial auto-correlation function (summation convention not applied for greek letters):

$$L^{\pm}_{u_\alpha x_\alpha} = \int_{r=0}^{r=R^*} \frac{\overline{u'_\alpha(x_\alpha)\, u'_\alpha(x_\alpha \pm r)}}{\overline{u'_\alpha(x_\alpha)\, u'_\alpha(x_\alpha)}}\mathrm{d}r \tag{6.13}$$

The upper integration limit R^* is reached when the auto-correlation function either crosses zero or reaches a minimum. The lengthscale fields were smoothed by averaging over the positive and negative x- and y-direction:

$$L = \frac{1}{4}\left(L^+_{ux} + L^-_{ux} + L^+_{vy} + L^-_{vy}\right) \tag{6.14}$$

The resulting conditional PDFs of the ratio of the grid resolution to the Kolmogorov length scales are presented in Fig. 6.3. The PDFs are conditioned on the progress of the reaction, as usually done to assess turbulent premixed combustion [17]. The respective regions (with somewhat arbitrary definition) for conditioning are shown in the laminar flamelet for the inlet equivalence ratio of ϕ = 0.75 in Fig. 6.4. The range $0.01 \leq \mathrm{C} < 0.02$ is considered as the unburned side of the flame, and is denoted *'uburn'*; $0.02 \leq \mathrm{C} < 0.6$ as the preheat zone is denoted *'pheat'*; $0.6 \leq \mathrm{C} < 0.8$ refers to the inner reaction zone, denoted *reac*, this zone was determined based on the species profile of the radical CH_3 (not shown in the plot); and $0.8 \leq \mathrm{C} < 0.98$ describes the burnout zone, denoted *'bout'*; finally $0.98 \leq \mathrm{C} < 0.99$ gives the burned side of the

This chapter was previously published [161] and is reprinted with permission of the journal.

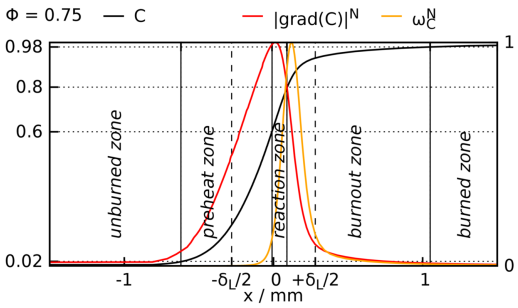

Figure 6.4.: Laminar freely propagating flame for an equivalence ratio of ϕ = 0.75. Plotted are the normalized progress variable C, the normalized progress variable gradient $|\mathrm{grad(C)}|^{\mathrm{N}}$ and the normalized progress variable source term $\dot{\omega}_{\mathrm{C}}^{\mathrm{N}}$. The different flame zones are separated by solid vertical lines. The range of the laminar flame thickness based on the thermal gradient centered at the location of maximum gradient of the progress variable C is marked by dashed vertical lines. [161]

flame, which is denoted *'burn'*. The above regions were found to provide a useful conditioning of the PDFs, yielding greater insights. Furthermore, the PDFs are shown for two regions, the *near* region up to 35mm above the burner and the *far* region, from 35mm to 70mm above the burner. This conditioning on the height above the burner reflects the fact that the flame will interact with strong turbulence in the far zone only, as can be seen in Fig. 6.12.

The ratio of the grid resolution to the Kolmogorov length scale in Fig. 6.3 is a common measure for the resolution of a DNS, as discussed e.g. by Moin and Mahesh [121]. For the reaction zone, which is of high importance for the correct flame propagation, the ratio of the grid resolution to the Kolmogorov length scale is below unity for the vast majority of points, which indicates that all velocity scales are resolved. For the unburned- and preheat region, the ratio of the grid resolution to the Kolmogorov length scale reaches values up to four. According to Moin and Mahesh [121], this resolution might be sufficient for a classical DNS of homogeneous turbulence with a higher-order spectral code. With the applied second-order scheme, this means that a certain small amount of unresolved velocity scales is left in the unburned- and preheat region.

6.5.2. Ratio of turbulent to laminar viscosity

The potential influence of these remaining unresolved velocity scales in the unburned- and preheat region on the flame propagation is assessed by the ratio of turbulent viscosity resulting from the σ-model to the laminar viscosity. Figure 6.5 presents the conditional PDFs of the viscosity ratio, where the data points within the co-flow were omitted to not bias the unburned gas PDF towards zero, as the co-flow points have zero turbulent viscosity. (These points were detected by an axial velocity component smaller than 1 m/s and a radius larger than 14 mm.)

A clear dependence of the viscosity ratio on the progress of the reaction can be seen in Fig. 6.5. In the inner reaction zone, the burnout zone and at the burned side of the flame, the viscosity ratio takes negligible values. In the preheat zone, at more than 80% of the points the viscosity ratio is below 0.1, which means that the diffusive flux due to unresolved velocity scales

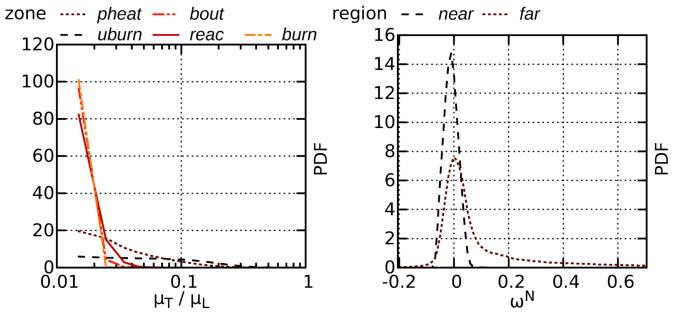

Figure 6.5.:
Left: PDFs of the ratio of turbulent to laminar viscosity (due to the logarithmic abscissa the area below the PDFs is not unity). *The different lines represent the conditioning on the progress of the reaction (see Section 6.5).*
Right: Progress variable source term integrated in C-space over the turbulent flamelets normalized by the exact one-dimensional laminar results (see Eq. (6.15)). *The different lines represent the conditioning on the height above the burner (see Section 6.5).* [161]

is at most 10% of the laminar diffusive flux. Just on the unburned side of the flame, the viscosity ratio can take slightly larger values, but also stays well below 0.4. It can be summarized that the influence of the unresolved scales stays very moderate on the unburned side of the flame and gets negligible inside the reaction zone on which the following investigations will focus.

6.5.3. Resolution of the progress variable field

The second point that needs to be demonstrated is whether the resolution of the progress variable field on the computational grid is sufficient. It is shown in Fig. 6.6 that the 'PsiPhi' code is able to predict a one-dimensional laminar freely propagating flame in good agreement with the Cantera reference solution on the applied grid resolution, the TVD scheme does not alter the diffusive fluxes. To assess the resolution of the turbulent flame, the structure of the local diffusive and reactive layers has been extracted from the simulation results. This was done by starting at all points that were located on the inner reaction zone iso-surface of C = 0.83, where the progress variable source term is largest, and moving for each of these points along the positive (respectively negative) local flame normal direction, until a value of C = 0.01 (respectively 0.99) was reached. Local distributions that were not strictly monotonic in progress variable were discarded, we did not check for potential intersections of individual distributions. That way, roughly 0.8 million individual distributions across reaction zones, named thereafter as 'flamelets', were extracted for the further analysis.

To judge the resolution of the flamelets, it was exploited that the source term $\dot{\omega}_C$ for a given mixture fraction is an unambiguous function of the progress variable C in the applied tabulated chemistry approach. Therefore, the integration of the source term along the turbulent flamelets in C-space should always yield the same result as in a properly resolved one-dimensional laminar flame when the spatial resolution of the progress variable field is sufficient. Figure 6.5 shows the PDFs of the normalized deviation of the integrated source term of the turbulent flamelets

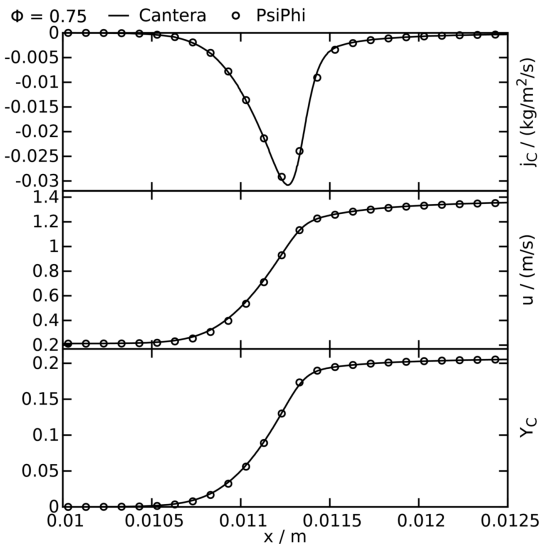

Figure 6.6.: Comparison of a one-dimensional laminar freely propagating flame computed with Cantera [64] (lines) and the 'PsiPhi' code (one circle per cell, grid resolution of 100 µm) with a Lewis number of unity for all species for an equivalence ratio ϕ of 0.75. Shown are the profiles of the progress variable (bottom), the velocity (middle) and the diffusive flux of the progress variable $j_k = -\lambda/(\mathrm{Le}\, c_p)\, \partial Y_k/\partial x$ (top). [161]

from the integrated source term of the properly resolved one-dimensional flame for the average mixture fraction of the turbulent flamelets (the dependency on the mixture fraction Z is omitted for clarity):

$$\omega^{\mathrm{N}} = \frac{\int_{C=0.01}^{C=0.99} \dot{\omega}_{\mathrm{C}}\, \mathrm{d}C|_T - \int_{C=0.01}^{C=0.99} \dot{\omega}_{\mathrm{C}}\, \mathrm{d}C\big|_R}{\int_{C=0.01}^{C=0.99} \dot{\omega}_{\mathrm{C}}\, \mathrm{d}C\big|_R} \tag{6.15}$$

A value of $\omega^{\mathrm{N}} = 0$ corresponds to a perfectly resolved source term for one individual flamelet. It can be seen in Fig. 6.5 that in most of the flow locations the source term is nearly perfectly resolved. In the near region, the integration error due to the lack of resolution is below 5% for 70% of the flamelets, and the maximum error stays well below 10%. For the far region, the PDF of the resolved source term is still below 10% error for more than 75% of the points, but has a long tail towards positive deviations in the far region. An explanation for this is the occurrence of stratified regions further downstream, due to mixing with the co-flow air. The principal alignment of flame normal and mixture fraction gradient is such that the flame propagates towards a leaner mixture, which is termed as back-supported stratification, Cruz et al. [40] and Nguyen et al. [128] have shown that this leads to an increase of the flame propagation speed for lean conditions - which also comes along with a higher value of the source term integral.

It can be summarized that inside the flame zone, which is the region of interest for the further analysis, the flame and velocity scales are resolved. A certain amount of unresolved velocity scales can still be found in the fresh gas. This means that the turbulent structures entering the flame zone might be influenced by a small degree, but that the interaction between turbulence and flame is fully resolved.

This chapter was previously published [161] and is reprinted with permission of the journal.

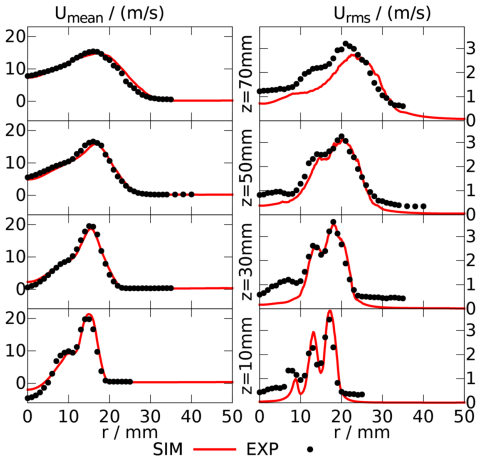

Figure 6.7.: Comparison of mean and fluctuation profiles of the axial velocity component at different axial positions against experimental data [220]. [161]

6.6. Comparisons of time-averaged statistics against measurements

To check the validity of the modeling approach and the general quality of the simulation results, statistical quantities (mean and rms) along sample lines are compared against experimental measurements. The sampling was started after 0.34 seconds, which corresponds to more than one flow-through time with respect to the co-flow velocity of 0.4 m/s. The sampling was carried out for another 0.14 seconds, which corresponds to more than 10 flow-through times with respect to the mean inner stream velocity of 8.31 m/s. It has been found in the preceding LES study of the same burner [158] that this sampling time was sufficient to obtain properly sampled statistics. The respective comparison against the LDA-measurements by Zhou et al. [220] (velocities) and the Raman/Rayleigh-measurements by Sweeney et al. [194] (temperature and species) are presented in Figs. 6.7 - 6.11 for heights of 10, 30, 50 and 70 mm above the burner exit. In general, a satisfactory agreement is found for all quantities for both mean and rms that is mostly better than in the previous LES studies of the same burner [16, 120, 126, 127, 158].

The comparison for the mean axial velocity component are presented in Fig. 6.7, it is over predicted at the centerline by the simulation at the first measurement position. This indicates that the strength of the recirculation zone in the region above the bluff-body is still under predicted, as it was already the case with LES [126, 158]. This could potentially be attributed to a minor influence of heat loss at the bluff-body in that region, which was shown in the LES of Mercier et al. [120]. However, this effect is limited to the small region above the bluff-body and does not influence much the flame dynamics and the good agreement for larger radii and further downstream. At the last measurement position, the mean axial velocity profile is shifted slightly towards larger radii in comparison with the experiment, which corresponds to the simultaneously occurring shift of the mean temperature profile in Fig. 6.9 towards larger radii. Towards the centerline, the simulated velocity components are lower than in the measurements.

This chapter was previously published [161] and is reprinted with permission of the journal.

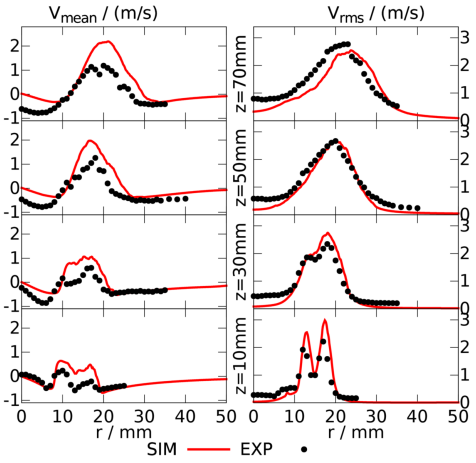

Figure 6.8.: Comparison of mean and fluctuation profiles of the radial velocity component at different axial positions against experimental data [220]. [161]

As this behavior can also be observed in the co-flow region, where the fluctuations should be negligible, the observed deviation might at least partially be attributed to measurement noise. A notable feature of the rms axial velocity profiles is the small peak at a radius of approximately 8 mm. Whereas this flow feature had no big influence in the previously performed LES of the burner [158], the magnitude of the fluctuations at this position turned out to be of great importance for the correct flame shape and position at the first measurement position in the presented quasi DNS.

The agreement for the rms of the radial velocity component in Fig. 6.8 is very similar to the agreement for the rms of the axial velocity component. In contrast, larger deviations are found for the mean radial velocity component. Whereas the simulation results revert to zero at the centerline (as it should be the case in an axial-symmetric configuration), the measured results show a remaining radial velocity component. As burner geometries like the one investigated are known to be sensitive against minute deviations of the geometry, the actually measured flow field might indeed have been slightly asymmetric - which of course is not reproduced by the three-dimensional symmetric simulation setup. Near the bluff-body, where also the measured radial velocity component goes back to zero, a slight over-prediction of the radial velocity component by the simulation can be observed.

At 50 mm, both the mean and rms temperature profiles in Fig. 6.9 show a small shift towards larger radii compared to the experimental values. The thickness of the mean flame brush and the rms profile is under predicted by the simulation at 30 mm.

The mean equivalence ratio profiles in Fig 6.10 are shifted slightly towards larger radii in the simulation, which corresponds to the shift in the axial velocity component (Fig. 6.7) and the temperature (Fig. 6.9). The rms of equivalence ratio is under predicted at the last measurement position and towards the centerline, where the latter deviation may be related to measurement noise in the experiment. A conspicuous feature of the measured mean equivalence ratio profiles is the kink towards the centerline near the bluff-body, which is not showing up at all in the

This chapter was previously published [161] and is reprinted with permission of the journal.

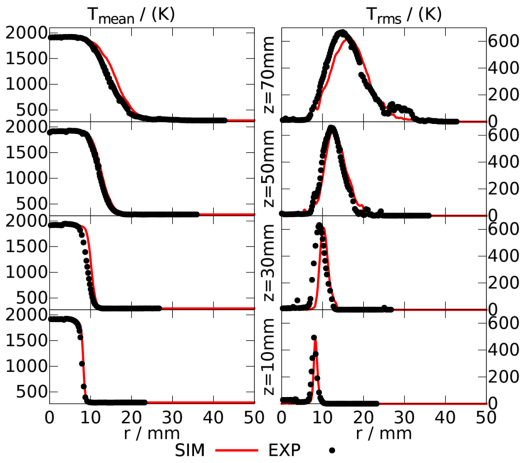

Figure 6.9.: Comparison of mean and fluctuation profiles of the temperature at different axial positions against experimental data [194]. [161]

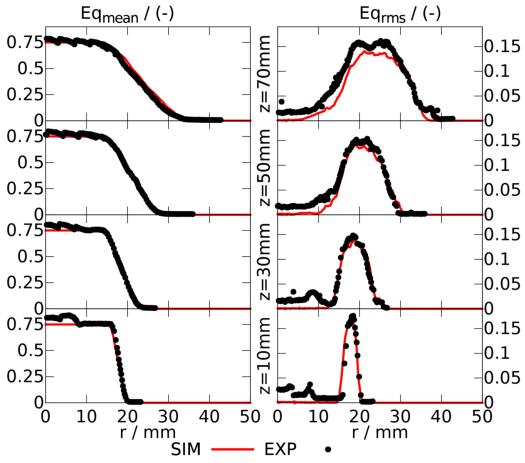

Figure 6.10.: Comparison of mean and fluctuation profiles of the equivalence ratio at different axial positions against experimental data [194]. [161]

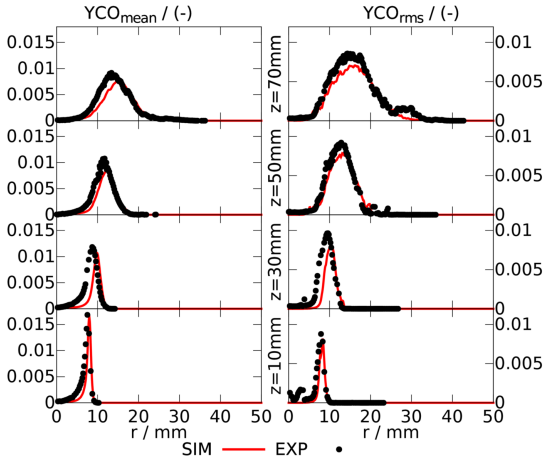

Figure 6.11.: Comparison of mean and fluctuation profiles of CO at different axial positions against experimental data [194]. [161]

simulation. According to Barlow et al. [7], this kink can be attributed to preferential transport of the major species CO_2 and H_2O as well as of the intermediate species CO and H_2. It was shown by Nambully et al. [126] that this phenomenon can be reproduced by solving an additional transport equation for the residence time of mixture fraction, although the obtained 'differential diffusion' mixture fraction was only used for post-processing. Nambully et al. [126] also discussed how the observation of differential diffusion on the mixture fraction is strongly influenced by the choice of the species to build the mixture fraction from the measurements.

To further assess the predictive capability of the tabulated chemistry approach, Fig. 6.11 presents a comparison between simulation and measurement for the intermediate species CO. The agreement of the mean CO profile in the flame zone is good, but the thickness of the burnout zone is under predicted by the simulation which leads to a faster decline of the mean CO value to zero towards the centerline than in the experiment. This can partially be attributed to the under-prediction of the mean temperature profile thickness at 30 mm in Fig. 6.9, another reason might be the Lewis number of unity assumption applied in the computation of the PFGM table. Corresponding to the observations made for the mean profiles, the rms profiles of CO also agree better within the flame region than in the burnout zone.

Overall, one can conclude that the simulation provides a good representation of the actual experiments. The large amount of additional information available in the database is now probed for deeper analysis of the ongoing physical phenomena.

6.7. Analysis of the turbulent flame structure

This section presents a detailed analysis of the turbulence-flame interaction in the investigated lab-scale burner, with respect to the findings from DNS of much simpler flow configurations. The main focus is on the comparison of the resulting turbulent flame structure to the laminar one, to progress in the context of flamelet-like sub-grid scale modeling. The first step is

This chapter was previously published [161] and is reprinted with permission of the journal.

a phenomenological analysis of the flame structure based on instantaneous two-dimensional and three-dimensional contour plots. Afterwards, the combustion process is characterized with regime diagrams, and the interaction between turbulence and flame is investigated by conditional PDFs and joint PDFs of the strain rate component fields and the curvature, gradient and propagation speed of the flame. To the best of our knowledge, this is the first time that this kind of DNS analysis is applied to a dataset devoted to a lab-scale burner, after extensively validating the results against experimental measurements.

6.7.1. Two-dimensional instantaneous contour plots

For a first impression of the flow and scalar fields, Fig. 6.12 shows instantaneous contour plots of different quantities in the mid-section of the burner. The flow field illustrated by the velocity components in axial (U), radial (V) and circumferential (W) direction is determined by the interaction between the faster outer and the slower inner stream, the bluff-body and the flame. In the near-burner region, the flow field is dominated by the recirculation zone above the bluff-body, which stabilizes the flame and is indicated by negative values of the axial velocity. The dilatation due to the temperature increase in the flame induces an additional radial velocity component, compared to non-reactive simulations and measurements of the investigated burner [119, 160, 220], which pushes the slower inner stream towards the faster outer stream and reduces the strength and length of the recirculation zone. Turbulent fluctuations are produced in the shear layers between the inner and outer stream, and between the outer stream and the co-flow. A large amount of the turbulent fluctuations is dissipated in the burned region (towards the centerline) due to the increase in viscosity caused by the temperature increase.

Because of the higher fluctuation level in the outer jet, the equivalence ratio field is getting wrinkled immediately after the burner exit. Turbulent mixing occurs in the mixing layer between the premixed streams and the air co-flow, which grows in thickness when moving downstream.

In contrast to the equivalence ratio field, the temperature field shows a relatively constant thickness of the interface between fresh and burned gas. This is due to the reaction source term, which counteracts the diffusion and steepens the reaction zone.

The flame front is indicated by the reaction source term of the progress variable. The flame is not influenced by strong turbulent fluctuations in the near region, where it is only moderately wrinkled. Things change in the far region, where the flame front gets wrinkled more strongly. Fresh gas starts penetrating into the burned region, this results in unburned mixture fingers as described in previous works [9, 109, 154, 155]. Also the opposite phenomenon can be observed, when narrow regions of burned gas penetrate into the fresh gas, which further downstream leads to regions where pockets of burned gas exist in the fresh gas and regions where fresh gas is surrounded by burned gas in the burner mid-section.

This chapter was previously published [161] and is reprinted with permission of the journal.

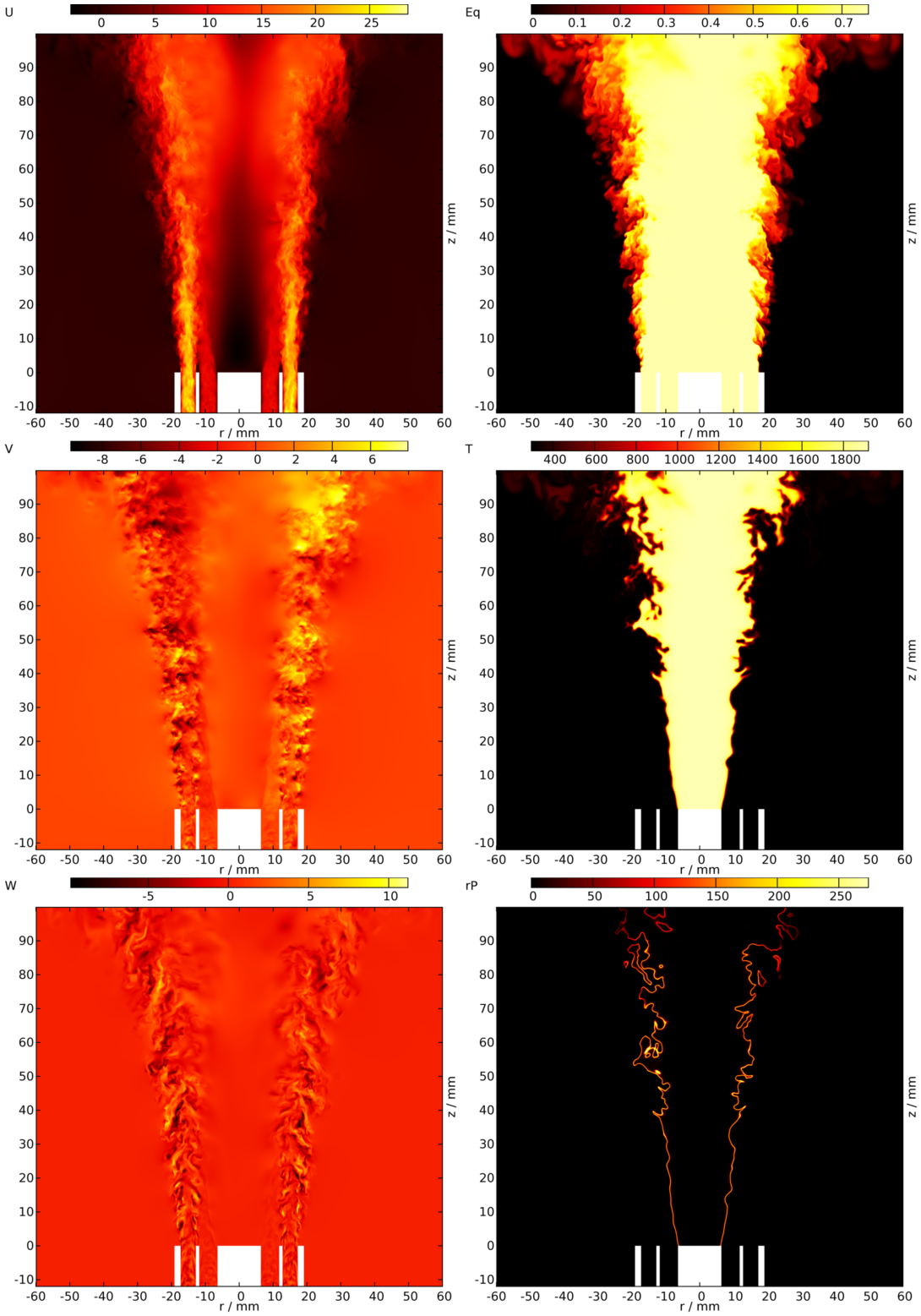

Figure 6.12.: Contour plots in the burner mid-section of the axial (U), radial (V) and circumferential (W) velocity component, the equivalence ratio (Eq), the temperature (T) and the reaction source term of the progress variable (rP). [161]

This chapter was previously published [161] and is reprinted with permission of the journal.

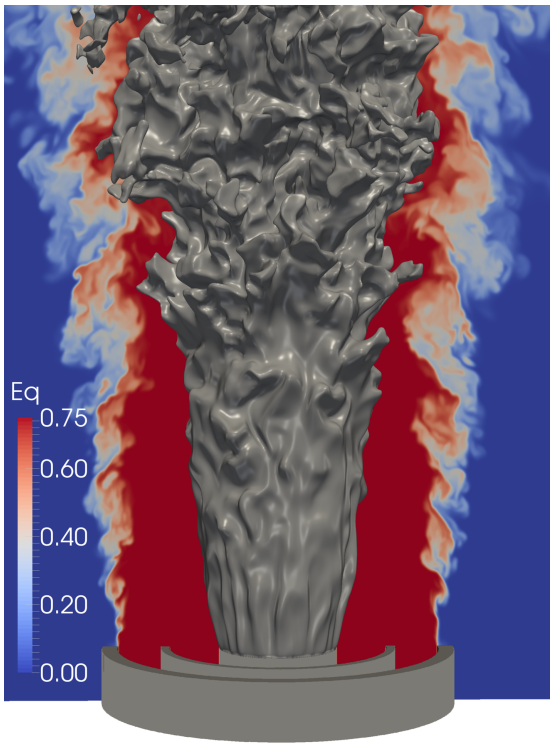

Figure 6.13.: Contour plot of equivalence ratio in the burner mid-section, superimposed is an iso-surface for a progress variable value of $C = 0.5$. [161]

6.7.2. Three-dimensional instantaneous visualization

To get a better understanding of the overall flame structure, Fig. 6.13 presents the three-dimensional iso-surface for a progress variable value of 0.5, which is superimposed on the contour plot of equivalence ration. Immediately after the burner exit in the near region, the flame front develops surface-wave patterns with a relatively constant amplitude that are aligned parallel to the flow direction. When moving downstream in the far region, these structures get less aligned with the axial direction and develop varying amplitudes. No Kelvin-Helmholtz rollers, as in the equivalence ratio distribution, are formed in the progress variable field, as the shedding frequency of the bluff body (12.7 mm diameter) is significantly smaller than the shedding frequency of the outer tube (1.65 mm wall thickness). As already observed in the two-dimensional burner mid section plots in Fig. 6.12, when moving downstream in the far region, the flame surface gets more and more corrugated and develops deep valleys and high peaks. The pockets of burned gas surrounded by fresh gas, observed in the two-dimensional burner mid-section plots (Fig. 6.12), are also visible in the three-dimensional plot, most obviously far downstream. However, there seems to be no regions where fresh gas is completely surrounded by burned gas in the three-dimensional plot. Therefore, the areas of fresh gas surrounded by burned gas observed in the two-dimensional burner mid-section plots shown in Fig. 6.12 may actually be just cuts through deep unburned mixture fingers pointing in the circumferential direction.

This chapter was previously published [161] and is reprinted with permission of the journal.

6.7.3. Temporal development of scalar quantities

To gain further insight into the interaction between turbulence, combustion and mixing, Fig. 6.14 shows contour plots of the circumferential velocity component for two different time steps. The two time steps are separated by 172 µs, which corresponds to the sampling interval for the statistics of 100 computational steps. Applying Taylor's hypothesis, this time difference corresponds to roughly three integral time scales with respect to the inner stream mean velocity of 8.31 m/s. As the investigated case is unswirled, the time-averaged circumferential velocity component is equal to zero, and therefore the instantaneous circumferential velocity directly gives the instantaneous circumferential velocity fluctuations. The flame position is represented by the red iso-line, which corresponds to a dimensionless progress variable value of C = 0.5. The mixing field is visualized by the white and the blue iso-line. The white iso-line represents the beginning of the mixing zone, to get a properly defined iso-line an equivalence ratio $\phi = 0.74$ is chosen, which is close to the $\phi = 0.75$ from the burner. The blue iso-line corresponds to the lean flammability limit of the methane-air mixture at $\phi = 0.45$, where the flame extinguishes.

In the near region, the flame is interacting with the velocity fluctuations originating from the inner stream. In the far region, the flame is exposed to the higher level of velocity fluctuations, originating from the outer stream and the shear layer between the inner and outer stream. The flame dampens the velocity fluctuations on the burned side significantly compared to non-reactive simulations and measurements of the investigated burner [119, 160, 220], and most of the turbulent structures are dissipated away.

Not only the structure of the flame in the two plots, but also the temporal change between the two plots is strongly affected by the level of turbulence. Whereas the flame shape is mainly shifted downstream in the near region, in the far region the flame shape is not only shifted, but also changed and deformed. Distinct features of the flame front are marked by circles in Fig. 6.14. The numbering and diameter of the circles in the plots is consistent, so that the structures can be compared.

Regions where burned mixture penetrates into the fresh gas are found to grow (1) and shrink (4) in thickness and depth. Pockets of fresh (burned) gas in burned (unburned) mixture can appear relatively rapidly, where this comes along with high magnitudes of circumferential velocity fluctuations, so that this actually seems to be due to the convection of three-dimensional structures into the mid-section (2 + 5).

The growth of pockets of fresh gas in burned mixture seems to come along with a narrowing of the 'neck' of the pocket (6), which leads to complex pocket structures further downstream (3). Regions where fresh gas is completely surrounded by burned gas can merge with the fresh gas side of the flame (8). As already discussed for Fig. 6.13, these seem to show cuts through fingers of unburned mixture, which are moved into the mid-plane by convection due to the high magnitude of circumferential velocity in these regions (8).

Regions of locally stratified combustion are found further downstream, where the flame wrin-

This chapter was previously published [161] and is reprinted with permission of the journal.

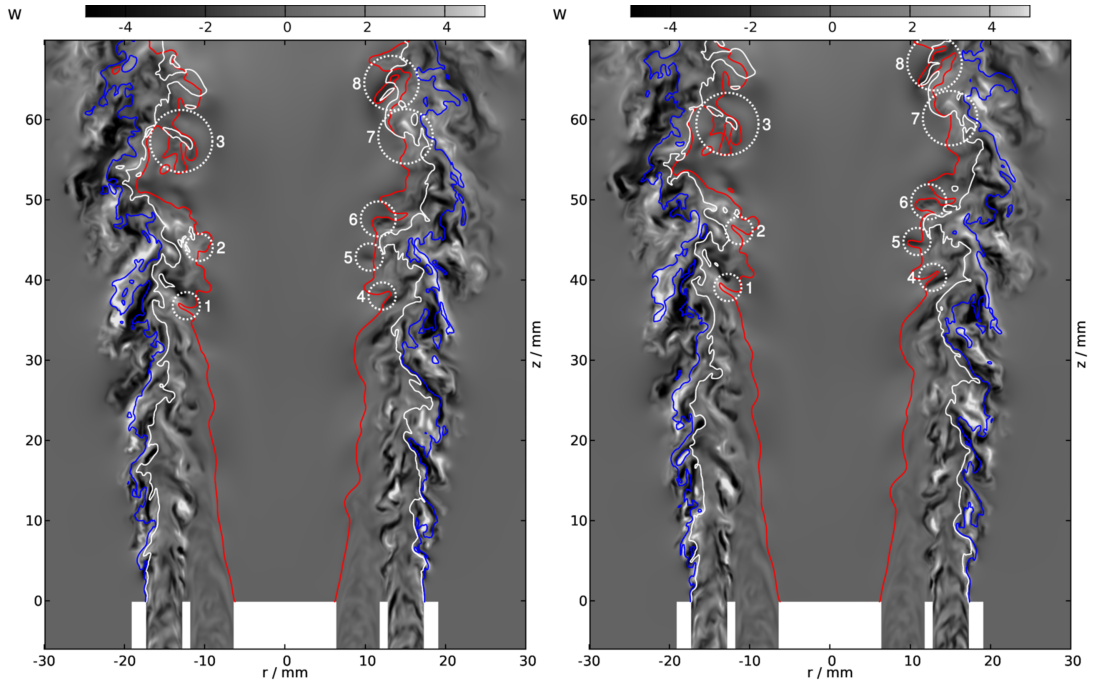

Figure 6.14.: Interaction of turbulence, flame and mixing at two different time steps which have a temporal distance of 172 µs in the burner mid-section. Shown are the contour plots of the circumferential velocity component (W) superimposed with isolines for C = 0.5 (red), Eq = 0.74 (white) and Eq = 0.45 (blue), where the latter represents the lean flammability limit. Distinct features of the flame front are marked by circles, the numbering and diameter of the individual circles is the same in both plots. [161]

kling does not seem to be altered significantly, whereas the wrinkling of the mixture fraction iso-surface is strongly affected by the damping of turbulent fluctuations by the flame (7).

6.7.4. Combustion regime diagrams

To characterize the interaction between turbulence and combustion, the combustion regime diagrams according to Borghi [14] and Peters [139] are usually drawn. For the generation of these diagrams, the turbulent velocity fluctuations and the integral lengthscales in the burner mid-section, as described in Section 6.5, have been normalized by the time-averaged laminar flame speed and the time-averaged laminar flame thickness, respectively:

$$\frac{\overline{u'}}{\overline{S_L(Z)}} \tag{6.16}$$

$$\frac{L}{\overline{\delta_L(Z)}} \tag{6.17}$$

The resulting regime diagrams are shown in Fig. 6.15. The conditioning was done on the height above the burner and the progress of the reaction, as above. To clarify to which extent the smallest scales in the unburned gas are actually able to penetrate into the reaction zone and how the turbulence level is altered by the flame, the regime diagrams are shown for all zones of the flame.

This chapter was previously published [161] and is reprinted with permission of the journal.

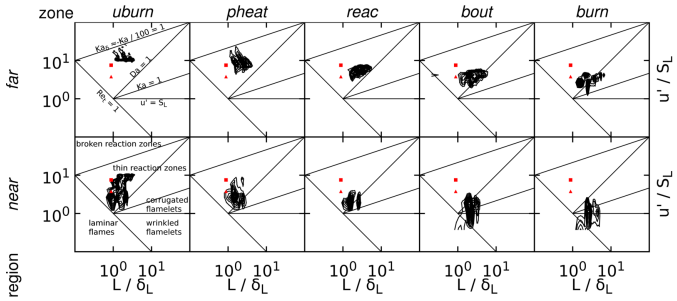

Figure 6.15.: Combustion regime diagrams as suggested by Borghi [14] and Peters [139] with the conditioned joint PDFs of the velocity fluctuations normalized by the laminar flame speed (see Eq. 6.16) as a function of the integral lengthscale of the velocity fluctuations normalized by the laminar flame thickness (see Eq. 6.17). The inlet conditions for the inner and outer stream as given in Table 6.1 are marked by triangles and squares, respectively. *The different plots represent the conditioning on increasing height above the burner from bottom to top and increasing progress of the reaction from left to right (see Section 6.5).* [161]

The diagrams for the unburned side of the flame indicate that the combustion process in the burner takes place in the thin reaction zone regime. However, with increasing progress of reaction, the locations of the JPDFs are shifted significantly towards the corrugated flamelets regime due to a reduction of the normalized velocity fluctuations and an increase of the normalized integral length scales. The increase of the integral lengthscales means that the small unresolved scales that are present in the fresh gas are not able to penetrate into the reaction zone, and thus have limited influence on the combustion process, as it has also been discussed for the DNS of a canonical flow in the thin reaction zone regime, first by Poinsot et al. [153] and more recently by Poludnenko and Oran [154, 155]. This is also a potential explanation why flamelet-based models are frequently found to work well for flames outside the corrugated and wrinkled flamelet regime – at least if the location in the regime diagram is calculated based on the unburned gas turbulence.

The JPDFs in Fig. 6.15 are multimodal, which shows that multiple sources of turbulent fluctuations exist in the investigated burner, which result in a broad turbulent spectrum. First, the two inlet streams supply two different levels of (artificially generated) turbulence as shown in Table 6.1. Second, the shear at the bluff body, between the inner and outer stream and between the outer stream and the co-flow produces additional turbulent fluctuations, where the magnitude of the latter two exceeds the inflow turbulence level, as it can be seen in the radial fluctuation profiles in Figs. 6.7 and 6.8. Far downstream, some further increase of the normalized velocity fluctuations and a decrease of the normalized lengthscales can occur in the fresh gases, due to the reduction of the mixture fraction towards leaner values caused by mixing with the co-flow air, which reduces the laminar flame speed and increases the laminar flame thickness. It should however be stressed that the influence of stratification is only very weak in the investigated burner setup. With growing distance from the burner, the induced turbulent fluctuations and integral lengthscales are decreased and increased by molecular friction, respectively. The broad range of varying fluctuation levels distinguishes the investigated burner from canonical flow

This chapter was previously published [161] and is reprinted with permission of the journal.

configurations, which isolate a single set of flow parameters. This confirms that the presented flame resolved simulation of a lab-scale burner is an interesting and challenging test case for combustion models.

6.7.5. Strain rate components in the flame-aligned coordinate system

The turbulence induced strain rate determines the production of flame wrinkling and therefore is a key quantity in the analysis of the local flame structure [1, 3, 24, 36, 73, 175].

For a closer analysis, the strain rate contributions in flame normal direction a_n and tangential to the flame front a_t are examined [139, 152]:

$$a_n = n_i n_j \frac{1}{2}\left(\frac{\partial u_i}{\partial x_j} + \frac{\partial u_j}{\partial x_i}\right) = n_i n_j \frac{\partial u_i}{\partial x_j} \tag{6.18}$$

$$\begin{aligned} a_t &= (\delta_{ij} - n_i n_j)\,\frac{1}{2}\left(\frac{\partial u_i}{\partial x_j} + \frac{\partial u_j}{\partial x_i}\right) \\ &= (\delta_{ij} - n_i n_j)\,\frac{\partial u_i}{\partial x_j} = -\left(a_n - \frac{\partial u_k}{\partial x_k}\right) \end{aligned} \tag{6.19}$$

The flame normal vector points into the fresh gas and is determined from:

$$\vec{n} = -\frac{\nabla Y_\mathrm{C}}{|\nabla Y_\mathrm{C}|} \tag{6.20}$$

A compressive strain rate component in flame normal direction is denoted by negative values, an expansive one by positive values. The last RHS expression in Eq. 6.19 expresses that the flame tangential strain rate is just the negative value of the flame normal strain rate with the velocity divergence subtracted.

6.7.5.1. Conditioned PDFs of the strain rate components

The PDFs of the described strain rate components conditioned on the progress of reaction and the axial position are shown in Fig. 6.16. At the unburned side of the flame, the flame normal strain rate component PDF is skewed towards negative values, i.e. there exists a compressive strain rate normal to the flame front. Furthermore, the PDF is broader in the more turbulent far region compared to the near region. In the burned gas, the PDF is less wide and symmetric than in the fresh gas. This can be explained by the significant increase of viscosity due to the temperature increase in the flame, which enlarges the diffusive flux and thereby reduces large strain rates. The mean of the flame normal strain rate component gets shifted towards positive values in the reaction zone due to dilatation.

This chapter was previously published [161] and is reprinted with permission of the journal.

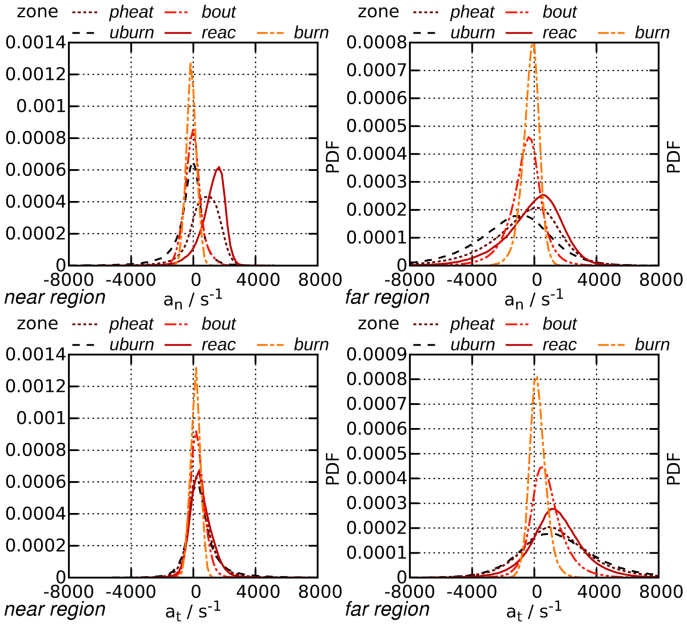

Figure 6.16.: Conditioned PDFs of the strain rate component normal (top, see Eq. 6.18) and tangential (bottom, see Eq. 6.19) to the flame front. *The different plots show the conditioning on the height above the burner, whereas the different lines represent the conditioning on the progress of the reaction (see Section 6.5).* [161]

In the PDFs of the tangential strain rate, most of the dilatation has been removed, therefore the positions of the PDF peak values for the different flame zones are nearly identical in the near region. The PDFs are skewed towards positive values in the unburned gas. Towards the burned side, the PDFs get significantly more symmetric, i.e. larger absolute values of tangential strain rate are reduced more. This is plausible as the strength of the molecular friction is proportional to the magnitude of the strain rate. In the far region the PDFs are much broader, and the peak values are shifted towards zero from the unburned to the burned side of the flame.

To investigate the reason for the observed skewness of the normal strain rate PDFs towards negative values at the unburned and burned side of the flame in the far region, Fig. 6.17 presents the conditional means of the flame normal strain rate, depending on the axial position and the progress of reaction. The left plot shows the conditional mean for the strain rate computed from the instantaneous velocity field in the last time step. (It must be stressed that due to the larger number of sample points and the rotationally symmetric setup, the resulting conditional mean is nearly identical for different time steps.) For the conditional mean in the right plot, the strain rate was computed for the time-averaged velocity field in the burner mid-section. (The operator $<|\mathrm{zone}>$ represents the average over all points conditioned on the dimensionless progress variable, the operator $<>$ the time-averaging.) The time-averaged conditional mean (right) results represent the general flow configuration determined by the flame position, the burner geometry and the mean inlet velocity profiles. The instantaneous conditional mean (left) results are a combination of the time-averaged strain rate and the strain rate due to turbulent velocity fluctuations. In the near region, the instantaneous conditional mean in the unburned

This chapter was previously published [161] and is reprinted with permission of the journal.

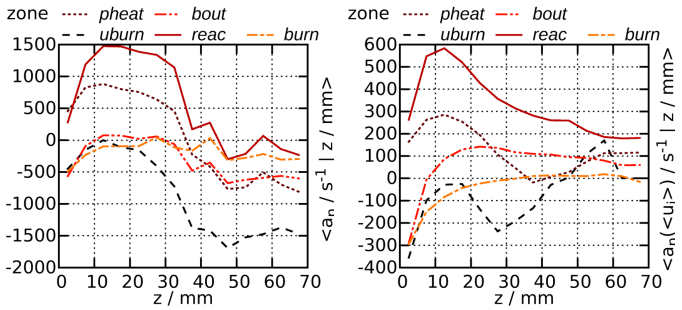

Figure 6.17.: Conditional mean of the strain rate component normal to the flame front (see Eq. 6.18) as a function of the distance from the burner exit. The left plot shows the results for the whole three-dimensional instantaneous field, the right for the time-averaged field in the burner mid-section. *The different lines represent the conditioning on the progress of the reaction (see Section 6.5).* [161]

gas is dominated by the time-averaged contribution. In the far region, the strain rate due to turbulence outweighs the time-averaged strain rate. The turbulence induced flame normal strain rate in the unburned gas takes negative values throughout the domain, the reason for this can be found in the alignment of the strain rate eigenvectors with the flame normal vector, a point that is now discussed.

6.7.5.2. Alignment statistics of the strain rate components and the flame normal vector

The alignment of the principal directions of the strain rate tensor with flame normal direction determines the evolution of scalar gradients and has been investigated before, based on simulation results [23, 29, 175] as well as on experimental measurements [71, 189, 191]. Figure 6.18 presents the conditional PDFs of the dot product of the flame normal vector with the most compressive and most extensive principal strain rate eigenvectors (the closer the dot product is to unity, the stronger is the alignment).

For the near region, the alignment PDFs in the unburned gas have a peak value at around 0.7 for both principal strain rate components, which corresponds to an angle of roughly $45°$ and is caused by the flow structures originated from the friction at the annular gap walls and in the shear layers. In the preheat, reaction and burnout zones, the flame induced extensive strain reduces the alignment with the most compressive strain rate eigenvector, in agreement with previous findings [e.g. 29, 71]. At the unburned side of the flame, the predominant alignment is again with the most compressive strain rate eigenvector, where the peak value has changed to around 0.83, corresponding to a shift by the approximate opening angle of the mean flame brush of $10°$ illustrated in Fig. 6.19.

For the far region, the alignment is predominantly with the most compressive strain rate eigenvector in the unburned gas, due to the stronger flame wrinkling and the large contribution of turbulence induced strain, which has been reported before for both non-premixed and premixed combustion [e.g. 29, 148, 175, 189, 191]. As in the near region, the alignment with the

This chapter was previously published [161] and is reprinted with permission of the journal.

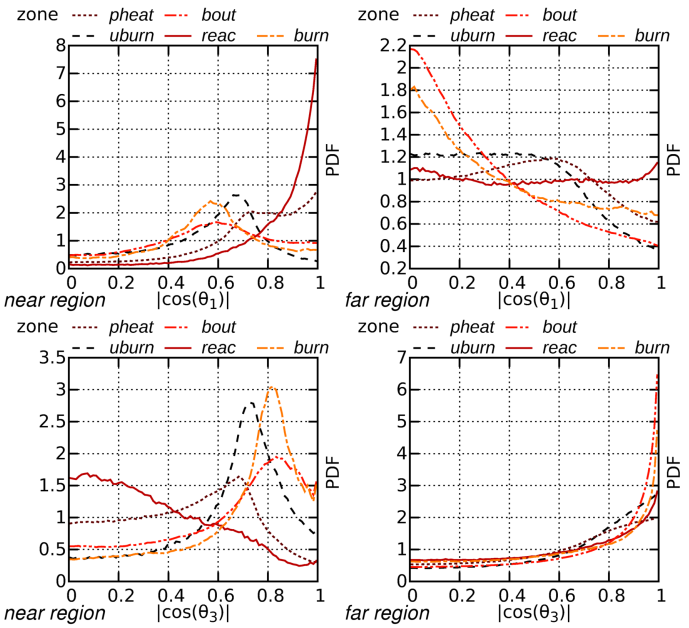

Figure 6.18.: Conditioned PDFs of the alignment angle between the eigenvectors belonging to the most extensive (Θ_1, top) and the most compressive (Θ_3, bottom) principal strain rate and the flame normal vector. *The different plots show the conditioning on the height above the burner, whereas the different lines represent the conditioning on the progress of the reaction (see Section 6.5).* [161]

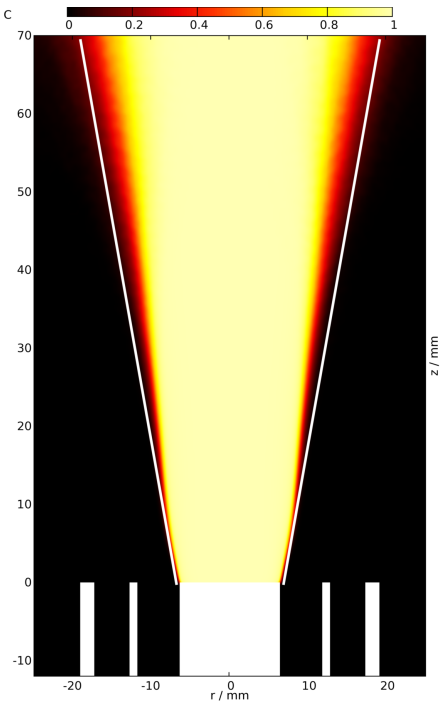

Figure 6.19.: Time-averaged dimensionless progress variable contours in the burner mid section, the approximate mean flame brush angle of 10° against the vertical direction is marked by white lines. [161]

This chapter was previously published [161] and is reprinted with permission of the journal.

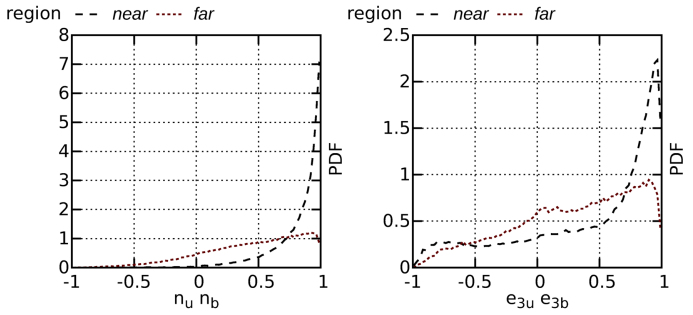

Figure 6.20.: Conditioned PDFs of the aligment between the unburned and burned side of the flamelets. The left plot shows the respective alignment for the flame normal vector, the right plot for the most compressive strain rate eigenvector. *The different lines represent the conditioning on the height above the burner (see Section 6.5). [161]*

most compressive strain rate eigenvector weakens inside the reaction zone because of the flame induced extensive strain and gets stronger again at the burned side of the flame.

Figure 6.20 shows the conditional PDFs of the dot product of the most compressive principal strain rate eigenvector as well as of the flame normal vector at the unburned and burned side of the extracted flamelets (see Section 6.5). In general, the change in direction is larger for the compressive strain rate eigenvector than for the flame normal vector. Especially in the near region, the compressive strain rate eigenvector alignment PDF has a distinct peak at a value that corresponds to roughly the opening angle of the mean flame brush (approximately 10°, see Fig. 6.19), whereas the most likely flame normal vector alignment is zero degree (corresponding to a value of unity in the plots). In the far region, there is a broader range of alignments also for the flame normal vector, which is however still much narrower than the range for the compressive strain rate eigenvector alignment. These observations indicate that the increased alignment of the flame normal vector with the most compressive strain rate eigenvector at the burned side of the flame compared to the unburned side seems to be mainly due to a change in the strain rate eigenvector direction, whereas the flame normal vector direction stays relatively unaffected throughout the flame.

6.7.6. Mean principal curvature of the progress variable field

The degree of flame surface wrinkling mainly determines the turbulent flame propagation speed for flamelet based combustion models, it can be measured by the mean principal curvature of the progress variable field (‘mean’ refers to the average of the principal curvatures and must not be confused with a temporal mean):

$$\kappa_m = \frac{1}{2}\frac{\partial n_i}{\partial x_i} \tag{6.21}$$

Positive (negative) values of the mean principal curvature connote that the flame front is convex (concave) towards the fresh gas, e.g. if a sphere of products (reactants) is surrounded by reactants (products). The spatial distribution of curvature and its importance for the turbulent flame

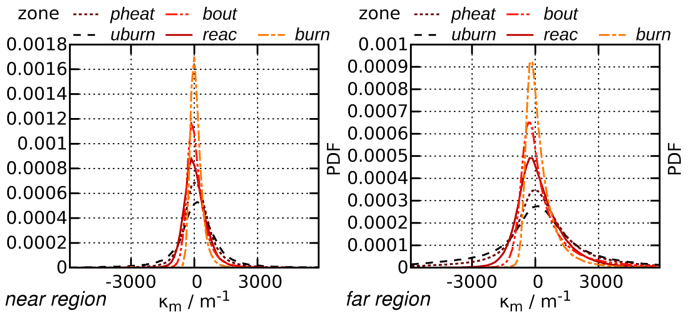

Figure 6.21.: Conditioned PDFs of the mean principal curvature of the flame front (see Eq. 6.21). *The different plots show the conditioning on the height above the burner, whereas the different lines represent the conditioning on the progress of the reaction (see Section 6.5).* [161]

propagation has been discussed in various previous works using DNS database of much simpler configurations [24, 28, 36, 49, 73, 132, 176, 196].

Figure 6.21 presents the PDFs of the mean principal curvature conditioned on the progress of reaction and the height above the burner. The PDFs are significantly broader in the far region in comparison to the near region, this can be explained by the higher turbulent fluctuation level further downstream, which causes stronger flame wrinkling. The PDFs are symmetric with respect to zero and bell-shaped in the fresh gas, which corresponds to the PDF shape of the turbulent velocity fluctuations that is typically Gaussian-like. With increasing progress of reaction, the PDFs get narrower and skewed towards positive values in the flame, the peaks are slightly shifted towards negative values. Similar shapes of the curvature PDFs were previously reported in the literature [24, 28, 36, 49, 176].

The narrowing of the curvature PDFs with increasing progress of reaction can mainly be attributed to the increase of the diffusivity and viscosity inside the flame due to the temperature rise. The increased diffusivity amplifies the diffusive fluxes mainly in strongly curved regions and thereby reduces large absolute values of curvature. The increased viscosity reduces the turbulent velocity fluctuations, which is reflected by the aforementioned reduction of the width and of the peak value of the PDF of the tangential strain rate component with increasing progress of reaction in Fig. 6.16. Figure 6.22 shows the JPDFs of the strain rate tangential to the flame and the mean principal curvature, a weak negative correlation is found, which is most significantly in the reaction zone and has also been observed in previous DNS of canonical flow configurations [1, 23, 24, 26, 200]. An increase (decrease) of tangential strain rate is related to a decrease (increase) of mean principal curvature. Therefore, the observed skewness of the mean principal curvature PDFs towards positive values, which increases with the progress of reaction, can be attributed to the shift of the peak values of the tangential strain rate PDFs in Fig. 6.16 towards smaller values inside the flame. Moreover, the reduction of the width of the tangential strain rate PDFs in the flame further reduces the width of the mean principal curvature PDFs.

This chapter was previously published [161] and is reprinted with permission of the journal.

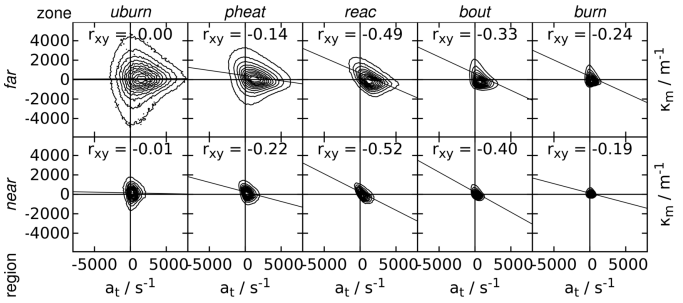

Figure 6.22.: Conditioned joint PDFs of the mean principal curvature of the flame front (see Eq. 6.21) as a function of the strain rate component tangential to the flame (bottom, see Eq. 6.19). *The different plots represent the conditioning on increasing height above the burner from bottom to top and increasing progress of the reaction from left to right (see Section 6.5). The Pearson correlation coefficients* r_{xy} *and linear regression lines are also given.* [161]

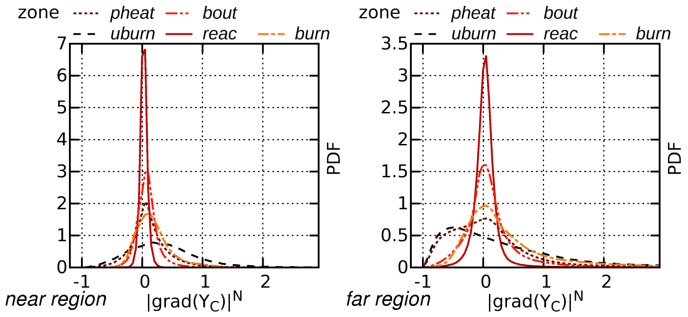

Figure 6.23.: Conditioned PDFs of the difference of the absolute value of the normalized gradient difference of the turbulent and the laminar flame (see Eq. 6.22). *The different plots show the conditioning on the height above the burner, whereas the different lines represent the conditioning on the progress of the reaction (see Section 6.5).* [161]

6.7.7. Gradient of the progress variable field

Besides the already discussed mean principal curvature of the progress variable field, the second quantity with influence on the turbulent flame speed in flamelet based combustion models is the local gradient of the progress variable field, which has been discussed at many occasions before [17, 27, 29, 45, 95, 132, 176]. To judge the deviation of the local gradient of the turbulent progress variable field from the gradient in the respective one-dimensional laminar flame for the local values of the dimensionless progress variable C and the mixture fraction Z, the following normalized difference is used (the dependency on C and Z is omitted for clarity):

$$|\nabla Y_C|^{\mathrm{N}} = \frac{|\nabla Y_C| - |\nabla Y_C|_L}{|\nabla Y_C|_L} \tag{6.22}$$

The normalized gradient difference is zero in a laminar flame, positive (negative) values indicate a thinned (thickened) turbulent flame structure, with respect to the laminar flame. The minimum possible value is -1, which corresponds to an absolute gradient value of zero in the turbulent flame.

Figure 6.23 shows the PDFs of the normalized gradient difference conditioned on the progress of reaction and the height above the burner. In contrast to the observations made for the PDFs

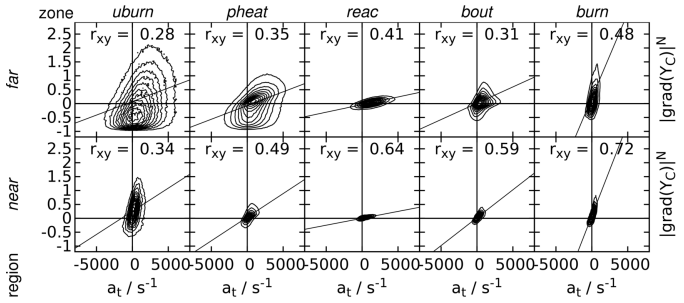

Figure 6.24.: Conditioned joint PDFs of the normalized gradient difference of the turbulent and the laminar flame (see Eq. 6.22) as a function of the strain rate component tangential to the flame (see Eq. 6.19). *The different plots represent the conditioning on increasing height above the burner from bottom to top and increasing progress of the reaction from left to right (see Section 6.5). The Pearson correlation coefficients* $\mathrm{r_{xy}}$ *and linear regression lines are also given.* [161]

of the mean principal curvature in the last section, the width of the PDFs of the normalized gradient difference depends on the local heat release rate rather than on the progress of the reaction, i.e. the PDFs are most narrow in the inner reaction zone and get broader in both the fresh and the burned gas. This indicates that the inner reaction zone, which is most important for the overall flame propagation as most of the heat is released here, has a structure that is close to the laminar flamelet and therefore can be described well by a flamelet-like modeling approach.

Except for the unburned side of the flame in the far region, the peaks of the PDFs are slightly shifted towards positive values which corresponds to a slightly thinner flame structure than the laminar one. The reason for the thinner flame structure can be found in the already discussed positive peak values of the tangential strain rate component PDFs in Fig. 6.16. As shown in Fig. 6.24, the correlation of the normalized gradient difference and the strain rate component tangential to the flame is positive everywhere in the domain, which corresponds to a negative correlation with the flame normal strain rate component that is in line with the classical theory and previous findings [17, 23, 25, 29]. The strength of the correlation increases from the unburned to the burned side of the flame, which implies that the effect of strain on the gradient becomes more significant the less the flame is wrinkled.

The thickening of the flame structure at the unburned side in the far region has also been reported before [17, 23, 25, 29] and can be explained by the already discussed predominant reduction of negative curvature values in the flame, as it can be seen in Fig. 6.21. This tends to reduce the flame propagation speed with increasing progress of reaction, which decreases the gradient of the progress variable as shown by Sankaran et al. [176].

In general, the peaks of the PDFs of the normalized gradient difference $|\nabla Y_C|^{\mathrm{N}}$ in Fig. 6.23 are located close to zero, which means that it is most likely to have the same gradient as in a laminar flame. This implies that the laminar flame structure is the stable solution of Eq. 6.3. This makes sense as the source term and the diffusion coefficient obtained from the PFGM-table are always identical to that in the laminar flame. This means that the main difference between the turbulent and laminar flame is a mean principal curvature unequal to zero. The most likely value for the mean principal curvature is approximately zero, as it can be seen in Fig. 6.21, thus

This chapter was previously published [161] and is reprinted with permission of the journal.

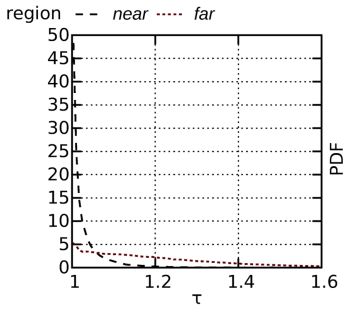

Figure 6.25.: Conditioned PDFs of the tortuosity of the flamelets (see Eq. 6.23). *The different lines represent the conditioning on the height above the burner (see Section 6.5).* [161]

the most likely flame structure should be very close, at least on average, to the laminar one.

To investigate the turbulent flame structure in more detail, the tortuosity τ of the extracted flamelets (see Section 6.5) has been determined:

$$\tau = \frac{L_f}{D_f} \tag{6.23}$$

Here, D_f denotes the shortest distance between the start and end point of the flamelet at $C = 0.01$ and $C = 0.99$, respectively. The distance between the start and end point of the flamelet when moving along the local flame normal direction is given by L_f. Figure 6.25 shows the conditioned PDFs of the tortuosity, a value of unity corresponds to a straight line and a value of infinity would correspond to a circle. The larger the tortuosity is, the more the respective flamelet deviates from a straight line. In the near region, approximately one third of the flamelets are 'perfectly' straight lines, the longest flamelets that are found are less than 20% longer than a straight line (corresponding to $\tau = 1.2$). In the far region, the flamelets are much more wrinkled and deviate more significantly from a straight line, values up to 1.6 are found for the tortuosity. This corresponds to the findings of Poludnenko and Oran [154], who observe that the turbulent flame structure consists of tightly folded flamelets for a canonical flame configuration in the thin reaction zone combustion regime.

6.7.8. Flame displacement speed

The flame displacement speed is the speed at which an isoline would propagate relatively to the flow, it reflects the local flux balance between convective fluxes, diffusive fluxes and reaction source term. It is computed from the following equation based on the non-normalized progress

This chapter was previously published [161] and is reprinted with permission of the journal.

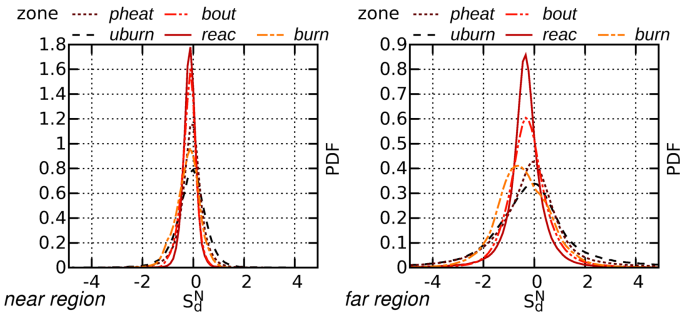

Figure 6.26.: Conditioned PDFs of the normalized deviation of the displacement speed of the flame front from the laminar flame speed (see Eq. 6.25). *The different plots show the conditioning on the height above the burner, whereas the different lines represent the conditioning on the progress of the reaction (see Section 6.5).* [161]

variable Y_C [50, 62, 156]:

$$\begin{aligned} S_d &= \frac{\nabla \cdot (\rho D \nabla Y_\mathrm{C}) + \dot{\omega}_\mathrm{C}}{\rho \left|\nabla Y_\mathrm{C}\right|} \\ &= \frac{\overbrace{\vec{N} \cdot \nabla \left(\rho D \vec{N} \cdot \nabla Y_\mathrm{C}\right)}^{S_n} \overbrace{-2\rho D_\mathrm{C}\, \kappa_m \left|\nabla Y_\mathrm{C}\right|}^{S_t} \overbrace{+\dot{\omega}_\mathrm{C}}^{S_r}}{\rho \left|\nabla Y_\mathrm{C}\right|} \end{aligned} \tag{6.24}$$

The contributions of the flame normal diffusion component, the diffusion due to the mean principal curvature (which is zero in a planar flame) and the chemical source term are denoted by S_n, S_t and S_r, respectively. As the focus in this work is on the comparison with the laminar flame, in the further analysis the normalized deviation of the displacement speed from the laminar flame speed for the local mixture fraction value Z will be analyzed (the dependency on Z is omitted for clarity):

$$S_d^\mathrm{N} = \frac{(\rho/\rho_u)\, S_d - S_L}{S_L} \tag{6.25}$$

In this equation, ρ_u denotes the density in the unburned gas that depends on the mixture fraction Z. The normalized deviation of the displacement speed from the laminar flame speed S_d^N takes a value of zero in a planar laminar flame, below a value of $S_d^\mathrm{N} = -1$ the displacement speed S_d is negative. The dependence of the flame displacement speed on the turbulent flame structure has been studied in numerous previous works [24, 29, 30, 45, 49, 96, 132, 138].

The PDFs of the normalized deviation of the displacement speed from the laminar flame speed conditioned on the progress of reaction and the height above the burner are given in Fig. 6.26. As observed for the PDFs of the normalized gradient difference $\left|\nabla Y_C\right|^\mathrm{N}$ discussed in the last section, the width of the PDFs of the normalized deviation of the displacement speed from the laminar flame speed is also most narrow in the inner reaction zone and gets wider in the fresh and burned gas. The PDFs are less wide in the near region than in the far region, the peak values are slightly shifted towards negative values, most visible in the inner reaction zone, the burnout zone and in the burned gas. Especially in the far region, a certain amount of negative

flame displacement speeds is found, indicated by values of the normalized displacement speed difference smaller than -1, a typical situation where this may occur is at the tip of a flame finger, i.e. at a point with strong positive curvature. This is due to the definition of the displacement speed that is an exact measure only for the movement of strictly parallel iso-surfaces, and has also been observed by others in simulations [28, 29, 67, 132] as well as in experiments [141].

The influence of the mean principal curvature and the normalized gradient difference, which have been discussed in the previous sections, on the normalized displacement speed difference is shown in Fig. 6.27. The mean principal curvature is negatively correlated with the normalized displacement speed difference, most significantly at the unburned side, in the preheat zone and in the reaction zone. The normalized gradient difference is positively correlated with the normalized displacement speed difference at the unburned side and in the preheat zone and negatively correlated at the burned side and in the burnout zone, however, no significant correlation exists in the reaction zone. In the unburned gas, the preheat zone and the reaction zone, the normalized displacement speed difference is most strongly correlated with the mean principal curvature. This reflects in the PDFs of the normalized displacement speed difference in Fig. 6.26, which are symmetric and bell-shaped at the unburned side and in the preheat zone and get narrower in the reaction zone. This observation is in agreement with the shape of the already discussed mean principal curvature PDFs in Fig. 6.21. In contrast, the normalized displacement speed difference is dominated by the negative correlation with the normalized gradient difference at the burned side and in the burnout zone. Therefore, the PDFs of the normalized displacement speed difference in Fig. 6.26 have long tails towards negative values and the peaks are shifted towards negative values at the burned side and in the burnout zone, which is the inverse behavior as observed for the already discussed normalized gradient difference PDFs in Fig. 6.23.

To investigate the potential influence of the stratification (with the co-flow air) on the normalized displacement speed difference, the mixture fraction gradient normal to the flame was evaluated:

$$(\nabla Z)_n = n_i \frac{\partial Z}{\partial x_i} \tag{6.26}$$

The JPDFs of the normalized displacement speed difference with the mixture fraction gradient, which are presented in Fig. 6.27, show no significant correlation. It should be noted that the mixture fraction gradient is very small in magnitude compared to the progress variable gradient, which takes values up to around 630 m^{-1} in the laminar flame. Therefore, the stratification has no dominating influence on the flame propagation in the investigated case, which very likely will be different for the stratified setups of the burner, which have also been measured [194, 220].

To avoid the aforementioned occurrence of negative displacement speeds due to local changes in the flame thickness, the displacement speed might be averaged over the extracted flamelets (see Section 6.5), as discussed by Poinsot and Veynante [152]. Figure 6.28 presents the PDFs of the normalized deviation of the displacement speed of the flame (Eq. 6.24) averaged over the

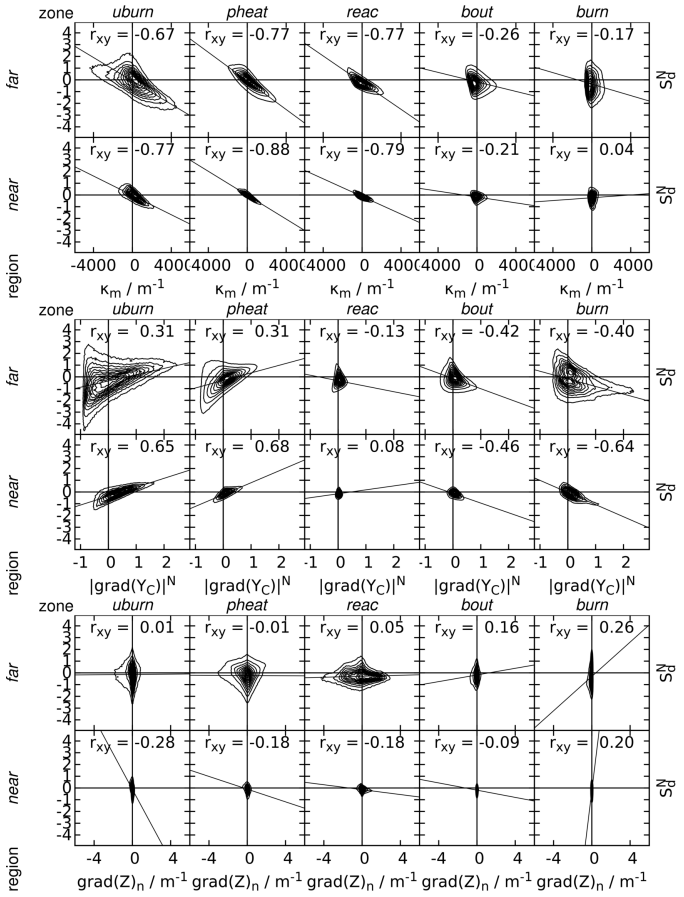

Figure 6.27.: Conditioned joint PDFs of the normalized deviation of the displacement speed of the flame front from the laminar flame speed (see Eq. 6.25) as a function of the mean principal curvature of the flame front (top, see Eq. 6.21), the normalized gradient difference of the turbulent and the laminar flame (middle, see Eq. 6.22) and the mixture fraction gradient normal to the flame (bottom, see Eq. 6.26). *The different plots represent the conditioning on increasing height above the burner from bottom to top and increasing progress of the reaction from left to right (see Section 6.5). The Pearson correlation coefficients* $\mathrm{r_{xy}}$ *and linear regression lines are also given.* [161]

This chapter was previously published [161] and is reprinted with permission of the journal.

flamelets from the laminar flame speed averaged over the flamelets:

$$S_{df}^{N} = \frac{\left\langle \frac{\rho S_d}{\rho_u} \right\rangle_f - \langle S_L \rangle_f}{\langle S_L \rangle_f} \text{ with } \langle S \rangle_f = \frac{1}{L_f} \int_{C=0.01}^{C=0.99} S \, \mathrm{d}n \tag{6.27}$$

The PDFs of the normalized displacement speed difference integrated over the flamelet in Fig. 6.28 are less wide and symmetric than the instantaneous ones in Fig. 6.26. This demonstrates again that many of the observed effects are due to the formulation of the displacement speed. However, the PDFs are still relatively broad and a small amount of slightly negative values of the displacement speed (corresponding to normalized displacement speed difference smaller than -1) still can occur in the far region, implying that the mean principal curvature is strongly positive. This corresponds to flamelets in regions where a burned mixture pocket penetrates deeply into the fresh gas. This is in discordance with the observations of Hilka [152], who found no negative values for the integrated displacement speed in a canonical flame configuration.

The flame speed definition that is most insensitive against curvature effects is the integrated consumption speed over the flamelet, in this work the normalized deviation from the laminar flame speed is considered:

$$S_{c}^{N} = \frac{S_c - \langle S_L \rangle_f}{\langle S_L \rangle_f} \text{ with } S_c = \frac{1}{\rho_u Y_{\mathrm{C},b}} \int_{C=0.01}^{C=0.99} \dot{\omega}_{\mathrm{C}} \, dn \tag{6.28}$$

In this equation, $Y_{\mathrm{C},b}$ denotes the progress variable value at the burned side of the flame that depends on the mixture fraction Z. The PDFs of the normalized consumption speed difference in Fig. 6.28 are much less wide than the ones for the normalized displacement speed difference, no negative values of the consumption speed occur (which would correspond to a normalized consumption speed difference smaller than -1). The absence of negative values follows from the definition of the consumption speed as the integral of reaction source term over the flame, which is always positive. In the far region, the PDF has a long tail towards positive values, which can be attributed to stratification effects, as already observed and discussed for the integrated progress variable source term in C-space shown in Fig. 6.5. Similar shapes of the consumption speed PDFs for a canonical configuration have also been reported by Dunstan et al. [45].

To find out to which extent the normalized displacement speed difference is a measure for the normalized consumption speed difference, the left two plots in Fig. 6.29 present the related JPDFs. It becomes clear that there is basically no correlation at all between the two quantities. When only the sum of displacement speed due to flame normal diffusion and reaction $S_n + S_r$ is considered, as in the right two plots of Fig. 6.29, a significant correlation is achieved for the flamelets in the near region. For the flamelets in the far region there is still a clear correlation, but it is much weaker and gets very broad especially towards higher normalized consumption

This chapter was previously published [161] and is reprinted with permission of the journal.

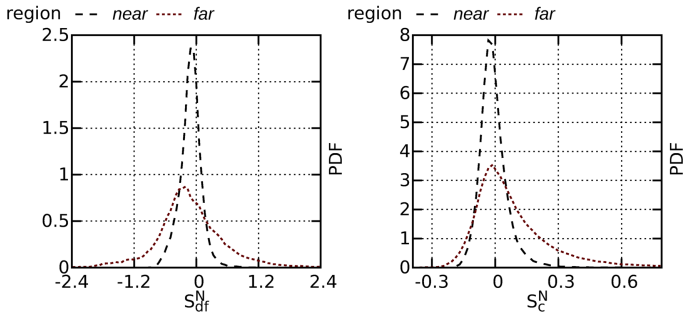

Figure 6.28.: Conditioned PDFs of the flamelet-averaged value of the normalized deviation of the displacement speed of the flame front from the laminar flame speed (left, Eq. 6.27) and the normalized deviation of the flamelet-integrated consumption speed (right, see Eq. 6.28) from the laminar flame speed. *The different lines represent the conditioning on the height above the burner (see Section 6.5). [161]*

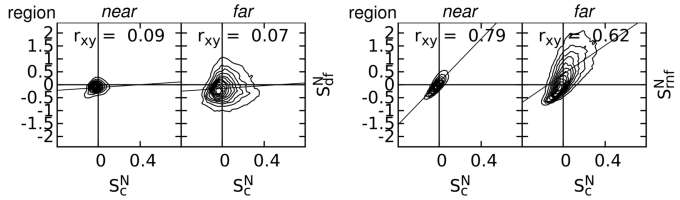

Figure 6.29.: Conditioned joint PDFs of the flamelet-averaged value of the normalized deviation of the displacement speed of the flame front from the laminar flame speed (left two plots, see Eq. 6.25) and the flamelet-averaged value of the normalized deviation of the displacement speed of the flame front only due to flame normal diffusion and reaction $S_n + S_r$ from the laminar flame speed (right two plot) as a function of the normalized deviation of the flamelet-integrated consumption speed (right, see Eq. 6.28) from the laminar flame speed. *The different plots represent the conditioning on increasing height above the burner from left to right (see Section 6.5). The Pearson correlation coefficients* $\mathrm{r_{xy}}$ *and linear regression lines are also given. [161]*

speed difference values. This makes the sum of the flame displacement speed only due to flame normal diffusion and reaction a better, but still not an ideal measure for the flame consumption speed.

6.8. Conclusions

An unsteady simulation of a lab-scale turbulent premixed flame experiment was presented, where the combustion process was modeled with the premixed flamelet generated manifold (PGFM) chemistry tabulation approach. It has been demonstrated that the applied grid resolution of $100\ \mu\mathrm{m}$ was indeed sufficient to resolve the flame without any sub-filter modeling and all velocity scales inside and in the vicinity of the flame region. Only on the unburned side of the flame, a small amount of unresolved velocity scales was present, which were modeled by the σ-model. A good agreement between experiment and simulation was found for mean and rms profiles.

The results were analyzed in detail with ensemble-averaged and flamelet-averaged PDFs, JPDFs and conditional means. It was found that the analysis needs to be carried out separately for the regions near and far from the burner exit, due to the different turbulence levels in the two

This chapter was previously published [161] and is reprinted with permission of the journal.

inlet streams and the additional turbulence produced in the shear layer between the streams. Furthermore, the location of the combustion process in the regime diagram depends on the progress of the reaction, as a large amount of the turbulent fluctuations were dissipated inside the flame.

A skewness towards negative values was found for the PDFs of the flame normal strain rate component, which could be attributed mainly to the mean flow configuration in the near region and mainly to turbulent fluctuations in the far region. The latter was due to a preferential alignment of the most compressive principal strain rate eigenvector with the flame normal direction, which became stronger at the burned side of the flame compared to the unburned side. It was demonstrated that this stronger alignment was mainly caused by a change of the most compressive principal strain rate eigenvector direction. The compressive strain was reduced with increasing progress of reaction.

The distribution of the mean principal curvature was broad and symmetric in the unburned gas, with increasing progress of reaction it became narrower and skewed towards positive values. This skewness could be attributed to the reduction of the compressive strain with increasing progress of reaction.

The magnitude of the progress variable gradient was close to the laminar flame value in the inner reaction zone and varied over a broad range at the unburned and burned side of the flame. The flame structure was slightly thinner than the laminar one except on the unburned side of the flame in the far region, where it was thicker. The thinning could be attributed to the predominantly compressive strain, the thickening to flame speed variations caused by the reduction of mean principal curvature. The deviation of the reaction zones from a straight line was determined by the tortuosity of the extracted turbulent flamelets, it was found that nearly straight flamelets were most likely in the near region, whereas the flamelets were more strongly folded in the far region.

The flame displacement speed showed a relatively broad distribution that was slightly shifted towards smaller values especially in the far region and the burned gas, where also negative values occurred. It was demonstrated that the flame displacement speed was mainly influenced by the mean principal curvature in the fresh gas, the preheat zone and the inner reaction zone. In contrast, in the burnout region and in the burned gas the flame displacement speed was dominated by the gradient of the progress variable field. The flame displacement speed was also averaged over the flamelets, it was demonstrated that it is hardly correlated with the integrated consumption speed over the flamelets. A more significant correlation was found between the consumption speed and the displacement speed due to reaction and flame normal diffusion component.

To the best of our knowledge, this is the first time that such detailed Direct Numerical Simulation (DNS) analysis was performed for a flame resolved simulation dataset, which has been extensively validated against experimental measurements. Overall, the present paper confirms many findings from DNS of simpler configurations and thereby demonstrates that these findings

This chapter was previously published [161] and is reprinted with permission of the journal.

can be translated to real turbulent flames, for which experimental validation data is available.

The flame resolved simulation database used in this paper is available to other researchers, respective queries can be addressed to the Chair of Fluid Dynamics of the University of Duisburg-Essen [85].

6.9. Acknowledgements

The authors gratefully acknowledge the funding from the state of North Rhine-Westphalia and the compute time granted on JUQUEEN at Jülich Supercomputing Centre (JSC), through the John von Neumann Institute for Computing (NIC). We also would like to thank Vincent Moureau and Martin Rieth for valuable discussions.

This chapter was previously published [161] and is reprinted with permission of the journal.

7. Flame resolved simulation of a turbulent premixed bluff-body burner experiment. Part II: A-priori and a-posteriori investigation of sub-grid scale wrinkling closures in the context of artificially thickened flame modeling [162]

Authors: F. Proch, P. Domingo, L. Vervisch, A.M. Kempf
This chapter including all figures and tables was previously published in 'Combustion and Flame, F. Proch, P. Domingo, L. Vervisch and A. M. Kempf, Flame resolved simulation of a turbulent premixed bluff-body burner experiment. Part II: A-priori and a-posteriori investigation of sub-grid scale wrinkling closures in the context of artificially thickened flame modeling, http://dx.doi.org/10.1016/j.combustflame.2017.02.012, Copyright © Elsevier (2017)' and is reprinted with permission from Elsevier. The author F. Proch developed the codes for the CFD simulations and the post-processing as well as the combustion model, ran all the simulations, wrote the paper and generated all figures and tables. The authors P. Domingo, L. Vervisch and A.M. Kempf contributed corrections, discussions and proof-reading.

7.1. Abstract

Dynamic sub-filter closures for artificially thickened flame (ATF) combustion models for large eddy simulation (LES) are investigated with consistent *a-priori* and *a-posteriori* analyses. The analyses are based on a flame resolved simulation (quasi DNS) and large eddy simulations of the bluff body burner experiment by Hochgreb and Barlow with premixed flamelet generated manifolds (PFGM). Both flame resolved simulation and LES are performed under the conditions of a single real flame experiment, using the same domain size, filter sizes, boundary conditions and

numerics, all with an additional validation by comparison to experimental data. For the evaluation of the sub-filter wrinkling factor, the well-established model by Charlette et al. (2002) in the modified version by Wang et al. (2011) is used with a static and with a dynamic model parameter, a new dynamic power-law model is discussed additionally. In the *a-priori* analysis, the probability density functions (PDFs) of the sub-grid scale (SGS) wrinkling factor are compared against the modeled ones based on the flame resolved simulation data. These *a-priori* modeled wrinkling factor PDFs are then compared against the *a-posteriori* ones from the LES results, where a similar shape is observed for all models. The static model tends to over-predict the wrinkling factor, a better agreement is found for the dynamic models for the medium and small filter width, where the new formulation improves the results for the latter. For the largest filter width, the wrinkling factor is under-predicted by the dynamic models. This under-prediction is, however, compensated by larger gradients of the progress variable field so that the mean flame surface density conditioned on the progress variable is in closer agreement with the flame resolved simulation than the wrinkling factor PDFs are. Finally, radial profiles of the time-averaged temperature from the LES, flame resolved simulation and experiment are compared against each other. With the dynamic SGS wrinkling models, the LES results converge with grid refinement against the flame resolved simulation results.

7.2. Introduction

Premixed flames are too thin to be resolved on cell sizes that are affordable in Reynolds-averaged Navier-Stokes (RANS) simulations or large eddy simulations (LES) of technical combustors. One possible alternative is to artificially thicken the flame (ATF) [13, 20, 31, 37, 60]. Although the ATF (or thickened flame LES, TFLES) approach preserves the self-induced propagation speed of the local interface between fresh and burnt gases, the response of the thickened reaction zone to turbulence differs from the original one. Therefore, additional modeling of the sub-grid scale wrinkling is required.

Among the models for sub-filter flame wrinkling, the one developed by Charlette et al. [31] has been frequently used with ATF with good success. This closure involves an exponent β that is related to the fractal dimension D of the flame surface by $\beta = D - 2$ and may either be set to a fixed value (typically $\beta = 0.5$), or alternatively be determined from a dynamic procedure. The performance and validity of the dynamic procedure has been assessed before *a-priori* based on DNS results [32, 105, 205, 206] and *a-posteriori* based on LES results [32, 105, 120, 180, 205, 211]. In these investigations, the dynamic procedure was applied in a formulation averaged for small volumes, over a homogeneous direction, or over the whole domain. The resulting β value was found to vary in space and time, generally β grew with the distance from the burner exit and with decreasing mesh resolution.

In most studies of SGS wrinkling modeling, DNS and LES were not performed under the same flow conditions (for obvious resolution requirements), making it hard to draw definitive

This chapter was previously published [162] and is reprinted with permission of the journal.

conclusions, for example about the role of compensating errors. The present work aims to further investigate the dynamic sub-filter modeling for thickened and filtered flame combustion models, with a consistent *a-priori* (flame resolved simulation, quasi a DNS) and *a-posteriori* (LES) analysis. Flame resolved simulation and LES are performed under the conditions of a single real flame experiment, using the same domain size, filter sizes, boundary conditions and numerics, all with an additional validation by comparison to experimental data [51, 80, 81, 194, 195, 220]. The first model that is investigated is the one by Charlette et al. [31] in the modified version by Wang et al. [211] with either a constant, or a dynamic model parameter [32, 205]. A new dynamic power-law model is then presented, where the lower cutoff depends on the sub-filter turbulence intensity and on the laminar flame speed.

The investigations are carried out for a premixed bluff body burner [194], for which a database from a flame resolved simulation is available [161]. In this flame resolved simulation, the progress variable and velocity fields were fully resolved inside the relevant flame region in a DNS-sense, although a small amount of unresolved velocity fluctuations is still present in the unburnt gas, away from the reaction zones. This database is used for the *a-priori* analysis, LES of the same burner are also reported to further assess the modeling.

7.3. Modeling approach

7.3.1. Combustion model

The focus of this work is on the investigation of sub-filter modeling for a real methane-air flame experiment over a wide range of filter widths, detailed chemistry tabulation was chosen to make the study computationally affordable: The premixed flamelet generated manifolds (PFGM) approach [204] has demonstrated its efficiency and suitability in previous work [e.g. 91, 101, 102, 158, 159, 171] already. Transport equations were solved in the flame resolved simulation and LES for the (non-normalized) progress variable $Y_C = Y_{\mathrm{CO_2}} + Y_{\mathrm{CO}} + Y_{\mathrm{H_2O}}$ based on product mass fractions and for the mixture fraction Z. The mixture fraction is linked to the fresh gas equivalence ratio by $\phi = [Z\,(1 - Z_s)] \,/\, [Z_s\,(1 - Z)]$ with the stoichiometric methane-air mixture fraction $Z_s = 0.054$.

Freely-propagating methane-air flames for varying initial compositions were computed with 'Cantera' [64] using the GRI-3.0 mechanism [188]. A Lewis number of unity was assumed for all species, which has only a negligible influence on the propagation speed of the flame for the lean equivalence ratios present in the studied burner [152].

The results were stored in a two-dimensional equidistant lookup table as a function of the mixture fraction Z and the normalized progress variable $C = Y_C / Y_C^b(Z)$, where the superscript b denotes the fully burnt state. Below the lean flammability limit of $\phi = 0.45$, a linear interpolation was used for the species mass fraction and the enthalpy. More details on the chemistry model are available from previous papers [158, 159, 161].

This chapter was previously published [162] and is reprinted with permission of the journal.

7.3.2. ATF model

To make the premixed flame resolvable on the LES grid, the artificial thickened flame (ATF) model [20, 31, 37] was applied. The broadening of the reaction zone is achieved by increasing the diffusivity by a thickening factor F_D and by decreasing the source term by the same factor in the Favre-filtered transport equation for the progress variable [107, 152]:

$$\begin{aligned} &\frac{\partial \bar{\rho}\tilde{Y}_C}{\partial t} + \nabla \cdot \left(\bar{\rho}\vec{\tilde{u}}\tilde{Y}_C\right) = \\ &\nabla \cdot \left(\left[F_D\, \Xi_\Delta\, \frac{\lambda}{c_p} + (1-\Omega)\, \frac{\mu_t}{\mathrm{Sc}_t}\right] \nabla \tilde{Y}_C\right) + \frac{\Xi_\Delta}{F_D}\dot{\omega}_C \end{aligned} \tag{7.1}$$

Favre-filtering of a quantity ϕ is denoted by $\tilde{\phi}$ and Reynolds-filtering by $\bar{\phi}$, the Favre-filtered velocity vector is represented by $\vec{\tilde{u}}$. The fluid density ρ, the thermal conductivity λ, the heat capacity c_p and the progress variable source term $\dot{\omega}_C$ are obtained from the PFGM table. Outside of the reaction zone, the effect of the unresolved velocity scales is modeled by an eddy diffusivity approach, which is blended in gradually with the flame sensor Ω [91, 102, 158]. We studied the effect of this additional (turbulent diffusivity) term on the turbulent flame propagation and found it to be very small. The turbulent viscosity μ_t is computed according to the σ-model by Nicoud et al. [131], with a modeling constant of $C_\sigma = 1.5$ and the turbulent Schmidt number set to $\mathrm{Sc}_t = 0.7$. The σ-model is retained even for the flame resolved simulation, but the turbulent viscosity is less than 10% of the laminar viscosity throughout the flame [161] in this case. In this context, the interaction between the filtered flame propagation and the modeling of the sub-filter scalar fluxes has been investigated in detail by Klein et al. [97, 98].

The thickening factor F_D is computed as a function of the normalized progress variable to avoid unnecessary thickening of the preheat- and burnout zones [107]:

$$F_D(C^*, Z) = \frac{(\mathrm{d}C/\mathrm{d}x)|_{C=C^*}}{(\mathrm{d}\overline{C}/\mathrm{d}x)|_{\overline{C}=C^*}} \tag{7.2}$$

The numerator $(\mathrm{d}C/\mathrm{d}x)|_{C=C^*}$ represents the gradient of the C-profile, taken at $C = C^*$, resulting from the computation of a one-dimensional freely propagating and unstrained premixed flame for the respective mixture fraction Z. The denominator $(\mathrm{d}\overline{C}/\mathrm{d}x)|_{\overline{C}=C^*}$ is obtained from Gaussian-filtering, at the filter width Δ, of the same C-profile and computing the resulting gradient at $\overline{C} = C^*$. Using the dynamic thickening factor formulation given by Eq. 7.2 in the ATF model exactly reproduces the Gaussian-filtered profile for a one dimensional flame, as shown in Fig. 7.1, and therefore can be expected to yield similar results for the turbulent flame structure as approaches based on filtering of laminar flames [120, 126]. That way, there is no need for an additional model factor to account for the difference between thickening and filtering when the dynamic wrinkling factor procedure is combined with the ATF model, as necessary in the work of Wang et al. [211]. The shape of the dynamic thickening factor and the resulting progress variable profile is compared to formulations used in other works [46, 158], as shown in Fig. 7.1.

This chapter was previously published [162] and is reprinted with permission of the journal.

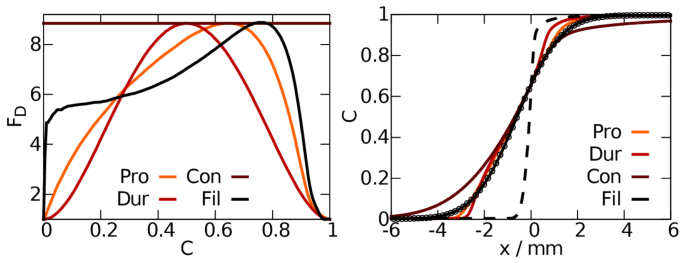

Figure 7.1.: Left: Comparison of the dynamic thickening factor as a function of the progress variable computed from Eq. 7.2 (Fil) to the formulations of Durand and Polifke (Dur [46]), Proch and Kempf (Pro [158]) and a constant thickening factor (Con) for a filter width of Δ = 5.0 mm and an equivalence ratio of $\phi = 0.75$.
Right: Resulting progress variable profiles compared to the original laminar flame profile (dashed line). The Gaussian-filtered laminar flame profile is indicated by black circles, it is identical to the profile resulting from the dynamic thickening factor computed from Eq. 7.2 (Fil). [162]

It can be seen that all dynamic thickening factor formulations avoid the strong broadening of the preheat and (especially) of the burnout zone, which can be observed for the classical ATF model. For the formulation of the dynamic thickening factor given by Eq. 7.2, the maximum of the thickening is shifted towards the burned side of the flame, to take larger values in the preheat zone compared to the alternative formulations [46, 158]. It has been demonstrated [158] that the physics of the flame propagation is well captured by such a dynamic thickening procedure.

For consistency with the dynamic thickening factor from Eq. 7.2, the flame sensor Ω in Eq. 7.1 is computed as the normalized dynamic thickening factor $\Omega = (F_D - 1)/(\max(F_D) - 1)$. The filter width in the LES simulation is set to:

$$\Delta = \max(n\,\Delta_m, \delta_l^0) \tag{7.3}$$

This ensures that the reaction zone is resolved on a minimum of n grid points. The mesh resolution is denoted by Δ_m and a value of $n = 5$ is used in this work. The filter width in Eq. 7.3 is limited to the laminar flame thickness δ_l^0 to avoid a 'thinning' of the flame when it is resolved on the computational grid. The laminar flame thickness δ_l^0 is computed from the maximum gradient of the temperature in the one-dimensional model flame for the respective mixture fraction $\delta_l^0 = (T^b - T^u)/(\max(dT/dx))$.

7.3.3. Sub-filter modeling

The algebraic sub-filter wrinkling factor model by Charlette et al. [31], with a constant model parameter $\beta = 0.5$ (labeled *'Static'*), is used in the version modified by Wang et al. [211] and will be denoted as Charlette/Wang model in the remaining part of the paper:

$$\Xi_\Delta = \left(1 + \min\left[F - 1, \Gamma_\Delta\left(F, \frac{u'_\Delta}{s_l^0}, Re_\Delta\right)\frac{u'_\Delta}{s_l^0}\right]\right)^\beta \tag{7.4}$$

This chapter was previously published [162] and is reprinted with permission of the journal.

The Charlette/Wang model was chosen as it is (probably) the most frequently used sgs model in the ATF context and it is still developing and evolving [102, 120, 158, 205, 206, 211]. Therefore, an extensive investigation of the model by *a-priori* and *a-posteriori* analysis with respect to dynamic model formulations is of high relevance. The Wang et al. [211] formulation in Eq. 7.4 differs from the original formulation by Charlette et al. [31] by the subtraction of unity from the thickening factor, which gives the correct reduction of the wrinkling factor to unity for a thickening factor of unity in combination with non-vanishing sub-filter velocity fluctuations $u_{\Delta}^{'}$. The correct capturing of this limiting behavior was not critical for the original Charlette model, which was designed under the assumption of large thickening factors that is no longer valid for the fine grid resolutions used nowadays [211]. The wrinkling factor predicted by the modified Charlette/Wang model is always lower or equal compared to the wrinkling factor predicted by the original Charlette model. The maximum thickening factor entering the Charlette/Wang model (Eq. 7.4) is computed from:

$$F = \frac{\Delta}{\delta_l^0} \tag{7.5}$$

It must be stressed that the maximum thickening factor F is basically just an abbreviation for the ratio of the upper cutoff (the filter width) and the lower cutoff (the laminar flame thickness) entering the fractal Charlette/Wang model and therefore has a different role than the dynamic thickening factor F_D entering Eq. 7.1, although the maximum value of F_D is usually equal to F. The laminar flame speed is denoted by s_l^0, the sub-filter velocity fluctuations are computed from the expression given by Colin et al. [37]:

$$u_{\Delta}^{'} = 2\Delta_m^3 \left|\nabla^2\left(\nabla\times\vec{\tilde{u}}\right)\right| \left(\frac{n}{10}\right)^{\frac{1}{3}} = 2\Delta_m^3 \left|\nabla\times\left(\nabla^2\vec{\tilde{u}}\right)\right| \left(\frac{n}{10}\right)^{\frac{1}{3}} \tag{7.6}$$

The detailed formulation of the efficiency function Γ_{Δ} that corrects for the unresolved velocity scales is omitted for brevity, it can be found in previous publications [31, 37, 158, 211]. It should however be noted that in the majority of points in the performed LES, the turbulence is so high that Ξ_{Δ} (Eq. 7.4) saturates at its maximum value, which is also the case in most practical applications [120, 205]:

$$\Xi_{\Delta} = \left(\frac{\Delta}{\delta_l^0}\right)^{\beta} = F^{\beta} \tag{7.7}$$

For the second investigated sub-filter model (labeled *'DynRef'*), the parameter β is evaluated from a dynamic procedure, which assumes that β is approximately independent of the filter width. It is also assumed that the same level of flame surface density is obtained by test-filtering the resolved flame surface density in the LES, and by computing the flame surface density of the test-filtered LES progress variable field [205]:

$$\left\langle \Xi_{\Delta}\widehat{|\nabla\overline{C}|}\right\rangle = \left\langle \Xi_{\gamma\Delta}|\nabla\widehat{\overline{C}}|\right\rangle \tag{7.8}$$

Here, $\gamma = \sqrt{\Delta^2+\hat{\Delta}^2}/\Delta$ represents the effective filter width ratio when combining the LES

This chapter was previously published [162] and is reprinted with permission of the journal.

filter Δ and the Gaussian test filter $\hat{\Delta}$, where the filter kernel is given as:

$$G(x,y,z) = \left(\frac{6}{\pi\,\hat{\Delta}^2}\right)^{3/2} \exp\left[-\frac{6}{\hat{\Delta}^2}(x^2+y^2+z^2)\right] \tag{7.9}$$

The test-filter width was set equal to the LES filter width $\hat{\Delta} = \Delta$ in this work, leading to a filter width ratio of $\gamma = \sqrt{2}$. The influence of the filter width ratio on the results was studied and found to be small, therefore a compact test-filter width was chosen to ensure scale similarity. The operator $\langle\cdot\rangle$ denotes spatial averaging, introduced to avoid unphysical local peaks of the dynamic wrinkling factor. In contrast to former works [120, 205], the averaging operation is not replaced by a Gaussian filter. This allows to use a more compact averaging volume, it was found that an averaging volume of 5x5x5 points centered at the respective grid point was sufficient in the LES due to the equal weighting of the averaging points. This more localized formulation of the model potentially improves the applicability to complex flows and geometries that are found in practical combustors. We found no notable influence on the results when using the dynamic version of the full Charlette/Wang model (Eq. 7.4) in the LES on the coarse grid and therefore used the simpler and numerically cheaper power-law formulation (Eq. 7.7) throughout this work, which is in line with former works [120, 205]. The final formulation of the model (*DynRef*) reads:

$$\Xi_\Delta = \left\langle \frac{\Delta}{\delta_l^0} \right\rangle^\beta = \langle F \rangle^\beta \quad \text{with} \quad \beta = \ln\left(\Xi_r\right) \,/\, \ln\left(\gamma\right) \tag{7.10}$$

Here, Ξ_r represents the resolved part of the wrinkling factor:

$$\Xi_r = \left\langle \widehat{|\nabla \overline{C}|} \right\rangle \Big/ \left\langle |\nabla \widehat{\overline{C}}| \right\rangle \approx \left\langle \widehat{|\nabla \widetilde{C}|} \right\rangle \Big/ \left\langle |\nabla \widehat{\widetilde{C}}| \right\rangle \tag{7.11}$$

Veynante and Moureau [205] have recently demonstrated that this model is nearly equivalent to the dynamic similarity model by Knikker et al. [99]. They discussed how the first RHS of Eq. 7.11 can be approximated by the second RHS in the LES, as the Favre-filtered governing equations are solved [205]. They furthermore addressed that this approximation of the filtered progress variable $\overline{C}$ by the Favre-filtered progress variable $\widetilde{C}$ would be fully valid only for an infinitely thin flame front, and how the resulting error is reduced by the additional spatial averaging used in Eq. 7.11. It must however be stressed that the impact of the filtering type on the wrinkling factor field predicted by the dynamic model is smaller than the impact of the filtering type on the progress variable field itself (this may be illustrated for a laminar planar flame, where the wrinkling factor predicted by the dynamic model is unity, independent of the filtering type, although the filtered progress variable field is significantly influenced by the filtering type). In the present work, we quantify the error resulting from the use of the Favre-filtering by performing the *a-priori* analysis in Section 7.5.1 for the filtered as well as for the

This chapter was previously published [162] and is reprinted with permission of the journal.

Favre-filtered progress variable and show that the effect of the filtering type on the predicted wrinkling factor is actually only minimal.

The starting point for the third investigated model (labeled *'DynNew'*) is also the fractal power-law formulation given by Eq. 7.7, which assumes a constant lower cutoff scale equal to the laminar flame thickness δ_l^0. It has been discussed extensively in the literature that the lower cutoff actually depends on the intensity and structure size of the turbulence as well as on the (laminar) flame thickness and propagation speed, various models for the lower cutoff scale with different results have been proposed in the past [33, 65, 69, 137, 205]. This accounts for the effect of turbulent fluctuations on the gradient of the flame, which is likely to become important for higher turbulence intensities and has been reported for the investigated burner [161] and in various previous works [17, 23, 25, 29]. We tried multiple formulations for the lower cutoff and found that replacing the constant lower cutoff by $\delta_l^0(s_l^0/u_\Delta^{'})^a$ improves the model performance in the *a-priori* analysis. To avoid wrinkling factors smaller than unity, the maximum value of the lower cutoff scale is limited to the value of the upper cutoff scale Δ, the final model (*DynNew*) reads:

$$\Xi_\Delta = \left[\frac{\Delta}{\min\left(\langle\delta_l^0\rangle\left\langle\frac{s_l^0}{u_\Delta^{'}}\right\rangle^a, \Delta\right)}\right]^\beta = \max\left[\left(\left\langle\frac{u_\Delta^{'}}{s_l^0}\right\rangle^a\langle F\rangle\right)^\beta, 1\right] \tag{7.12}$$

If the sub-filter velocity fluctuations are equal to the laminar flame speed, Eq. 7.12 reduces to Eq. 7.7. For sub-filter velocity fluctuations lower than the laminar flame speed, Eq. 7.12 predicts a decreased wrinkling factor due to the increase of the lower cutoff scale similar to the full Eq. 7.4. In case of the sub-filter velocity fluctuations being greater than the laminar flame speed, Eq. 7.12 predicts an increased wrinkling factor as a consequence of the decreased lower cutoff scale. The *a-priori* and the *a-posteriori* analyses were carried out for different values of the exponent a to study the sensitivity of the model to it. It was found that the model is not overly sensitive to the value of a, a value of $a = 0.1$ yielded the overall best model performance for all filter-widths *a-priori* and *a-posteriori* and was therefore used for the following investigations. The coefficient β in Eq. 7.12 is computed again from the dynamic procedure given by Eq. 7.8:

$$\beta = \frac{\ln\left(\Xi_r\right)}{\ln\left(\frac{\left(\gamma^{1/3}\left\langle u_\Delta^{'}/s_l^0\right\rangle\right)^a\left(\gamma\langle F\rangle\right)}{\left\langle u_\Delta^{'}/s_l^0\right\rangle^a\langle F\rangle}\right)} = \frac{\ln\left(\Xi_r\right)}{\ln\left(\gamma^{1+a/3}\right)} \tag{7.13}$$

Figure 7.2 shows a comparison of the wrinkling factors resulting from the new model (DynNew) and from the dynamic (DynRef) and static (Static) Charlette/Wang model, versus the maximum thickening factor F and the resolved wrinkling factor Ξ_r. The filter width ratio was set to $\gamma = \sqrt{2}$, the ratio of the sub-filter velocity fluctuations to the laminar flame speed to $u_\Delta^{'}/s_l^0 = 10$, which is a representative value in the downstream region of the burner [161]. The wrinkling factor predicted by all models increases as a function of the thickening factor, with

This chapter was previously published [162] and is reprinted with permission of the journal.

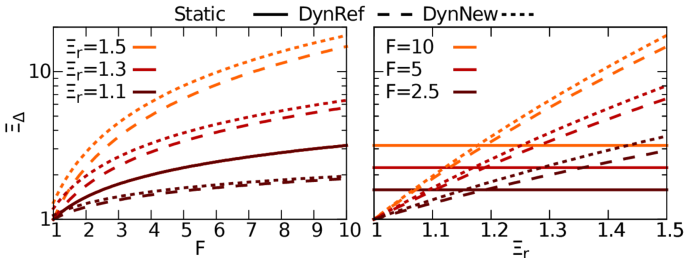

Figure 7.2.: Comparison of the wrinkling factor resulting from the static and dynamic Charlette/Wang models (Static, DynRef) and the new model (DynNew), as a function of the maximum thickening factor F (Eq. 7.5, left) and the resolved wrinkling factor Ξ_r (Eq. 7.11, right). The effective filter width ratio was set to $\gamma = \sqrt{2}$, the ratio of the sub-filter velocity fluctuations to the laminar flame speed to $u'_\Delta / s^0_l = 10$. [162]

a slope that decreases towards larger values of F. For a thickening factor of unity, the static and dynamic version of the Charlette/Wang model predict a wrinkling factor of unity. Due to the aforementioned dependency of the lower cutoff scale on the sub-filter velocity fluctuations, the new model predicts a remaining wrinkling factor of $(u'_\Delta / s^0_l)^{a\,\beta}$ for a thickening factor of unity when the turbulent sub-filter velocity fluctuations are larger than the laminar flame speed. This corresponds to a situation where the local progress variable gradient is increased by the turbulence induced strain, i.e. where the turbulent flame brush is thinner than the laminar flame thickness. The wrinkling factor resulting from the static Charlette/Wang model is independent of the resolved wrinkling factor, whereas the wrinkling factor resulting from both dynamic models (DynRef, DynNew) increases as a function of the resolved wrinkling factor, with a slope that decreases towards larger values of the resolved wrinkling factor. The new model predicts slightly larger wrinkling factors than the dynamic Charlette/Wang model, most significantly for larger values of the resolved wrinkling factor and smaller values of the thickening factor. For a resolved wrinkling factor of unity in combination with non-vanishing velocity fluctuations, which indicates that the wrinkling is fully resolved on the computational grid but turbulent motion and flame surface are not in equilibrium [205], both dynamic models predict the correct wrinkling factor of unity, whereas the static model predicts a wrinkling factor greater than unity.

7.4. Numerical setup for LES and flame resolved simulation

The investigated burner has been build and examined at the University of Cambridge by Hochgreb and co-workers and was also investigated at the Sandia National Labs by Barlow et al. [51, 80, 81, 194, 195, 220]. It consists of a central bluff-body that is surrounded by two co-annular premixed streams of methane-air with an equivalence ratio of $\phi = 0.75$. These streams are surrounded by a co-flow of air, the burner is operated at 295 K and ambient pressure. The burner is illustrated in Fig. 7.3. The bulk velocities in the inner stream, the outer stream and the co-flow are 8.31, 18.7 and 0.4 m/s, respectively. This results in Reynolds number of approximately

This chapter was previously published [162] and is reprinted with permission of the journal.

5,960 and 11,500 in the inner and outer stream, respectively. The burner was investigated with LES by different groups [16, 120, 126, 127, 158] already and is a target of the TNF workshop [6].

The flame resolved simulation was performed with a grid resolution of 0.1 mm, which is fine enough to resolve the flame with the PFGM-approach without any thickening. However, in the fresh gas in the shear layers upstream of the nozzle exit, this grid resolution is not sufficient to fully resolve the Kolmogorov scale. It was demonstrated in the previous analysis of the flame resolved simulation fields [161] that the influence of these scales stays very moderate and gets negligible in the flame region for which the following investigations are performed.

The simulations were conducted with the 'PsiPhi' code that solves the Navier-Stokes equations in a Low-Mach number formulation and was developed by Kempf and co-workers [87, 158, 159, 161, 170, 171]. The investigated configuration is unbounded and without thermoacoustic interactions with a maximum Mach number of well below 0.1, therefore the low-Mach number formulation can be expected to not influence the results while enabling a much larger computational time step. The code was parallelized using the message passing interface (MPI), where non-blocking communication with overlayed computational work ensures high parallel efficiency. The convective fluxes for momentum and scalars were discretized by a central difference and a total variation diminishing (TVD) scheme with the non-linear CHARM limiter [219], respectively. The TVD scheme ensures the boundedness of the scalar transport while avoiding the excessive smoothing of upwind-schemes. The Poisson-equation for the pressure was solved with a successive over-relaxated Gauss-Seidel solver. At the inlet, pseudo turbulent fluctuations with magnitudes of 10% of the bulk velocities and an integral length-scale of 0.5 mm were imposed by the filtering method introduced by Klein et al. [94] in its numerically efficient implementation [88]. Zero gradient boundary conditions were set at the outlet for all transported quantities. The last 12 mm of the burner geometry were included in the simulation domain with the immersed boundary technique. The computational domain size was $112\times120\times120$ mm, leading to an overall number of 1.6 billion equidistant Cartesian grid cells for the flame resolved simulation. The simulations were performed on up to 64,000 Blue Gene/Q cores on the JUQUEEN machine at the Jülich Supercomputing Centre, 0.34 seconds of physical time were simulated for properly sampled statistics, corresponding to 24 flow-through times of the inner stream, at a total cost of 10 million core hours.

Figure 7.3 shows instantaneous contour plots for the axial and radial velocity component, the temperature and the equivalence ratio in the burner-mid section. It was found in the previous analysis of the flame resolved simulation data [161] that the flame develops two characteristic regions, due to the different levels of turbulence in the inner and outer stream. These regions should be treated separately for a meaningful analysis of the flame dynamics. Therefore, the analysis is carried out separately for the '*near*' and '*far*' region, reaching from 0 to 35 mm and from 35 to 70 mm above the burner, respectively. These two regions are indicated in Fig. 7.3 by dashed lines, where the higher level of flame wrinkling in the far region compared to the near

This chapter was previously published [162] and is reprinted with permission of the journal.

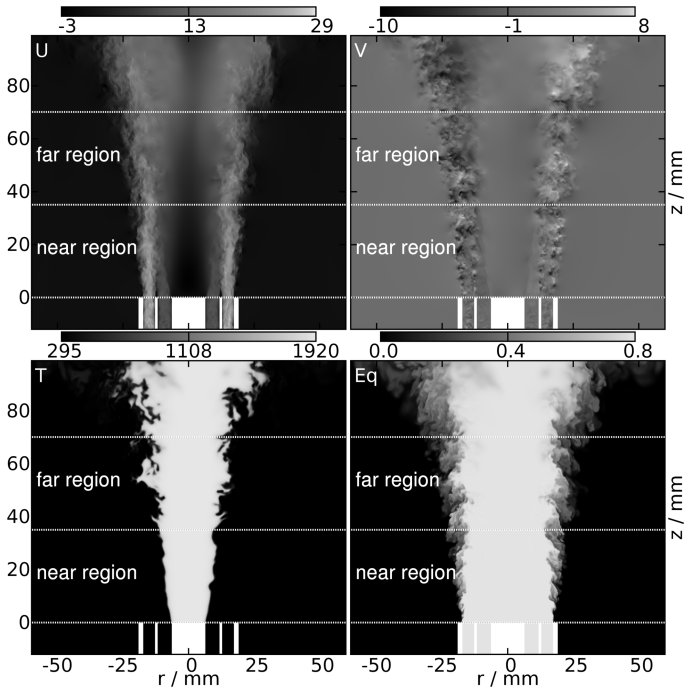

Figure 7.3.: Contour plots in the burner mid-section for the axial velocity component (U), radial velocity component (V), Temperature (T) and equivalence ratio (Eq) from the flame resolved simulation of the investigated burner [161]. The 'near' and 'far' region for the subsequent analysis are separated by dashed lines. [162]

region becomes visible, for instance when inspecting the temperature plot.

For the *a-priori* analysis, the progress variable field from the flame resolved simulation was filtered at the filter-widths Δ and subsequently test-filtered at $\hat{\Delta}$ as given in Table 7.1. To be able to compute the filtering operations with the required large stencils with up to 50^3 cells in a feasible amount of computational time, the Gaussian filter was implemented in a sequential order for the three spatial directions as described by Kempf et al. [88], exploiting the advantages of the applied simple grid structure.

For the *a-posteriori* analysis, LES with the grid resolutions given in Table 7.1 were performed for all three models. The CFD solver, the numerical setup, the boundary conditions and the

Table 7.1.: Parameters of the simulations: LES cell size Δ_m, ATF filter width Δ, test-filter width $\hat{\Delta}$, effective filter width ratio γ, averaging-box width $\langle\Delta\rangle$, maximum thickening factor F and number of computational cells n_{Cells} used in the *a-priori* and *a-posteriori* analyses. The laminar flame thickness for the thickening factor calculation was set to δ_L = 0.565 mm corresponding to the inlet equivalence ratio of $\phi = 0.75$. For the finest grid (F), the filter width for the *a-priori* analysis (given in brackets) had to be set to a multiple of the flame resolved simulation mesh resolution of 0.1 mm and therefore slightly deviates from the *a-posteriori* width. [162]

	Δ_m mm	Δ mm	$\hat{\Delta}$ mm	γ	$\langle\Delta\rangle$ mm	F	n_{Cells} M
Coarse (C)	1.0	5.0	5.0	$\sqrt{2}$	5.0	8.8	1.7
Medium (M)	0.5	2.5	2.5	$\sqrt{2}$	2.5	4.4	13.8
Fine (F)	0.25	1.25 (1.2)	1.25 (1.2)	$\sqrt{2}$	1.25 (1.2)	2.2 (2.1)	106.0
Flame resolved sim. (RES)	0.1	-	-	-	-	-	1612.8

This chapter was previously published [162] and is reprinted with permission of the journal.

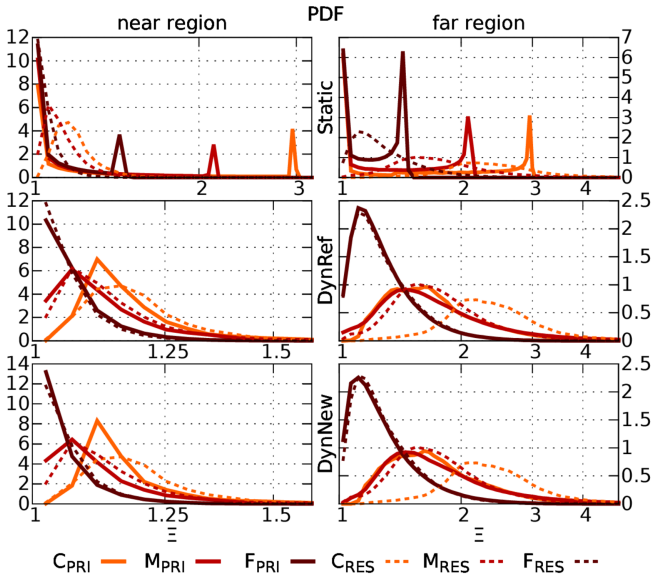

Figure 7.4.: *A-priori* PDFs of the modeled wrinkling factors (solid lines) and the exact wrinkling factor (dashed lines) for the filter widths given in Table 7.1. The analysis is carried out separately for the near and far region of the burner (see Section 7.4) (x-axis is scaled individually). [162]

FGM model were the same as for the flame resolved simulation. The only difference between LES and flame resolved simulation was the use of the ATF model combined with the respective sub-filter model. The dynamic procedure applied at every computational point for every time step increased the computational costs of the LES by around 30%.

7.5. Results

7.5.1. *A-priori* analysis of the wrinkling factor PDFs

The progress variable field C from the flame resolved simulation and the absolute value of its gradient $|\nabla C|$ were filtered at the respective filter width Δ. The reference wrinkling factor value from the flame resolved simulation was then computed from $\Xi_\Delta^{RES} = \left\langle \overline{|\nabla C|} \right\rangle \Big/ \langle |\nabla \overline{C}| \rangle$. Here, the averaging was done over the same volume as in the LES, which corresponds to 12^3, 25^3 and 50^3 averaging points for the fine, medium and large filter width, respectively.

The resulting filtered progress variable field $\overline{C}$ and the absolute value of its gradient $|\nabla \overline{C}|$ were filtered again at the test-filter width $\hat{\Delta}$. Afterwards, the investigated models were used to compute the wrinkling factors as a function of the resolved wrinkling factor, which is calculated from $\Xi_r = \left\langle \widehat{|\nabla \overline{C}|} \right\rangle \Big/ \left\langle |\nabla \widehat{\overline{C}}| \right\rangle$, the maximum thickening factor F and the effective filter width ratio γ together with the mixture fraction and velocity field from the flame resolved simulation. The sub-filter velocity fluctuations were computed based on the flame resolved simulation velocity field with Eq. 7.6. As mentioned before, the same procedure was repeated for Favre-filtering by replacing $\bar{C}$ with $\tilde{C}$.

Figure 7.4 shows the probability density functions (PDFs) of the *a-priori* modeled wrinkling

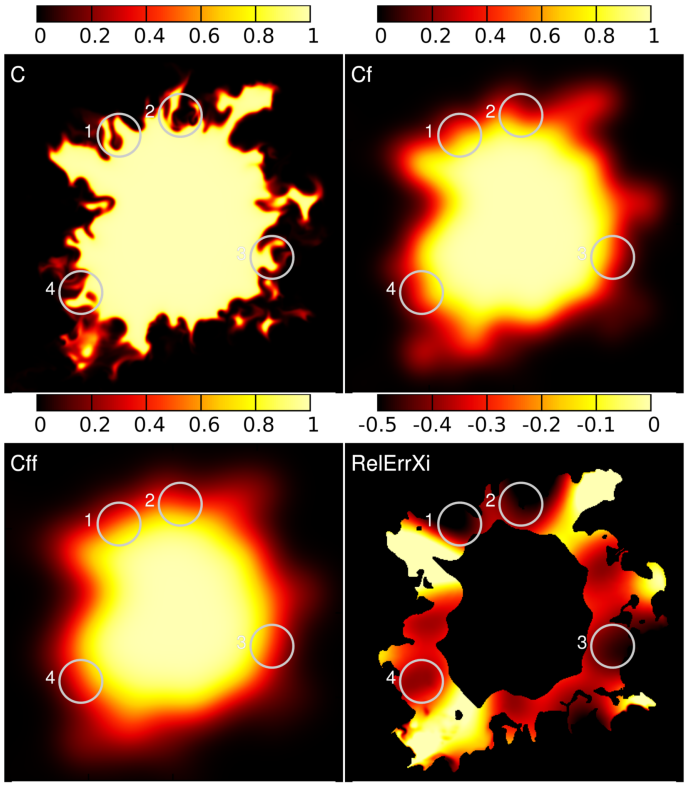

Figure 7.5.: Illustration of the underestimation of the wrinkling factor by the dynamic models for the largest filter width in a cross-section 50 mm downstream of the burner exit. Shown are the unfiltered progress variable C (top left), the filtered progress variable (Cf, top right), the subsequently test-filtered progress variable (Cff, bottom left) and the relative deviation of the wrinkling factor resulting from the dynamic Charlette/Wang model from the exact wrinkling factor (RelErrXi, bottom right). The circle diameter corresponds to the filter width of 5 mm, the location of the circles 1-4 is the same in all plots. [162]

factors compared to the exact wrinkling factors from the flame resolved simulation, where separate PDFs were computed for the weakly turbulent near burner region and the more turbulent region far from it. All computational points inside the flame region, *i.e.* $0.01 < \overline{C} < 0.99$, were taken into account, with the exception of points where the thickening factor, or the exact wrinkling factor, was smaller than 1.001. This additional constraint was included to avoid a bias of the PDFs towards unity, which indicates a resolved flame, and affected less than 5% of the points in the flame region. The total number of points used for the generation of the individual PDFs was more than 5 Million. With growing filter width, the PDFs of the exact wrinkling factor get broader and the peak values get shifted towards higher wrinkling factor values, as expected. The PDFs are much broader in the far region than in the near region, due to the higher level of turbulence in the far region which comes along with additional flame wrinkling. The static model (Static) shows nearly bimodal PDFs, where the first peak is located at a wrinkling factor of unity and the second one at the maximum wrinkling factor value from Eq. 7.7. The peak at unity can be explained by an efficiency function Γ_Δ value of zero, due to zero sub-filter velocity fluctuations.

The two dynamic models (DynRef and DynNew) are both able to capture the principal shape of the wrinkling factor PDF for the smallest and the intermediate filter width. However, for

This chapter was previously published [162] and is reprinted with permission of the journal.

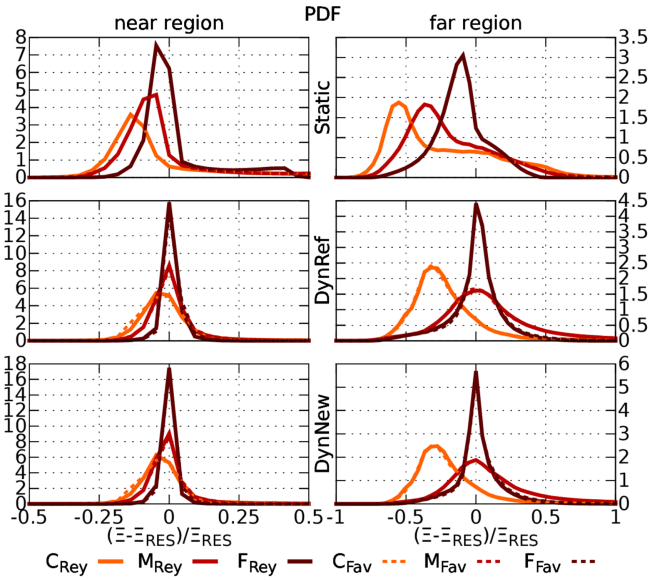

Figure 7.6.: *A-priori* PDFs of the normalized deviation of the modeled (DynNew, DynRef, Static) from the exact (REF) wrinkling factor. The analysis is carried out separately for the near and far region of the burner (see Section 7.4). The solid lines result from Reynolds-filtering, the dashed lines from Favre-filtering. [162]

the largest filter width notable differences exist between the PDFs of the modeled and the exact wrinkling factor, in general the dynamic models under-predict the wrinkling factor. This is mostly visible in the far region, where the peaks of the modeled wrinkling factor PDFs are located at significantly smaller values than the peaks of the exact wrinkling factor PDFs. A potential explanation of this under-prediction of the wrinkling factor is that finger-like structures vanish during the first filtering operation. In the subsequent test-filtering operation, these regions appear as closed and smooth, thus only very little or no wrinkling is predicted there by the dynamic models. This behavior is illustrated in Fig. 7.5, which shows cross sections of the original progress variable field and of the resulting progress variable fields after the first and second filtering operation with the largest filter width. Furthermore, Fig. 7.5 includes the relative deviation of the wrinkling factor resulting from the dynamic Charlette/Wang model from the exact wrinkling factor in the respective cross section. Four regions with a large under-prediction of the wrinkling factor are marked by circles, in all of these regions the originally strongly wrinkled flame structure is vastly smoothened during the first filtering operation, so that the effect of the second filtering operation is only minute. A further explanation is that the scale similarity, which is the underlying assumption for the dynamic models, is no longer sufficiently fulfilled at the largest filter width. The modeled wrinkling factor PDFs for the largest filter width are indeed relatively similar to the ones for the intermediate filter width. This suggests that an 'upper cutoff' has been reached, above which additional test-filtering yields not enough information to reconstruct the flame wrinkling with high accuracy.

To enable a detailed local comparison of the investigated wrinkling factor models, Fig. 7.6 shows the PDFs of the normalized deviation of the modeled wrinkling factors from the exact

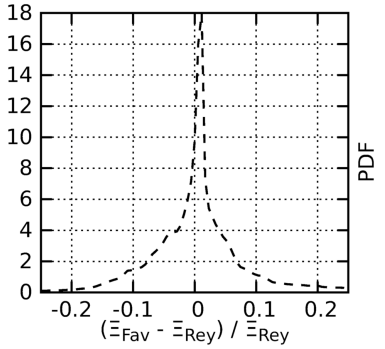

Figure 7.7.: *A-priori* PDF of the normalized deviation of the wrinkling factor resulting from the Favre-filtered progress variable from the wrinkling factor resulting from the Reynolds-filtered progress variable for the dynamic Charlette/Wang model on the largest filter width. [162]

one (DNS). In general, the PDFs get broader with an increase of the filter width and growing distance from the burner.

The static Charlette/Wang model gives broad PDFs of the deviation with heavy tails on the right, meaning an over-prediction of the wrinkling factor by the model. The peaks, however, are located at negative deviations. The PDFs of both dynamic models (DynRef and DynNew) have peaks at approximately zero, except for the largest filter width. This implies that in most of the points, the correct wrinkling factor is obtained by the dynamic models. For the intermediate and smallest filter width, the PDFs of the dynamic Charlette/Wang model are skewed towards positive deviations, indicating a slight overestimation of the wrinkling factor by the model. For the smallest filter width, the new models results in more narrow and symmetric PDFs than the dynamic Charlette/Wang model, demonstrating that the new model has the potential to improve the results. We however note that the improvements are very moderate, which implies that the assumption of a constant lower cutoff scale equal the laminar flame thickness is admissible for the investigated case.

The normalized deviation PDFs in Fig. 7.6 are only very weakly affected by the type of filtering (Reynolds or Favre) that is used. To investigate the effect of filtering on the wrinkling factor further, Fig. 7.7 shows the PDF of the normalized deviation of the wrinkling factor for the Favre-filtered progress variable from the wrinkling factor for the Reynolds-filtered progress variable for the dynamic Charlette/Wang model on the largest filter width. For more than 60% of the flame points the deviation is below 5%, only in less than 15% of the points the deviation exceeds 10%. This demonstrates that the use of Favre-filtering instead of Reynolds-filtering introduces only a minor error in the wrinkling factor prediction that is smaller the model uncertainty.

7.5.2. *A-posteriori* analysis of the wrinkling factor PDFs

The analysis presented in the previous section was then applied to the LES results. All computational points in the flame region with a thickening factor larger than 1.001 were taken into

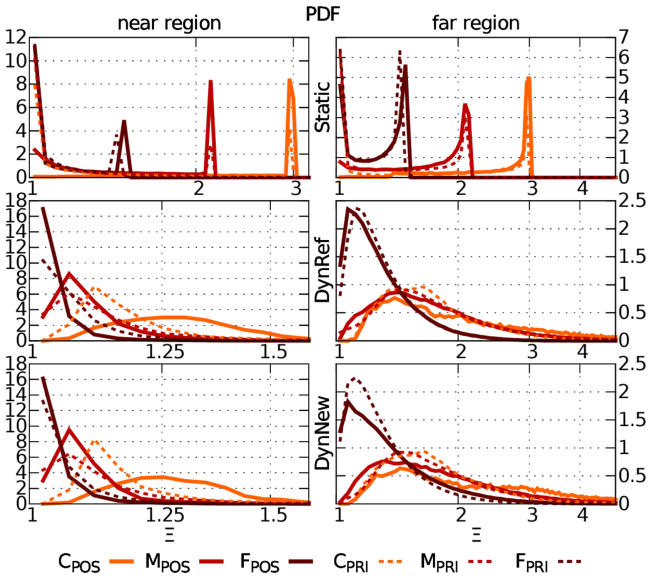

Figure 7.8.: *A-posteriori* PDFs of the wrinkling factor for the different models for the filter widths given in Table 7.1. The analysis is carried out separately for the near and far region of the burner (see Section 7.4). The solid lines give the *a-posteriori* results from the LES, the dashed lines show again the *a-priori* results from Fig. 7.4 (x-axis is scaled individually). [162]

account. The resulting PDFs are shown in Fig. 7.8. To simplify the comparison, the *a-priori* results (PRI) from Fig. 7.4 are displayed again in Fig. 7.8. In general, the *a-posteriori* wrinkling factor PDFs are similar to the *a-priori* ones, which means that the *a-priori* analysis based on flame resolved simulation data yields results that are comparable to the results from *a-posteriori* analysis based on LES data, demonstrating that the findings from flame resolved simulation analysis are relevant in the actual LES. The aforementioned under-prediction of the wrinkling factor by the dynamic models for the largest filter-size occurs in a comparable manner in the *a-posteriori* analysis and in the *a-priori* analysis, which implies that the dynamic models need a sufficient range of scales left in the progress variable field to reconstruct the wrinkling factor with high accuracy.

For the static model (Static), differences between the *a-posteriori* and *a-priori* PDFs occur mainly in the magnitude of the peaks at unity, which get smaller with increasing filter width and vanish for the largest filter width in the *a-posteriori* PDFs. This can be explained by the increased level of sub-filter velocity fluctuations in the LES, whereas the flame resolved simulation velocity field was used in Eq. 7.6 for all filter widths in the *a-priori* analysis. The slight shift of the right peak of the PDFs for the smallest filter width corresponds to the small difference between *a-priori* and *a-posteriori* filter-widths given in Table 7.1.

The dynamic models (DynRef and DynNew) show a comparable agreement between the *a-priori* and *a-posteriori* PDFs. The most notable differences between the wrinkling factor PDFs of the dynamic models occurs for the smallest filter width, where the thickening factor is small and thus the difference between the models is most significant, as demonstrated in Fig. 7.2. In the near region for the smallest filter width, the new model gives a better agreement between

This chapter was previously published [162] and is reprinted with permission of the journal.

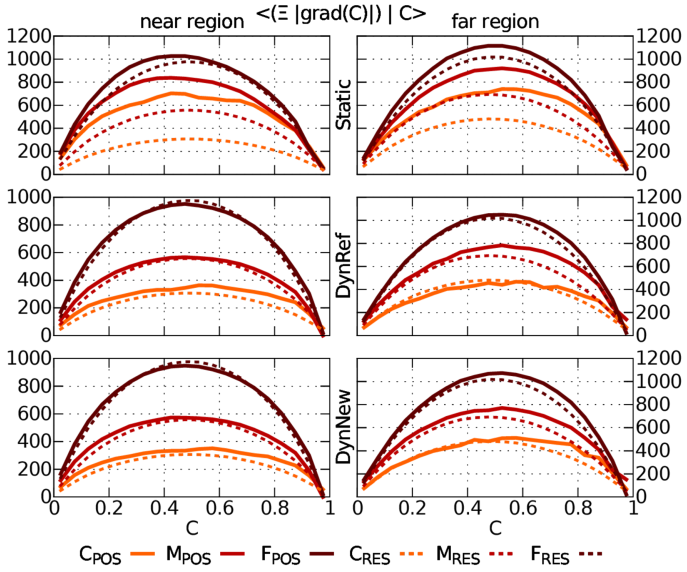

Figure 7.9.: Comparison of the mean values of the flame surface density conditioned on the progress variable from the LES (solid lines) and the flame resolved simulation (RES, dashed lines) for the different models for the filter widths given in Table 7.1. The analysis is carried out separately for the near and far region of the burner (see Section 7.4). [162]

the *a-priori* and *a-posteriori* PDFs than the dynamic Charlette/Wang model. In contrast, in the far region and for the smallest filter width, the dynamic Charlette/Wang model gives a better agreement between the *a-priori* and *a-posteriori* PDFs than the new model. The reason for this may be due to the additional dependency of the new model on the sub-filter velocity fluctuations, which are resolved differently on the LES grid compared to the flame resolved simulation grid.

To investigate how the deviations observed in the wrinkling factor PDFs actually reflect in the flame propagation, Fig. 7.9 presents the comparison of the mean values, conditioned on the progress variable, of the modeled flame surface density from the LES, $\Xi_\Delta|\nabla\tilde{C}|$, and the exact flame surface density from the flame resolved simulation, $\overline{|\nabla C|}$. As the absolute value of the progress variable gradient depends on the equivalence ratio, only flame points with the inlet equivalence ratio of 0.75 were used to make the plots comparable. For the static Charlette/Wang model (Static), the over-prediction of the wrinkling factor in the LES observed in Fig. 7.8 causes a significant over-prediction of the conditional mean of the flame surface density in the LES, most significantly for the largest and intermediate filter width. For the smallest filter width, the over-prediction of the conditional mean of the flame surface density in the LES gets less significant but is still visible.

For the dynamic models (DynRef and DynNew), however, the significant under-prediction of the wrinkling factor in the LES observed in Fig. 7.8 does not result in a comparable under-prediction of the flame surface density in the LES. This might imply that an under-prediction of the wrinkling factor comes along with an over-prediction of the progress variable gradient, which would represent a self-adjusting mechanism as suggested by Veynante and Moureau [205]. However, it will be mandatory to check in the future whether this really is a self-adjusting

This chapter was previously published [162] and is reprinted with permission of the journal.

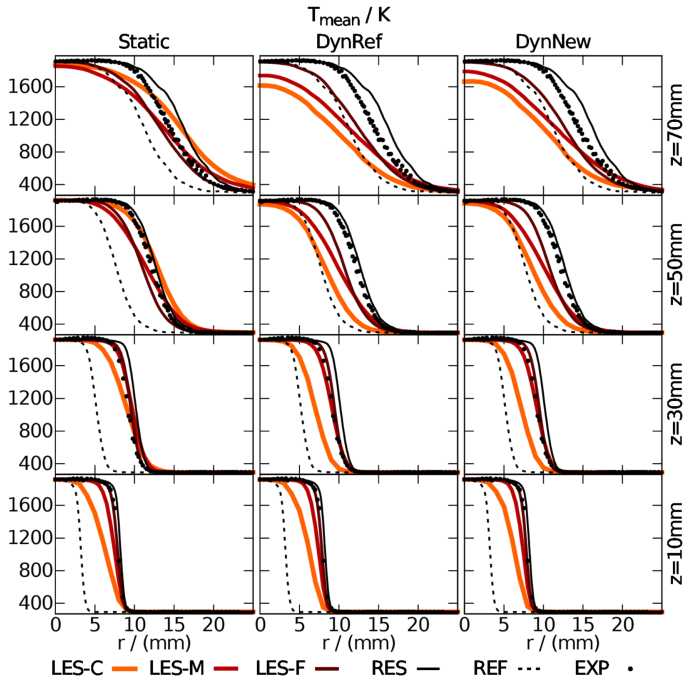

Figure 7.10.: Comparison of mean profiles of the temperature from the LES at different axial positions against flame resolved simulation (RES) data [161], the experimental data from [194] (EXP) is also given as an additional reference. To indicate the range in which the LES results should lie for a mean propagation speed and angle of the flame similar to the flame resolved simulation, the flame resolved simulation profiles have been plotted again shifted by 5 mm towards the centerline (REF). [162]

mechanism, or just the benefit of error compensation. If the latter holds, errors might not equilibrate that well for other burner configurations and larger filter widths. In the near region, both dynamic models yield comparable agreement of the conditional mean of the flame surface density. For the largest filter width, the conditional mean of the flame surface density is slightly over-predicted in the LES with both models. In the far region, the conditional mean of the flame surface density in the LES agrees with the one from the flame resolved simulation for lower values of the progress variable. Towards higher values of the progress variable, the deviation becomes more significant.

7.5.3. *A-posteriori* analysis of the model effects on the time-averaged flame structure

The focus of this section is on the comparison of the resulting time-averaged temperature and velocity fields from the LES against their flame resolved simulation counterparts. The experimental data is given as additional reference, where the comparison of the flame resolved simulation against the experiment has already been discussed in a companion paper [161] and is therefore not repeated here.

Figure 7.10 shows radial profiles of the time-averaged temperature at different heights above the burner from the LES, the flame resolved simulation and the experiment [194]. At the first measurement position, all models predict similar flame structures for all filter widths. Due to

This chapter was previously published [162] and is reprinted with permission of the journal.

the anchoring of the unburnt side of the flame at the bluff-body, the temperature profiles from the LES align with the flame resolved simulation profile at the unburnt side. As a result of the thickening procedure, the temperature profiles deviate towards the burnt side of the flame, meaning that the LES temperature profiles are shifted to the 'left' of the flame resolved simulation ones. If the mean propagation speed and opening angle of the flame would be the same in the LES and in the flame resolved simulation, the shift of the temperature profiles in the radial direction should stay constant from one measurement position to the next. This means that the LES temperature profiles should stay in the range 'left' of the flame resolved simulation ones throughout the whole domain. To indicate this range, the flame resolved simulation temperature profiles have been plotted a second time in Fig. 7.10, shifted by 5 mm towards the centerline. The 5 mm correspond to the five grid points over which the flame is resolved on the coarse grid, the additional lines are labeled 'REF'.

For the dynamic models (DynRef and DynNew), the LES temperature profiles roughly maintain their position compared to the flame resolved simulation profile at the downstream measurement positions, moreover they converge against the flame resolved simulation profile with grid refinement. The flame resolved simulation temperature profile gets flatter with growing distance from the burner due to an increase of turbulent fluctuations, this flattening can also be observed for the LES profiles. When the alignment of the unburnt side of the temperature profiles from the LES with the flame resolved simulation profile is taken as evaluation criteria, both dynamic models reconstruct the mean flame propagation speed of the flame resolved simulation with good accuracy. On the coarse grid, the propagation speed is slightly under predicted for both dynamic models, which likely can be explained with the under-prediction of the wrinkling factor, as discussed above.

The static model (Static) gives comparable results to the dynamic models on the finest grid. Due to the aforementioned over-prediction of the flame surface density, the static model overestimates the mean flame propagation speed on the coarse and medium grid, which is indicated by a shift of the temperature profiles to the 'right'.

The time-averaged flame length is under-predicted on the medium and coarse grid for both dynamic models, as seen in the decrease of the center-line temperature at the last measurement position. This under-prediction of the flame length on the medium and coarse grid is reduced by the new model compared to the dynamic Charlette/Wang model, but the flame length is still shorter than in the experiments also for the new model. In contrast, the static Charlette/Wang model is able to predict the flame length correctly also on the coarse and medium grid. This might convey the impression that the static model predicts the flame propagation better than the dynamic ones, which in our opinion is wrong for the following reason: As it was demonstrated in the last section, the flame surface density (which determines the flame propagation speed) is notably over-predicted by the static Charlette/Wang model in the LES. Therefore, the better prediction of the flame length is likely due to the compensation of numerical dissipation effects by the over-prediction of the flame propagation by the static model. Nevertheless, the under-

This chapter was previously published [162] and is reprinted with permission of the journal.

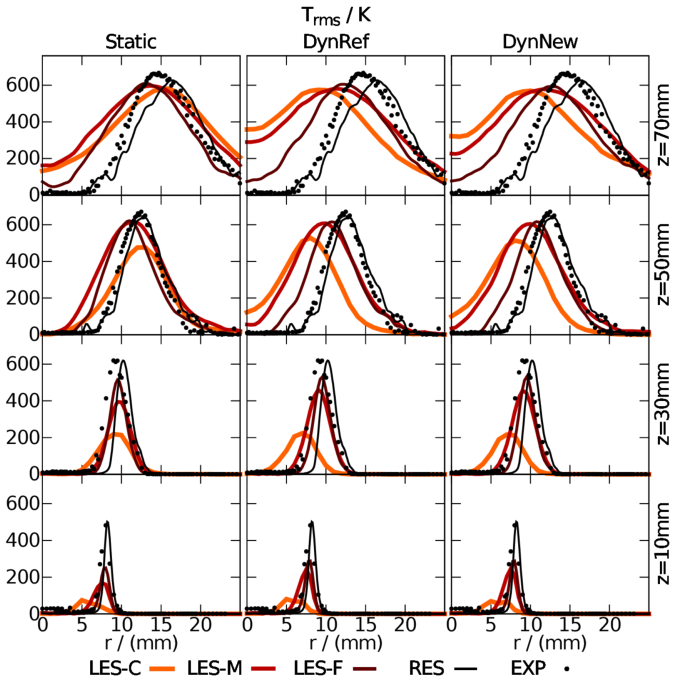

Figure 7.11.: Comparison of fluctuation profiles of the temperature from the LES at different axial positions against flame resolved simulation (RES) data [161], the experimental data from [194] (EXP) is also given as an additional reference. [162]

prediction of the flame length by the dynamic models implies that these models only work fully if the grid resolution is fine enough to resolve a sufficient amount of the flame wrinkling. Such details of the model behavior can only be revealed by a combined *a-priori* and *a-posteriori* analysis as performed in the present work.

To check potential sensitivities of higher order statistics, Fig. 7.11 shows radial profiles of the rms fluctuations of the temperature compared against DNS and experiment. In general, most of the conclusions drawn for the mean value profiles of temperature also hold for the rms profiles. The rms profiles get broader with decreasing grid resolution and increasing distance from the burner exit. The rms profiles are roughly aligned at the unburned side of the flame for both dynamic models (DynRef and DynNew), whereas for the static Charlette/Wang models (Static), the rms profiles on the coarse and medium grid are shifted towards larger radii with increasing distance from the burner exit. A notable feature is the dependency of the peak value of the rms profiles on the grid resolution, which can be attributed to the thickening of the local flame structure by the ATF model and has been observed before [102, 158]. The increased amount of temperature fluctuations at the centerline on the medium and coarse grid for both dynamic models can be explained by the aforementioned under-prediction of the flame length, which leads to an unstable and thus more fluctuating temperature distribution far downstream.

To determine how strong the influence of the variations in the flame structure is on the velocity field, Fig. 7.12 presents the radial profiles of the mean axial velocity component compared against flame resolved simulation and experiment [220]. In general, the influence of the combustion model and the grid resolution on the mean axial velocity components is much smaller

This chapter was previously published [162] and is reprinted with permission of the journal.

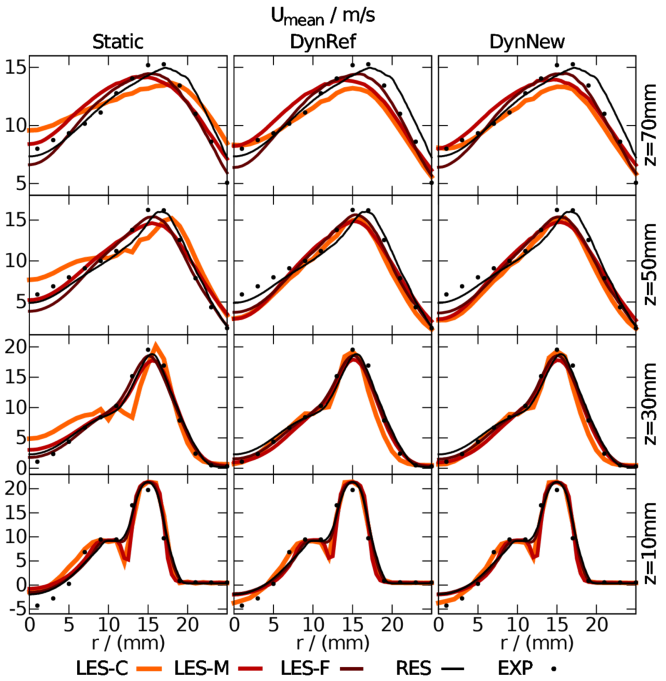

Figure 7.12.: Comparison of mean profiles of the axial velocity component from the LES at different axial positions against flame resolved simulation (RES) data [161], the experimental data from [220] (EXP) is also given as an additional reference (y-axis is scaled individually for every row). [162]

than on the mean temperature profiles. For the dynamic models (DynRef and DynNew), the radial profiles are very similar for all grid resolutions, the main differences are a slight shift towards lower radii of the LES mean profiles, compared to the flame resolved simulation ones, and a lower centerline velocity on the coarsest grid, compared to the finer grids. For the static model (Static), the mean axial velocity component profiles are comparable to the ones resulting from the dynamic models for the medium and fine grid resolution. On the coarse grid, the discussed overestimation of the flame propagation speed also reflects in a shift of the mean axial velocity component profiles towards larger radii and an increased centerline mean axial velocity component. A notable feature is the slight overestimation of the mean axial velocity component near the bluff-body on the centerline by the simulation compared to the experiment, this can be attributed to a slight heat loss at the bluff body as shown by Mercier et al. [120], which cannot be captured by the adiabatic combustion model applied in the present LES and flame resolved simulation.

7.6. Conclusions

Consistent *a-priori* and *a-posteriori* analyses of dynamic sub-filter closures for large eddy simulation (LES) with artificially thickened flames (ATF) and chemistry tabulated with flame generated manifolds (FGM) were presented for a laboratory flame. The term ‘consistent’ refers to the simulation setup, the same domain sizes, boundary conditions, numerics and flame formulation were applied for LES and flame resolved simulation [161]. The simulation results were

This chapter was previously published [162] and is reprinted with permission of the journal.

validated by comparison against experimental data [194, 220]. The established Charlette/Wang model was used in its static and dynamic version, and a modified dynamic power-law model was introduced where the lower cutoff depends on the sub-filter turbulent velocity fluctuations.

For the *a-priori* analysis, the PDFs of the exact wrinkling factor were evaluated from the flame resolved simulation data for varying filter widths and compared to the PDFs of the wrinkling factors resulting from the investigated models. A good agreement was found for the dynamic Charlette/Wang model and for the new model for moderate filter widths, where the new model yielded slightly better results for small filter widths and comparable results for larger filter widths. For the largest filter width, the dynamic models notably under-predicted the flame wrinkling compared to the flame resolved simulation. The static Charlette/Wang model showed larger deviations of the predicted wrinkling factor from the flame resolved simulation wrinkling factor for all filter widths, the flame wrinkling was over-predicted on average.

For the *a-posteriori* analysis, the PDFs of the modeled wrinkling factors were also extracted from the LES and compared against the *a-priori* (flame resolved simulation) PDFs. A good agreement was found for moderate filter widths, where the under-prediction of the wrinkling factor for the dynamic models on the largest filter width as observed *a-priori* was also observed *a-posteriori*. This implies that the dynamic models need a sufficient range of scales left in the progress variable field to reconstruct the wrinkling factor with high accuracy. However, it was shown by comparing the mean flame surface density conditioned on the progress variable from the LES and the flame resolved simulation, that the observed under-prediction of the wrinkling factor for the dynamic models on the coarse grid resolution is mostly compensated by larger gradients of the progress variable field in the LES, so that the important flame surface density agrees much better than the wrinkling factor that is used for its modeling. This observation is consistent with the findings of Veynante and Moureau [205], who made an attempt to analyze the cause [205]. For the static Charlette/Wang model, in contrast, the over-prediction of the wrinkling factor also resulted in an over-prediction of the flame surface density. The time-averaged length of the flame was under-predicted by both dynamic models to a certain degree, where the new model slightly improved the predictions. This implies that the dynamic models work entirely only if a sufficient amount of flame wrinkling is resolved in the simulation, which requires a relatively fine grid. It was furthermore discussed how the aforementioned over-prediction of the flame surface density with the static model improves the prediction of the flame length as a consequence of error compensation.

To assess the effects of the models on the turbulent flame structure, time-averaged temperature profiles at different heights above the burner from the LES were compared against the flame resolved simulation profiles and measurements. The LES with the dynamic models was able to reconstruct the mean flame propagation speed of the flame resolved simulation, only on the coarse grid a slight under prediction was observed. The LES solution for the dynamic models converged towards the flame resolved simulation data with grid refinement.

The flame resolved simulation database used in this paper is available to other researchers, re-

This chapter was previously published [162] and is reprinted with permission of the journal.

spective queries can be addressed to the Chair of Fluid Dynamics of the University of Duisburg-Essen [85].

Acknowledgements

The authors gratefully acknowledge the funding from the state of North Rhine-Westphalia and the compute time granted on JUQUEEN at Jülich Supercomputing Centre (JSC), through the John von Neumann Institute for Computing (NIC). We also would like to thank Johannes Sellmann for valuable discussions.

This chapter was previously published [162] and is reprinted with permission of the journal.

8. Conclusions and outlook

In the presented work, the details of premixed and stratified combustion processes were investigated with highly resolved large eddy simulation (LES) and direct numerical simulation (DNS) using tabulated detailed chemistry. The flamelet generated manifolds (FGM) model was implemented and tested in a massively parallel LES and DNS solver. This solver was originally created by Kempf and has been significantly improved, extended and accelerated in the presented work, it was made suitable for efficient use of ten thousands of processor cores. The FGM model was then extended to make it suitable for the description of stratified and non-adiabatic combustion processes. These models were tested and validated by comparison of LES results of lab-scale burners for different grid resolutions with measurement data. After the extension of the chemical model, a DNS of a lab scale burner has been performed in order to further investigate and understand the details of the turbulence-flame interaction in realistic flame setups. Subsequently, the DNS results were spatially filtered in order to test, extend and validate sub-filter closures for LES. These sub-filter closures were then also used for LES of the same lab scale burner, the results were compared against the DNS results and against measurements.

The FGM model was made suitable for stratified combustion processes by adding the mixture fraction as an additional control variable and FGM table dimension. This model was then applied for LES of a bluff-body burner investigated experimentally at the University of Cambridge and the Sandia National Labs, the artificially thickened flame model (ATF) was used to make the flame resolvable on the LES grid. Computations have been performed for varying grid resolutions and levels of stratification. Radial mean and rms profiles from the simulations have been compared against the measurements for axial- and radial velocity components, temperature, equivalence ratio and major species mass fractions. An overall good agreement was found, certain deviations near the bluff-body were found to be likely caused by effects of preferential diffusion and heat loss. The influence of the sub-filter distribution of the control variable on the results was investigated and found to be negligible. The combustion process in the burner was analyzed closer with probability density functions (PDFs) and joint probability density functions (JPDFs), it was found that the flame burns in a premixed regime near the burner exit and in a stratified regime down to the flammability limit further downstream. It was shown that, although the mixture fraction varies, the combustion process can be well described by an ensemble of premixed flamelets burning at the local mixture fraction.

A further extension of the FMG model was presented for the computation of non-adiabatic configurations. This was achieved by adding the sum of sensible and chemical enthalpy as a fur-

ther table dimension and control variable. In this context, a new method based on scaling of the energy equation source term was introduced to compute the one-dimensional flamelets which form the basis of the FGM table. The new method was compared against other established methods for the inclusion of heat loss by means of LES of a model gas turbine combustor investigated at the DLR Stuttgart, again with the ATF model. The burner features a very significant amount of heat loss towards the walls of the combustion chamber resulting in peak temperatures that were several hundred Kelvin below the adiabatic flame temperature. The simulations were again performed for varying grid resolutions and validated by comparing mean and rms radial profiles from the simulation against measurement data. It was found that the new model yields a comparably good agreement of the simulation with the measurements as the best of the established models, where the new model allows to cover a broader range of heat losses. It was shown that the model predictions further downstream can be improved by reducing the reaction source term by a correction factor that depends on the local value of the flame normal strain rate.

To enable a closer analysis of the turbulence-flame interaction in a lab-scale burner, the Cambridge bluff-body burner was computed again, this time with a grid resolution of $100\ \mu\mathrm{m}$ which led to a computational domain size of 1.6 billion cells and required 10 million core hours on 64,000 processor cores. This grid resolution was fine enough to resolve the flame directly on the computational grid, without the need for a sub-filter model. It was shown that this grid resolution is furthermore sufficient to resolve all the relevant velocity scales in the reaction zone in a DNS sense. The radial mean and rms profiles obtained from the simulation agreed well with the experimental data. The turbulent flame structure was then carefully analyzed with PDFs, JPFDs and averages along turbulent flamelets, where the analysis was carried out with respect to findings from previous DNS of simpler flame configurations. It was shown that the location of the local turbulence-flame interaction parameters in the combustion regime diagram depends on the distance from the burner exit as well as on the progress of the reaction. The turbulent flame thickness was found mostly slightly smaller than the unstrained laminar one due to a predominant alignment of the most compressive strain rate with the flame normal direction. The displacement speed of the progress variable iso-surfaces was found to take partially slightly negative values, it was mainly determined by the mean principal curvature of the iso-surfaces at the unburned side of the flame and by the gradient of the progress variable on the burned side. To the best of our knowledge, this was the first time that such a DNS analysis was performed for a real flame experiment that has been carefully validated against measurement data. This enables to test if findings from previous DNS of simpler configurations also hold for technically more relevant configurations. It was found that most of the conclusions and observations made for the performed DNS of a lab-scale burner were in line with the findings from previous DNS of simpler configurations, which confirms the relevance of these simpler configurations for the combustion model development.

The obtained DNS results for the Cambridge bluff-body burner were then used for the a-priori

and a-posteriori investigation of dynamic models for the sub-filter flame wrinkling. For the a-priori analysis, the DNS results were Gaussian filtered at different filter widths, the exact values of the sub-filter wrinkling factor were compared against the predictions of different sub-filter wrinkling models. Three sub-filter wrinkling factor models were compared, the commonly used one by Charlette with a static as well as with a dynamic model factor, and a newly introduced dynamic power-law model. The static model led to an over-prediction of the average wrinkling factor, while both dynamic models were able to reproduce the exact average wrinkling factor except for the largest filter width. For the a-posteriori analysis, again LES simulations of the burner were carried out for all three models with different grid resolutions corresponding to the a-priori filter widths. The resulting sub-filter wrinkling factor PDFs were comparable to the a-priori ones, which underlines the relevance of the a-priori analysis for the actual LES. The under-prediction of the sub-filter wrinkling factor with the dynamic models was, however, over-compensated in the LES by larger progress variable gradients. This means that the flame surface density, which determines the flame propagation, was in closer agreement with the DNS than the sub-filter wrinkling factor. With the dynamic models, the LES results converged against the DNS results when the grid was refined.

In summary, it was shown in this work that reasonably resolved LES in combination with tabulated chemistry and state of the art sub-filter modeling is able to predict technically relevant lab-scale burners with good accuracy. It was demonstrated that the applied tabulated chemistry approach, originally developed for premixed combustion, can be extended to successfully predict stratified and non-adiabatic combustion processes. However, certain higher-order chemical effects related to preferential diffusion and dilution with exhaust gases could not be fully captured by the used models, although the effect of the latter could be reproduced by a simple correction factor depending on the local flame normal strain rate. The extension of the tabulated chemistry model for inclusion of higher-order chemistry effects would therefore be a worthwhile future development. However, it should be considered that the tabulated chemistry approach only is feasible as long as the number of control variables stays small, as otherwise the memory requirement of the lookup tables gets prohibitive. Therefore, a combination of the ATF model with reduced chemical mechanisms as already applied by other researchers might be the more promising approach if the focus is on the details of the chemical process. It was also demonstrated in this work that fully resolved tabulated chemistry simulations of lab-scale burners are becoming more and more affordable with the computer power available today. These simulations have the potential to generate new insights in the interaction of turbulence and chemistry, although it was confirmed in this work that many of the findings can also be generated based on computations of simpler canonical flame configurations. The performed a-priori and a-posteriori investigations imply that the largest potential of the fully resolved tabulated chemistry simulations of lab-scale burners lies in the investigation of the turbulence-flame interaction under more realistic conditions. It was demonstrated that the existing algebraic models for the sub-filter wrinkling work reasonably well, provided that the grid resolution is not too

coarse. For coarser grid resolutions, the quality of the model predictions for both the dynamic and static formulation diminishes. The improvement of the predictions on coarser grids is a further possibility for future developments, together with the investigation of the influence of stratification and heat loss on the modeling of the sub-filter flame wrinkling.

A. Co-author publications

This chapter gives a brief overview of the papers that the author of this thesis contributed to as a co-author. Given are always the paper abstracts and a short summary what parts the author of this thesis contributed.

A.1. Comparison of the Sigma and Smagorinsky LES models for grid generated turbulence and a channel flow [170]

Authors: M. Rieth, F. Proch, O. T. Stein, M. W. A. Pettit, A. M. Kempf
The paper was published in 'Computers & Fluids, 99(0), M. Rieth, F. Proch, O. T. Stein, M. W. A. Pettit and A. M. Kempf, Comparison of the Sigma and Smagorinsky LES models for grid generated turbulence and a channel flow, 172 – 181, Copyright © Elsevier (2014)', the abstract is reprinted with permission from Elsevier. The author F. Proch contributed the basic CFD code, supervision of M. Rieth who was undergraduate at the time the paper was written, the implementation of the dynamic model versions based on former work of M. W. A. Pettit, support with code development, discussions, corrections and proof-reading.

Abstract

Context: A new and promising Large-Eddy simulation (LES) subgrid model, the Sigma model, has been developed by Nicoud, Baya-Toda and co-workers. Its performance in different codes and test cases compared to the Smagorinsky model is of interest.
Objective: The present work investigates how suitable different subgrid stress (SGS) models, i.e. the static and dynamic Smagorinsky and in particular Sigma models are for a Turbulent Opposed Jet (TOJ) configuration and evaluates the differences between the models for a TOJ and channel flow configurations.
Method: The Sigma model has been implemented in a dedicated LES/DNS code and is tested against Direct Numerical Simulation (DNS) data from channel flow and grid turbulence data obtained from DNS and from measurements in a TOJ configuration. The flow through the turbulence generating plate (TGP) of the TOJ configuration constitutes a very sensitive test case for fluid flow simulations. Hence, it is a suitable case for a comparison of different SGS

models for LES. To compare the SGS models, only the isothermal flow through one of the opposed nozzles, including the TGP has been simulated. LES and DNS have been performed using different grid resolutions down to a grid spacing smaller than the Kolmogorov length scale estimated for the region between the nozzles. The DNS results are being compared to experimental results, while LES results are compared to the DNS data in turn. To underline the differences between the SGS models and to show the general applicability of the newly implemented Sigma model, simulations of the turbulent channel flow have been performed additionally.
Results: The TOJ and channel flow simulations show good agreement between DNS and LES. It has been found, that the Sigma model is a better alternative to the static Smagorinsky model with comparable results to the dynamic Smagorinsky model for most of the settings examined.

A.2. Large Eddy Simulation of coal combustion in a large-scale laboratory furnace [164]

Authors: M. Rabaçal, B. M. Franchetti, F. Cavallo Marincola, F. Proch, M. Costa, C. Hasse, A. M. Kempf

The paper was published in 'Proceedings of the Combustion Institute, 35(3), M. Rabaçal, B. M. Franchetti, F. C. Marincola, F. Proch, M. Costa, C. Hasse and A. M. Kempf, Large eddy simulation of coal combustion in a large-scale laboratory furnace, 3609 – 3617, Copyright © Elsevier (2015)', the abstract is reprinted with permission from Elsevier. The author F. Proch contributed the basic CFD code for Euler fields and Lagrangian particles, support with code development, discussions, corrections and proof-reading.

Abstract

A detailed Large Eddy Simulation (LES) of pulverised coal combustion in a large-scale laboratory furnace is presented. To achieve a detailed representation of the flow, mixing and particle dispersion, a massively parallel LES was performed. Different phenomenological network models were applied and compared to each other in order to obtain the most adequate devolatilization kinetic data for the LES. An iterative procedure allowed to optimise the devolatilization kinetic data for the studied coal and operating conditions. The particle combustion history is studied by analysing particle instantaneous properties giving a perspective on coal combustion that currently is not available by other means than LES. Predicted major species and temperature were compared with measurements and a good agreement was obtained. The finely resolved near burner region revealed that the flame is stabilised very close to the burner. Furthermore, two distinct zones of CO2 production were found one in the internal recirculation zone (IRZ) due to gaseous combustion, and one downstream of the vortex breakdown, due to intense char combustion. It was found that particle properties are inhomogeneous within the IRZ, whereas

in the external recirculation zone (ERZ) and downstream of the vortex breakdown they were found to be homogeneous.

A.3. LES of the Sydney piloted spray flame series with the PFGM/ATF approach and different sub-filter models [171]

Authors: A. Rittler, F. Proch, A. M. Kempf
The paper was published in 'Combustion and Flame, 162(4), A. Rittler, F. Proch and A. M. Kempf, LES of the sydney piloted spray flame series with the PFGM/ATF approach and different sub-filter models, 1575 – 1598, Copyright © Elsevier (2015)', the abstract is reprinted with permission from Elsevier. The author F. Proch contributed the basic CFD code for Euler fields and Lagrangian particles, the combustion model for the gas-phase, support with code development, discussions, corrections and proof-reading.

Abstract

Detailed numerical investigations of the Sydney spray flame series [66] are presented for ethanol flames referred to as "EtF3, EtF6 and EtF8", which feature identical ethanol mass flow rates but different carrier gas mass flow rates. Large eddy simulations (LES) are performed, where the gaseous and liquid phases are modelled by an Eulerian/Lagrangian approach. The turbulent sub-filter stresses (sgs) are modelled with Nicoud's sigma model [131] on grids with two different resolutions. Combustion is modelled with the premixed flamelet generated manifold approach (PFGM), which is combined with the artificially thickened flame (ATF) method. The sub-filter distributions of the control variables are modelled with (a) a β function (β-fdf) and (b) a top-hat function (TH). First, the influence of the variance in the mixture fraction and reaction progress variable is investigated separately, where the variances are either determined from an algebraic model or a transport equation model. Subsequently, the TH model is used to account for the joint impact of Z and Y_p. The results are compared against the experimental measurements and reference simulations without sub-filter model. The particle statistics are in good agreement with the experimental data. The variances predicted by the two algebraic models are quite similar, whereas the transport equation model predicts variances which are one order of magnitude higher. The results obtained with the TH and the β-fdf model are comparable. It is found that the impact of the sgs models for the mixture fraction and the progress variable increases with an increasing carrier gas mass flow rate.

A.4. Challenging modeling strategies for LES of non-adiabatic turbulent stratified combustion [56]

Authors: B. Fiorina, R. Mercier, G. Kuenne, A. Ketelheun, A. Avdić, J. Janicka, D. Geyer, A. Dreizler, E. Alenius, C. Duwig, P. Trisjono, K. Kleinheinz, S. Kang, H. Pitsch, F. Proch, F. C. Marincola, A. M. Kempf

The paper was published in 'Combustion and Flame, 162(11), B. Fiorina, R. Mercier, G. Kuenne, A. Ketelheun, A. Avdić, J. Janicka, D. Geyer, A. Dreizler, E. Alenius, C. Duwig, P. Trisjono, K. Kleinheinz, S. Kang, H. Pitsch, F. Proch, F. C. Marincola and A. M. Kempf, Challenging modeling strategies for LES of non-adiabatic turbulent stratified combustion, 4264 – 4282, Copyright © Elsevier (2015)', the abstract is reprinted with permission from Elsevier. The author F. Proch contributed the parts of the paper from the 'UDE' group, including the CFD code and the combustion model, all the simulations runs, text and all figures and tables.

Abstract

Five different low-Mach large eddy simulations are compared to the turbulent stratified flame experiments conducted at the Technical University of Darmstadt (TUD). The simulations were contributed by TUD, the Institute for Combustion Technology (ITV) at Aachen, Lund University (LUND), the EM2C laboratory at Ecole Centrale Paris, and the University of Duisburg-Essen (UDE). Combustion is modeled by a premixed flamelet tabulation with local flame thickening (TUD), a premixed flamelet progress variable approach coupled to a level set method (ITV), a 4-steps mechanism combined with implicit LES (LUND), the F-TACLES model that is based on filtered premixed flamelet tabulation (EM2C), and a flame surface density approach (UDE). An extensive comparison of simulation and experimental data is presented for the first two moments of velocity, temperature, mixture fraction, and major species mass fractions. The importance of heat-losses was assessed by comparing simulations for adiabatic and isothermal boundary conditions at the burner walls. The adiabatic computations predict a flame anchored on the burner lip, while the non-adiabatic simulations show a flame lift-off of one half pilot diameter and a better agreement with experimental evidence for temperature and species concentrations. Most simulations agree on the mean flame brush position, but it is evident that subgrid turbulence must be considered to achieve the correct turbulent flame speed. Qualitative comparisons of instantaneous snapshots of the flame show differences in the size of the resolved flame wrinkling patterns. These differences are (a) caused by the influence of the LES combustion model on the flame dynamics and (b) by the different simulation strategies in terms of grid, inlet condition and numerics. The simulations were conducted with approaches optimized for different objectives, for example low computational cost, or in another case, short turn around.

A.5. Large Eddy Simulation of an Internal Combustion Engine Using an Efficient Immersed Boundary Technique [129]

Authors: T. M. Nguyen, F. Proch, I. Wlokas, A. M. Kempf
The paper was published in 'Flow, Turbulence and Combustion, 97(1), T. M. Nguyen, F. Proch, I. Wlokas and A. M. Kempf, Large Eddy Simulation of an Internal Combustion Engine Using an Efficient Immersed Boundary Technique, 191 – 230, Copyright © Springer (2016)', the abstract is reprinted with permission from Springer. The author F. Proch contributed the basic CFD code for Euler fields and Lagrangian particles, the combustion model for the gas-phase, support with code development, smaller parts of the text, discussions, corrections and proof-reading.

Abstract

This paper presents highly resolved large eddy simulations (LES) of an internal combustion engine (ICE) using an immersed boundary method (IBM), which can describe moving and stationary boundaries in a simple and efficient manner. In this novel approach, the motion of the valves and the piston is modeled by Lagrangian particles, whilst the stationary parts of the engine are described by a computationally efficient IBM. The proposed mesh-free technique of boundary representation is simple for parallelization and suitable for high performance computing (HPC). To demonstrate the method, LES results are presented for the flow and the combustion in an internal combustion engine. The Favre-filtered Navier-Stokes equations are solved for a compressible flow employing a finite volume method on Cartesian grids. Non-reflecting boundary conditions are applied at the intake and the exhaust ports. Combustion is described using a flame surface density (FSD) model with an algebraic reaction rate closure. A simplified engine with a fixed axisymmetric valve (see Appendix A) is employed to show the correctness of the method while avoiding the uncertainties which may be induced by the complex engine geometry. Three test-cases using a real engine geometry are investigated on different grids to evaluate the impact of the cell size and the filter width. The simulation results are compared against the experimental data. A good overall agreement was found between the measurements and the simulation data. The presented method has particular advantages in the efficient generation of the grid, high resolution and low numerical dissipation throughout the domain and an excellent suitability for massively parallel simulations.

B. Parallel scaling of the CFD code

The ‘PsiPhi’ CFD code, which has originally been developed by Kempf, was improved, extended, accelerated and made suitable for efficient computations on ten thousands of processor cores for this work. The code relies on a Cartesian equidistant cuboid computational domain, where cells inside the geometry are blocked by the immersed boundary approach as described in Section 3.4.4. The Cartesian grid grid allows for good vectorization performance by avoiding non-sequential memory access, which often outweighs the additional computational effort of the immersed boundary method. The code is written in Fortan 90/95, which has proven since many years to be a well-suited programming language for engineering purposes due to its simple syntax and the good computational performance of the resulting code. The code is parallelized with the message passing interface (MPI), the overhead of the communication routines is partially compensated by using non-blocking communication overlayed with computational work as described in Section 3.4.1. The parallel scaling behavior of the code has been tested on the IBM Blue Gene/Q-System JUQUEEN at the at Jülich Supercomputing Centre (JSC) on up to 128,000 cores, as shown in Fig. B.1. The scaling test was performed for the 1.6 billion

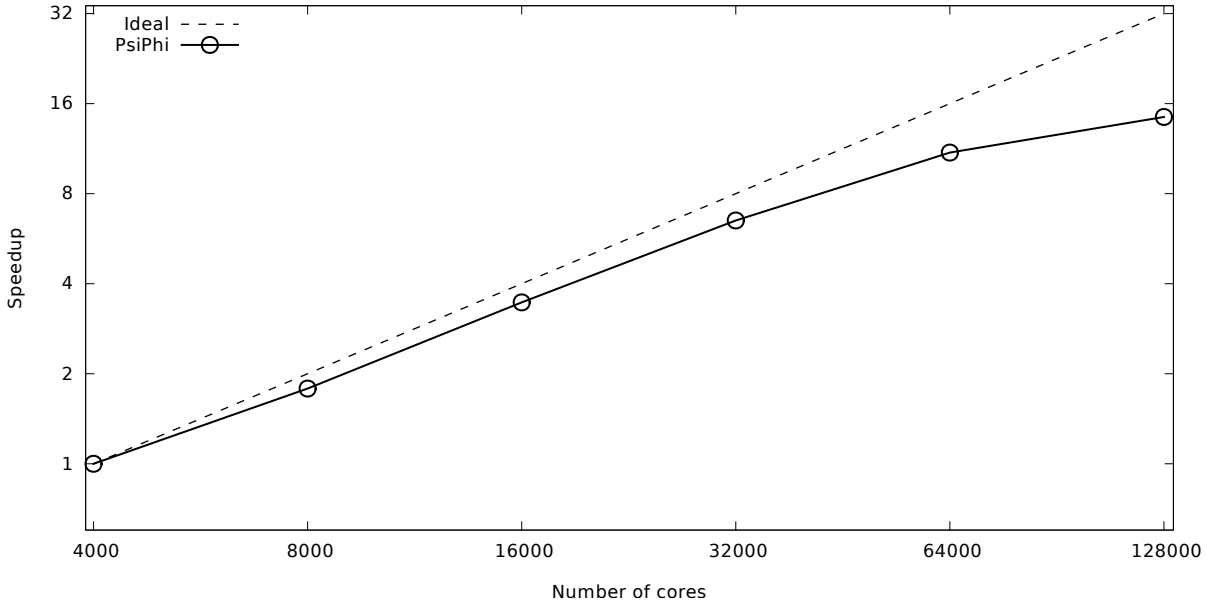

Figure B.1.: Parallel scaling behavior of the ‘PsiPhi’ code on the JUQUEEN machine at the Jülich Supercomputing Centre (JSC).

cell computations of the Cambridge/Sandia bluff-body burner that is discussed in Chapters 6 and 7, which was computed on a successively growing number of processor cores. The scaling

behavior is comparable to other CFD codes tailored for massively parallel computations, for the 64,000 processor cores that were used for the productive runs the parallel efficiency is around 70% with respect to 4000 processor cores. As the Mach-numbers in the burner are below 0.1, the incompressible version of the code is more efficient overall in spite of its lower parallel efficiency, as the required number of time steps for the density-based solution algorithm would be very large. For higher Mach-number cases, the density-based version of the code can be used, which avoids the communication-intensive Poisson solver and thereby improves the parallel efficiency by approximately 10%.

Bibliography

[1] A. Amato, M. Day, R. K. Cheng, J. Bell, D. Dasgupta, and T. Lieuwen. Topology and burning rates of turbulent, lean, H2/air flames. *Combust. Flame*, 162(12):4553 – 4565, 2015.

[2] C. Angelberger, D. Veynante, F. Egolfopoulos, and T. J. Poinsot. Large Eddy Simulation of combustion instabilities in turbulent premixed flames. *Proceedings of the Summer Programm, Center for Turbulence Research, Stanford*, pages 61–82, 1998.

[3] W. T. Ashurst, N. Peters, and M. D. Smooke. Numerical Simulation of Turbulent Flame Structure with Non-unity Lewis Number. *Combust. Sci. Technol.*, 53(4-6):339–375, 1987.

[4] A. J. Aspden, M. S. Day, and J. B. Bell. Three-dimensional direct numerical simulation of turbulent lean premixed methane combustion with detailed kinetics. *Combust. Flame*, 166:266 – 283, 2016.

[5] P. Auzillon, O. Gicquel, N. Darabiha, D. Veynante, and B. Fiorina. A Filtered Tabulated Chemistry model for LES of stratified flames. *Combust. Flame*, 159(8):2704 – 2717, 2012.

[6] R. S. Barlow. International Workshop on Measurement and Computation of Turbulent Nonpremixed Flames. http://www.sandia.gov/TNF/abstract.html, 2016.

[7] R. S. Barlow, M. J. Dunn, M. S. Sweeney, and S. Hochgreb. Effects of preferential transport in turbulent bluff-body-stabilized lean premixed CH4/air flames. *Combust. Flame*, 159(8):2563 – 2575, 2012.

[8] G. K. Batchelor. Small-scale variation of convected quantities like temperature in turbulent fluid Part 1. General discussion and the case of small conductivity. *J. Fluid Mech.*, 5:113–133, 1959.

[9] J. Bell, M. Day, J. Grcar, and M. Lijewski. Active control for statistically stationary turbulent premixed flame simulations. *Comm. Appl. Math. Comp. Sci.*, 1(1):29–51, 2007.

[10] J. H. Bell, M. S. Day, J. F. Grcar, M. J. Lijewski, J. F. Driscoll, and S. A. Filatyev. Numerical simulation of a laboratory-scale turbulent slot flame. *Proc. Combust. Inst.*, 31 (1):1299–1307, 2007.

[11] R. W. Bilger, S. H. Stårner, and R. J. Kee. On reduced mechanisms for methane-air combustion in nonpremixed flames. *Combust. Flame*, 80(2):135 – 149, 1990.

[12] R. B. Bird, W. E. Stewart, and E. N. Lightfoot. *Transport phenomena*. John Wiley & Sons, 2nd edition, 2002.

[13] M. Boger, D. Veynante, H. Boughanem, and A. Trouve. Direct numerical simulation analysis of flame surface density concept for large eddy simulation of turbulent premixed combustion. *Symp. (Int.) on Combust.*, 27(1):917 – 925, 1998.

[14] R. Borghi. Turbulent combustion modelling. *Prog. Energy Combust. Sci.*, 14:245–292, 1988.

[15] N. Branley and W. P. Jones. Large Eddy Simulation of a Turbulent Non-premixed Flame. *Combust. Flame*, 127(1-2):1914–1934, Oct. 2001.

[16] T. Brauner, W. P. Jones, and A. J. Marquis. LES of the Cambridge Stratified Swirl Burner using a Sub-grid pdf Approach. *Flow Turbul. Combust.*, pages 1–21, 2016.

[17] K. N. C. Bray. The Challenge of turbulent combustion. *Proc. Combust. Inst.*, 26:1–26, 1996.

[18] K. N. C. Bray and J. B. Moss. A unified statistical model of the premixed turbulent flame. *Acta Aeronautica*, 4:219–319, 1977.

[19] I. N. Bronstein, K. A. Semendjajew, G. Musiol, and H. Mühlig. *Taschenbuch der Mathematik*. Verlag Harri Deutsch, 5 edition, 2001.

[20] T. D. Butler and P. J. O'Rourke. A numerical method for two dimensional unsteady reacting flows. *Symp. (Int.) on Combust.*, 16(1):1503 – 1515, 1977.

[21] F. Cavallo Marincola, T. Ma, and A. M. Kempf. Large eddy simulations of the Darmstadt turbulent stratified flame series. *Proc. Combust. Inst.*, 34(1):1307 – 1315, 2013.

[22] D. Cecere, E. Giacomazzi, F. Picchia, N. Arcidiacono, F. Donato, and R. Verzicco. A Non-Adiabatic Flamelet ProgressVariable Approach for LES of Turbulent Premixed Flames. *Flow Turbul. Combust.*, 86(3-4):667–688, 2011.

[23] N. Chakraborty. Comparison of displacement speed statistics of turbulent premixed flames in the regimes representing combustion in corrugated flamelets and thin reaction zones. *Phys. Fluids*, 19(10):105109, 2007.

[24] N. Chakraborty and R. S. Cant. Influence of Lewis number on curvature effects in turbulent premixed flame propagation in the thin reaction zones regime. *Phys. Fluids*, 17(10): 105105/1–105105/20, 2005.

[25] N. Chakraborty and R. S. Cant. Effects of strain rate and curvature on surface density function transport in turbulent premixed flames in the thin reaction zones regime. *Phys. Fluids*, 17(6):065108, 2005.

[26] N. Chakraborty and R. S. Cant. Influence of Lewis number on strain rate effects in turbulent premixed flame propagation. *Int. J. Heat Mass Tran.*, 49(1314):2158 – 2172, 2006.

[27] N. Chakraborty and R. S. Cant. Direct Numerical Simulation analysis of the Flame Surface Density transport equation in the context of Large Eddy Simulation. *Proc. Combust. Inst.*, 32(1):1445 – 1453, 2009.

[28] N. Chakraborty and S. Cant. Unsteady effects of strain rate and curvature on turbulent premixed flames in an inflowoutflow configuration. *Combust. Flame*, 137(12):129 – 147, 2004.

[29] N. Chakraborty and N. Swaminathan. Influence of the Damköhler number on turbulence-scalar interaction in premixed flames. I. Physical insight. *Phys. Fluids*, 19(4):045103, 2007.

[30] N. Chakraborty, M. Klein, and R. S. Cant. Stretch rate effects on displacement speed in turbulent premixed flame kernels in the thin reaction zones regime. *Proc. Combust. Inst.*, 31(1):1385–1392, 2007.

[31] F. Charlette, C. Meneveau, and D. Veynante. A Power-Law Flame Wrinkling Model for LES of Premixed Turbulent Combustion Part I- Non-Dynamic Formulation and Initial Tests. *Combust. Flame*, 131:159–180, 2002.

[32] F. Charlette, C. Meneveau, and D. Veynante. A Power-Law Flame Wrinkling Model for LES of Premixed Turbulent Combustion Part II - Dynamic Formulation. *Combust. Flame*, 131:181–197, 2002.

[33] O. Chatakonda, E. R. Hawkes, A. J. Aspden, A. R. Kerstein, H. Kolla, and J. H. Chen. On the fractal characteristics of low Damkoehler number flames. *Combust. Flame*, 160 (11):2422 – 2433, 2013.

[34] J. H. Chen. Petascale direct numerical simulation of turbulent combustion - fundamental insights towards predictive models. *Proc. Combust. Inst.*, 33:99–123, 2011.

[35] A. J. Chorin. A numerical method for solving incompressible viscous flow problems. *J. Comput. Phys.*, 2(1):12 – 26, 1967.

[36] L. Cifuentes, C. Dopazo, J. Martin, P. Domingo, and L. Vervisch. Local volumetric dilatation rate and scalar geometries in a premixed methane-air turbulent jet flame. *Proc. Combust. Inst.*, 35:1295–1303, 2015.

[37] O. Colin, F. Ducros, D. Veynante, and T. J. Poinsot. A thickened flame model for large eddy simulations of turbulent premixed combustion. *Phys. Fluids*, 12(7):1843–1863, 2000.

[38] R. Courant, K. Friedrichs, and H. Lewy. Über die partiellen Differenzengleichungen der mathematischen Physik. *Math. Ann.*, 100(1):32–74, 1928.

[39] J. Crank and P. Nicolson. A practical method for numerical evaluation of solutions of partial differential equations of the heat-conduction type. *Proc. Camb. Phil. Soc.*, 43: 50–67, 1 1947.

[40] A. P. D. Cruz, A. M. Dean, and J. M. Grenda. A numerical study of the laminar flame speed of stratified methane/air flames. *Proc. Combust. Inst.*, 28(2):1925 – 1932, 2000.

[41] M. Di Domenico, P. Gerlinger, and B. Noll. Numerical simulations of confined, turbulent, lean, premixed, flames using a detailed chemistry combustion model. Proceedings of the ASME Turbo Expo 2011, 2011.

[42] P. Domingo, L. Vervisch, S. Payet, and R. Hauguel. DNS of a premixed turbulent V flame and LES of a ducted flame using a FSD-PDF subgrid scale closure with FPI-tabulated chemistry. *Combust. Flame*, 143:566–586, 2005.

[43] A. Donini, S. M. Martin, R. J. M. Bastiaans, J. A. van Oijen, and L. P. H. de Goey. Numerical simulations of a premixed turbulent confined jet flame using the flamelet generated manifold approach with heat loss inclusion. Proceedings of the ASME Turbo Expo 2013, 2013.

[44] M. J. Dunn and R. S. Barlow. Effects of preferential transport and strain in bluff body stabilized lean and rich premixed CH4/air flames. *Proc. Combust. Inst.*, 34(1):1411 – 1419, 2013.

[45] T. D. Dunstan, N. Swaminathan, and K. N. C. Bray. Influence of flame geometry on turbulent premixed flame propagation: a DNS investigation. *J. Fluid Mech.*, 709:191–222, 10 2012.

[46] L. Durand and W. Polifke. Implementation of the Thickened Flame Model for Large Eddy Simulation of Turbulent Premixed Combustion in a Commercial Solver. In *Turbo Expo*. ASME, 2007.

[47] M. Düsing, A. M. Kempf, F. Flemming, A. Sadiki, and J. Janicka. Combustion LES for Premixed and Diffusion Flames. *Prog. Comp. Fluid Dyn.*, 5:363–374, 2005.

[48] C. Duwig. Study of a Filtered Flamelet Formulation for Large Eddy Simulation of Premixed Turbulent Flames. *Flow Turbul. Combust.*, 79(4):433–454, 2007.

[49] T. Echekki and J. H. Chen. Unsteady strain rate and curvature effects in turbulent premixed methane-air flames. *Combust. Flame*, 106(12):184 – 202, 1996.

[50] T. Echekki and J. H. Chen. Analysis of the contribution of curvature to premixed flame propagation. *Combust. Flame*, 118(12):308 – 311, 1999.

[51] M. Euler, R. Zhou, S. Hochgreb, and A. Dreizler. Temperature measurements of the bluff body surface of a Swirl Burner using phosphor thermometry. *Combust. Flame*, 161(11): 2842 – 2848, 2014.

[52] J. H. Ferziger and M. Perić. *Computational Methods for Fluid Dynamics*. Springer Verlag, 3rd edition, 2002.

[53] B. Fiorina, R. Baron, O. Gicquel, D. Thevenin, S. Carpentier, and N. Darabiha. Modelling non-adiabatic partially premixed flames using flame-prolongation of ILDM. *Combust. Theory Model.*, 7(3):449–470, 2003.

[54] B. Fiorina, O. Gicquel, L. Vervisch, S. Carpentier, and N. Darabiha. Approximating the chemical structure of partially premixed and diffusion counterflow flames using FPI flamelet tabulation. *Combust. Flame*, 140(3):147 – 160, 2005.

[55] B. Fiorina, R. Vicquelin, P. Auzillon, N. Darabiha, O. Gicquel, and D. Veynante. A filtered tabulated chemistry model for LES of premixed combustion. *Combust. Flame*, 157(3):465 – 475, 2010.

[56] B. Fiorina, R. Mercier, G. Kuenne, A. Ketelheun, A. Avdić, J. Janicka, D. Geyer, A. Dreizler, E. Alenius, C. Duwig, P. Trisjono, K. Kleinheinz, S. Kang, H. Pitsch, F. Proch, F. Cavallo Marincola, and A. M. Kempf. Challenging modeling strategies for LES of non-adiabatic turbulent stratified combustion. *Combust. Flame*, 162(11):4264 – 4282, 2015.

[57] J. Floyd, A. M. Kempf, A. Kronenburg, and R. H. Ram. A simple model for the filtered density function for passive scalar combustion LES. *Combust. Theory Mod.*, 13(4):559–588, 2009.

[58] B. M. Franchetti, F. Cavallo Marincola, S. Navarro-Martinez, and A. M. Kempf. Large Eddy simulation of a pulverised coal jet flame. *Proc. Combust. Inst.*, 34(2):2419 – 2426, 2013.

[59] C. Fureby. A fractal flame-wrinkling large eddy simulation model for premixed turbulent combustion. *Proc. Combust. Inst.*, 30(1):593 – 601, 2005.

[60] J. Galpin, A. Naudin, L. Vervisch, C. Angelberger, O. Colin, and P. Domingo. Large-eddy simulation of a fuel-lean premixed turbulent swirl-burner. *Combust. Flame*, 155: 247–266, 2008.

[61] M. Germano, U. Piomelli, P. Moin, and W. H. Cabot. A dynamic subgrid-scale eddy viscosity model. *Phys. Fluids A*, 3(7):1760–1765, 1991.

[62] C. H. Gibson. Fine Structure of Scalar Fields Mixed by Turbulence. I. ZeroGradient Points and Minimal Gradient Surfaces. *Phys. Fluids*, 11(11):2305–2315, 1968.

[63] O. Gicquel, N. Darabiha, and D. Thévenin. Laminar premixed hydrogen/air counterflow flame simulations using flame prolongation of ILDM with differential diffusion. *Proc. Combust. Inst.*, 28(2):1901 – 1908, 2000.

[64] D. G. Goodwin. Cantera. http://code.google.com/p/cantera, 2009.

[65] F. C. Gouldin. An Application of Fractals to Modeling Premixed Turbulent Flames. *Combust. Flame*, 68:249–266, 1987.

[66] J. D. Gounder, A. Kourmatzis, and A. R. Masri. Turbulent piloted dilute spray flames: Flow fields and droplet dynamics. *Combust. Flame*, 159(11):3372 – 3397, 2012.

[67] I. R. Gran, T. Echekki, and J. H. Chen. Negative flame speed in an unsteady 2-D premixed flame: A computational study. *Proc. Combust. Inst.*, 26(1):323 – 329, 1996.

[68] A. Gruber, E. R. Hawkes, J. H. Chen, and R. Sankaran. Turbulent flame-wall interaction: a direct numerical simulation study. *J. Fluid Mech.*, 658:5–32, 2010.

[69] Ö. L. Gülder and G. J. Smallwood. Inner cutoff scale of flame surface wrinkling in turbulent premixed flames. *Combust. Flame*, 103(12):107 – 114, 1995.

[70] F. H. Harlow and J. E. Welch. Numerical Calculation of Time-Dependent Viscous Incompressible Flow of Fluid with Free Surface. *Phys. Fluids*, 8(12):2182–2189, 1965.

[71] G. Hartung, J. Hult, C. F. Kaminski, J. W. Rogerson, and N. Swaminathan. Effect of heat release on turbulence and scalar-turbulence interaction in premixed combustion. *Phys. Fluids*, 20(3):035110, 2008.

[72] E. R. Hawkes and J. H. Chen. Comparison of direct numerical simulation of lean premixed methaneair flames with strained laminar flame calculations. *Combust. Flame*, 144 (12):112 – 125, 2006.

[73] D. C. Haworth and T. J. Poinsot. Numerical simulations of Lewis number effects in turbulent premixed flames. *J. Fluid Mech.*, 244:405–436, 11 1992.

[74] J. O. Hirschfelder, C. F. Curtiss, and R. B. Bird. *Molecular theory of gases and liquids*. John Wiley & Sons, 1966.

[75] M. Ihme and H. Pitsch. Modeling of radiation and nitric oxide formation in turbulent nonpremixed flames using a flamelet/progress variable formulation. *Phys. Fluids*, 20(5): 055110, 2008.

[76] M. Ihme, L. Shunn, and J. Zhang. Regularization of reaction progress variable for application to flamelet-based combustion models. *J. Comput. Phys.*, 231(23):7715 – 7721, 2012.

[77] International Energy Agency. World Energy Outlook 2015. http://www.iea.org/publications/freepublications/, 2015.

[78] International Energy Agency. Key World Energy Statistics 2015. http://www.iea.org/publications/freepublications/, 2015.

[79] B. Janus, A. Dreizler, and J. Janicka. Experiments on swirl stabilized non-premixed natural gas flames in a model gasturbine combustor. *Proc. Combust. Inst.*, 31(2):3091 – 3098, 2007.

[80] M. M. Kamal, R. S. Barlow, and S. Hochgreb. Conditional analysis of turbulent premixed and stratified flames on local equivalence ratio and progress of reaction. *Combust. Flame*, page 10.1016/j.combustflame.2015.07.026, 2015.

[81] M. M. Kamal, R. Zhou, S. Balusamy, and S. Hochgreb. Favre- and Reynolds-averaged velocity measurements: Interpreting PIV and LDA measurements in combustion. *Proc. Combust. Inst.*, 35(3):3803 – 3811, 2015.

[82] V. Katta and W. M. Roquemore. C/H atom ratio in recirculation-zone-supported premixed and nonpremixed flames. *Proc. Combust. Inst.*, 34(1):1101 – 1108, 2013.

[83] R. J. Kee, M. E. Coltrin, and P. Glarborg. *Chemically reacting flow: theory and practice*. John Wiley & Sons, 2003.

[84] A. M. Kempf. *Large-Eddy Simulation of Non-Premixed Turbulent Flames*. PhD thesis, Darmstadt University of Technology, Germany, 2003.

[85] A. M. Kempf and F. Proch. https://www.uni-due.de/ivg/fluiddynamik/, 2016.

[86] A. M. Kempf, M. Klein, and J. Janicka. Efficient Generation of Initial- and Inflow-Conditions for Transient Turbulent Flows in Arbitrary Geometries. *Flow Turbul. Combust.*, 74(1):67–84, 2005.

[87] A. M. Kempf, B. Geurts, and J. C. Oefelein. Error Analysis of Large-Eddy Simulation of the Turbulent Non-premixed Sydney Bluff-Body Flame. *Combust. Flame*, 158:2408–2419, 2011.

[88] A. M. Kempf, S. Wysocki, and M. Pettit. An Efficient, Parallel Low-Storage Implementation of Klein's Turbulence Generator for LES and DNS. *Comput. Fluids*, 60:58–60, 2012.

[89] C. A. Kennedy, M. H. Carpenter, and R. M. Lewis. Low-storage, explicit Runge-Kutta schemes for the compressible Navier-Stokes equations. *Appl. Numer. Math.*, 35(3):177 – 219, 2000.

[90] D. I. Ketcheson. Runge-Kutta methods with minimum storage implementations. *J. Comput. Phys.*, 229(5):1763 – 1773, 2010.

[91] A. Ketelheun, G. Kuenne, and J. Janicka. Heat Transfer Modeling in the Context of Large Eddy Simulation of Premixed Combustion with Tabulated Chemistry. *Flow Turbul. Combust.*, 91:867–893, 2013.

[92] J. Kim and P. Moin. Application of a fractional-step method to incompressible Navier-Stokes equations. *J. Comput. Phys.*, 59(2):308 – 323, 1985.

[93] J. Kim, P. Moin, and R. Moser. Turbulence statistics in fully developed channel flow at low Reynolds number. *J. Fluid Mech.*, 177:133–166, 1987.

[94] M. Klein, A. Sadiki, and J. Janicka. A digital filter based generation of inflow data for spatially developing direct numerical or large eddy simulations. *J. Comput. Phys.*, 186: 652–665, 2003.

[95] M. Klein, N. Chakraborty, K. W. Jenkins, and R. S. Cant. Effects of initial radius on the propagation of premixed flame kernels in a turbulent environment. *Phys. Fluids*, 18(5): 055102, 2006.

[96] M. Klein, N. Chakraborty, and R. S. Cant. Effects of Turbulence on Self-sustained Combustion in Premixed Flame Kernels: A Direct Numerical Simulation (DNS) Study. *Flow Turbul. Combust.*, 81(4):583–607, 2008.

[97] M. Klein, N. Chakraborty, and Y. Gao. Scale similarity based models and their application to subgrid scale scalar flux modelling in the context of turbulent premixed flames. *Int. J. Heat Fluid Flow*, 57:91 – 108, 2016.

[98] M. Klein, N. Chakraborty, and M. Pfitzner. Analysis of the Combined Modelling of Sub-grid Transport and Filtered Flame Propagation for Premixed Turbulent Combustion. *Flow Turbul. Combust.*, pages 1–18, 2016.

[99] R. Knikker, D. Veynante, and C. Meneveau. A dynamic flame surface density model for large eddy simulation of turbulent premixed combustion. *Phys. Fluids*, 16(11):L91–L94, 2004.

[100] A. N. Kolmogorov. The Local Structure of Turbulence in Incompressible Viscous Fluid for Very Large Reynolds Numbers. *Proc. R. Soc. A*, 434:9 – 13, 1991.

[101] G. Kuenne, A. Ketelheun, and J. Janicka. LES modeling of premixed combustion using a thickened flame approach coupled with FGM tabulated chemistry. *Combust. Flame*, 158(9):1750 – 1767, 2011.

[102] G. Kuenne, F. Seffrin, F. Fuest, T. Stahler, A. Ketelheun, D. Geyer, J. Janicka, and A. Dreizler. Experimental and numerical analysis of a lean premixed stratified burner using 1D Raman/Rayleigh scattering and large eddy simulation. *Combust. Flame*, 159 (8):2669 – 2689, 2012.

[103] O. Lammel, M. Stöhr, P. Kutne, C. Dem, W. Meier, and M. Aigner. Experimental Analysis of Confined Jet Flames by Laser Measurement Techniques. *J. Eng. Gas Turb. Power*, 134(4):041506–041506, 2012.

[104] J. Lamouroux, M. Ihme, B. Fiorina, and O. Gicquel. Tabulated chemistry approach for diluted combustion regimes with internal recirculation and heat losses. *Combust. Flame*, 161(8):2120 – 2136, 2014.

[105] I. Langella, N. Swaminathan, Y. Gao, and N. Chakraborty. Assessment of dynamic closure for premixed combustion large eddy simulation. *Combust. Theory Model.*, 19(5): 628–656, 2015.

[106] E. V. Lavante and R. A. Strehlow. The mechanism of lean limit flame extinction. *Combust. Flame*, 49(13):123 – 140, 1983.

[107] J. P. Legier, T. J. Poinsot, and D. Veynante. Dynamically thickened flame LES model for premixed and non-premixed turbulent combustion. *Proceedings of the Summer Programm, Center for Turbulence Research, Stanford*, pages 157–168, 2000.

[108] D. K. Lilly. A proposed modification of the Germano subgridscale closure method. *Phys. Fluids A*, 4(3):633–635, 1992.

[109] A. N. Lipatnikov, J. Chomiak, V. A. Sabelnikov, S. Nishiki, and T. Hasegawa. Unburned mixture fingers in premixed turbulent flames. *Proc. Combust. Inst.*, 35(2):1401 – 1408, 2015.

[110] T. S. Lund, X. Wu, and K. D. Squires. Generation of Turbulent Inflow Data for Spatially-Developing Boundary Layer Simulations. *J. Comput. Phys.*, 140(2):233–258, Mar. 1998.

[111] T. Ma, O. Stein, N. Chakraborty, and A. M. Kempf. A-posteriori testing of Algebraic Flame Surface Density models for LES. *Combust. Theory Model.*, 17(3):431–482, 2013.

[112] T. Ma, O. T. Stein, N. Chakraborty, and A. M. Kempf. A posteriori testing of the flame surface density transport equation for LES. *Combust. Theory Model.*, 18(1):32–64, 2014.

[113] U. Maas and S. B. Pope. Simplifying chemical kinetics: Intrinsic low-dimensional manifolds in composition space. *Combust. Flame*, 88(34):239 – 264, 1992.

[114] B. Marracino and D. Lentini. Radiation Modelling in Non-Luminous Nonpremixed Turbulent Flames. *Combust. Sci. Technol.*, 128(1-6):23–48, 1997.

[115] G. Marsaglia. Random Number Generators. *J. Mod. App. Stat. Meth.*, 2(1):2 – 13, 2003.

[116] B. J. McBride, S. Gordon, and M. A. Reno. Coefficients for Calculating Thermodynamic and Transport Properties of Individual Species. Technical Report TM-4513, NASA, 1993.

[117] W. Meier, P. Weigand, X. R. Duan, and R. Giezendanner-Thoben. Detailed characterization of the dynamics of thermoacoustic pulsations in a lean premixed swirl flame. *Combust. Flame*, 150(12):2 – 26, 2007.

[118] S. Menon, P. K. Yeung, and W. W. Kim. Effect of subgrid models on the computed interscale energy transfer in isotropic turbulence. *Comput. Fluids*, 25(2):165 – 180, 1996.

[119] R. Mercier, B. Fiorina, F. Proch, and A. M. Kempf. Numerical and modeling strategies for the simulation of the Cambridge stratified flame series. In *TSFP digital library online*. Begel House Inc., 2013.

[120] R. Mercier, T. Schmitt, D. Veynante, and B. Fiorina. The influence of combustion SGS submodels on the resolved flame propagation. Application to the LES of the Cambridge stratified flames. *Proc. Combust. Inst.*, 35(2):1259 – 1267, 2015.

[121] P. Moin and K. Mahesh. Direct numerical simulation: A tool in turbulence research. *Annu. Rev. Fluid Mech.*, 30:539–578, 1998.

[122] P. Moin, K. Squires, W. Cabot, and S. Lee. A dynamic subgridscale model for compressible turbulence and scalar transport. *Phys. Fluids A*, 3(11):2746–2757, 1991.

[123] V. Moureau, B. Fiorina, and H. Pitsch. A level set formulation for premixed combustion LES considering the turbulent flame structure. *Combust. Flame*, 156(4):801 – 812, 2009.

[124] V. Moureau, P. Domingo, and L. Vervisch. From Large-Eddy Simulation to Direct Numerical Simulation of a lean premixed swirl flame: Filtered laminar flame-PDF modeling. *Combust. Flame*, 158(7):1340 – 1357, 2011.

[125] S. P. R. Muppala, N. K. Aluri, F. Dinkelacker, and A. Leipertz. Development of an algebraic reaction rate closure for the numerical calculation of turbulent premixed methane, ethylene, and propane/air flames for pressures up to 1.0 MPa. *Combust. Flame*, 140(4): 257 – 266, 2005.

[126] S. Nambully, P. Domingo, V. Moureau, and L. Vervisch. A filtered-laminar-flame PDF sub-grid scale closure for LES of premixed turbulent flames. Part I: Formalism and application to a bluff-body burner with differential diffusion. *Combust. Flame*, 161(7): 1756–1774, 2014.

[127] S. Nambully, P. Domingo, V. Moureau, and L. Vervisch. A filtered-laminar-flame PDF sub-grid-scale closure for LES of premixed turbulent flames: II. Application to a stratified bluff-body burner. *Combust. Flame*, 161(7):1775–1791, 2014.

[128] P.-D. Nguyen, L. Vervisch, V. Subramanian, and P. Domingo. Multidimensional flamelet-generated manifolds for partially premixed combustion. *Combust. Flame*, 157(1):43–61, 2010.

[129] T. M. Nguyen, F. Proch, I. Wlokas, and A. M. Kempf. Large Eddy Simulation of an Internal Combustion Engine Using an Efficient Immersed Boundary Technique. *Flow Turbul. Combust.*, 97(1):191–230, 2016.

[130] F. Nicoud and F. Ducros. Subgrid-Scale Stress Modelling Based on the Square of the Velocity Gradient Tensor. *Flow Turbul. Combust.*, 62(3):183–200, 1999.

[131] F. Nicoud, H. B. Toda, O. Cabrit, S. Bose, and J. Lee. Using singular values to build a subgrid-scale model for large eddy simulations. *Phys. Fluids*, 23(8):085106, 2011.

[132] Z. M. Nikolaou and N. Swaminathan. Direct Numerical Simulation of Complex Fuel Combustion with Detailed Chemistry: Physical Insight and Mean Reaction Rate Modeling. *Combust. Sci. Technol.*, 187(11):1759–1789, 2015.

[133] S. Nishiki, T. Hasegawa, R. Borghi, and R. Himeno. Modeling of flame-generated turbulence based on direct numerical simulation databases. *Proc. Combust. Inst.*, 29(2):2017 – 2022, 2002.

[134] Y.-S. Niu, L. Vervisch, and P. D. Tao. An optimization-based approach to detailed chemistry tabulation: Automated progress variable definition. *Combust. Flame*, 160(4):776 – 785, 2013.

[135] C. Olbricht, O. T. Stein, J. Janicka, J. A. van Oijen, S. Wysocki, and A. M. Kempf. LES of lifted flames in a gas turbine model combustor using top-hat filtered PFGM chemistry. *Fuel*, 96:100–107, 2012.

[136] S. Patankar. *Numerical heat transfer and fluid flow*. CRC Press, 1980.

[137] N. Peters. A spectral closure for premixed turbulent combustion in the flamelet regime. *J. Fluid Mech.*, 242:611–629, 9 1992.

[138] N. Peters. The turbulent burning velocity for large-scale and small-scale turbulence. *J. Fluid Mech.*, 384:107–132, 4 1999.

[139] N. Peters. *Turbulent Combustion*. Cambridge University Press, 2000.

[140] N. Peters and J. Warnatz. *Numerical Methods in Laminar Flame Propagation*. Vieweg+Teubner Verlag, 1st edition, 1982.

[141] B. Peterson, E. Baum, B. Böhm, and A. Dreizler. Early flame propagation in a spark-ignition engine measured with quasi 4D-diagnostics. *Proc. Combust. Inst.*, 35(3):3829 – 3837, 2015.

[142] M. Pettit, B. Coriton, A. Gomez, and A. M. Kempf. Large-Eddy Simulation and Experiments on Non-Premixed Highly Turbulent Opposed Jet Flows. *Proc. Combust.Inst.*, 33: 1391–1399, 2011.

[143] M. W. A. Pettit. *A Joint Eulerian-Lagrangian Method for the Solution of Multi-Scale Flow Problems*. PhD thesis, Imperial College London, 2013.

[144] C. D. Pierce. *Progress-variable approach for large-eddy simulation of turbulent combustion*. PhD thesis, Stanford University, 2001.

[145] C. D. Pierce and P. Moin. Progress-variable approach for large-eddy simulation of non-premixed turbulent combustion. *J. Fluid Mech.*, 504:73–97, 2004.

[146] U. Piomelli and J. Liu. Large-eddy simulation of rotating channel flows using a localized dynamic model. *Phys. Fluids*, 7(4):839–848, 1995.

[147] H. Pitsch. A consistent level set formulation for large-eddy simulation of premixed turbulent combustion. *Combust. Flame*, 143(4):587 – 598, 2005.

[148] H. Pitsch and H. Steiner. Scalar mixing and dissipation rate in Large-Eddy Simulations of non-premixed turbulent combustion. *Proc. Combust. Inst.*, 28:41–49, 2000.

[149] H. Pitsch and H. Steiner. Large-eddy simulation of a turbulent piloted methane/air diffusion flame (Sandia flame D). *Phys. Fluids*, 12(10):2541–2554, 2000.

[150] R. H. Pletcher, J. C. Tannehill, and D. Anderson. *Computational fluid mechanics and heat transfer*. CRC Press, 2012.

[151] T. J. Poinsot and S. K. Lelef. Boundary conditions for direct simulations of compressible viscous flows. *J. Comput. Phys.*, 101(1):104 – 129, 1992.

[152] T. J. Poinsot and D. Veynante. *Theoretical and Numerical Combustion*. Aquaprint, Bordeaux, France, 3rd edition, 2012.

[153] T. J. Poinsot, S. Candel, and A. Trouvé. Applications of Direct Numerical Simulation to premixed turbulent combustion. *Prog. Energ. Combust.*, 21:531–576, 1996.

[154] A. Y. Poludnenko and E. S. Oran. The interaction of high-speed turbulence with flames: Global properties and internal flame structure. *Combust. Flame*, 157(5):995 – 1011, 2010.

[155] A. Y. Poludnenko and E. S. Oran. The interaction of high-speed turbulence with flames: Turbulent flame speed. *Combust. Flame*, 158(2):301 – 326, 2011.

[156] S. B. Pope. The evolution of surfaces in turbulence. *Int. J. Eng. Sci.*, 26(5):445 – 469, 1988.

[157] S. B. Pope. *Turbulent Flows*. Cambridge University Press, 2000.

[158] F. Proch and A. M. Kempf. Numerical analysis of the Cambridge stratified flame series using artificial thickened flame LES with tabulated premixed flame chemistry. *Combust. Flame*, 161(10):2627 – 2646, 2014.

[159] F. Proch and A. M. Kempf. Modeling heat loss effects in the large eddy simulation of a model gas turbine combustor with premixed flamelet generated manifolds. *Proc. Combust. Inst.*, 35(3):3337 – 3345, 2015.

[160] F. Proch, M. W. A. Pettit, T. Ma, M. Rieth, and A. M. Kempf. *Direct and Large-Eddy Simulation IX*, chapter Investigations on the Effect of Different Subgrid Models on the Quality of LES Results, pages 141–147. Springer International Publishing, Cham, 2015. ISBN 978-3-319-14448-1.

[161] F. Proch, P. Domingo, L. Vervisch, and A. M. Kempf. Flame resolved simulation of a turbulent premixed bluff-body burner experiment. Part I: Analysis of the reaction zone dynamics with tabulated chemistry. *Combust. Flame*, 2017. *http://dx.doi.org/10.1016/j.combustflame.2017.02.011*.

[162] F. Proch, P. Domingo, L. Vervisch, and A. M. Kempf. Flame resolved simulation of a turbulent premixed bluff-body burner experiment. Part II: A-priori and a-posteriori investigation of sub-grid scale wrinkling closures in the context of artificially thickened flame modeling. *Combust. Flame*, 2017. *http://dx.doi.org/10.1016/j.combustflame.2017.02.012*.

[163] U. Prüfert, S. Hartl, F. Hunger, D. Messig, M. Eiermann, and C. Hasse. A Constrained Control Approach for the Automated Choice of an Optimal Progress Variable for Chemistry Tabulation. *Flow Turbul. Combust.*, 94(3):593–617, 2015.

[164] M. Rabaçal, B. M. Franchetti, F. Cavallo Marincola, F. Proch, M. Costa, C. Hasse, and A. M. Kempf. Large Eddy Simulation of coal combustion in a large-scale laboratory furnace. *Proc. Combust. Inst.*, 35(3):3609 – 3617, 2015.

[165] M. M. Rai and P. Moin. Direct Simulations of Turbulent Flow Using Finite-Difference Schemes. *J. Comput. Phys.*, 96:15–53, 1991.

[166] C. M. Rhie and W. L. Chow. Numerical Study of the Turbulent Flow Past an Airfoil with Trailing Edge Separation. *AIAA J.*, 21(11):1525–1532, 1983.

[167] S. Richard, O. Colin, O. Vermorel, A. Benkenida, C. Angelberger, and D. Veynante. Towards large eddy simulation of combustion in spark ignition engines. *Proc. Combust. Inst.*, 31(2):3059–3066, 2007.

[168] E. S. Richardson, R. Sankaran, R. W. Grout, and J. H. Chen. Numerical analysis of reaction-diffusion effects on species mixing rates in turbulent premixed methane-air combustion. *Combust. Flame*, 157(3):506 – 515, 2010.

[169] L. F. Richardson. *Weather Prediction by Numerical Process*. Cambridge University Press, 2nd edition, 2007.

[170] M. Rieth, F. Proch, O. T. Stein, M. W. A. Pettit, and A. M. Kempf. Comparison of the Sigma and Smagorinsky LES models for grid generated turbulence and a channel flow. *Comput. Fluids*, 99(0):172 – 181, 2014.

[171] A. Rittler, F. Proch, and A. M. Kempf. LES of the Sydney piloted spray flame series with the PFGM/ATF approach and different sub-filter models. *Combust. Flame*, 162(4):1575 – 1598, 2015.

[172] P. Roe. Characteristic-based schemes for the Euler equations. *Ann. Rev. Fluid Mech.*, 18 (1):337–365, 1986.

[173] D. H. Rudy and J. C. Strikwerda. A nonreflecting outflow boundary condition for subsonic navier-stokes calculations. *J. Comput. Phys.*, 36(1):55 – 70, 1980.

[174] C. J. Rutland and R. S. Cant. Turbulent transport in premixed flames. *Proceedings of the Summer Programm, Center for Turbulence Research, Stanford*, pages 75–94, 1994.

[175] C. J. Rutland and A. Trouvé. Direct simulations of premixed turbulent flames with nonunity Lewis numbers. *Combust. Flame*, 94(12):41 – 57, 1993.

[176] R. Sankaran, E. R. Hawkes, J. H. Chen, T. Lu, and C. K. Law. Structure of a spatially developing turbulent lean methane-air Bunsen flame. *Proc. Combust. Inst.*, 31(1):1291 – 1298, 2007.

[177] R. Sankaran, E. R. Hawkes, C. S. Yoo, and J. H. Chen. Response of flame thickness and propagation speed under intense turbulence in spatially developing lean premixed methane-air jet flames. *Combust. Flame*, 162(9):3294 – 3306, 2015.

[178] R. F. Sawyer. Science based policy for addressing energy and environmental problems. *Proc. Combust. Inst.*, 32(1):45 – 56, 2009.

[179] P. Schmitt, T. J. Poinsot, B. Schuermans, and K. Geigle. Large-eddy simulation and experimental study of heat transfer, nitric oxide emissions and combustion instability in a swirled turbulent high-pressure burner. *J. Fluid Mech.*, 570(1):17–46, 2007.

[180] T. Schmitt, A. Sadiki, B. Fiorina, and D. Veynante. Impact of dynamic wrinkling model on the prediction accuracy using the F-TACLES combustion model in swirling premixed turbulent flames. *Proc. Combust. Inst.*, 34(1):1261 – 1268, 2013.

[181] Y. C. See and M. Ihme. Large eddy simulation of a partially-premixed gas turbine model combustor. *Proc. Combust. Inst.*, 35(2):1225 – 1234, 2015.

[182] F. Seffrin, F. Fuest, D. Geyer, and A. Dreizler. Flow field studies of a new series of turbulent premixed stratified flames. *Combust. Flame*, 157(2):384 – 396, 2010.

[183] L. Selle, F. Nicoud, and T. J. Poinsot. Actual Impedance of Nonreflecting Boundary Conditions: Implications for Computation of Resonators. *AIAA Journal*, 42(5):958–964, 2016.

[184] Y. Shoshin, L. Tecce, and J. Jarosinski. Experimental and Computational Study of Lean Limit Methane-Air Flame Propagating Upward in a 24mm Diameter Tube. *Combust. Sci. Technol.*, 180(10-11):1812–1828, 2008.

[185] N. Sikalo, O. Hasemann, C. Schulz, A. M. Kempf, and I. Wlokas. A Genetic Algorithm-Based Method for the Automatic Reduction of Reaction Mechanisms. *Int. J. Chem. Kinet.*, 46(1):41–59, Jan. 2014.

[186] N. Sikalo, O. Hasemann, C. Schulz, A. M. Kempf, and I. Wlokas. A Genetic Algorithm-Based Method for the Optimization of Reduced Kinetics Mechanisms. *Int. J. Chem. Kinet.*, 47(11):695–723, Nov. 2015.

[187] J. S. Smagorinsky. General Circulation Experiments with the Primitive Equations, 1, The Basic Experiment. *Mon. Weather Rev.*, 91(1):99–164, 1963.

[188] G. P. Smith, D. M. Golden, M. Frenklach, N. W. Moriarty, B. Eiteneer, M. Goldenberg, C. T. Bowman, R. K. Hanson, S. Song, W. C. Gardiner, Jr., V. V. Lissianski, and Z. Qin. http://www.me.berkeley.edu/gri_mech, 2000.

[189] T. Sponfeldner, I. Boxx, F. Beyrau, Y. Hardalupas, W. Meier, and A. M. K. P. Taylor. On the alignment of fluid-dynamic principal strain-rates with the 3D flamelet-normal in a premixed turbulent V-flame. *Proc. Combust. Inst.*, 35(2):1269 – 1276, 2015.

[190] O. Stein. *Large Eddy Simulation of Combustion in Swirling and Opposed Jet Flows*. PhD thesis, Imperial College London, 2008.

[191] A. M. Steinberg, J. F. Driscoll, and N. Swaminathan. Statistics and dynamics of turbulence-flame alignment in premixed combustion. *Combust. Flame*, 159(8):2576 – 2588, 2012.

[192] W. Sutherland. LII. The viscosity of gases and molecular force. *Philosophical Magazine Series 5*, 36(223):507–531, 1893.

[193] P. K. Sweby. High resolution schemes using flux limiters for hyperbolic conservation laws. *SIAM journal on numerical analysis*, 21(5):995–1011, 1984.

[194] M. S. Sweeney, S. Hochgreb, M. J. Dunn, and R. S. Barlow. The structure of turbulent stratified and premixed methane/air flames I: Non-swirling flows. *Combust. Flame*, 159 (9):2896 – 2911, 2012.

[195] M. S. Sweeney, S. Hochgreb, M. J. Dunn, and R. S. Barlow. The structure of turbulent stratified and premixed methane/air flames II: Swirling flows. *Combust. Flame*, 159(9): 2912 – 2929, 2012.

[196] M. Tanahashi, M. Fujimura, and T. Miyauchi. Coherent fine-scale eddies in turbulent premixed flames. *Proc. Combust. Inst.*, 28(1):529 – 535, 2000.

[197] L. Tay Wo Chong, T. Komarek, M. Zellhuber, J. Lenz, C. Hirsch, and W. Polifke. Influence of strain and heat loss on flame stabilization in a non-adiabatic combustor. *Proceedings of the European Combustion Meeting*, 4, 2009.

[198] A. S. Tomlin, T. Turányi, and M. J. Pilling. Mathematical tools for the construction, investigation and reduction of combustion mechanisms. In M. J. Pilling, editor, *Low-Temperature Combustion and Autoignition*, volume 35 of *Comprehensive Chemical Kinetics*, chapter 4, pages 293 – 437. Elsevier, 1997.

[199] P. Trisjono, K. Kleinheinz, H. Pitsch, and S. Kang. Large Eddy Simulation of Stratified and Sheared Flames of a Premixed Turbulent Stratified Flame Burner Using a Flamelet Model with Heat Loss. *Flow Turbul. Combust.*, 92(1-2):201–235, 2014.

[200] A. Trouvé and T. J. Poinsot. The evolution equation for the flame surface density in turbulent premixed combustion. *J. Fluid Mech.*, 278:1–31, 1994.

[201] B. Van Leer. Towards the ultimate conservative difference scheme. II. Monotonicity and conservation combined in a second-order scheme. *J. Comput. Phys.*, 14(4):361–370, 1974.

[202] J. A. van Oijen and L. P. H. de Goey. Modelling of Premixed Laminar Flames using Flamelet-Generated Manifolds. *Combust. Sci. Technol.*, 161(1):113–137, 2000.

[203] J. A. van Oijen, R. J. M. Bastiaans, G. R. A. Groot, and L. P. H. De Goey. Direct Numerical Simulations of Premixed Turbulent Flames with Reduced Chemistry: Validation and Flamelet Analysis. *Flow Turbul. Combust.*, 75(1-4):67–84, 2005.

[204] J. A. van Oijen, R. J. M. Bastiaans, and L. P. H. de Goey. Low-dimensional manifolds in direct numerical simulations of premixed turbulent flames. *Proc. Combust. Inst.*, 31(1): 1377–1384, 2007.

[205] D. Veynante and V. Moureau. Analysis of dynamic models for large eddy simulations of turbulent premixed combustion. *Combust. Flame*, 162(12):4622–4642, 2015.

[206] D. Veynante, T. Schmitt, M. Boileau, and V. Moureau. Analysis of dynamic models for turbulent premixed combustion. *Proceedings of the Summer Programm, Center for Turbulence Research, Stanford*, pages 387–396, 2012.

[207] A. W. Vreman. An eddy-viscosity subgrid-scale model for turbulent shear flow: Algebraic theory and applications. *Phys. Fluids*, 16(10):3670–3681, 2004.

[208] A. W. Vreman, B. A. Albrecht, J. A. van Oijen, L. P. H. de Goey, and R. J. M. Bastiaans. Premixed and nonpremixed generated manifolds in large-eddy simulation of Sandia flame D and F. *Combust. Flame*, 153(3):394 – 416, 2008.

[209] A. W. Vreman, J. A. Oijen, L. P. H. DeGoey, and R. J. M. Bastiaans. Subgrid Scale Modeling in Large-Eddy Simulation of Turbulent Combustion Using Premixed Flamelet Chemistry. *Flow Turbul. Combust.*, 82(4):511–535, 2009.

[210] A. W. Vreman, J. A. van Oijen, L. P. H. de Goey, and R. J. M. Bastiaans. Direct numerical simulation of hydrogen addition in turbulent premixed Bunsen flames using flamelet-generated manifold reduction. *Int. J. Hydrogen Energ.*, 34(6):2778 – 2788, 2009.

[211] G. Wang, M. Boileau, and D. Veynante. Implementation of a dynamic thickened flame model for large eddy simulations of turbulent premixed combustion. *Combust. Flame*, 158(11):2199 – 2213, 2011.

[212] N. P. Waterson and H. Deconinck. Design principles for bounded higher-order convection schemes a unified approach. *J. Comput. Phys.*, 224(1):182 – 207, 2007.

[213] H. G. Weller, G. Tabor, A. D. Gosman, and C. Fureby. Application of a flame-wrinkling les combustion model to a turbulent mixing layer. *Proc. Combust. Inst.*, 27(1):899–907, 1998.

[214] C. R. Wilke. A viscosity equation for gas mixtures. *J. Chem. Phys.*, 18(4):517–519, 1950.

[215] J. H. Williamson. Low-Storage Runge-Kutta Schemes. *J. Comput. Phys.*, 35(1):48–56, 1980.

[216] I. Wlokas. *Simulation von Mehrkomponenten-Strömungen bei kleinen Mach-Zahlen*. PhD thesis, University of Duisburg-Essen, Germany, 2006.

[217] I. Wlokas, A. Faccinetto, B. Tribalet, C. Schulz, and A. M. Kempf. Mechanism of Iron Oxide Formation from Iron Pentacarbonyl-Doped Low-Pressure Hydrogen/Oxygen Flames. *Int. J. Chem. Kinet.*, 45(8):487–498, 2013.

[218] H. Yamashita, M. Shimada, and T. Takeno. A numerical study on flame stability at the transition point of jet diffusion flames. *Symp. (Int.) on Combust.*, 26(1):27 – 34, 1996.

[219] G. Zhou. *Numerical simulations of physical discontinuities in single and multi-fluid flows for arbitrary Mach numbers*. PhD thesis, Chalmers University of Technology, Goteborg, Sweden, 1995.

[220] R. Zhou, S. Balusamy, M. S. Sweeney, R. S. Barlow, and S. Hochgreb. Flow field measurements of a series of turbulent premixed and stratified methane/air flames. *Combust. Flame*, 160(10):2017 – 2028, 2013.